CURRENT RESEARCH IN ENGINEERING

EDITORS

ASSOC. PROF. DR. SELAHATTIN BARDAK

MARCH 2022

Current Research in Engineering

March 2022

CONTENTS

CHAPTER 1

INDOORS THERMAL COMFORT IN MOSQUES AND AFFECTING FACTORS

Mariam SHEHATA[1], Uğur ÖZCAN [2]

1 Architect, FSM Vakıf University, Graduate School of Education, Department of Architecture, Masters of Architecture, Istanbul, Turkey, e-mail: mariam.shehata@ stu.fsm.edu.tr (ORCID: 0000-0003-2654-8157)

2 Assist. Prof. Dr., FSM Vakıf University, Faculty of Architecture and Design, Department of Architecture, Istanbul, Turkey, e-mail: uozcan@fsm.edu.tr (ORCID: 0000-0003-0002-4478)

The building industry's demand has grown in proportion to the growth of the cities' population. Since people spend 85-90 percent of their time indoors, it is has become crucial that their comfort levels are met (Atmaca & Zorer Gedik, 2017, 1254). This comfort ranges from visual and physical comfort, all the way to thermal comfort as well. Simultaneously, the built environment has become the world's largest energy consumer in the mission to provide the users with required comfort levels indoors, accounting for 40-50 percent of global resources (Azmi et al., 2021, p. 5), and this has caused many drawbacks to the environment such as depletion of resources and pollution.

With urbanization and the booming of the industrial industry, the need for buildings that meet the community's spiritual needs, such as Mosques, has also increased. Mosques have been an essential structure to Muslim communities as mosques have been utilized for a variety of purposes, including prayer (salah), remembrance of Allah's name (dhikr), reading the Quran, religious classes (madrassa), and many other social and charitable activities. Therefore, mosques in particular require special attention when it comes to achieving indoor comfort levels in order to achieve a sense of peace, quiet, and a spiritual state for the worshipers (Ibrahim et al., 2014, p. 327).

Being the center of Muslim communities and significantly to the social aspect of sustainability, mosques are often accompanied by high-quality construction and architectural works. However, it has been observed that the environmental aspect of sustainability and energy efficiency have been ignored for many years. Studies on contemporary mosques have shown that modern-day mosques consume an excessive amount of electricity (Harsritanto et al., 2021, p. 723), and despite the high operational costs, low levels of comfort in terms of indoor temperature and humidity have been detected (Azmi et al., 2021, p. 5).

On the other hand, it is also visible that historic mosques seem to meet the comfort levels of worshipers, especially thermal comfort, in a superior manner than recently build contemporary mosques. The goal of this study is to investigate the link between energy efficiency and indoor thermal comfort in contemporary mosques, as well as to identify potential solutions and variables to consider when constructing a mosque in today's environment.

THERMAL COMFORT AND ENERGY EFFICIENCY IN MOSQUES

It is critical to investigate the elements that influence indoor thermal comfort and their effect on energy efficiency. The operation schedule, location and environment, design parameters and envelope thermal design,

and the dimensions of the prayer hall are all important aspects that impact thermal comfort. This section will be discussing the formerly mentioned factors simultaneously.

Operation Program

Regionally, all mosques would be more or less operating at the time of the day due to the fixed time of the prayers. Intermittently occupied five times a day all year round, prayers usually do not arrive or leave the mosque at the exact same time around prayer times. In addition, each of the five daily prayers usually lasts 30-45 minutes, while the weekly Friday prayer takes about two hours, including the Friday sermon before, and sometimes after, prayer is commenced. Moreover, the occupancy rate can drop to only 10 to 30 percent of the weekly Friday prayer on daily prayers (Azmi et al., 2021, p. 1). An exception to this usage is the Tarawih prayer (in Ramadan) and other special occasions such as lectures and seminars where users tend to stay longer in the mosque (Abdou et al., 2005, p. 166).

Three mosques in Johor, Malaysia were chosen for a case study by Azmi and Kandar. The number of users for different prayers was counted and the average of daily prayers was calculated separately for weekdays and weekends. The average number of users for the Friday prayer accounted for 100 percent of the maximum occupancy rate for each mosque and accordingly, the average peak number of occupants for the five daily prayers was calculated as shown in figure 1 below. The results clearly show a variation in the occupancy rate and all three mosques had significantly fewer occupants for daily prayers compared to Friday prayers (Azmi and Kandar, 2019, p. 32-34). As a result, mosques are characterized by having a unique occupation schedule compared to other building types.
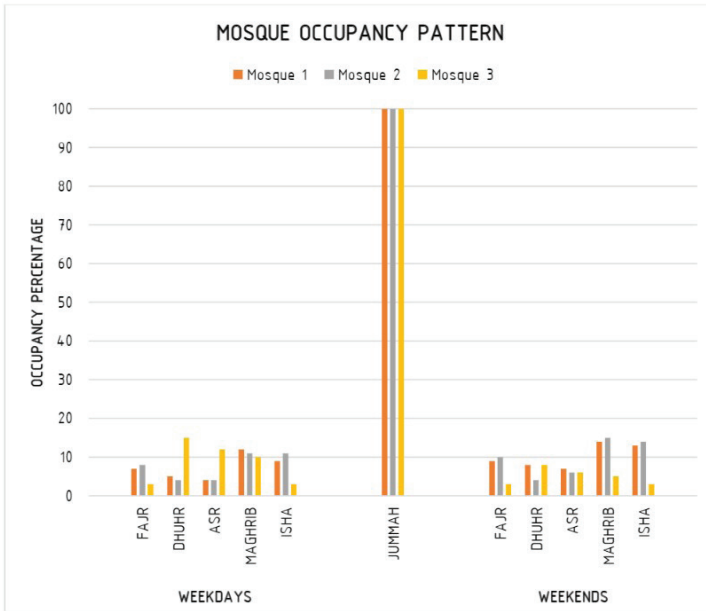
Figure 1: Occupancy model for case mosques (Azmi and Kandar, 2019, p. 21)

This occupancy model makes it difficult to maintain constant thermal comfort throughout the day. Mechanical heating, ventilation, and air-conditioning (HVAC) systems are common in modern mosques, and these systems frequently follow prayer and occupancy schedules, while remaining closed in the period between prayers. This can reduce user comfort, and because the prayer hall is a huge area with high ceilings, an excessive quantity of energy is required, which can be up to three times the amount of energy used in an office (Azmi et al., 2021, p. 5). To ensure thermal comfort while reducing energy loss, a proposed alternative would be to design a distinct spatial zoning system for high and low occupancy rates as shown in figure 2. (Azmi and Kandar, 2019, p.32-34).
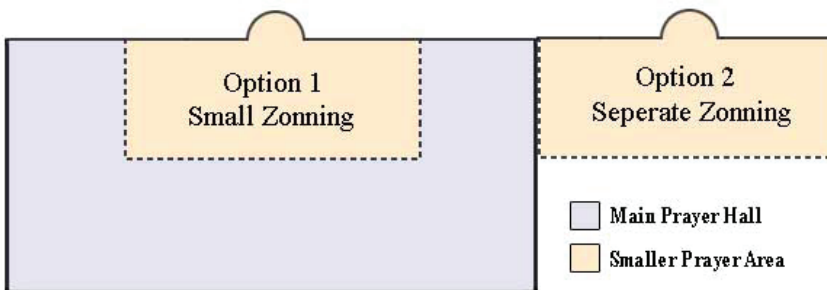
Figure 2: Suggested solution for high and low occupancy (Azmi and Kandar, 2019, p.32-34)

Location and Environment

The building's thermal performance and energy efficiency can be influenced by its location and surroundings (Azmi et al., 2021, p. 6). Thermal comfort in mosques is an important functional need and a major factor of their performance in hot regions like Saudi Arabia. In such temperatures, most mosques are fitted with air conditioning and ceiling fans to ensure thermal comfort, resulting in high energy consumption (Budaiwi & Abdou, 2013, p.37). This can have a significant impact on energy usage, particularly if it is not adequately planned.

The electrical energy use statistics of mosques for the whole twelve months of 2002 were tracked in research done in the Saudi Arabian towns of Dammam and Al-Khobar, and it was discovered that the HVAC system is the highest energy consumer among air conditioning systems (Al-Homoud et al., 2009, p. 609). Due to its reliance on multiple passive cooling strategies, a study of more than fifty mosques in Baghdad indicated that old mosques performed better and consumed less energy than modern mosques partially due to the suitability of the location chosen (Azmi et al., 2021, p. 6). Various studies reveal that owing to the compact urban layout and the choice of materials with thermal mass suited for climatic circumstances, historic buildings often have lower thermal loads (Azmi vd., 2021, s. 7). Therefore, the first influencer of thermal comfort and energy efficiency is determined before even the design process of plans and elevations begins.

Design Parameters and Envelope Thermal Design

Design considerations in mosques can minimize energy usage by improving the building's performance (Azmi et al., 2021, p. 7). The climate influences decisions such as window orientation, materials, and size. The more climate-friendly a structure is the more passive the design, which reduces energy consumption and improves user comfort (Alharbi and Zin, 2020, p. 5957). According to studies, adapting the mosque's facade design for the climate optimizes the mosque's thermal efficiency and results in a more than one-third decrease in energy usage (Azmi et al., 2021, p. 5).

Furthermore, the facade is an essential component of the design process. It is not only the first and most crucial point of contact between the worshipper and the mosque, but it also contributes significantly to energy efficiency. The facade, which gives natural lighting and ventilation to the inside of the building, will reduce energy usage and consequently mechanical maintenance costs, according to Baharudin and Ismail (2014). Passive design, which provides an adequate level of thermal comfort to the inside environment, may be used to create a decent facade design for urban mosques. As a result, the energy consumption in urban mosques will be

determined by the facade design, which takes into consideration passive design (Abdullah et al., 2016, p. 420). The facade design parameters are summarised in figure 3 below.
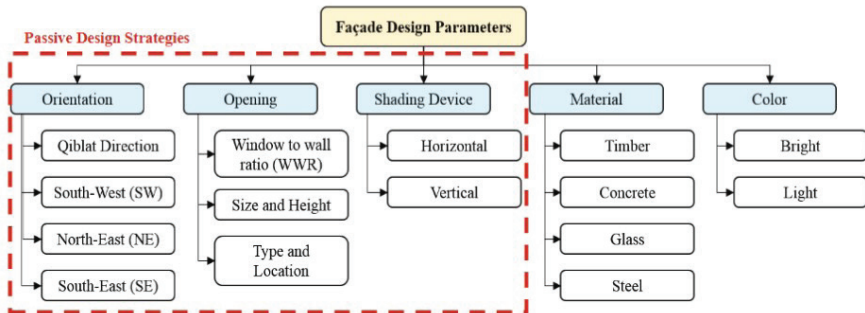
Figure 3: Facade design parameters (Abdullah et al., 2016, p. 420)

The mosque's thermal load is mostly driven by external climatic variables, with negligible contributions from equipment and occupancy loads. The most essential factor in a building's thermal performance and thermal load is the envelope thermal design. For the best performance of the building envelope, many characteristics of the walls, roof, windows, and openings must be tuned. Due to reduced heat gain through the building fabric, buildings with an improved thermal envelope have a 20 percent lower thermal load (Azmi et al., 2021, p. 9).

Prayer Hall Dimensions

There was no conclusive evidence of a direct correlation between the size of the prayer hall and its energy use. On this matter, various investigations have reached different conclusions. For example, Egyptian research found that smaller prayer areas use more energy (Abdallah, 2016, p. 288), whereas a Saudi Arabian study (Nedhal & Qathan, 2018, p. 201) found that energy consumption increases with the increase in the area of the prayer hall, demonstrating proportionate relationship. When studied over the same time period for five years, larger prayer halls were shown to use three times their overall energy consumption (Azmi et al., 2021, p. 7). Of course, other variables, such as whether the cooling and heating systems are turned on and off manually or automatically, may have influenced these findings.

As a result, while a definitive connection between the dimensions of a house of worship and its energy consumption cannot be established, it is advised, as noted before in this article, to design multiple places of worship for varied prayer capacities. The impact of such a design solution on overall energy usage, on the other hand, should be continuously monitored and assessed. It is significant to mention that the parameters discussed in this section are not the only ones that influence energy efficiency and

indoor thermal comfort. Furthermore, there are no clear distinctions between these variables. All elements interact, and combining various circumstances might result in drastically varied effects on overall energy usage and thermal comfort.

SOLUTIONS TO PROVIDE THERMAL COMFORT IN MOSQUES

This section will showcase and assess methods used in mosques to address the point of discussion (energy efficiency and indoor thermal comfort). Different aspects of a mosque will be examined individually in this section.

Layout and Volume of Prayer Hall

Prior to the development of electric illumination, the masjid's enhanced height supplied light to the deepest portions of the mosque through high windows. In warmer areas, these windows or other high openings allowed ventilation through the chimney effect, allowing the space to stay pleasant as the sun heated the air closer to the ceiling while the prayer chamber remained cool (Coşkuner Pamuk et al., 2020).

Some mosques have been built at a considerably higher height for the prayer area historically than necessary for lighting and ventilation alone. This was aimed at giving the space a grand scale so that the inside would have a spiritual quality to it. The need for such a high ceiling was reduced to sustaining a scale and proportion of the interior for psychological comfort with the introduction of mechanical ventilation and artificial lighting. Many mosques today, however, continue to develop an unnecessary grand scale prayer hall for the sole purpose of showing off.

Since a lot of energy is typically wasted controlling the temperature of such a large volume, and because of its height, most of this volume remains vacant, this spatial aspect of the hall is extremely crucial for the thermal needs. If a grand volume is necessary, the additional height can be utilized, particularly in warmer areas where the stack effect of air can be employed to the benefit of indoor thermal comfort as shown in figure 4 using the window catcher effect. Warm air will rise due to convection current, and the airflow caused by the air pressure differential will cool the interior via ventilation through the dome of the mosque. However, in air-conditioned mosques or regions with cooler climate conditions, the unnecessary volume of the prayer hall may contribute to energy loss (Azmi & Kandar, 2019, p. 31).
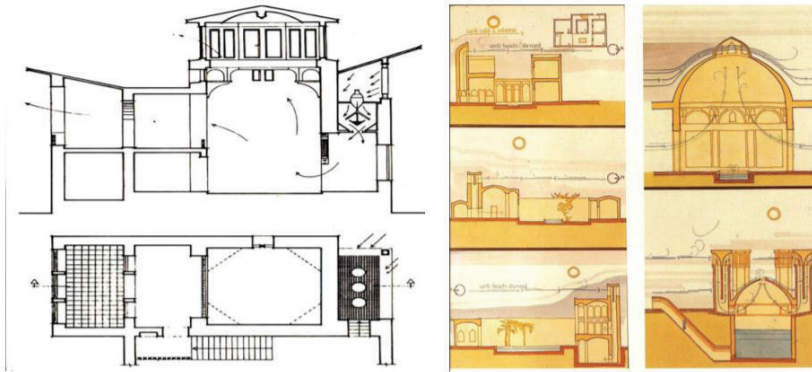
Figure 4: Photograph showing the stack effect and windcatcher concept
(Alsuliman, 2014, p. 131)

Wind catchers provide much more benefits than just energy savings. Because the air supply is high and flows within regardless of the building's orientation or connection to the wind, wind catchers provide natural ventilation free of pollution and dirt. Unlike ventilation through windows, ventilation from wind catchers does not raise interior noise levels, which is important in holy places to reduce distractions. The size of the cross-section of the windcatcher tower is determined by the temperature of the surrounding environment. The cross-section size should be decreased if the air temperature at the catcher's mouth is higher than the maximum allowable interior air temperature. This is because damped charcoal sheets placed between wet fabrics or steel grills are used to chill the air as it passes through. Wind may be directed over a water feature, such as a fountain, to enhance the moisture levels of the air (Alsuliman, 2014, p. 131).

To minimize leakage and waste, the masjid and the heat management system should be meticulously planned. This may be accomplished by establishing a buffer zone that prevents heat from entering hot regions and exiting in cold climates like in the conceptual design of the Green Mosque competition. The mosque's double-wall design generates a thermal buffer zone between the main mass and the outside environment. This technology, which also contributes to the tranquility of the prayer space, allows for internal heating in the winter and protects the interior from rain, snow, and wind. On the other hand, the thermal buffer zone generates a cooler zone for the main mass in the summer. In addition, vertical glass surfaces provide the worship space with a spiritual atmosphere (Url-1).

Another system that can be utilized is using underfloor cooling or heating systems, as implemented in the Salepçiolu Mosque in Izmir. This allows only thermal management of the used area and can considerably minimize energy waste. The simulation results demonstrated that using a low-temperature electric radiant system for floor heating improves

the thermal comfort of the main prayer space significantly (Bughrara et al., 2017). Although underfloor heating is the most effective technique for enhancing comfort conditions in the winter, fall, and spring, the assigned local council has not authorized this system initially since it may harm the paintings found in the prayer area (Bughrara et al., 2018, p. 369). As a result, when using this technique, it is crucial to take into account the mosque's furnishings and other aspects.

Passive Cooling Systems

A human being's main concern was to ensure that the environment he lived in provided two vital elements: weather protection and interior thermal comfort. In hot climates, passive cooling systems rely on two major factors: first, controlling sunlight penetration into the building, and second, making effective use of natural air movement to offer a degree of internal natural ventilation.

In the summer, the interior temperature drops due to the lack of sunshine. Warm sunshine, on the other hand, boosts interior temperature and natural illumination in the winter. On the other side, while natural ventilation is important, protection from undesirable winds is required, which may be achieved by plantation of trees or appropriately orienting the building mass and external openings.

A mosque's location is extremely crucial to consider. Dusty and sandy winds are dampened by narrow and compacted roadways, which are shaded and cool during the day and warm at night. Furthermore, the city's green spaces increase natural ventilation surrounding mosque premises, reducing the demand for air conditioning within the mosque and contributing to air pollution reduction.

The courtyard is another feature that aids natural ventilation. Courtyards have long been an important element of mosques, and it's unfortunate that we undervalue their importance today. The size and design of the courtyard may be determined by variables such as available space and the mosque's location. In any size or shape, courtyards contribute a positive impact on natural ventilation and indoor air quality in mosques.

The green roof is another method of keeping interior spaces cool. Green roofs are not always doable, but they should always be explored as a passive cooling strategy. According to research done in Riyadh, Saudi Arabia, merely putting a green roof for a mosque under construction was found to result in a 10% reduction in energy usage (Alabdullatief and Omer, 2017). This technology has also been employed to improve the thermal comfort of worshipers in the prayer hall at Sancaklar Mosque in Turkey, as illustrated in figure 5, and Pamulang Bioclimatic Community Mosque in Indonesia.
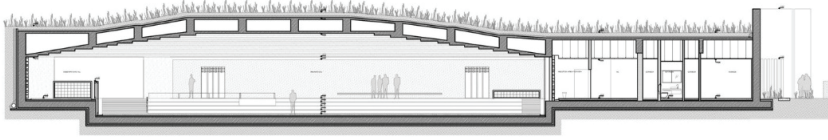
Figure 5: Section showing the green roof of the Sancaklar Mosque. (Url-2)

The use of only mechanical means to provide thermal comfort in built environments has resulted in the current energy challenges. As a result, when renewable energy sources like wind or solar energy are coupled with passive approaches, this would considerably diminish energy consumption while also improving thermal comfort in sustainable mosques.

Orientation of the Mosque

In a specific region, the orientation of the place of worship stays constant, as prayer must be conducted in the direction of the qibla. Because most mosques are symmetrical, with the prayer hall on the central axis (Azmi & Kandar, 2019, p. 32), this fixed orientation means that for a given region, one side of all mosques will receive the morning sun while the other will be hot at all time. The roof and building envelope are critical components of the design because they govern the amount of energy entering and leaving the structure. As a result, many passive design techniques that allow for the utilization of natural energy in the environment for heating or ventilation need careful planning and guidance.

In warmer climes, the west side of the building, which is exposed to the afternoon light and causes heat buildup within, requires the most consideration. To reduce heat gain and cooling load, the prayer hall should be positioned away from the hot afternoon sun. Creating buffer spaces and rearranging the spaces in the design such that other spaces occupy the western side of the plan would serve to reduce cooling loads in prayer halls (Azmi & Kandar, 2019, p. 32).

In cold climates, sunlight may be used to heat interiors. This may be accomplished by orienting the masjid toward the afternoon sun, allowing the spaces to get the most exposure to the hot sun. The prayer hall can also be situated on the plan's furthest perimeter, as long as the envelope is appropriately maintained to avoid heat loss. In the winter, a proper glass ratio can be employed to allow both radiative and conductive heat gains.

Similar forms of glazing should be integrated with proper shading strategies in regions with diverse climates so that winter sun rays are welcomed inside while summer sun rays are prevented. Glazing and shading are discussed in further depth in the next section.

Optimum Facade Solutions

To ensure that mosques are minimally affected by outdoor climate changes, improving the properties of the building envelope should have the highest priority. These optimal features of the building envelope should be compatible with thermal comfort in mosques. The proposed methods will guide designers and building occupants in the design process of new mosques or in the use of existing mosques.

The climate of the region where the mosque is located has a great influence on the selection of the optimum combination. For example, Atmaca et al. (2021) conducted a study evaluating different scenarios of the exterior of a mosque in a temperate humid climate. In this study, conditions such as transparency ratio, wall thickness, and shading devices were changed and compared with a baseline scenario. Figure 6 illustrates the different scenarios.

All facades 50% transparency All facades 25% transparency All facades 75% transparency

Variable transparency: 50% - 15% Variable transparency: 25% - 15% All facades 50% transparency and shading devices
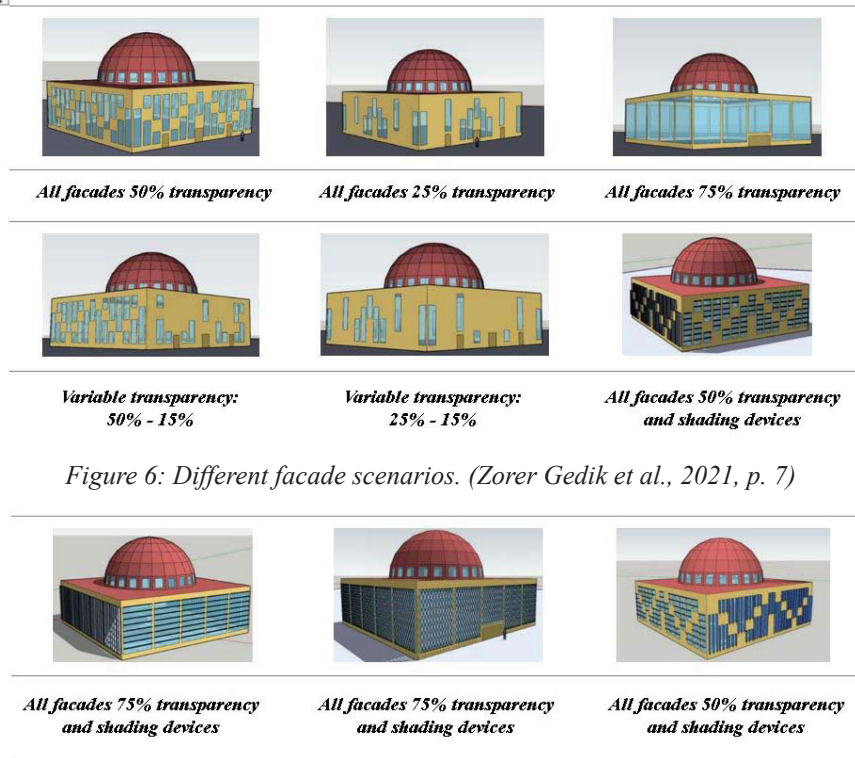
Figure 6: Different facade scenarios. (Zorer Gedik et al., 2021, p. 7)

All facades 75% transparency and shading devices All facades 75% transparency and shading devices All facades 50% transparency and shading devices

Figure 6 (continued): Different facade scenarios. (Zorer Gedik et al., 2021, p. 7)

Accordingly, it has been determined that the increase in the thickness of the thermal insulation material used in the building envelope contributes positively to energy saving. However, after a certain thickness, the energy-saving rate decreased. In addition, thermal comfort was provided in 25%,

50%, and 75% of the transparency ratio of the building envelope of the mosques, but the minimum energy consumption was provided at 25% and 50% transparency. On the other hand, the transparency rate of the building envelope is 15% and 25% increased the heating load. Finally, it has been found that shading elements increase heating loads despite reducing cooling loads in all cases (Zorer Gedik et al., 2021, 7).

Based on these results, it can be assumed that it should be the optimum option without shading elements, as the 50% transparency rate reaches all the positive points. This may or may not be an accurate result (depending on several other factors as explained earlier), this solution would not be suitable in a hot and dry climate.

The United Arab Emirates, although a study conducted in the city of Sharjah (Mushtaha, 2014, p.936) showed that shading devices alone have minimal contribution when it comes to conserving cooling energy, there are other studies on two mosques in Riyadh and Jeddah (Saudi Arabia). In a study, shading devices are an important part of the optimum facade solution (Al-Homoud, 2009, p.79). It is also recommended to use the minimum possible ratio of openings and double-glazed glazing in hot climatic regions.

DISCUSSION AND CONCLUSION

Mosques are structures with a distinct occupancy pattern as well as distinct energy and water consumption pattern. Typically, during the design, construction, and operation phases of such buildings, energy efficiency measures and sustainability principles are not used. Surprisingly, these landmark monuments have the potential to raise sustainability awareness and promote cleaner energy solutions.

Unfortunately, the majority of green or eco mosques in the literature that is referred to as sustainable mosques are concept designs or competition presentations. Usually, these designs are just developed to the concept stage, and the visuals offered are only the artist's conception of the design, with no further development or viability testing. Despite the fact that it claims to be an eco-mosque or green mosque design, there is no assurance or proof that the project, if built, would be environmentally sustainable or supply the necessary indoor thermal comfort in places of worship.

By using renewable resources in the surroundings, passive design is one of the most fundamental techniques to assure environmental sustainability at a minimal cost. In the passive design of a building, the climatic conditions of a geographic location play a significant impact. As a consequence, each site will have its unique set of passive design principles, many of which will be mirrored in the region's native architecture,

wastewater availability, urbanization, etc. Although microclimate elements like climate change have a part in creating a place's features, regions with comparable temperature and precipitation ranges have a lot in common when it comes to thermal and ventilation requirements. As a consequence, mosques' incomparable climate zones will have similar comfort needs, which can be provided through passive design solutions.

When selecting suitable passive design approaches and appropriate design components, an architect should keep in mind the crucial features highlighted in this article and how they might affect the mosque's sustainable design. Instead of adjusting to comfort and thermal demands after the mosque is constructed, the climate aspects should be considered from the beginning of the design stages. It is indeed possible that elements that function in one climate would not work in another. The more environmentally friendly a structure is, the more passive the design will be, resulting in energy savings and improved user comfort. As a result, it is the architect's responsibility to develop a mosque while taking into account passive design techniques..

Testing the viability of a specific design component for a building may be done immediately and simply with today's technologies. The building's occupancy level may also be analyzed early in the design process using simulation tools, and appropriate building components that allow for optimal energy usage can be chosen (Ibrahim et al., 2014; Zorer Gedik et al., 2021). Furthermore, because many climatic elements influence passive design techniques, research and simulation of various variables can aid in standardizing passive design components in the context of mosque architecture for a certain site.

Most mosques nowadays are constructed without regard for climate or topography, resulting in high energy consumption and a lack of user comfort. This essay emphasizes the significance of environmentally friendly mosques. Unfortunately, case studies and instances of such mosques are scarce, in addition to the limited number of studies. Moreover, this article provides several design methodologies and introduces some concepts for ensuring a long-term mosque design. The importance of doing more work in this area cannot be stressed enough. Climate-specific suggestions and criteria can be developed in future research to achieve indoor thermal comfort.

REFERENCES

Abdou, A. A., Al-Homoud, M. S., and Budaiwi, I. M. (2005). Mosque Energy Performance, Part I: Energy Audit and Use Trends Based on the Analysis of Utility Billing Data. King Abdulaziz *Journal for Science and Engineering, JKAU: Eng. Sci.*, 16(1), 165-184.

Abdullah, A. (2016). Benchmark for mosque energy consumption in hot arid climate, Assiut, Egypt. *First International Conference on Mosque Architecture*, (p. 277-290). Saudi Arabia: Dammam, December 5-7.

Abdullah, F. , Majid, N. , & Othman, R. (2016). Defining Issue of Thermal Comfort Control through Urban Mosque Façade Design. *Procedia - Social and Behavioral Sciences*, 234. doi: 10.1016/j.sbspro.2016.10.259

Alabdullatief A. & Omer S. (2017). Sustainable techniques for thermal comfort in buildings designed by worshipers, *16th International Conference on Sustainable Energy Technologies*– SET). Italy: Bologna, July 17-20.

Alharbi E., & Zin R.M. (2020). Identify Significant Parameters Enhance Energy Consumption to Support Decision Making of Mosque Design: Review Paper. *Journal of Critical Reviews*, 7(15), 5951-5958. doi:10.31838/jcr.07.15.763

Al-Homoud M.S., Abdou A.A., & Budaiwi I.M. (2009). Assessment of monitored energy use and thermal comfort conditions in mosques in hot-humid climates. *Energy and Buildings*. 41(6), 607-614, doi.org/10.1016/j.enbuild.2008.12.005

Al-Homoud, M.S. (2009). Envelope Thermal Design Optimization of Buildings with Intermittent Occupancy. *Journal of Building Physics*, 33, 65–82, doi.org/10.1177/1744259109102799

Alsuliman A. (2014). Wind Catchers and Sustainable Architecture in the Arab World. *Journal of Civil and Environmental Research*, 6, 130-136.

Atmaca, A. & Gedik, G. (2017). Dini Yapıların Isıl Konurunun İncelemesi: Marmara İlahiyat Cami ve Hz. Ali Cami Örneklemeleri. *13th National Installation Engineering Congress,* (p. 1252-1262). Turkey: Izmir, April 19-22.

Azmi N.A., & Kandar M.Z. (2019). Factors contributing in the design of environmentally sustainable mosques. *Journal of Building Engineering.* 23, 27-37, doi.org/10.1016/j.jobe.2019.01.024

Azmi N.A., Arıcı M., & Baharun A. (2021). A review on the factors influencing energy efficiency of mosque buildings. *Journal of Cleaner Production*, 292, 2-52. doi.org/10.1016/j.jclepro.2021.126010

Baharudin N.A., & Ismail A.S. (2014). ScienceDirect Communal Mosques: Design functionality towards the development of sustainability for community. *Procedia - Social and Behavioral Sciences*, 153, 106–120. doi.org/10.1016/j.sbspro.2014.10.046

Budaiwi I., & Abdou A., (2013). HVAC system operational strategies for reduced energy consumption in buildings with intermittent occupancy: The case of mosques. *Energy Conversion and Management*, 73, 37-50, doi. org/10.1016/j.enconman.2013.04.008

Bughrara K., Arsan Z., & Gökçen Akkurt G. (2017). Applying underfloor heating system for improvement of thermal comfort in historic mosques: the case study of Salepçioğlu Mosque, Izmir, Turkey. *Energy Procedia*. 133. 290-299. doi.org/10.1016/j.egypro.2017.09.390

Coşkuner Pamuk A., Taştemir İ. A., & Arpacıoğlu Ü. (2020). A Comparative Study on Daylight Performance of Konya Mosques Built in Anatolian Seljuk and Ottoman Period. *ICONARP International Journal of Architecture and Planning*, 8, 102–123. doi.org/10.15320/ICONARP.2020.145

Harsritanto, B., Nugroho, S., Dewanta, F. & Prabowo, A. (2021). Mosque design strategy for energy and water saving. *Open Engineering*, 11(1), 723-733.

Ibrahim S.H., Baharun A., Nawi M.N.M., & Junaidi E. (2014). Assessment of thermal comfort in the mosque in Sarawak, Malaysia. *International Journal of Energy and Environment.* 5(3), 327-334.

Mushtaha, E. (2014). Thermal Performance of Mosque Archıtectural Forms and its Impacts on Indoor Temperature and Thermal Comfort: Sharjah as a Case Study. *International Journal of Sustainable Energy*, 36(10), 926-944. doi.org/10.1080/14786451.2015.1127234

Nedhal, A.T. & Qahtan, A. (2018). Assessment of Thermal Behaviour and Energy Consumption of Small Mosques in Hot-arid Climate of Najran City, *KSA. International Conference on Sustainable Design of the Built Environment SDBE,* (p. 193-202). United Kingdom: London.

Zorer Gedik, G., Atmaca, A.B., & Wagner, A. (2021). Determination of Optimum Envelope of Religious Buildings in Terms of Thermal Comfort and Energy Consumption: Mosque Cases. Energies, 14(20):6597, doi. org/10.3390/en14206597

Bughrara K.S.M., Durmuş Arsan Z., & Gökçen Akkurt G. (2018). Effect of intervention strategies on seasonal thermal comfort conditions in a historic mosque in the Mediterranean climate. *In the 3rd International Conference on Energy Efficiency in Historic Buildings (EEHB2018).* (p. 363-371), Uppsala University, Visby, Sweden: September 26-27.

WEBSITE REFERENCES

Url - 1 < *https://funci.org/the-green-mosque/?lang=en/ >,* date retrieved 08.12.2021.

Url - 2 < *https://mosqpedia.org/en/mosque/60#&gid=1&pid=5>,* date retrieved 08.01.2022.

CHAPTER 2

DESIGN OF CONCRETE-FILLED STEEL-CONCRETE COMPOSITE COLUMNS IN HIGH DUCTILITY CLASS MOMENT RESISTING FRAMES DESIGNED ACCORDING TO TDBY-2018

Dr. Serkan ETLİ [1], Dr. Osman HANSU[2]

1 Munzur University, Faculty of Engineering, Departmant of Civil Engineering, serkanetli@munzur.edu.tr

2   Gaziantep University, Faculty of Engineering, Departmant of Civil Engineering o_hansu@hotmail.com

Elements designed and produced by combining the superior properties of concrete and steel have been used frequently in the literature. These elements, whose properties are reinforced by the high ductility of the confining effect in concrete-filled steel column (CFST) elements, are normally used to meet the extra stresses that may occur in concrete columns due to structural reasons. With this element design technique, it can be used during reinforcement in the literature, or it can be produced as a new element in high-rise buildings designed with wide openings. It has been proven in studies that the higher ductility provided by CFST elements is sufficient for energy dissipation during design for earthquake resistant structures that cannot be ignored. Moreover, thanks to their higher rigidity and higher strength, these elements not only play a leading role in the earthquake resistant design of structures, but are also frequently used in bridge piers where impact and dynamic loads occur (Etli and Güneyisi 2020, 2021; Lee et al. 2009; Shanmugam and Lakshmi 2001). In the literature, various studies have been carried out for different nonlinear modeling strategies to model the response of such composite column members subjected to dynamic loads. It is seen that steel and concrete components are generally modeled separately in studies on concrete-filled steel pipe elements using software using finite element methods such as ABAQUS, ANSYS and LS-DYNA, which have been used in the literature in recent years. To simulate the interaction between these element models, the help of another connector or interface element is needed. Therefore, the biggest disadvantage of using commercial packages is that very complex calculations arise using much smaller parts of the element to be analytically modeled and interaction structures to be produced between them. As a result, the necessity of computationally intensive and at the same time long-term work arises. The suitability of experimental, theoretical, and analytical analyzes was evaluated in studies using fiber elements. It is also important to calculate correctly instead of reaching a faster solution using fiber elements (Etli 2021).

During the design of the moment-resisting frame (MRF) type structural systems created with CFST, the details of the design calculations of the dimensioning of the CFST elements in the current Turkish Standards will be examined. During these calculations, Section 9.11 of the Turkish Building Earthquake Code (TBDY-2018) is used. In addition, necessary calculations should be made by considering the rules given in Chapter 12 of the Regulation on the Design, Calculation and Construction Principles of Steel Structures (ÇYTHYE-2018). On the other hand, for MRFs designed as structural systems, the regulation divides the design of these structures into two classes. These classes are studied as High Ductility Systems (DCH) and Ductility Limited Systems (DCM). In this context, there are

different calculation rules in the designs of the columns to be used in MRF systems. For this Chapter, the design rules of the CFST elements to be used in the design for the MRF, which is designed as a DCH system, are given in the scope of TBDY-2018 and ÇYTHYE-2018.

1.1. Loads Acting on CFST Elements in DCH-MRF Systems

For the ductility classification of the systems under this title to be determined as DCH level, 2 conditions are required.

- MRF systems consisting of reinforced concrete beams meeting the condition in Section 7.4 of TBDY-2018 and steel encased composite columns meeting the conditions in Sections 9.11.2.1 and Section 9.11.3 of TBDY-2018.

- MRF systems consisting of steel beams meeting the condition in Section 9.3 of TBDY-2018 and CFST columns meeting the conditions in Section 9.11.2.2 and Section 9.11.4 in TBDY-2018.

1.1.1. Condition for CFST Column Members to be Stronger than Steel Beams

It should be shown that the condition given in TBDY-2018 Equation 9.7 is met in MRF systems produced by connecting steel beams to CFST elements in section 9.11.2, clause 2, considering the calculated earthquake direction.

$$\frac{\sum M_{pc}^*}{\sum M_{pb}^*} > 1 \qquad \textbf{(TBDY-2018/E.9.7)}$$

TBDY-2018 Equation 9.8.a or 9.8.b is used in the calculations of M_{pc}^* (column bending moment) in TBDY-2018 Equation 9.7. The first of these equations is used within the scope of Design with Factors of Safety (GKT) and the second under the principles of Design with Load and Strength Factors (YKT).

$$\sum M_{pc}^* = \sum W_{pc} \times (F_{yc} - 1.5 \times P_{ac}/A_g) \qquad \textbf{(TBDY-2018/E.9.8.a)}$$

$$\sum M_{pc}^* = \sum W_{pc} \times (F_{yc} - P_{uc}/A_g) \qquad \textbf{(TBDY-2018/E.9.8.b)}$$

P_{ac} and P_{uc} are defined as the axial compressive force calculated for the GKT and YDKT load combinations, considering the increased earthquake effects, respectively. In the calculation of the column bending moment capacities, P_{ac} and P_{uc}, which are expressed in TBDY-2018 Section 9.3.1.3, which make these bending moment capacities the smallest in accordance with the direction of the earthquake, will be used. In the calculations of

M_{pb}^* (beam bending moment), moment capacity calculations are proposed for two types of sections. While TBDY-2018 Equation 9.9.a or 9.9.b is used for non-weakened beam cross-section connections, TBDY-2018 Equation 9.9.c or 9.9.d is used for non-weakened beam cross-section connections. In addition, TBDY-2018 Equation 9.9.a and Equation 9.9.c are given for design with GKT, TBDY-2018 Equation 9.9.b and Equation 9.9.d are given for design with YDKT.

$$\sum M_{pb}^* = \sum (1.1 \times R_y \times F_{yb} \times W_{pb} + 1.5 \times M_{av}) \quad \textbf{(TBDY-2018/E.9.9.a)}$$

$$\sum M_{pb}^* = \sum (1.1 \times R_y \times F_{yb} \times W_{pb} + M_{uv}) \quad \textbf{(TBDY-2018/E.9.9.b)}$$

$$\sum M_{pb}^* = \sum (1.1 \times R_y \times F_{yb} \times W_{RBS} + 1.5 \times M_{av}) \quad \textbf{(TBDY-2018/ E.9.9.a)}$$

$$\sum M_{pb}^* = \sum (1.1 \times R_y \times F_{yb} \times W_{RBS} + 1.5 \times M_{uv}) \quad \textbf{(TBDY-2018/E.9.9.b)}$$

R_y, F_{yb}, W_{pb} and W_{RBS} are given as the ratio of possible yield stress to characteristic yield stress, characteristic yield stress of beam material, plastic strength moment of unattenuated beam and plastic strength moment of weakened beam cross section, respectively. Regarding R_y and F_{yb} in question, the values in Table 9.2 in TBDY-2018 Section 9.2.4 are used.

Table 1. R_y *and* R_t *coefficients in TBDY-2018 Table 9.2*

Structural Steel Grade and Element Type	R_y	R_t
S235 Roll profiles and plates made of steel	1.4	1.1
S275 Roll profiles and plates made of steel	1.3	1.1
S355 Roll profiles and plates made of steel	1.25	1.1
S460 Rolling profiles made of steel	1.1	1.1
Pipe and Box profiles	1.4	1.3
Reinforcing steel	1.2	1.2

TBDY-2018 Section 9.2.4, F_{yb} calculation, which is the expression of steel beam characteristic yield stress of possible material strength, is given as $F_{yb} = R_y \times F_y$ and $F_u = R_t \times F_u$. M_{av} and M_{uv} are defined as the additional bending moment that will occur in the column axis due to the shear force on the plastic hinge point that may occur at the beam ends, based on the load combinations used for GKT and YDKT, respectively.

1.1.2. Situations where CFST column members are not required to be stronger than steel beams

i)   In the columns where the condition given by TBDY-2018 Equation 9.10 is met, the condition given by TBDY-2018 Equation 9.7 is not sought.

In addition, TBDY-2018 Equation 9.10.a is given for design with GKT, and TBDY-2018 Equation 9.10.b is given for design with YDKT. Moreover, P_a and P_u are defined as the required axial force strength calculated for GKT and YDKT, respectively. A_g in the equation is given as the total cross-sectional area of the composite element.

$$P_a < 0.3 \times (F_y \times A_g / 1.5)$$ (TBDY-2018/E.9.10.a)

$$P_u < 0.3 \times (F_y \times A_g)$$ (TBDY-2018/E.9.10.b)

ii) This condition is not sought in buildings consisting of a single story and in columns located on the top floor in multi-story structures.

iii) When the calculated sum of the calculated shear force strengths of the columns in the direction taken into account during the design and which do not fulfill the condition that the columns in a floor are stronger than the beams, are calculated, if the sum of the shear strengths of the columns in the MRF system in the same direction at that floor is less than 20%, and for each MRF The case where the sum of the shear strengths of the columns on the axis of the column is less than 33% of the sum of the shear strength of the moment-transmitting frame columns on that column axis. However, when examining this condition, the "column axis" is defined as the axis with parallel rows of columns located at the boundary within 10% of the building plan size, perpendicular to the column axis examined. In addition, the design shear strength of the column will be obtained by dividing the sum of the bending moment strengths of the beams connected to both ends of the elements, or of the column ends bending moment strength in columns where this condition is not met, by dividing the column's strength from the beams.

iv) For the earthquake direction considered in the design, when the ratio of the existing shear strengths of the columns located on any of the building's i^{th} floor to the required shear strength is calculated, the case that the current shear strength of the columns located on the upper floor of the calculated floor is 50% greater than the ratio of the required shear strength. If it is, the condition that the columns are stronger than the beams will not be required.

For the conditions ii, iii and iv mentioned above, the 0.3 coefficient in the equation given in TBDY-2018 Equation 9.10 will be replaced with 0.1 (in accordance with TBDY-2018 Section 9.11.2), necessary controls will be provided. The equation given in TBDY-2018 Equation 9.10 is updated according to the GKT and YDKT design features as follows.

$$P_a < 0.1 \times (F_y \times A_g/1.5)$$ **(TBDY-2018/C.9.11.2/E.9.10.a)**

$$P_u < 0.1 \times (F_y \times A_g)$$ **(TBDY-2018/C9.11.2/E.9.10.b)**

1.1.3. Axial Force Calculation in CFST Elements

1.1.3.1. Axial Force Calculation for YDKT in CFST Elements

In the calculation of P_{ac} and P_{uc} forces, it is given in TBDY-2018 Section 9.3.1.3 that the loading conditions given in Section 9.2.5 for DCH-MRF systems are valid. Among these design methods, modifications will be made in the loading combinations in the case given for YDKT. In general, given loading combination TBDY-2018 Equation (4.11) will be updated as follows. TBDY-2018 Equation (4.12) will be used as it is.

$$1.2 \times G + ¥ \times Q + 0.2 \times S + E_d^{(H)} + 0.3 \times E_d^{(Z)}$$ **(TBDY-2018/E.4.11)**

$Q \leq 5$ and (other than garages and occupied buildings) $¥ = 0.5$

$$0.9 \times G + H + E_d^{(H)} - 0.3 \times E_d^{(Z)}$$ **(TBDY-2018/E.4.12)**

G, Q, S, H and $E_d^{(H)}$, respectively fixed load, live load, snow load, horizontal ground thrust, strike-through combination is applied and the horizontal earthquake effect TBDY-2018 is defined as the basis for the design. In addition, $E_d^{(Z)}$, TBDY-2018 is defined as the design-based earthquake effect under the influence of the earthquake in the z direction. In addition, there are two situations when calculating $E_d^{(H)}$ in TBDY-2018 Section 4.4.2 for combining earthquake effects in horizontal directions perpendicular to each other.

- In the first case, TBDY-2018 Equation (4.9) is used in case of using linear earthquake calculation with the equivalent earthquake load method in TBDY-2018 Section 4.7 or TBDY-2018 Section 4.8.2 or in case of using mode combination method and earthquake calculation. $E_d^{(X)}$ and $E_d^{(Y)}$ show the earthquake effect based on the design under the influence of the earthquake in the x and y directions, respectively.

$$E_d^{(H)} = \mp E_d^{(X)} \mp 0.3 \times E_d^{(Y)}$$ **(TBDY-2018/E.4.9)**

$$E_d^{(H)} = \mp 0.3 \times E_d^{(X)} \mp E_d^{(Y)}$$ **(TBDY-2018/E.4.9)**

- In the second case, since the earthquake components of the ground motion recording applied to the structure in the horizontal (x and

y) directions of the horizontally perpendicular to each other during the time history analysis made in TBDY-2018 Section 4.8.3, are applied to the structure simultaneously as specified in TBDY-2018 Section 2.5. The combined horizontal earthquake effect $E_d^{(H)}$ is calculated directly from the analysis because of these calculations.

1.1.3.2. Axial Force Calculation for GKT in CFST Elements

In the design of GKT and CFST elements, TBDY-2018 Equations (9.1.a), (9.1.b) and (9.1.c) are used as load combinations that include the earthquake effect in the calculation of P_{ac} and P_{uc} forces.

$$G + 0.75 \times Q + 0.75 \times S \pm 0.75 \times (0.7 \times E_d) \qquad \text{(TBDY-2018/E.9.1.a)}$$

$$G \pm 0.7 \times E_d \qquad \text{(TBDY-2018/E.9.1.b)}$$

$$0.6 \times G + 0.75 \times H \pm 0.7 \times E_d \qquad \text{(TBDY-2018/E.9.1.c)}$$

1.2. Design of CFST Elements in DCH-MRF Systems

1.2.1 Section Design of CFST Elements in DCH-MRF Systems

In TBDY-2018 Section 9.11.4, it is done after determining the flange width/thickness, body height/thickness and diameter/wall thickness ratios to be used during the design of DCH-MRF system elements consisting of steel beams and CFST columns. The values obtained should be compared with the λ_{hd} limit values given in TBDY-2018 Table 9.3 and CFST designs should be made.

Table 2. λ_{hd} coefficients in TBDY-2018 Table 9.3

Element Definition	Slenderness Ratio	Limit values for Elements with High Ductility Level, λ_{hd}	Explanation
Wall thicknesses of composite elements with box cross-section	b/t	$1.4 \times \sqrt{\dfrac{E}{F_y}}$	
Wall thicknesses of pipe cross-section composite elements	D/t	$0.076 \times \dfrac{E}{F_y}$	
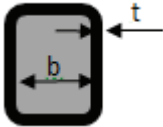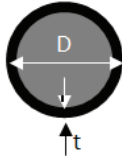
In ÇYTHYEY-2018 Section 12.3.2.1, in CFST members, the structural steel cross-sectional area should not be less than 1% of the total composite cross-sectional area. Also, in the same section, it is not necessary to use longitudinal reinforcement in the Composite cross-section. If longitudinal reinforcement is used, it is stated that transverse reinforcement is not required during strength calculations.

1.2.2 Axial Load Capacity of CFST Elements in DCH-MRF Systems

In TBDY-2018 Section 9.11.4, during the column cross-section calculations, the load reduction coefficients defined for live loads in "Calculation values of the loads to be taken in the dimensioning of the building elements" (TS-498 1987) will be examined in the analyzes made under vertical loads, and load compositions consisting of the combined effect of vertical loads and earthquake will be considered. This loading combination will be used as follows.

$$1.2 \times G + Q + 0.2 \times S \pm E_d \qquad \textbf{(TBDY-2018/C.9.11.4.2)}$$

Considering the load combination above, N_{dm} will be defined as the largest of the axial compressive forces, and the condition of TBDY-2018 Equation (9.6) will be met.

$$N_{dm} \leq 0.4 \times P_{no} \qquad \textbf{(TBDY-2018/E.9.6)}$$

TBDY-2018 defines the axial compressive force strength of the composite column cross-section, with P_{no} in Equation (9.6). However, the 0.85 coefficient and the 0.95 coefficient value in the TBDY-2018 Equation (9.27) will be updated and used.

$$P_{no} = 0.95 \times A_c \times f_{ck} + A_s \times F_y + A_{sr} \times F_{ysr} \quad \textbf{(TBDY-2018/E.9.27/C.9.11.4.2)}$$

A_c, f_{ck}, A_s, A_{sr} and F_{ysr} in the equation are defined as concrete cross-sectional area, concrete characteristic compressive strength, steel cross-sectional area, longitudinal reinforcement area and characteristic yield stress of reinforcing steel, respectively.

1.2.3 Shear Capacity of CFST Elements in DCH-MRF Systems

In TBDY-2018 Section 9.11.4.3, it is stated that in calculating the characteristic shear strength of the CFST column, calculations are made using only the effective shear area of the structural steel cross-section. Characteristic shear strength will be used for the box cross-section elements in ÇYTHYE-2018 Equation (10.12).

$$V_n = 0.6 \times F_y \times A_w \times C_{v2} \qquad \text{(ÇYTHYE-2018/E.10.12)}$$

For A_w, the box is defined as the area of the hull plates of the cross-section and is calculated as $A_w = 2 \times h \times t$ is defined as the hull buckling coefficient under shear effect. In ÇYTHYE-2018 Section 10.3, the C_{v2} coefficient will be taken from ÇYTHYE-2018 Section 10.2.2 by using h/t instead of h/t_w and taking $k_v = 5$. Equation (10.6.a, b and c) for C_{v2} is given in ÇYTHYE-2018 Section 10.2.2.

$$\frac{h}{t} \leq 1.1 \times \sqrt{k_v \times E/F_y}$$

$$\rightarrow C_{v2} = 1.0 \qquad \text{(ÇYTHYE-2018/E.10.6.a)}$$

$$1.1 \times \sqrt{k_v \times E/F_y} < \frac{h}{t} \leq 1.37 \times \sqrt{k_v \times E/F_y}$$

$$\rightarrow C_{v2} = \frac{1.1 \times \sqrt{k_v \times E/F_y}}{\frac{h}{t}} \qquad \text{(ÇYTHYE-2018/E.10.6.b)}$$

$$\frac{h}{t} > 1.37 \times \sqrt{k_v \times E/F_y}$$

$$\rightarrow C_{v2} = \frac{1.51 \times k_v \times E}{\left(\frac{h}{t}\right)^2 \times F_y} \qquad \text{(ÇYTHYE-2018/E.10.6.c)}$$

1.2.4 Axial Load and Flexural Capacity of CFST Elements in DCH-MRF Systems

In ÇYTHYE-2018 Section 12.2.4, there is a classification for two groups of load effects. The first of these classifications is given as CFST elements under the influence of axial compressive force and the second under the effect of bending moment.

1.2.4.1 Axial Load Capacity of CFST Elements in DCH-MRF Systems

In ÇYTHYE-2018 Section 12.3.2.2, there are definitions for compact/non-compact sections and slender sections in the calculation of compressive strength of CFST elements with double symmetry axes under the influence of axial compressive force. ÇYTHYE-2018 λ_p limit value defined in Table 12.1A is defined for compact and non-compact sections. Sections that do not exceed the λ_p limit value are defined as compact sections. In addition, sections exceeding the λ_r limit value defined in Table 12.1A of ÇYTHYE-2018 are defined as slender.

Table 3. λ_p *and* λ_r *coefficients in ÇYTHYE-2018 Table 12.1A*

Element definition	Wide to Thickness Ratio	λ_p (Compact / Non-compact)	λ_r (Non-Compact / Slender)	Maximum Limit Value
Wall thicknesses of uniform thickness box sections	b/t	$2.26 \times \sqrt{\dfrac{E}{F_y}}$	$3.0 \times \sqrt{\dfrac{E}{F_y}}$	$5.0 \times \sqrt{\dfrac{E}{F_y}}$
Wall thicknesses of pipe cross-section elements	D/t	$0.15 \times \dfrac{E}{F_y}$	$0.19 \times \dfrac{E}{F_y}$	$0.31 \times \dfrac{E}{F_y}$

Compressive strengths of compact cross-sections under the influence of only axial compressive force are given in Equations (12.8 and 12.9) in ÇYTHYEY-2018 Section 12.3.2.2 for P_{no}. For the C_2 value, it is given as 0.85 for box cross-sections and 0.95 for pipe cross-sections.

$$P_{no} = P_p \qquad \text{(ÇYTHYE-2018/E.12.8)}$$

$$P_p = F_y \times A_s + C_2 \times f_{ck} \times \left(A_c + A_{sr} \times \frac{E_{sr}}{E_c} \right) \qquad \text{(ÇYTHYE-2018/E.12.9)}$$

For the P_{no} value of non-compact cross-sections, Equations (12.10) and (12.11) are given in ÇYTHYE-2018 Section 12.3.2.2.

$$P_{no} = P_p - \frac{(\lambda - \lambda_p)^2}{(\lambda_r - \lambda_p)^2} \times (P_p - P_y) \qquad \text{(ÇYTHYE-2018/E.12.10)}$$

$$P_y = F_y \times A_s + 0.7 \times f_{ck} \times \left(A_c + A_{sr} \times \frac{E_{sr}}{E_c} \right) \qquad \text{(ÇYTHYE-2018/E.12.11)}$$

For the P_{no} value of the slender sections, Equation (12.12) is given in ÇYTHYE-2018 Section 12.3.2.2. The F_{cr} value, which is defined as the critical buckling stress, is defined in ÇYTHYE-2018 Equation (12.13) and Equation (12.14) for box and pipe section members, respectively.

$$P_{no} = F_{cr} \times A_s + 0.7 \times f_{ck} \times \left(A_c + A_{sr} \times \frac{E_{sr}}{E_c} \right) \qquad \text{(ÇYTHYE-2018/E.12.12)}$$

$$F_{cr} = 9 \times \left(\frac{E_s}{\left(\frac{b}{t} \right)^2} \right) \qquad \text{(ÇYTHYE-2018/E.12.13)}$$

$$F_{cr} = 0.72 \times \left(\frac{F_y}{\left[\left(\frac{D}{t} \right) \times \frac{F_y}{s} \right]^{0.2}} \right) \qquad \text{(ÇYTHYE-2018/E.12.14)}$$

1.2.4.2 Bending Moment Capacity of CFST Elements in DCH-MRF Systems

• In ÇYTHYE-2018 Section 12.4.4, calculation methods are given for the design bending moment strength $\Phi_b M_n$ in designs made with YDKT and for safe bending moment strength M_n/Ω_b in designs made with GKT. The values for Φ_b and Ω_b are given as 0.90 and 1.67, respectively. It is calculated according to the features of being compact, not being and being slender. ÇYTHYE-2018 λ_p limit value defined in Table 12.1B is defined for compact and non-compact sections. Sections that do not exceed the λ_p limit value are defined as compact sections. In addition, sections exceeding the λ_r limit value defined in Table 12.1A of ÇYTHYE-2018 are defined as slender.

Table 3. *ÇYTHYE-2018 λ_p and λ_r coefficients in Table 12.1B*

Element definition	Wide to Thickness Ratio	λ_p (Compact / Non-compact)	λ_r (Non-Compact / Slender)	Maximum Limit Value
Flanges of box cross-sections with uniform thickness	b/t	$2.26 \times \sqrt{\dfrac{E}{F_y}}$	$3.0 \times \sqrt{\dfrac{E}{F_y}}$	$5.0 \times \sqrt{\dfrac{E}{F_y}}$
Webs of uniform-thickness box cross-sections	h/t	$3.0 \times \sqrt{\dfrac{E}{F_y}}$	$5.7 \times \sqrt{\dfrac{E}{F_y}}$	$5.7 \times \sqrt{\dfrac{E}{F_y}}$
Pipe cross-section elements	D/t	$0.09 \times \dfrac{E}{F_y}$	$0.31 \times \dfrac{E}{F_y}$	$0.31 \times \dfrac{E}{F_y}$

For the characteristic bending strengths M_n of compact cross-sections, Equation (12.26.a) is given in ÇYTHYE-2018 Section 12.4.4.

$$M_n = M_p \qquad \text{(ÇYTHYE-2018/E.12.26.a)}$$

For the M_n value of non-compact cross-sections, Equation (12.26.b) is given in ÇYTHYE-2018 Section 12.4.4.

$$M_n = M_p - \frac{(\lambda - \lambda_p)}{(\lambda_r - \lambda_p)} \times (M_p - M_y) \qquad \text{(ÇYTHYE-2018/E.12.26.b)}$$

If the composite member satisfies the slender cross-section condition, the characteristic bending moment strength will be determined by M_n, the critical bending moment M_{cr}. In this case, the stress in the pressure head of the steel element will be limited by the critical local buckling stress,

F_{cr}, defined in ÇYTHYE-2018 Equation (12.13) and Equation (12.14). For the maximum compressive stress, the linear elastic stress distribution in the concrete will be considered, using the limit value $0.7 \times f_{ck}$. The yield moment determined by the elastic stress distribution pattern based on the yield limit state, assuming that the maximum compressive stress in the outermost concrete fiber of the compression zone is $0.7 \times f_{ck}$ and the maximum stress in the tension head is equal to F_y. The relationship between M_n and M_p-M_y is presented in ÇYTHYE-2018 Figure (12.5).
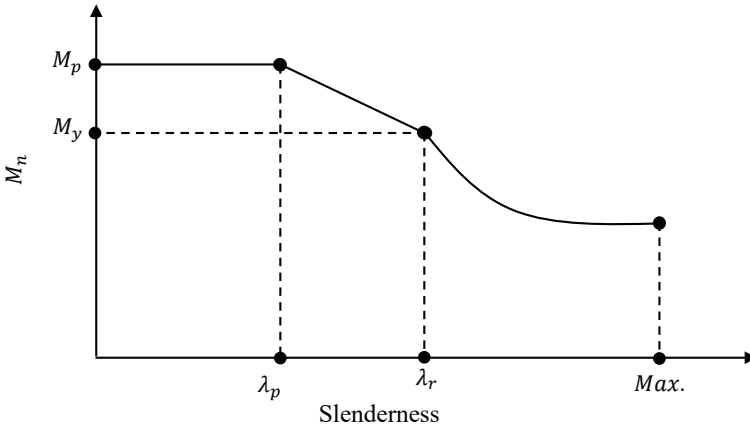
Figure-1. ÇYTHYE-2018 (Figure 12.5), characteristic bending moment strength in CFSTs

1.2.5 Combined Effect of Axial Force and Bending Moment of CFST Elements in DCH-MRF Systems

The stability analysis methods given in ÇYTHYE-2018 Chapter 6 will be used when designing composite elements under the combined load effect, where axial force and bending moment take place together. In ÇYTHYE-2018 Section 6.1, the superposition principle cannot be used because the calculations are not linear in the second order theory. Therefore, the system is calculated according to the second order theory under the total loads amplified by using their respective load coefficients for the respective load combinations of the service loads. While calculating the total loads, the loads obtained from the load combinations given for the YDKT calculations given in the ÇYTHYE-2018 Section 5.3.1 can be used.

(a) $1.4 \times G$

(b) $1.2 \times G + 1.6 \times (Q_r \text{ or } S \text{ or } R)$

(c) $1.2 \times G + 1.6 \times Q + 0.5 \times (Q_r \text{ or } S \text{ or } R)$

(d) $1.2 \times G + 1.6 \times (Q_r \text{ or } S \text{ or } R) + (Q \text{ or } 0.8 \times W)$

(e) $1.2 \times G + 1.0 \times Q + 0.5 \times (Q_r \text{ or } S \text{ or } R) + 1.6 \times W$ **(ÇYTHYE-2018/C.5.3.1)**

(f) $1.2 \times G + 1.0 \times Q + 0.2 \times S + 1.0 \times E$

(g) $0.9 \times G + 1.6 \times W$

(h) $0.9 \times G + 1.0 \times E$

In the loading combinations given in ÇYTHYE-2018 Section 5.3, G (fixed load), Q (live load), Q_r (roof live load), S (snow load), R (rain load), W (wind load), E (earthquake effect), T (temperature change and/or support collapse effects).

➢ If there is a fluid pressure effect given with the abbreviation F, this load will be combined with the coefficient of the G load in (a)-(e) combinations.

➢ If the force given by the abbreviation H (horizontal ground pressure, ground water pressure or bulk material pressure) is present, it will join the combination with a coefficient of 1.6 if this effect will increase the required strength, and a coefficient of 0.9 if it will decrease the required strength. The contribution of this horizontal force to the load combinations including the earthquake effect will be evaluated within the scope of TBDY-2018.

➢ In case of temperature change and/or support collapse effects defined by T, these effects will be added to all joints with a coefficient of 1.0 if these effects will increase the required strength.

While calculating the total loads for GKT calculations, the loads obtained from the load combinations given in ÇYTHYE-2018 Section 5.3.2 can be used.

(1) G

(2) G + Q

(3) G + (Q_r or S or R)

(4) G + 0.75 × Q + 0.75 × (Q_r or S or R)

(5) G + 1.0 × W

(6) G + 0.7 × E

(7) G + 0.75 × Q + 0.75 × (Q_r or S or R) + 0.75 × W

(8) G + 0.75 × Q + 0.75 × S + 0.75 × (0.75 × E)

(9) 0.6 × G + 1.0 × W

(10) 0.6 × G + 0.7 × E

(ÇYTHYE-2018/C.5.3.2)

In addition to the loading combinations given in ÇYTHYE-2018 Section 5.3.2.

➢ If it has the effect given by the abbreviation F, this load will combine with the coefficient of the G load in (1)-(8) combinations.

➢ If there is a force with H, if this effect is in the direction of increasing the required strength, it will be added to the combination with a coefficient of 1.0, if it is in the direction of decreasing the required strength, with a coefficient of 0.6. The contribution of this horizontal force to the load combinations including the earthquake effect will be evaluated within the scope of TBDY-2018.

➢ If there are effects defined by T, if these effects are in the direction of increasing the required strength, they will be added to all joints with a coefficient of 0.75.

The characteristic load values to be used for the design of the building systems will be determined in accordance with TS 498. The conditions given in "Actions on structures–Part 1-3: General actions–Snow loads" (TS EN 1991-1-3 2007) for snow loads and "Actions on structures–Part 1-4: General action–Wind actions" (TS EN 1991-1-4 2007) for wind loads are reflected in the calculations. For the detailed definition of E, which is defined as an earthquake effect, TBDY-2018 conditions will be taken as basis. The basic value of the wind speed, etc., shall not be less than $v_{b,o}$ =28 m/s (100 km/h) and the characteristic wind loads acting on the building's main carrier system, exterior cladding and structural and non-structural elements exposed to the wind shall not be less than 0.5 kN/m² .

1.2.5.1 Approximate second order analysis

It is based on the principle of increasing the internal forces (P and M) to be obtained by using the first order analysis method with certain

coefficients. The required bending moment strength including the second order effects of the loading elements in the system, the required axial force strength given by M_r, and P_r are calculated as given in ÇYTHYE-2018 Equation (6.7) and Equation (6.8), respectively.

$$M_r = B_1 \times M_{nt} + B_2 \times M_{1t} \qquad \text{(ÇYTHYE-2018/E.6.7)}$$

$$P_r = P_{nt} + B_2 \times P_{1t} \qquad \text{(ÇYTHYE-2018/E.6.8)}$$

M_r , is defined by the required bending moment strength including second order effects calculated under YDKT or GKT load combinations. P_r , is given as the required axial force strength including second order effects calculated under YDKT or GKT load combinations. M_{nt}, will be included in the calculations as the first order bending moment calculated under the YDKT or GKT load combinations in the system without horizontal translation. P_{nt}, is considered as the first order axial force calculated under the YDKT or GKT load combinations in the system with horizontal displacement prevented. M_{lt}, is the first order bending moment that occurs in the relevant element under YDKT or GKT load combinations because of only the lateral drift of the structural system. P_{lt}, is given as the first order axial force calculated under YDKT or GKT load combinations due to the horizontal displacements of the structural system.

1.2.5.1.1 B₁ increment coefficient

For the elements under the effect of bending moment and axial pressure force, the B₁ increase coefficient to be applied in both bending directions of the element will be calculated with ÇYTHYE-2018 Equation (6.9).

$$B_1 = \frac{C_m}{1 - \dfrac{\alpha \times P_r}{P_{el}}} \geq 1.0 \qquad \text{(ÇYTHYE-2018/E.6.9)}$$

The α value is taken as 1.0 or 1.6, respectively, depending on whether the calculations are made with YDKT and GKT. C_m is the conversion coefficient to equivalent constant torque dissipation. This coefficient will be calculated with the ÇYTHYE-2018 Equation (6.10) for the elements of the systems that are assumed to have no lateral displacement. However, for elements with lateral loads between the supports in the bending plane, the value C_m =1.0 can be used in the calculations, keeping the safe direction.

$$C_m = 0.6 - 0.4 \times (M_1 - M_2) \qquad \text{(ÇYTHYE-2018/E.6.10)}$$

Here M_1 and M_2 represent the small and large bending moments, respectively, calculated by first-order analysis at the ends of the element.

M_1/M_2 will be taken as positive in double curvature bending and negative in single curvature bending. If M_1 and M_2 create pressure on the same side of the column (single curvature column), in the opposite case (double curvature column), this ratio is taken as negative. P_{el} is the elastic buckling load in the bending plane, assuming that the end points of the element do not make lateral displacements and will be calculated by ÇYTHYE-2018 Equation (6.11).

$$P_{el} = \frac{\pi^2 \times EI^*}{(K_1 \times L)^2} \qquad \text{(ÇYTHYE-2018/E.6.11)}$$

With the general analysis method, EI^* values will be calculated by using the conditions given in ÇYTHYE-2018 Section 12.2.5 in the design. In the design with the buckling length method, $EI^* = EI$ will be used in the calculations. In addition, in accordance with ÇYTHYE-2018 Section 6.2.3, bending, shear and axial stiffnesses of all structural elements will be multiplied by 0.80 and reduced.

➤ The characteristic bending stiffness of the elements under compressive load will be taken as $(EI)_e$, which is defined as the effective stiffness of the composite section defined in ÇYTHYE-2018 Section 12.3.

➤ The characteristic axial stiffness of the members under compressive load will be equal to the sum of the elastic axial stiffnesses of the components forming the section.

➤ Only structural steel and concrete steel will be considered in determining the stiffness of the elements under tension.

➤ The bending stiffness of the elements will be reduced by multiplying the coefficient $\tau_{rb} = 0.8$.

The effective bending stiffness of all concrete filled composite elements with pipe and box cross-section, $(EI)_e$, will be calculated using ÇYTHYE-2018 Equation (12.15).

$$(EI)_e = E_s \times I_s + E_{sr} \times I_{sr} + C_3 \times E_c \times I_c$$

$$C_3 = 0.45 + 3 \times \left(\frac{A_s + A_{sr}}{A_g}\right) \leq 0.90 \qquad \text{(ÇYTHYEY-2018/E.12.15)}$$

$$E_c = 0.43 \times w_c^{1.5} \times \sqrt{f_{ck}}$$

E_s *and* E_{sr} are modulus of elasticity for structural steel and concrete steel, respectively, with a value of 200000 MPa. I_s is defined as the moment of inertia of the structural steel cross-section, while Ir_s and I_c are the moment of inertia of the reinforcement bars and concrete cross-section

with respect to the elastic neutral axis of the composite cross-section, respectively. A_s, A_{sr} and A_g are given as structural steel cross-sectional area, longitudinal reinforcement area and total cross-sectional area of the composite element, respectively. E_c to be used as a concrete elasticity module, the characteristic concrete strength is f_{ck}, its unit is MPa, w_c is the concrete unit volume weight, and its unit is included in the calculations for E_c in kg/m³. Also,

➤ The characteristic concrete compressive strength used in the calculation of the capacities of the composite elements, f_{ck} will be between 20 and 70MPa.

➤ The characteristic yield stress of concrete steel, F_{ysr}, is limited to 500 MPa.

➤ The characteristic yield stress of structural steel members, $F_{y,,}$ is limited to 460 MPa.

1.1.5.1.2 B₂ increment coefficient

For the elements under the effect of bending moment and axial compressive force, B₂ increase coefficient to be applied in both bending directions of the element will be calculated with ÇYTHYE-2018 Equation (6.12).

$$B_2 = \frac{C_m}{1 - \dfrac{\alpha \times P_{kat}}{P_{e,kat}}} \geq 1.0 \qquad \text{(ÇYTHYE-2018/E.6.12)}$$

For P_{kat}, YDKT or GKT load combinations, it is calculated as the total vertical load acting on all vertical load-bearing elements (including elements outside the horizontal load-bearing system) of the floor in question. $P_{e,kat}$ is calculated as the elastic buckling load of said ply, for the direction of lateral displacement under consideration. $P_{e,kat}$ value will be calculated with ÇYTHYE-2018 Equation (6.13).

$$P_{e,kat} = R_m \times \frac{H \times L}{\Delta_H} \qquad \text{(ÇYTHYE-2018/E.6.13)}$$

$$R_m = 1 - 0.15 \times \left(\frac{P_{mf}}{P_{kat}}\right) \qquad \text{(ÇYTHYE-2018/E.6.14)}$$

While the second order effects in the elements of the system with the horizontal displacement are given with P-δ, the second order effects in the whole system without the horizontal translation are given with P-Δ.

The coefficient R_m is the coefficient in which the effect of P-δ on P-Δ is reflected. P_{mf} is defined as the total vertical load acting on the floor columns of these frames, if there are frames that transmit moment in the considered direction. However, zero will be taken in braced frames. Δ_H is the first-order relative story drift in the considered direction, under selected lateral loads, using the system stiffness. H is defined as the floor shear force consisting of horizontal loads used to calculate Δ_H, in the considered direction.

1.2.5.2 Axial Force and Bending Moment Interaction with General Interaction Diagrams

For CFST concrete filled composite typical cross-sections, the interaction diagrams given in ÇYTHYE-2018 Table 12.4 and Table 12.5 can be used. The strength expressions given for the mutual influence diagrams describe the typical points available in ÇYTHYE-2018 Figure 12.7, which constitutes the interaction diagram. The strength expressions given for the creation of the interaction diagram do not include the slenderness effect of the composite element. To take this effect into account, the strengths determined in the mutual influence diagram will be multiplied by the reduction coefficient. The strength reduction coefficient, λ, is calculated by ÇYTHYE-2018 Equation (12.27).

$$\lambda = \frac{P_n}{P_{no}} \geq 0.2 \qquad \text{(ÇYTHYE-2018/E.12.27)}$$

For composite elements subject to axial force and biaxial bending, this method will be simplified, and the following interaction expressions obtained by linear interpolation between A", C", and B" points will be used.

$$P_r < P_C$$

$$\left(\frac{M_{rx}}{M_{Cx}} + \frac{M_{ry}}{M_{Cy}}\right) \leq 1.0 \qquad \text{(ÇYTHYE-2018/E.12.28.a)}$$

$$P_r \geq P_C$$

$$\frac{P_r - P_C}{P_A - P_C} + \frac{M_{rx}}{M_{Cx}} + \frac{M_{ry}}{M_{Cy}} \leq 1.0 \qquad \text{(ÇYTHYE-2018/E.12.28.b)}$$

P_r indicates the required axial compressive force strength under YDKT or GKT load combinations. P_A is the current axial compressive force strength calculated in ÇYTHYE-2018 Section 12.3 for point A" in the interaction diagram. P_C, is the current axial compressive force strength

calculated in ÇYTHYE-2018 Section 12.3 for point C" in the interaction diagram. M_r, indicates the required bending moment strength under YDKT or GKT load combinations. M_c, is the current bending moment strength calculated in ÇYTHYE-2018 Section 12.4 for point C" in the interaction diagram. Ø=0.90 and Ω=1.67 are included in the calculations.

If there is a bending moment effect around both axes, the axial compressive strength, P_c, can take different values according to the strong and weak axes of the composite element at point C. In this case, the smaller of the P_c values determined in ÇYTHYE-2018 Equation (12.28.a) and Equation (12.28.b) will be used.
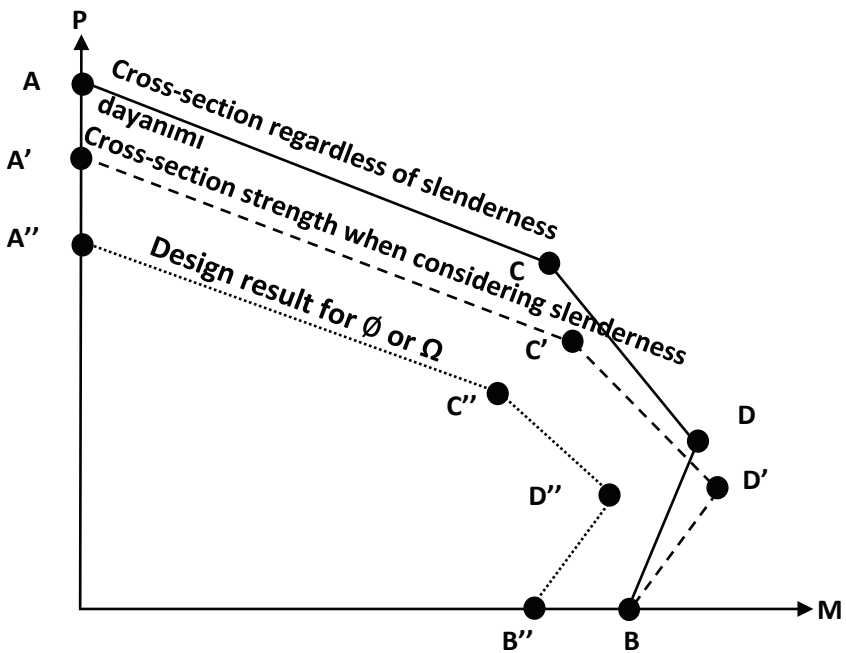

Figure-2. ÇYTHYE-2018 (Figure 12.7) Interaction diagram developed for CFST elements

The calculation of the points in the interaction diagram in ÇYTHYE-2018 (Figure 12.7) will be made using ÇYTHYE-2018 Table (12.4) and ÇYTHYE-2018 Table (12.5).

Table 4. ÇYTHYE-2018 (Table 12.4) Composite elements with CFST box cross-section (combined bending)

$b_i = B - 2 \times t$ $h_i = H - 2 \times t$ $r_i = t$ and $r_o = 1.5 \times t$ (hot finished) $r_i = t$ and $r_o = 2.0 \times t$ (cold finished $t \leq 6\ mm$) $r_i = 1.5 \times t$ and $r_o = 2.5 \times t$ (cold finished $6 < t \leq 10\ mm$) $r_i = 2.0 \times t$ and $r_o = 3.0 \times t$ (cold finished $t > 10\ mm$) $A_c = b_i \times h_i - 0.8584 \times r_i^2$ $A_s = B \times H - b_i \times h_i$ $P_A = A_s \times F_y + 0.85 \times f_{ck} \times A_c$ $M_A = 0$	(ÇYTHYE-2018/T.12.4.A)
$P_D = \dfrac{0.85 \times f_{ck} \times A_c}{2}$ $W_c = \dfrac{b_i \times h_i^2}{4} - 0.192 \times r_i^3$ $A_{g,y} = \left(1 - \dfrac{\pi}{4}\right) \times r_o^2$ $A_{\xi,\xi} = \left(1 - \dfrac{\pi}{4}\right) \times r_i^2$ $h_{g,y} = \dfrac{H}{2} - r_o \times (10 - 3 \times \pi)/(12 - 3 \times \pi)$ $h_{\xi,y} = \dfrac{h_i}{2} - r_i \times (10 - 3 \times \pi)/(12 - 3 \times \pi)$ $W_{px} = \dfrac{B \times H^2}{4} - \dfrac{b_i \times h_i^2}{4} - 4 \times A_{g,y} \times h_{g,y} + 4 \times A_{\xi,\xi} \times h_{\xi,y}$ $M_D = W_{px} \times F_y + \dfrac{W_c}{2} \times (0.85 \times f_{ck})$	(ÇYTHYE-2018/T.12.4.D)
$h_n = \dfrac{0.85 \times f_{ck} \times A_c}{2 \times [0.85 \times f_{ck} \times b_i + 4 \times F_y \times t]} \leq \dfrac{h_i}{2}$ $h_E = \dfrac{h_n}{2} + \dfrac{H}{4}$ $P_E = \dfrac{0.85 \times f_{ck} \times A_c}{2} + 0.85 \times f_{ck} \times b_i \times h_E + 4 \times F_y \times t \times h_E$ $W_{cE} = b_i \times h_E^2$ $W_{sE} = 2 \times t \times h_E^2$ $M_E = M_D - F_y \times W_{sE} - \dfrac{W_{cE}}{2} \times (0.85 \times f_{ck})$	(ÇYTHYE-2018/T.12.4.E)
$P_B = 0$ $W_{sn} = 2 \times t \times h_n^2$ $W_{cn} = b_i \times h_n^2$ $M_B = M_D - F_y \times W_{sn} - \dfrac{W_{cn}}{2} \times (0.85 \times f_{ck})$	(ÇYTHYE-2018/T.12.4.B)

$$P_C = 0.85 \times f_{ck} \times A_c$$

$$M_C = M_B$$

(ÇYTHYE-2018/T.12.4.C)

Table 5. *ÇYTHYE-2018 (Table 12.5) Composite elements with CFST pipe cross-section (combined bending)*

$$M_A = 0$$

$$h = d - 2 \times t$$

(ÇYTHYEY-2018/T.12.5.A)

$$A_s = \pi \times (d \times t - t^2)$$

$$A_c = \frac{\pi \times h^2}{4}$$

$$P_A = A_s \times F_y + 0.95 \times f_{ck} \times A_c$$

$$P_D = \frac{0.95 \times f_{ck} \times A_c}{2}$$

$$W_c = \frac{h^3}{6}$$

(ÇYTHYEY-2018/T.12.5.D)

$$W_p = \frac{d^3}{6} - W_c$$

$$M_D = W_p \times F_y - \frac{W_c}{2} \times (0.95 \times f_{ck})$$

$$K_c = f_{ck} \times h^2$$

$$K_s = F_y \times \left(\frac{d-t}{2}\right) \times t$$

$$\theta = \frac{0.0260 \times K_c - 2 \times K_s}{0.0848 \times K_c}$$

$$+ \frac{\sqrt{(0.0260 \times K_c + 2 \times K_s)^2 + 0.857 \times K_c \times K_s}}{0.0848 \times K_c} \text{ (rad)}$$

(ÇYTHYEY-2018/T.12.5.E)

$$h_n = \frac{h}{2} \times \sin\left(\frac{\pi - \theta}{2}\right) \leq \frac{h}{2}$$

$$h_E = \frac{h_n}{2} - \frac{h}{4}$$

$$\theta_2 = \pi - arcsin\left(\frac{2 \times h_E}{h}\right) \text{ (rad)}$$

$$P_E = P_A - \frac{1}{4} \times \left[F_y \times (d^2 - h^2) + \frac{095 \times f_{ck}}{2} \times h^2\right] \times (\theta_2 - \sin\theta_2)$$

$$W_{cE} = \frac{h^3}{6} \times \sin^3\left(\frac{\theta_2}{2}\right)$$

$$W_{sE} = \frac{(d^3 - h^3)}{6} \times \sin\left(\frac{\theta_2}{2}\right)$$

$$M_E = F_y \times W_{sE} - \frac{W_{cE}}{2} \times (0.95 \times f_{ck})$$

$$P_B = 0$$

(ÇYTHYEY-2018/T.12.5.B)

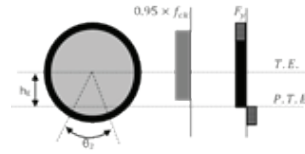$$W_{sB} = \frac{(d^3 - h^3)}{6} \times \sin\left(\frac{\theta}{2}\right)$$

$$W_{cB} = \frac{h^3}{6} \times \sin^3\left(\frac{\theta}{2}\right)$$

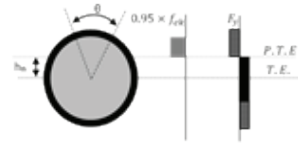$$M_B = F_y \times W_{sB} + \frac{W_{cB}}{2} \times (0.95 \times f_{ck})$$

(ÇYTHYEY-2018/T.12.5.C)

$$P_C = 0.95 \times f_{ck} \times A_c$$

$$M_C = M_B$$

### References

ÇYTHYE-2018. 2018. "Çelik Yapıların Tasarım Hesap Ve Yapım Esaslarına Dair Yönetmelik."

Etli, Serkan. 2021. "Analytical Evaluation of Behavior of Composite Columns Under Axial Load." *International Journal of Pure and Applied Sciences*. doi: 10.29132/ijpas.991166.

Etli, Serkan, and Esra Mete Güneyisi. 2020. "Seismic Performance Evaluation of Regular and Irregular Composite Moment Resisting Frames." *Latin American Journal of Solids and Structures* 17(7):1–22. doi: 10.1590/1679-78255969.

Etli, Serkan, and Esra Mete Güneyisi. 2021. "Assessment of Seismic Behavior Factor of Code-Designed Steel–Concrete Composite Buildings." *Arabian Journal for Science and Engineering* 46(5):4271–92. doi: 10.1007/s13369-020-04913-9.

Lee, Eun-Taik, B. H. Yun, H. J. Shim, K. H. Chang, and George C. Lee. 2009. "Torsional Behavior of Concrete-Filled Circular Steel Tube Columns." *Journal of Structural Engineering* 135(10):1250–58. doi: 10.1061/(asce)0733-9445(2009)135:10(1250).

Shanmugam, N. E., and B. Lakshmi. 2001. "State of the Art Report on Steel-Concrete Composite Columns." *Journal of Constructional Steel Research* 57(10):1041–80. doi: 10.1016/S0143-974X(01)00021-9.

TBDY-2018. 2018. "Türkiye Bina Deprem Yönetmeliği." *Http://Www.Resmigazete.Gov.Tr/Eskiler/2018/03/20180318M1-2-1.Pdf* 416.

TS-498. 1987. "Yapı Elemanlarının Boyutlandırılmasında Alınacak Yüklerin Hesap Değerleri." *Türk Standartları Enstitüsü*.

TS EN 1991-1-3. 2007. "Yapılar Üzerindeki Etkiler - Bölüm 1-3: Genel Etkiler - Kar Yükleri." *Turkish Standards Institute*.

TS EN 1991-1-4. 2007. "Yapılar Üzerindeki Etkiler- Bölüm 1-4: Genel Etkiler - Rüzgâr Etkileri." *Turkish Standards Institute*.
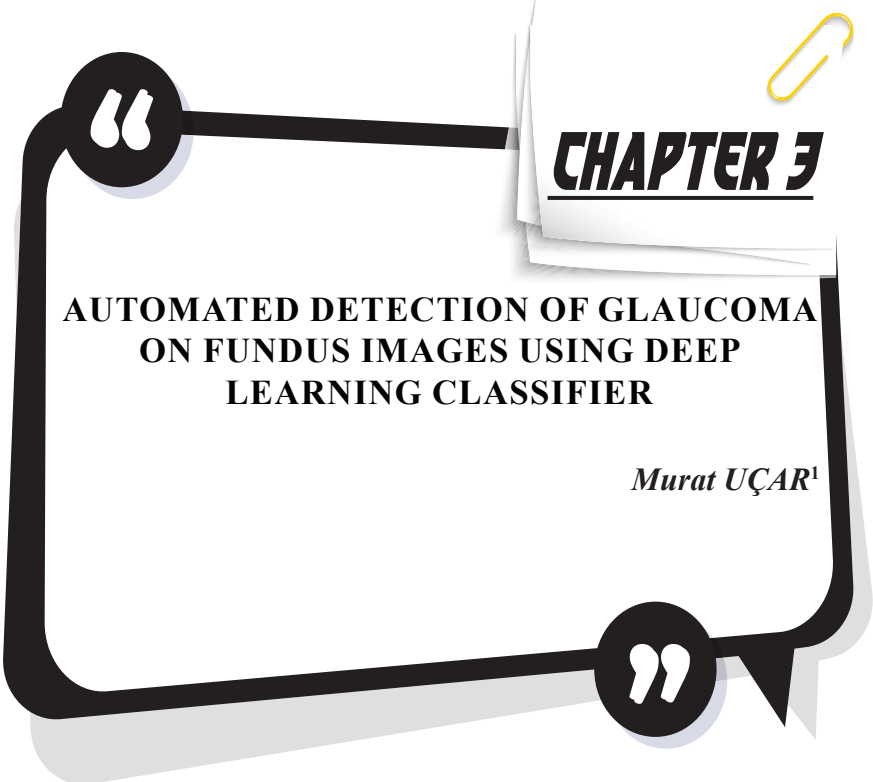
CHAPTER 3

AUTOMATED DETECTION OF GLAUCOMA ON FUNDUS IMAGES USING DEEP LEARNING CLASSIFIER

Murat UÇAR[1]

1 Asst. Prof. Dr. Murat UÇAR, İskenderun Technical University, Faculty of Business and Management Sciences, Department of Management Information Systems, Hatay, TURKEY, murat.ucar@iste.edu.tr, https://orcid.org/0000-0001-9997-4267

1 Introduction

Glaucoma is a group of eye diseases that harm the optic nerve, which is vital for healthy vision. This damage is usually caused by a very high pressure in the eye. 76 million person in 2020 and 111.8 million person in 2040 are expected to be affected by glaucoma (Tham et al., 2014). Glaucoma, a disease that can progress without being noticed until the last stage of the disease, can cause permanent non-healing blindness that cannot be treated if diagnosed late. Since there is currently no cure yet, it is essential to detect glaucoma early to prevent vision loss in the eye.

Glaucoma is usually diagnosed by ophthalmologists using extensive examinations such as tonometry, ocular motility, examination of the pupil and external examination of the eye. However, in recent years, many researchers have been working on automatic diagnosis of glaucoma using retinal images. The first studies on this subject generally used traditional image processing methods (Maheshwari et al., 2017; Kolář & Jan 2008; Acharya et al., 2011; Mookiah et al., 2012).

Additionally deep learning (DL) approaches have been used extensively in object recognition, image segmentation and classification of medical and ophthalmological images and very good outcomes have been achieved. In particular, convolutional neural networks (CNNs) have been used for early detection and identification of retinal diseases such as diabetic retinopathy (Gulshan et al., 2016), age-related macular degeneration (Lee et al., 2017) and glaucoma from retinal images (Chen et al., 2015).

Studies suggesting deep learning-based methods to detect glaucoma are being conducted, but are limited. Raghavendra et al. (2018) have developed a new model based on DL for the diagnosis of glaucoma. The developed model used an eighteen layer CNN for feature extraction from digital fundus images. Later, they classified these features as normal and glaucoma at the test stage using Linear Discriminant Analysis (LDA) classifier. This proposed method has achieved an accuracy rate of 98.13%. In another study, Chai et al. (2018) suggested a multi-branch neural network approach to diagnose the glaucoma. They reported that the proposed model could both automatically distinguish important areas of images with a lot of detail and remove hidden features from the image at the same time. When they tested the proposed model on real datasets, the model was achieved an accuracy rate of 0.9151. Gómez-Valverde et al. (2019) used transfer learning models such as Standard CNN, VGG19, ResNet, GoogleNet and two versions of DeNet for the diagnosis of glaucoma. The trained model was tested on three different datasets and the VGG19 model had the best results. Fu et al. (2018) have proposed a new ensemble network that combines different CNNs for automatic glaucoma diagnosis. They trained the proposed model with the images in the ORIGA dataset and tested

on SCES and SINDI datasets. They reported that the developed method performs better than other algorithms. L. Li et al. (2019) first created a large-scale dataset for glaucoma detection, then developed an attention-based model and combined it with CNNs. Experimental results showed that the model they suggested significantly increased the correct detection of glaucoma. J. Lee et al. (2020) used a spectral-domain optical coherence tomography to detect glaucoma. They reported that the model they proposed was neural architecture search (NASNet) architecture and it was able to diagnose glaucoma with 0.990 AUC, 94.7% sensitivity and 100% specificity.

Z. Li et al. (2018) suggested a DL model based on Inception architecture to detect glaucomatous optic neuropathy (GON) from retinal images. They stated that the proposed model achieved an AUC of 0.986 in the distinction between GON diseases and healthy images. Christopher et al. (2018) examined the effectiveness of transfer learning using ResNet, VGG16 and Inception-V3 algorithms for the diagnosis of GON. They reported that the best model for separating GON disease from healthy eyes was the Resnet50 model with 0.91 AUC value.

In some studies, segmentation and classification-based models have been developed for automatic glaucoma diagnosis. Bajwa et al. (2019) developed two-step model, first of all detecting the optic disc from the retinal fundus image and then classifying it as a healthy or glaucomatous. They evaluated the proposed model on ORIGA dataset and reported that it achieved 0.874 AUC value. dos Santos Ferreira et al. (2018) first performed optical disc segmentation using the CNN and then classified the glaucoma. They reported that this method was an effective method for glaucoma diagnosis by obtaining 100% accuracy, sensitivity and specificity on the public datasets. Martins et al. (2020) developed a segmentation and classification based on CNNs by combining several publicly available datasets for the diagnosis of glaucoma. They reported that the proposed system achieved 0.87 accuracy, 0.85 precision and 0.93 AUC value. Bisneto et al. (2020) used the Generative Adversarial Network and taxonomic diversity index based on segmentation for automatic detection of glaucoma. The proposed method has been examined on the public datasets and has been declared as an auxiliary model for specialists with 100% accuracy rate.

Some of the researchers developed DL models for optic disc and optic cup segmentation. Zilly et al. (2017) developed a new ensemble model based on CNN architectures to segment the optic disc and cup. They reported that the developed model outperformed the existing methods in the DRISHTI-GS dataset. Shankaranarayana et al. (2017) suggested a DL model based on the fully convolutional networks model for optic disc and optic cup segmentation. As a result of their tests on the RIM-ONE dataset, the developed model achieved higher results than other methods.

As can be seen from the previous studies mentioned above, despite the significant number of deep learning architectures proposed for automatic detection of glaucoma from retinal images, there are still gaps in the use of new DL architectures. In this study, a new DL model has been presented by modifying DarkNet architecture, one of the DL classifiers, for automatic diagnosis of glaucoma. In addition, developing an efficient algorithm using a large scale dataset containing many images is another contribution of the study.

This paper is arranged as follows. Section II explains the data and developed method in detail. Section III indicates the experimental setup. Section IV gives results and comparison with findings from similar studies in the literature. At last, the paper is concluded by Section V.

2 Materials and Methods

2.1 Dataset

In this study, a large scale dataset newly created by L. Li et al. (2019) was used. This dataset contains total 5824 fundus images, 2392 glaucoma and 3432 normal, obtained from Beijing Tongren Hospital. The labelling of each fundus image in the dataset as glaucoma or normal was done by ophthalmologists. However, in this study, 4854 fundus images could be used since only a first part of the dataset was shared with the researchers. In this part, there were 1711 glaucoma and 3143 normal images and all fundus images were with 500x500 pixels. Sample fundus images of the dataset were shown in Figure 1.
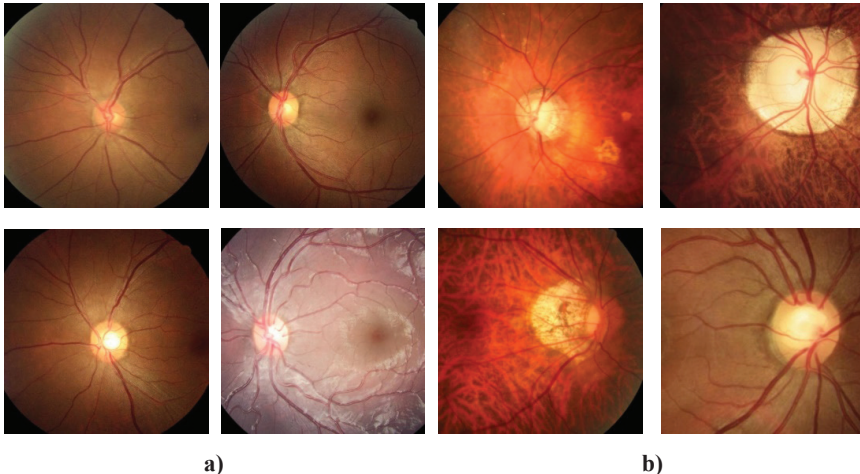

a)   b)

Figure 1. Sample fundus images a) Normal b) Glaucoma

2.2 Method

In this paper, a new approach was presented organised on DarkNet model, used as a classifier, in the real-time object recognition system called Yolo9000. DarkNet classifier is a successful architecture designed

for object detection and has proven itself in deep learning. It includes 19 convolution layers and 5 max pooling layers. Similar to VGG models, 3 × 3 filters are often used after each pooling step and the number of channels is doubled. It uses batch normalization to stabilize training and the model (Redmon & Farhadi, 2017).

The proposed model, developed by inspiring from the DarkNet deep learning model, has fewer layers. It includes 13 convolution layers, 2 fully connected layers and an output layer with Softmax activation function. In addition, this model has 5 pooling layers with concatenated average and max pooling. Layer and layer parameters of the proposed model were presented in Table 1. The schematic representation of the model is given in Figure 2.

Table 1. Layer and layer parameters of the proposed model

|	Filter	Size/Stride	Output
Image input	-		224 X 224 X 7
Convolution	32		3 X 3 224 X 224
[Maxpool-Averagepool]		2X2 / 2	112 X 112
Convolution	64	3 X 3	112 X 112
[Maxpool-Averagepool]		2X2 / 2	56 X 56
Convolution	128	3 X 3	56 X 56
Convolution	64	1 X 1	56 X 56
Convolution	128	3 X 3	56 X 56
[Maxpool-Averagepool]		2X2 / 2	28 X 28
Convolution	256	3 X 3	28 X 28
Convolution	128	1 X 1	28 X 28
Convolution	256	3 X 3	28 X 28
Convolution	128	1 X 1	28 X 28
Convolution	256	3 X 3	28 X 28
[Maxpool-Averagepool]		2X2 / 2	14 X 14
Convolution	512	3 X 3	14 X 14
Convolution	256	1 X 1	14 X 14
Convolution	512	3 X 3	14 X 14
[Maxpool-Averagepool]		2X2 / 2	7 X 7
Dense			4096
Dense			2048
Dense			2
Soft-Max			2
Classification Output			2
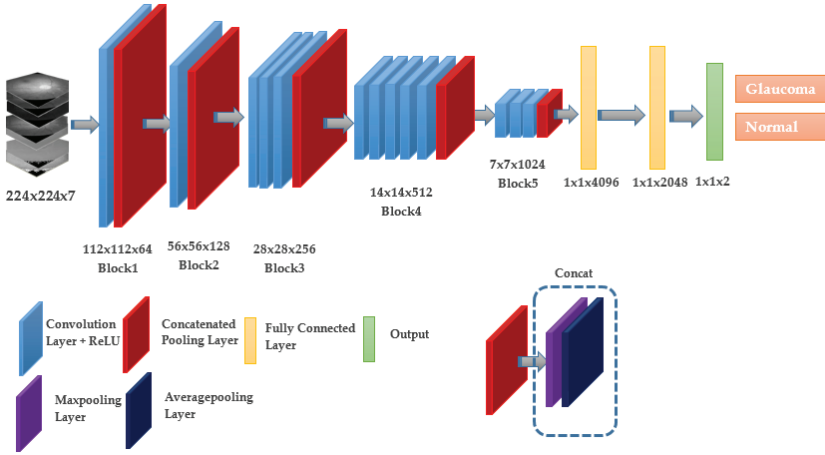
Figure 2. The schematic representation of the model

3   Experiments

3.1 Experiment Setup

Google Cloud environment equipped with NVIDIA T80 GPU graphics card, Intel (R) Xeon (R) 2.00 GHz CPU and 12GB memory was utilized for the experimental studies. All codes of the proposed model have been developed with the Keras Library written in Python language on the Tensorflow framework.

3.2 Training

3143 images of the normal class and 1711 images of the glaucoma class were used. The dataset used in the study was first divided into 80% training and 20% testing. Then 10 percent of the training data were utilized as validation data. While training and validation images were used only for training and fit of the model, test images were used to assess the model's predictive performance on images that it did not seen before. According to these ratios, the number of images included in the datasets is presented in Table 2.

Table 2. Division of images into train, validation and test sets

	Train	*Validation*	*Test*
Normal	2262	253	628
Glaucoma	1232	136	343
TOTAL	3494	389	971

For obtaining the best performance results 4 different image channels from CIELAB and Hue Saturation Value (HSV) colour space were combined with Red Green Blue (RGB) channels and a 7-channel image matrix was created. As a result of the experimental tests, $L*a*$ channels were selected from CIELAB colour space and h, s channels were selected

from HSV colour space. Due to the increase in the amount of parameters to be calculated and the memory requirement, the image sizes were resized to 224x224 as in the L. Li et al. (2019) for the input layer of the model.

The rectified linear unit (ReLU) function, which is frequently preferred in deep learning models, was chosen as the activation function in each convolution layer in the model. Batch normalization was applied after convolution layers. Pooling layers reduce the information of the width and height by keeping constant the channels' number in the input matrix. This reduces the complexity of calculation but can result in data loss. For pooling, one can choose either Max pooling or Average pooling. In the proposed model, the results of the both pooling methods were concatenated to keep data loss to a minimum. As a result, while the width and height of the input matrix of pooling layers decreased, the number of channels doubled. Two fully connected layers with ReLU were added at the end of the model. To prevent over-fitting problem, dropouts of 0.3 and 0.2 were applied after these layers, respectively. In the output layer, Softmax activation function was utilized, and the number of neurons was set to 2.

During the training of the model, categorical cross entropy was chosen as the loss function and it was tried to be minimized with the Adam optimizer. Mini-batch size was utilized as 16 and the learning rate value for Adam optimizer was determined as 0.0001. Over-fitting problem may occur during the training of DL models. To eliminate this issue, the accuracy of the model was tested with the images in the validation set after each training step, and the weight values with the lowest error rate were recorded. The epoch number was determined as 100. After the training was completed, the weight values with the lowest error rate were loaded on the validation set and utilized for determining the accuracy of model with the test dataset that was not encountered before.

3.3 Performance metrics

In this study, a binary classification was applied. Due to the imbalanced dataset, the method was assessed using different performance criteria such as Balanced Accuracy (BAcc), Sensitivity (Sen), Specificity (Spe), Precision (Pre) and F1-score. These metrics given in equation 1- 5 were calculated using values such as True Positive (TP), True Negative (TN), False Positive (FP) and False Negative (FN) obtained in the confusion matrix. Here, TP; occurs when the model correctly predicts an instance belonging to the glaucoma class. FP; occurs when the model incorrectly predicted an instance of a normal class as belonging to glaucoma class. TN occurs when the model correctly predicts an instance belonging to the normal class. Finally, FN occurs when the model incorrectly classifies an instance belonging to the glaucoma class as belonging to the normal class.

Balanced accuracy is a method used to assess the performance of the method in imbalanced datasets and is calculated by taking the arithmetic mean of sensitivity and specificity metrics. Sen also known as recall is the rate at which glaucoma class cases are rightly classified among the total number of glaucoma class cases. Spe is the rate at which normal class cases are rightly classified among the total number of normal class cases. Pre is the rate at which glaucoma class cases are rightly classified among the total number of correctly and incorrectly classified glaucoma cases. F1-score is another evaluation metric used to assess the performance of the method in unbalanced datasets and is defined as harmonic mean of both precision and recall.

$$Balanced\ Accuracy = \frac{Sensitivity + Specificity}{2} \qquad (1)$$

$$Sensitivity = Recall = \frac{TP}{TP + FN} \qquad (2)$$

$$Specificity = \frac{TN}{TN + FP} \qquad (3)$$

$$Precision = \frac{TP}{TP + FP} \qquad (4)$$

$$F1 - score = 2\ \frac{Precision\ x\ Recall}{Precision + Recall} \qquad (5)$$

Moreover, another popular metric (AUC-ROC) curve was also used in this study to evaluate classification success. The larger the AUC shows, the better the model used to predict the disease.

4   Results and Discussion

The main objective of this study is to examine the performance of the modified DarkNet deep learning architecture in detecting glaucoma and normal cases on a large-scale dataset and to compare the performance results with current studies in this area. The proposed model was trained according to the parameters presented in Section 3.2. The accuracy and loss curves of the training and validation dataset were presented in Figure 3. The training of the network was initially set as 100 epochs and the weights of the network which had best validation accuracy were used in the final model. As can be seen in Figure 3 best validation accuracy was obtained at epoch 99.
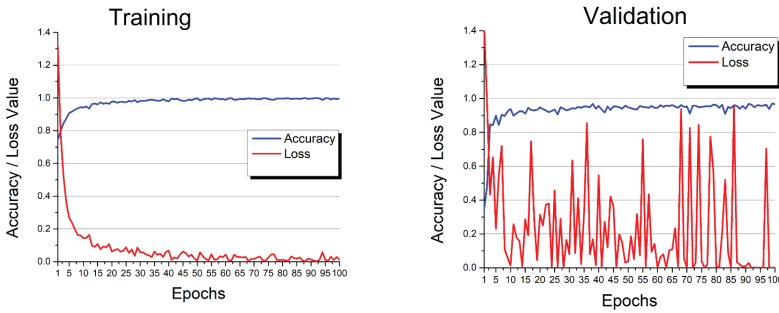
Figure 3. Accuracy and loss curves of training and validation

The BAcc, Sen, Spe, Pre and F1-score values for which the best performance was obtained on the test dataset were indicated in Table 3. As can be seen from the values in the table, although the dataset used in this study was imbalanced, the proposed model produced acceptable results with 0.9650 BAcc and 0.9573 F1-score value.

Table 3. The results of proposed model on the test dataset

Model	BAcc	Sen	Spe	Pre	F1- Score
Modified DarkNet	0,9650	0,9475	0,9825	0,9673	0,9573

And also, Figure 4 presents the confusion matrix obtained by proposed model. It can be observed from the figure that out of 343 glaucoma images 325 are rightly classified and 18 glaucoma images are misclassified. On the other hand, 617 of total 628 healthy images were rightly classified and 11 images were incorrectly classified as glaucoma.
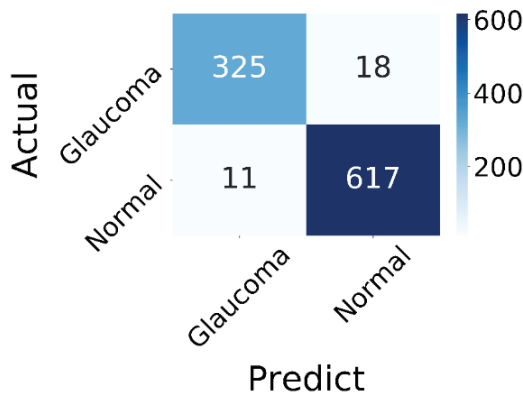

Figure 4. Confusion Matrix obtained by proposed model.

To illustrate the success of developed deep learning method more concretely, ROC curves and AUC values were also given in Figure 5. Figure 5 shows that the ROC curves had very high values.
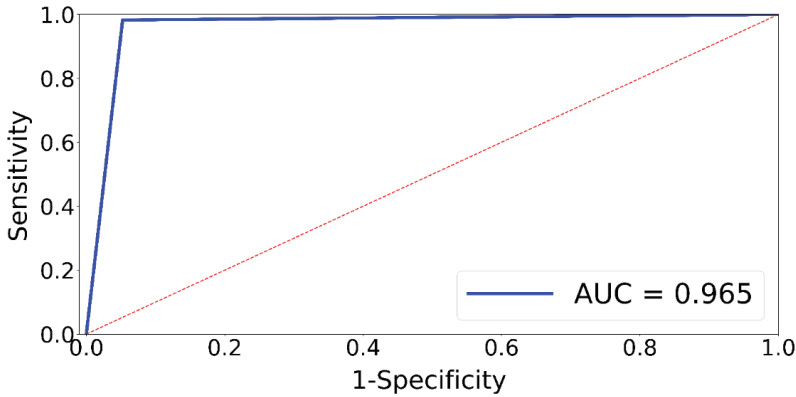
Figure 5. ROC curves of the proposed model

For comparing the classification performance of the developed model, detailed information on existing studies using DL architecture for diagnosing glaucoma from digital fundus images is summarized in Table 4. However, it is not possible to make a one-to-one comparison with other studies due to the differences in the datasets and image numbers used in the studies given in this table. The performance of the developed model in this study can only be compared with (L. Li et al., 2019). Considering the results obtained in both studies, it was seen that results were very close to each other. In addition, as can be seen from Table 4, the number of glaucoma and normal images is not balanced in studies (Chen et al., 2015), (Gómez-Valverde et al., 2019), (Fu et al., 2018) and (Bajwa et al., 2019), as in our study. Considering the BAcc and AUC values obtained in these studies, it can be said that the developed model shows a higher outcome in imbalanced data in contrast to other studies.

Table 4. Accuracy results of proposed model and related studies in the literature

Author	Method	Datasets (G: Glaucoma, N: NonGlaucoma)	Performance (%)
(Chen et al., 2015)	CNN	**ORIGA** -168 G -482 N **SCES** -16 G -1630 N	AUC: 0.8870
(Raghavendra et al., 2018)	Eighteen layer CNN + LDA	**Private Dataset** -837 G -589 N	Acc: 0.9813 Sen: 0.9800 Spe: 0.9830
(Chai et al., 2018)	Multi-branch neural network	**Private Dataset** -1023 G -1531 N	Acc: 0.9151 Sen: 0.9233 Spe: 0.9090

(Gómez-Valverde et al., 2019)	VGG19	**RIM-ONE (R1,R2,R23)** -311 G -455 N **DRISHTI-GS** -70 G -31 N **Private Dataset (ESPERANZA)** -113 G -1333 N	Bacc: 0.8805 Sen: 0.8701 Spe: 0.8901 AUC: 0.9420
(Fu et al., 2018)	Ensemble deep learning	**ORIGA** -168 G -482 N **SCES** -16 G -1630 N **SINDI** -113 G -5670 N	**SCES Dataset** BAcc: 0.8429 Sen: 0.8478 Spe: 0.8380 AUC: 0.9183 **SINDI Dataset** BAcc: 0.7495 Sen: 0.7876 Spe: 0.7115 AUC: 0.8173
(L. Li et al., 2019)	Attention-based CNN	**Private Dataset** -2392 G -3432 N	Acc: 0.9530 Sen:0.9540 Spe: 0.9520 AUC:0.9750 F2-score:0.9510
(Bajwa et al., 2019)	CNN	**ORIGA** -168 G -482 N **HRF** -15 G -15 N **OCT&CFI**-100 N	AUC: 0.8680 Pre:0.7797 Recall:0.7938 F1-score:0.7788
(dos Santos Ferreira et al., 2018)	CNN U-Net	**RIM-ONE** -51 G -119 N **DRISHTI-GS** -70 G -31 N **DRIONS-DB** -110 retinal images	Acc: 100.00 Sen:100.00 Spe:100.00 F1-Score: 1
(Martins et al., 2020)	CNN (Inception V3)	**ORIGA** -168 G -482 N **RIM-ONE (R1,R2,R23)** -388 G -543 N **DRISHTI-GS** -70 G -31 N **iChallenge** -80 G -720 N **RIGA**749 retinal images	Acc: 0.9000 Sen: 0.8000 Spe: 0.9400 AUC: 0.9500
Proposed model	**Modified DarkNet**	**First part of the dataset created by** (L. Li et al., 2019) **-1711 G -3143N**	**BAcc: 0.9650** **Sen:0.9475** **Spe:0.9825** **Pre:0.9673** **F1-score:0.9573** **AUC:0.9650**

5   Conclusion

A novel deep learning model is proposed in this study for automatic detection and classification of glaucoma cases from fundus images. The model, trained on the database of large-scale fundus images, has high

performance to diagnose glaucoma and normal cases. The developed system can perform binary classification process with 96.50% balanced accuracy, 96.73% precision, 98.25% specificity, 94.75% sensitivity and 95.73% F1-score. In general, the developed model can help ophthalmologists for checking the clinical diagnosis.

Acknowledgment

References

Acharya, U. R., Dua, S., Du, X., Chua, C. K., & others. (2011). Automated diagnosis of glaucoma using texture and higher order spectra features. *IEEE Transactions on Information Technology in Biomedicine*, *15*(3), 449–455.

Bajwa, M. N., Malik, M. I., Siddiqui, S. A., Dengel, A., Shafait, F., Neumeier, W., & Ahmed, S. (2019). Two-stage framework for optic disc localization and glaucoma classification in retinal fundus images using deep learning. *BMC Medical Informatics and Decision Making*, *19*(1), 136.

Bisneto, T. R. V., de Carvalho Filho, A. O., & Magalhães, D. M. V. (2020). Generative adversarial network and texture features applied to automatic glaucoma detection. *Applied Soft Computing*, *90*, 106165.

Chai, Y., Liu, H., & Xu, J. (2018). Glaucoma diagnosis based on both hidden features and domain knowledge through deep learning models. *Knowledge-Based Systems*, *161*, 147–156.

Chen, X., Xu, Y., Wong, D. W. K., Wong, T. Y., & Liu, J. (2015). Glaucoma detection based on deep convolutional neural network. *2015 37th Annual International Conference of the IEEE Engineering in Medicine and Biology Society (EMBC)*, 715–718.

Christopher, M., Belghith, A., Bowd, C., Proudfoot, J. A., Goldbaum, M. H., Weinreb, R. N., Girkin, C. A., Liebmann, J. M., & Zangwill, L. M. (2018). Performance of deep learning architectures and transfer learning for detecting glaucomatous optic neuropathy in fundus photographs. *Scientific Reports*, *8*(1), 1–13.

dos Santos Ferreira, M. V., de Carvalho Filho, A. O., de Sousa, A. D., Silva, A. C., & Gattass, M. (2018). Convolutional neural network and texture descriptor-based automatic detection and diagnosis of glaucoma. *Expert Systems with Applications*, *110*, 250–263.

Fu, H., Cheng, J., Xu, Y., Zhang, C., Wong, D. W. K., Liu, J., & Cao, X. (2018). Disc-aware ensemble network for glaucoma screening from fundus image. *IEEE Transactions on Medical Imaging*, *37*(11), 2493–2501.

Gómez-Valverde, J. J., Antón, A., Fatti, G., Liefers, B., Herranz, A., Santos, A., Sánchez, C. I., & Ledesma-Carbayo, M. J. (2019). Automatic glaucoma classification using color fundus images based on convolutional neural networks and transfer learning. *Biomedical Optics Express*, *10*(2), 892–913.

Gulshan, V., Peng, L., Coram, M., Stumpe, M. C., Wu, D., Narayanaswamy, A., Venugopalan, S., Widner, K., Madams, T., Cuadros, J., & others. (2016). Development and validation of a deep learning algorithm for detection of diabetic retinopathy in retinal fundus photographs. *Jama*, *316*(22), 2402–2410.

Kolář, R., & Jan, J. (2008). Detection of glaucomatous eye via color fundus images using fractal dimensions. *Radioengineering*, *17*(3), 109–114.

Lee, C. S., Baughman, D. M., & Lee, A. Y. (2017). Deep learning is effective for classifying normal versus age-related macular degeneration OCT images. *Ophthalmology Retina*, *1*(4), 322–327.

Lee, J., Kim, Y. K., Park, K. H., & Jeoung, J. W. (2020). Diagnosing Glaucoma With Spectral-Domain Optical Coherence Tomography Using Deep Learning Classifier. *Journal of Glaucoma*, *29*(4), 287–294.

Li, L., Xu, M., Wang, X., Jiang, L., & Liu, H. (2019). Attention based glaucoma detection: A large-scale database and CNN Model. *Proceedings of the IEEE Conference on Computer Vision and Pattern Recognition*, 10571–10580.

Li, Z., He, Y., Keel, S., Meng, W., Chang, R. T., & He, M. (2018). Efficacy of a deep learning system for detecting glaucomatous optic neuropathy based on color fundus photographs. *Ophthalmology*, *125*(8), 1199–1206.

Maheshwari, S., Pachori, R. B., Kanhangad, V., Bhandary, S. V, & Acharya, U. R. (2017). Iterative variational mode decomposition based automated detection of glaucoma using fundus images. *Computers in Biology and Medicine*, *88*, 142–149.

Martins, J., Cardoso, J. S., & Soares, F. (2020). Offline computer-aided diagnosis for Glaucoma detection using fundus images targeted at mobile devices. *Computer Methods and Programs in Biomedicine*, *192*, 105341.

Mookiah, M. R. K., Acharya, U. R., Lim, C. M., Petznick, A., & Suri, J. S. (2012). Data mining technique for automated diagnosis of glaucoma using higher order spectra and wavelet energy features. *Knowledge-Based Systems*, *33*, 73–82.

Raghavendra, U., Fujita, H., Bhandary, S. V, Gudigar, A., Tan, J. H., & Acharya, U. R. (2018). Deep convolution neural network for accurate diagnosis of glaucoma using digital fundus images. *Information Sciences*, *441*, 41–49.

Redmon, J., & Farhadi, A. (2017). YOLO9000: better, faster, stronger. *Proceedings of the IEEE Conference on Computer Vision and Pattern Recognition*, 7263–7271.

Shankaranarayana, S. M., Ram, K., Mitra, K., & Sivaprakasam, M. (2017). Joint optic disc and cup segmentation using fully convolutional and adversarial networks. In *Fetal, Infant and Ophthalmic Medical Image Analysis* (pp. 168–176). Springer.

Tham, Y.-C., Li, X., Wong, T. Y., Quigley, H. A., Aung, T., & Cheng, C.-Y. (2014). Global prevalence of glaucoma and projections of glaucoma burden through 2040: a systematic review and meta-analysis. *Ophthalmology*, *121*(11), 2081–2090.

Zilly, J., Buhmann, J. M., & Mahapatra, D. (2017). Glaucoma detection using entropy sampling and ensemble learning for automatic optic cup and disc segmentation. *Computerized Medical Imaging and Graphics*, *55*, 28–41.
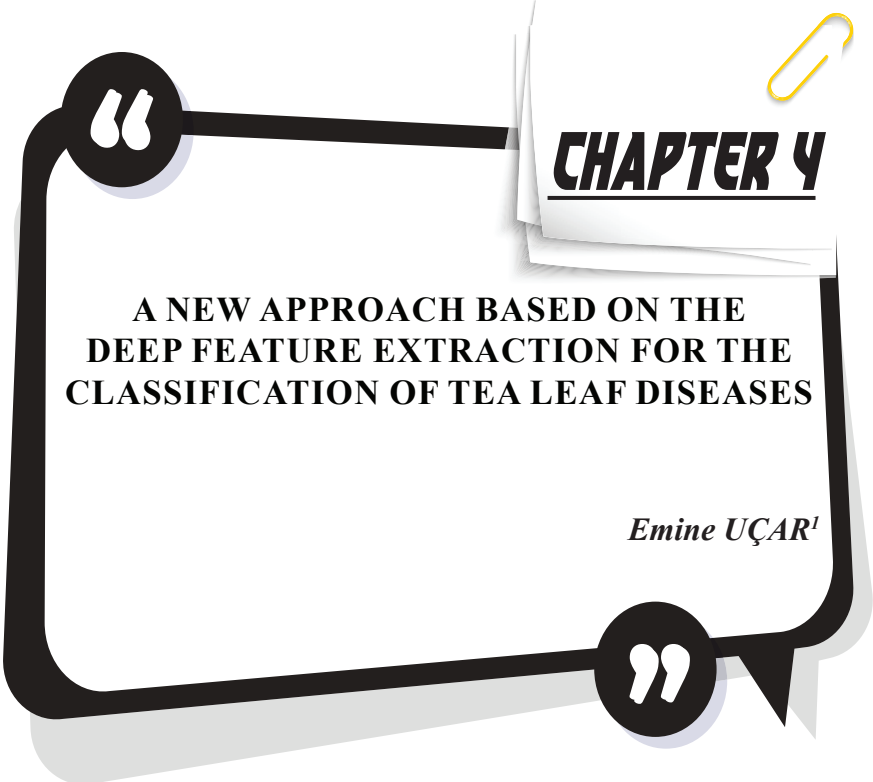
CHAPTER 4

A NEW APPROACH BASED ON THE DEEP FEATURE EXTRACTION FOR THE CLASSIFICATION OF TEA LEAF DISEASES

Emine UÇAR[1]

1 Asst. Prof. Dr. Emine UÇAR, İskenderun Technical University, Faculty of Business and Management Sciences, Department of Management Information Systems, Hatay, TURKEY, emine.ucar@iste.edu.tr, https://orcid.org/0000-0002-6838-3015

1. INTRODUCTION

Tea is the most consumed beverage in the world after water. The homeland of the tea plant, which was first grown in China and India, is the Azsam region of India (Üstün and Demirci 2013). According to a recent report of the United Nations Food and Agriculture Organization (FAO), when looking at the average of 2011-2016, China and India make up about 60% of the world's tea production (FAOSTAT 2018).

Turkey is a country that produces and consumes substantial amounts of tea. Cultivating tea in Turkey started in Bursa in the 1900s but was unsuccessful due to the lack of proper ecological structure of the tea production. Then, with the successful trials conducted in 1940 in Rize, Turkey started the production of tea (Alikılıç 2016). Tea production in Turkey has increased over the years and between 2011 and 2016 has reached an annual production of 228,000 average tons of dry tea. Turkey ranks 5th in the world with 4.23% of tea production (Szegedy 2017).

The aim of tea farmers is to produce high_quality tea, but many tea leaf diseases cause tea plants to grow poorly and lower tea yield. Since these diseased leaves affect tea quality, they cause economic damage to tea farmers. For this reason, it is of great importance to correctly identify the types of tea leaf diseases and take appropriate preventive measures over time, reduce tea yield loss, and improve the quality of tea.

The mathematical model of human brain cells that form the basis of artificial neural networks; has been used in many areas such as computer vision, signal processing, sound processing, classification, and diagnosis. (Krizhevsky et al. 2012; LeCun et al. 1998). Computer vision technology has great success in classification and identification processes. It provides faster and easier access to the results in environments where analysis and diagnostics are high in time and cost. On the other hand, the high accuracy rate makes the computer vision system reliable (Szegedy 2017). In recent years the rapid improvement of smart agricultural practices has caused widespread use of computer aided image processing technologies for the solution of problems in agricultural sciences. For example, researchers have utilized image processing techniques to classify plant species, predict plant nutrient content and determine plant diseases.

Sulistyo et al. put forward an image processing approach for predicting the nutrient content of wheat leaves by analyzing the color properties of the leaf images they obtained under various light conditions. The authors stated that the proposed approach gives better results in terms of color normalization, image segmentation and nutritional estimation compared to other methods available in terms of quality and processing speed (Sulistyo et al. 2017). Dyrmann et al. proposed an approach to prevent yield loss

caused by uncontrolled weeds in the agricultural field. Their study performed a model that can distinguish plant species in color images by using the convolutional neural network. The authors stated that the method they used was able to classify weeds with an accuracy rate of 86.2% (Dyrmann et al. 2016). Al Bashish et al. developed an image processing-based model to detect and classify the plant leaf diseases automatically. Their results showed that the proposed approach can significantly perform automatic leaf disease detection (Al Bashish et al. 2011). Rumpf et al. carried out a study for early detection of sugar beet plant diseases using the support vector machine method. They stated that the proposed method could separate healthy sugar beet leaves from diseased leaves with a classification accuracy of approximately 97% (Rumpf et al. 2010). Chaudhary et al. developed a random forest algorithm by combining a feature assessment method and filter method to classify peanut plant diseases. Their results confirmed that the develeeped random forest classifier approach performed better than the random forest algorithm (Chaudhary et al. 2016). Tetila et al. compared the performances of some classifiers such as decision trees, k nearest neighbors, Adaboost and random forest algorithms to detect diseases in soybean leaves (Tetila et al. 2017). In another study, Kiani and Mamedov proposed a novel image processing method based on the fuzzy logic classifier to distinguish healthy and diseased strawberry leaves. They stated that the fuzzy logic-based classifier method accurately distinguished diseased and healthy leaves (Kiani and Mamedov 2017). Karmokar et al. detected the tea leaf diseases by using the artificial neural networks method by extracting features from the images. They reported that the developed method was successful with a high accuracy value in disease detection (Karmokar et al. 2015). Hossain et al. utilized support vector machines to detect brown blight disease and the algal leaf disease which is the most common tea leaf disease in Bangladesh. They reported that the proposed method increased efficiency in detecting, identifying and classifying diseases (Hossain et al. 2018). Chen et al. used convolutional neural networks, support vector machines, and multi-layer sensor methods to identify and classify diseases in tea leaves. As a result of the study, they reported that the convolutional neural networks have the best classification accuracy in identifying diseases in tea plants (Chen et al. 2019). Hu et al. produced new training samples using deep generative adversarial networks and used the VGG16 deep learning model for detecting diseases in tea leaves. They reported that the proposed method can accurately identify the diseased tea leaves and has reached approximately 90% identification accuracy (Hu et al. 2019a). In addition to Hu et al. utilized a deep learning architecture for tea leaf diseases. In this model they added a multiscale feature extraction module to the CIFAR10 model. They reported that the proposed method was successful with an accuracy rate of 92.25% (Hu et al. 2019b).

It is seen that traditional machine learning methods are mostly used in the previous studies mentioned above. However, the extraction of features required for classification in traditional machine learning methods contains complicated processes and must be performed manually. In addition, since feature extraction directly affects classification performance, it can negatively affect classification performance in cases where it is not done carefully. Therefore, this study proposes a deep learning model that can automatically classify tea red scab, tea red leaf spot and tea leaf blight diseases from tea leaf images. In the proposed approach, pre-trained CNN models such as VGG16, ResNet152, DenseNet201 and EfficientNetB0 were used for feature extraction. During the feature extraction process, 4000 features were obtained by combining these features extracted from the last layer of these models. Afterward, two new feature sets were created using Analysis of Variance (ANOVA) f value and Recursive Feature Elimination (RFE) feature selection methods. Finally, the classification process has been made via the SVM method by extracting the common features of these two feature sets.

The rest of the article was organized as follows. In the second section, previous studies were presented. In the third section, detailed information about the used dataset and proposed method was given. In the fourth section, experimental studies were presented. In the fifth section, the findings obtained from the proposed method and a comparison of the classification performance of studies conducted to detect tea leaf disease were included. The sixth section concluded the study.

2. MATERIALS AND METHODS

2.1. Proposed Model

The main objective of this study is to create an efficient model that can successfully detect tea leaf diseases. For this purpose, firstly, the feature extraction process was performed by using four pre-trained deep learning models. Later, the obtained 4000 features by combining 1000 features extracted from these models were ordered via ANOVA f value and RFE feature selection methods. Then, intersecting features were extracted from among the best 500, 1000, 1500, 2000, 2500 and 3000 features. Finally, the classification was made with these intersecting features using the support vector machines method. The block diagram of the proposed method is presented in Figure 1.
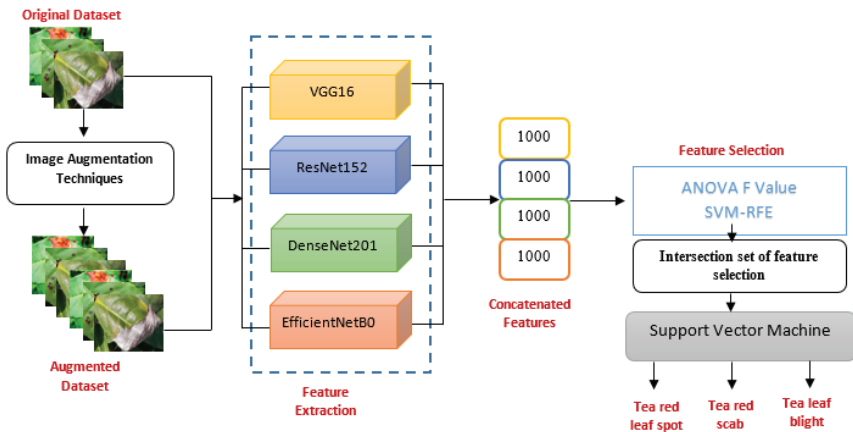
Figure1. Block diagram of the proposed model

2.2. Dataset

The dataset was taken through the public Mendeley database (Mendeley 2019). The dataset created by Hu et al. (2019a) contains 120 tea leaf disease images. The images in the dataset were divided into 20 training images and 20 test images for each leaf disease. The 3 types of diseases called tea red scab, tea red leaf spot and tea leaf blight were taken in Tianjingshan National Forest Park of China. Another part of images came from Anhui Provincial Agricultural Committee's pest and disease agricultural graphic database. Sample images of tea leaf diseases were given in Figure 2.
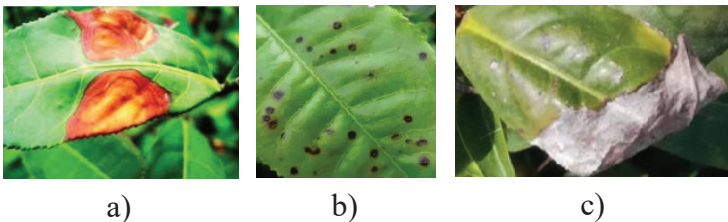

a)   b)   c)

Figure 2. Sample tea leaf disease images: a) tea red leaf spot b) tea red scab c) tea leaf blight

2.3. Pre-trained models for feature extraction

In the study, VGG16, ResNet152, DenseNet201 and EfficientNetB0 CNN architectures were used for feature extraction. These CNN models were chosen because of being modern transfer learning approaches that produce highly efficient solutions and due to their higher accuracy value in the ImageNet competition.

The VGG16 (Visual Geometry Group) model proposed by Simonyan and Zisserman was the winner of the ImageNet Large Scale Visual

Recognition Competition (ILSVRC) in 2014 (Simonyan and Zisserman 2014). This architecture, which has approximately 138 million parameters, takes an image size of 224×224 pixels in the input layer. VGG16 architecture includes thirteen 3x3 convolution layers and three fully connected layers. All convolutional layers are divided into five blocks, each one having more than one convolution layer. The ReLU activation function is used in each divided block and convolutional layers are followed by the maximum pool layer. Two of the three fully connected layers have 4096 channels and the last one has 1000 channels as it fulfills the purpose of classifying the ILSVRC dataset of 1000 objects. The last layer is the soft-max layer.

The ResNet architecture proposed by He et al. was trained on the ImageNet dataset, and achieved a 3.57% error rate in the ILSVRC competition classification task held in 2015 (He et al. 2016). Increasing the depth in convolutional neural networks, in other words increasing the number of layers, increases the training accuracy performance of the model. However, as the depth increases, the problem of distortion and gradient vanishing occurs. In order to avoid these problems, the ResNet architecture adds residual blocks. The aim here is to ensure that the values trained in the previous layers are transmitted more strongly to the following layer. ResNet architecture includes ResNet18, ResNet34, ResNet50, ResNet101 and ResNet152 variants.

The DenseNet architecture proposed by Huang et al. has a different connection structure than other CNNs (Huang et al. 2017). Unlike the ResNet architecture, the inputs are combined using a composite function, resulting in a simpler and more efficient solution. In this way, deep layers in the networks can access all feature maps produced by previous layers and thus reuse the features. Bottleneck and transition layers are used to reduce the number of feature maps and increase computational efficiency. Also, the reuse of features further reduces the disappearing gradient problem.

The EfficientNet architecture proposed by Tan and Le stands out with the advantage of providing better classification accuracy with fewer parameters. The EfficientNet family includes models from B0 to B7, and when applied to the ImageNet dataset, it outperformed all previous models. The EfficientNet architecture evenly scales width, depth, and resolution sizes with a fixed scaling coefficient set. Thanks to this property, model performance is improved effectively (Tan and Le 2019). The basic building block of EfficientNet architecture is Mobile inverted bottleneck convolution (MBConv). In MBConv, blocks consist of a layer that expands first and then compresses channels, so direct connections are used between bottlenecks connecting far fewer channels than expansion layers (Sandler et al. 2018).

During the feature extraction phase, 1000 features were extracted from each model, and then these features were combined and a total of 4000 features were obtained.

2.4. Feature Selection Methods

Feature selection methods are effective methods used in data pre-processing to increase classification performance. These methods aim to find the best data models by selecting better features from among the features extracted from the models. In this study, ANOVA f value and RFE feature selection methods were used for feature selection tasks. In the ANOVA f value method, features with high variance are selected and used in the analysis. To select the features with the best variance, the k value is used to indicate the number of features we want in the dataset (ANOVA Feature Selection 2021). ANOVA f (f_classif) was used with SelectKBest from scikit-learn Python library. In this study, the k value was used as 500, 1000, 1500, 2000, 2500 and 3000 respectively, in the experiments. The ANOVA f function aims to find dependencies in the data and uses dispersion analysis based on investigating the significance of differences in the mean values of the features to calculate the F-criterion. The formula of the function is as in equation 1.

$$F = \frac{\frac{1}{C-1} \sum_{i=1}^{C} N_i (\bar{x}_i - \bar{x})^2}{\frac{1}{N-C} \sum_{i=1}^{C} \sum_{j=1}^{N_i} (x_{i,j} - \bar{x}_i)^2} \tag{1}$$

Here, represents the number of classes, represents the number of records in the dataset, and represents the number of records with class label i. th value of the feature in class i, the mean feature value in class i and the mean feature value in the dataset (Sheluhin and Ivannikova 2020).

The SVM-RFE method proposed by Guyon in 2002 for feature selection is classified as an embedded method (Guyon et al. 2002). This method is a recursive feature elimination application which uses SVM weights as ranking criteria. First, it trains the model on the original number of features, and a severity rating is given to each feature. The features with the least severity are then removed, and then the process is repeated for a certain number of features.

At the intersection of the features, the features which were common to both methods were selected among the effective features obtained by ANOVA f value and RFE feature selection methods and presented to the classifier.

2.5. SVM Classifier

In this study, the SVM method has been preferred because it is a method generally used in classification problems and it gives effective results in the multiple classification process. SVM draws a line to separate points placed on a plane. SVM tries to minimize the risk by defining the support vectors that best separate the classes by drawing a hyperplane passing through these points. The SVM algorithm reduces the generalization error by maximizing the margin among the hyperplane and support vectors. SVM performs better on linearly separable data, but it processes nonlinear data by transforming it into a high-dimensional feature space using the kernel function. These functions are generally called kernel tricks (Meyer and Wien 2015). SVM's advantages include its ability to process high-dimensional data easily, handle unstructured datasets and structured datasets, and directly identify appropriate classes in the dataset. On the other hand, the disadvantages of the SVM method are that the calculation time for data training is too high and the correct kernel function is determined (Cristianini and Shawe-Taylor 2000).

In this study the trainings were carried out with different numbers of input parameters selected from the features extracted by deep learning methods. A linear kernel was used for SVM experiments. During the training phase, the initial weights were chosen randomly, and the tolerance value for stopping the training was determined as 0.001. Since the study classified 3 types of diseases called tea red scab, tea red leaf spot and tea leaf blight, the output number was 3 and multi-class method parameter was chosen as one-vs-rest.

2.6. Performance metrics

Since there is a tea leaf image belonging to three different classes in the dataset used in the study, a multi-class classification was carried out. Accuracy (Acc), Sensitivity (Sen), Specificity (Spe) and Precision (Pre) performance metrics were used to measure the classification success of the SVM method. In the calculation of these metrics, true positive (TP), true negative (TN), false positive (FP) and false negative (FN) values obtained in the confusion matrix were used. Here TP is the number of correctly classified images in each disease class. TN represents the sum of correctly classified images in all other classes except the relevant disease class. FN gives the number of misclassified images in the relevant class, while FP gives the number of misclassified images in all other classes except that class. Equations for these performance metrics were given in equation 2-5. For a class k,

$$Acc(k) = \frac{TP(k)+TN(k)}{TP(k)+FN(k)+TN(k)+FP(k)}$$

$$(2)$$

$$Sen(k) = \frac{TP(k)}{TP(k)+FN(k)}$$

(3)

$$Spe(k) = \frac{TN(k)}{TN(k)+FP(k)}$$

(4)

$$Pre(k) = \frac{TP(k)}{TP(k)+FP(k)}$$

(5)

In the study, ROC curves were also used to test the performance of the proposed model. The ratio of sensitivity to precision forms the ROC curve. Although the ROC curves show distinctiveness, the area under the curve (AUC) is needed to compare different tests. The value of the area under the ROC curve gives the ROC score.

3. EXPERIMENTS

3.1. Experimental setup

All models utilized in this study were compiled with TESLA K80 hardware via Google Colaboratory free GPU service. All codes are carried out with Keras (Chollet et al. 2015) library in Python programming language.

3.2. Data augmentation

Due to the limited number of images in this study, the training images given to the model were altered using rotation, zoom and horizontal flip. During the image rotation method, the rotation angle was set from 0° to 180° in the step of 30°. Some of the images obtained as a result of applied data augmentation methods were as in Figure 3.
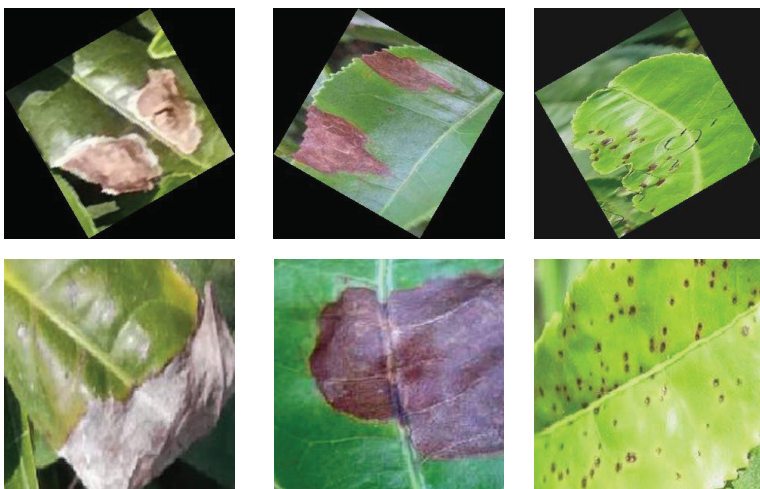

Figure 3. New images obtained after the data augmentation

In total, 11 new images were generated for each original image in the training set. A new augmented dataset was created for training by combining the original dataset and the augmented dataset. The evaluation was performed over the test set, and detailed information about the number of images was given in Table 1.

Table 1. Description of original and augmented dataset

Dataset	Tea red scab	Tea red leaf spot	Tea leaf blight
Original training	20	20	20
Augmented training	240	240	240
Test	20	20	20

4. RESULTS AND DISCUSSIONS

In this study, all experimental studies for the classification of tea leaf diseases were performed on the original dataset consisting of 120 images and an augmented dataset consisting of 780 images.

In experimental studies, firstly, deep features were extracted from the fc8 and fc1000 layers of the pre-trained deep learning models VGG16, ResNet152, DenseNet201 and EfficientNetB0. Afterward, the classification was made using the SVM method for the scenarios containing different number of feature selections by using the ANOVA f value and RFE feature selection methods. The values obtained by the SVM classifier on the original and augmented dataset in different scenarios were presented in Table 2 and Table 3, respectively.

Table 2. The performance results of SVM classifier on original dataset

Classifier	Feature Selection Method	Number of Features	OverAll Accuracy	Average Sensitivity	Average Specifity	Average Precision
SVM	-	4000	0.9000	0.9000	0.9500	0.8995
	Anova F	500	0.8167	0.8167	0.9083	0.8175
		1000	0.9000	0.9000	0.9500	0.9007
		1500	0.9000	0.9000	0.9500	0.9000
		2000	0.9167	0.9167	0.9583	0.9157
		2500	0.9000	0.9000	0.9500	0.8990
		3000	0.9167	0.9167	0.9583	0.9157
	RFE	500	0.9167	0.9167	0.9583	0.9173
		1000	0.9167	0.9167	0.9583	0.9180
		1500	0.8833	0.8833	0.9417	0.8815
		2000	0.8833	0.8833	0.9417	0.8815
		2500	0.9000	0.9000	0.9500	0.8995
		3000	0.9000	0.9000	0.9500	0.8995
	Anova F 500 &RFE 500 Intersection	125	0.8000	0.8000	0.9000	0.8051
	Anova F 1000 &RFE 1000 Intersection	431	0.8833	0.8833	0.9417	0.8911
	Anova F 1500 &RFE 1500 Intersection	856	0.9167	0.9167	0.9583	0.9182
	Anova F 2000 &RFE 2000 Intersection	1312	**0.9333**	**0.9333**	**0.9667**	**0.9332**
	Anova F 2500 &RFE 2500 Intersection	1795	0.9000	0.9000	0.9500	0.8990
	Anova F 3000 &RFE 3000 Intersection	2328	0.9167	0.9167	0.9583	0.9157

Table 3. The performance results of SVM classifier on augmented dataset

Classifier	Feature Selection Method	Number of Features	OverAll Accuracy	Average Sensitivity	Average Specifity	Average Precision
SVM	-	4000	0.9000	0.9000	0.9500	0.9147
	Anova F	500	0.9167	0.9167	0.9583	0.9262
		1000	0.9167	0.9167	0.9583	0.9190
		1500	0.9500	0.9500	0.9750	0.9499
		2000	0.9833	0.9833	0.9917	0.9841
		2500	0.9333	0.9333	0.9667	0.9387
		3000	0.9333	0.9333	0.9667	0.9387
	RFE	500	0.9167	0.9167	0.9583	0.9262
		1000	0.9167	0.9167	0.9583	0.9254
		1500	0.9167	0.9167	0.9583	0.9254
		2000	0.9000	0.9000	0.9500	0.9147
		2500	0.9000	0.9000	0.9500	0.9147
		3000	0.9000	0.9000	0.9500	0.9147
	Anova F 500 &RFE 500 Intersection	147	0.9167	0.9167	0.9583	0.9262
	Anova F 1000 &RFE 1000 Intersection	428	0.9500	0.9500	0.9750	0.9524
	Anova F 1500 &RFE 1500 Intersection	792	0.9500	0.9500	0.9750	0.9524
	Anova F 2000 &RFE 2000 Intersection	1233	**1**	**1**	**1**	**1**
	Anova F 2500 &RFE 2500 Intersection	1729	0.9333	0.9333	0.9667	0.9387
	Anova F 3000 &RFE 3000 Intersection	2254	0.9333	0.9333	0.9667	0.9387

In the first scenario created in experimental studies, the success of the classification was measured by using all the features without making any selection. In the classification using all features, a 90% accuracy rate was achieved in both datasets. In the second scenario, the classification performance of the model was measured using the best 500, 1000, 1500, 2000, 2500 and 3000 features selected from the combined feature dataset with each feature selection method. In this scenario, the highest accuracy rate achieved on the original dataset with both feature selection methods was 91.67%. The highest accuracy was obtained on the augmented dataset

in the test performed with the best 2000 features selected using the ANOVA f value method with 98.33%. In the third scenario, the classification was made with different numbers of features obtained due to the intersection of the best features selected using both feature selection methods. The classification accuracy rate obtained by using 1312 intersecting features among the best 2000 features selected using both feature selection methods on the original dataset was the highest with 93.33%. Likewise, the classification accuracy obtained by using 1233 intersecting features among the best 2000 features selected using both feature selection methods on the augmented dataset was the highest with 100%. As shown from Table 2 and Table 3, using feature selection methods had positive effects on classifier performance. In addition, as expected, the accuracy of the classification has increased considerably after increasing the data. Figure 4 shows the intersecting 1233 feature images from the top 2000 features selected using ANOVA f value and RFE feature selection methods, in which the best classification accuracies were obtained in the original dataset and the augmented dataset.
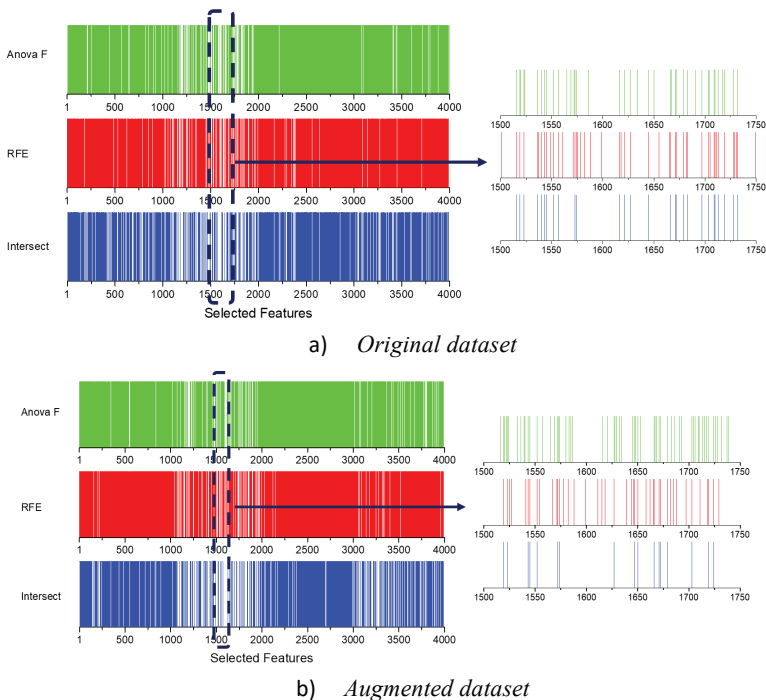

a)   *Original dataset*

b)   *Augmented dataset*

Figure 4. Graphical representation of features selected from ANOVA F value and REF methods and intersected features

Before and after data augmentation, the confusion matrices of the models were given in Figure 5. As shown in from Figure 5, the proposed method achieved 100% accuracy for all diseases in the augmented dataset.

In the original dataset, it achieved 100% accuracy in test images of tea red scab disease, and 90% accuracy in tea red leaf spot and tea leaf blight diseases.
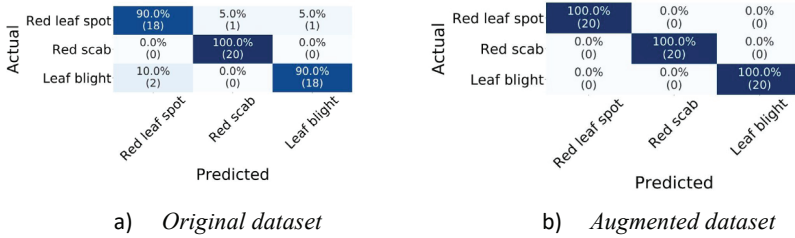

a) *Original dataset* b) *Augmented dataset*
Figure 5. Confusion matrices for original and augmented dataset

The AUC-ROC curves of the models with the best results in the approach proposed in the study were presented in Figure 6. The best AUC value was 0.95 in the model that uses 1312 features intersect among the best 2000 features selected using both feature selection methods on the original dataset. The best AUC value was 1.00 in the model that uses 1233 features intersect among the best 2000 features selected using both feature selection methods on the augmented dataset.
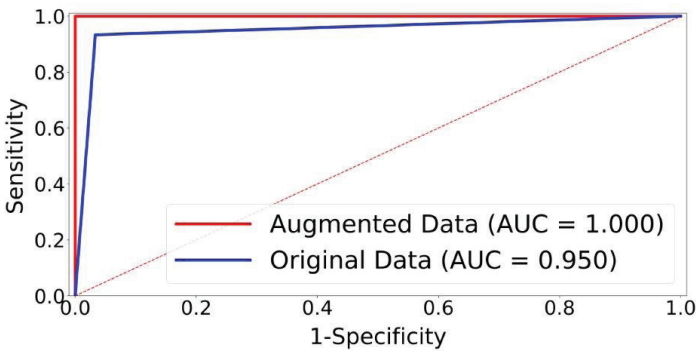

Figure 6. ROC curves of the models.

In Table 4, the models developed for the diagnosis of tea leaf disease and their performances on the datasets used in the literature were presented. As seen in the table, the researchers used traditional machine learning methods and deep learning techniques to diagnose tea leaf diseases. When studies using traditional machine learning methods were examined, Karmokar et al. used the artificial neural networks (ANN) method for the diagnosis of 5 different tea leaf diseases and obtained an accuracy value of 0.9 (Karmokar et al. 2015). On the other hand, Hossain et al. made a classification using the SVM method on a dataset containing three different tea leaf diseases and obtained an accuracy of 0.9333 (Hossain et al. 2018).

When the studies using deep learning methods were examined, it was seen that the studies were generally carried out in 3 classes. Only Chen et al. was classified on a dataset containing many images of 7 different tea leaf diseases. In that study, they proposed a CNN-based model called LeafNet and obtained an accuracy of 0.9016 (Chen et al. 2019). Hu et al. used C-DCGAN and VGG16 deep learning methods together to diagnose three different tea leaf diseases and obtained an accuracy of 0.90 (Hu et al. 2019a). In another CNN-based study, they obtained an accuracy rate of 0.9225 on the augmented dataset (Hu et al. 2019b). In addition, the dataset shared by Hu et al. (2019a) was used to test the performance of the deep learning-based model proposed in this study. The accuracy of the developed model in this study was tested on both the original dataset and the augmented dataset. While the proposed approach achieved a 0.9333 accuracy rate on the original dataset, it achieved a very high accuracy rate with 1.0000 in the augmented dataset.

Table 4. Comparison of the classification performance of studies conducted to detect tea leaf disease

Author	Method	Dataset	Accuracy
(Karmokar et al.2015)	ANN	5 types of tea leaf disease (50 images)	0.9100
(Hossain et al. 2018)	Feature extraction and Feature Selection + SVM	3 types of tea leaf disease (200 images)	0.9333
(Chen et al. 2019)	CNN (LeafNet)	7 types of tea leaf disease (7905 images)	0.9016
(Hu et al. 2019a)	C-DCGAN+VGG16	3 types of tea leaf disease (120 images)	0.9000
(Hu et al. 2019b)	Improved CNN	3 types of tea leaf disease Original Dataset: 108 images Augmented Dataset: 238 images	Augmented Dataset: 0.9225
Proposed Model	**Deep feature extraction, Feature Selection + SVM**	3 types of tea leaf disease **Original Dataset**:120 images **Augmented Dataset**:780 images	**Original Dataset: 0.9333** **Augmented Dataset: 1.0000**

5. CONCLUSION

In this study, a deep learning-based approach was proposed to identify and classify diseases in tea leaves. The best features were selected among the features extracted using deep learning models and classified with SVM in the proposed approach. The proposed method achieved a classification

accuracy of 0.9333 in the original dataset and 1.0000 in the augmented dataset, showing that the accuracy rate of the data augmentation method increased significantly. Consequently, these results obtained in experimental studies show that the proposed model can be used to classify of tea leaf diseases effectively.

The limited number of images of tea leaf diseases in the dataset is one of the limitations of this study. In future studies, it is planned to create a model with higher generalization capacity by using tea leaf disease varieties and images from different sources.

REFERENCES

Alikılıç, D. (2016). Çay'ın Karadeniz Bölgesi için önemi ve tarihi seyri. *Karadeniz* İncelemeleri *Dergisi*, *11*(21)*,* 269–280.

Al Bashish, D., Braik, M., & Bani-Ahmad, S. (2011). Detection and classification of leaf diseases using K-means-based segmentation and. *Information technology journal*, *10*(2), 267-275.

ANOVA Feature Selection (2021) Feature selection with ANOVA method. https://scikit-learn.org/stable/modules/generated/sklearn.feature_selection.SelectKBest.html Accessed 3 March 2021

Chaudhary, A., Kolhe, S., & Kamal, R. (2016). An improved random forest classifier for multi-class classification. *Information Processing in Agriculture*, *3*(4), 215-222.

Chen, J., Liu, Q., & Gao, L. (2019). Visual tea leaf disease recognition using a convolutional neural network model. *Symmetry*, *11*(3), 343.

Chollet F (2015) Keras documentation. keras. io, 33

Cristianini, N., & Shawe-Taylor, J. (2000). *An introduction to support vector machines and other kernel-based learning methods*. Cambridge university press.

Dyrmann, M., Karstoft, H., & Midtiby, H. S. (2016). Plant species classification using deep convolutional neural network. *Biosystems engineering*, *151*, 72-80.

FAOSTAT (2018) Tea Production. http://www.fao.org/3/BU642en/bu642en.pdf Accessed 5 February 2021

Guyon, I., Weston, J., Barnhill, S., & Vapnik, V. (2002). Gene selection for cancer classification using support vector machines. *Machine learning*, *46*(1), 389-422.

He, K., Zhang, X., Ren, S., Sun, J. (2016). Deep residual learning for image recognition. *arXiv Prepr. arXiv1512.03385*

Hossain, S., Mou, R. M., Hasan, M. M., Chakraborty, S., & Razzak, M. A. (2018, March). Recognition and detection of tea leaf's diseases using support vector machine. In *2018 IEEE 14th International Colloquium on Signal Processing & Its Applications (CSPA)* (pp. 150-154). IEEE.

Hu, G., Wu, H., Zhang, Y., & Wan, M. (2019a). A low shot learning method for tea leaf's disease identification. *Computers and Electronics in Agriculture*, *163*, 104852.

Hu, G., Yang, X., Zhang, Y., & Wan, M. (2019b). Identification of tea leaf diseases by using an improved deep convolutional neural network. *Sustainable Computing: Informatics and Systems*, *24*, 100353.

Huang, G., Liu, Z., Van Der Maaten, L., & Weinberger, K. Q. (2017). Densely connected convolutional networks. In *Proceedings of the IEEE conference on computer vision and pattern recognition* (pp. 4700-4708).

Karmokar, B. C., Ullah, M. S., Siddiquee, M. K., & Alam, K. M. R. (2015). Tea leaf diseases recognition using neural network ensemble. *International Journal of Computer Applications*, *114*(17).

Kiani, E., & Mamedov, T. (2017). Identification of plant disease infection using soft-computing: Application to modern botany. *Procedia computer science*, *120*, 893-900.

Krizhevsky, A., Sutskever, I., & Hinton, G. E. (2012). Imagenet classification with deep convolutional neural networks. *Advances in neural information processing systems*, *25*, 1097-1105.

LeCun, Y., Bottou, L., Bengio, Y., & Haffner, P. (1998). Gradient-based learning applied to document recognition. *Proceedings of the IEEE*, *86*(11), 2278-2324.

Mendeley (2019) Tea Leaf Disease Dataset. https://data.mendeley.com/datasets/dbjyfkn6jr/1 Accessed 29 July 2020

Meyer, D., & Wien, F. T. (2015). Support vector machines. *The Interface to libsvm in package e1071*, *28*.

Rumpf, T., Mahlein, A. K., Steiner, U., Oerke, E. C., Dehne, H. W., & Plümer, L. (2010). Early detection and classification of plant diseases with support vector machines based on hyperspectral reflectance. *Computers and electronics in agriculture*, *74*(1), 91-99.

Sandler, M., Howard, A., Zhu, M., Zhmoginov, A., & Chen, L. C. (2018). Mobilenetv2: Inverted residuals and linear bottlenecks. In *Proceedings of the IEEE conference on computer vision and pattern recognition* (pp. 4510-4520).

Sheluhin, O. I., & Ivannikova, V. P. (2020). Comparative analysis of informative features quantity and composition selection methods for the computer attacks classification using the UNSW-NB15 dataset. *T-Comm-Телекоммуникации и Транспорт*, *14*(10).

Simonyan, K., & Zisserman, A. (2014). Very deep convolutional networks for large-scale image recognition. *arXiv preprint arXiv:1409.1556*.

Sulistyo, S. B., Wu, D., Woo, W. L., Dlay, S. S., & Gao, B. (2017). Computational deep intelligence vision sensing for nutrient content estimation in agricultural automation. *IEEE Transactions on Automation Science and Engineering*, *15*(3), 1243-1257.

Szegedy, C., Ioffe, S., Vanhoucke, V., & Alemi, A. A. (2017, February). Inception-v4, inception-resnet and the impact of residual connections on learning. In *Thirty-first AAAI conference on artificial intelligence*.

Tan, M., & Le, Q. (2019, May). Efficientnet: Rethinking model scaling for convolutional neural networks. In *International Conference on Machine Learning* (pp. 6105-6114). PMLR.

Tetila, E. C., Machado, B. B., Belete, N. A., Guimarães, D. A., & Pistori, H. (2017). Identification of soybean foliar diseases using unmanned aerial vehicle images. *IEEE Geoscience and Remote Sensing Letters*, *14*(12), 2190-2194.

Üstün, Ç., & Demirci, N. (2013). Çay bitkisinin (camellia sınensıs l.) tarihsel gelişimi ve tıbbi açıdan değerlendirilmesi. *Mersin Üniversitesi Tıp Fakültesi Lokman Hekim Tıp Tarihi ve Folklorik Tıp Dergisi*, *3*(3), 5-12.
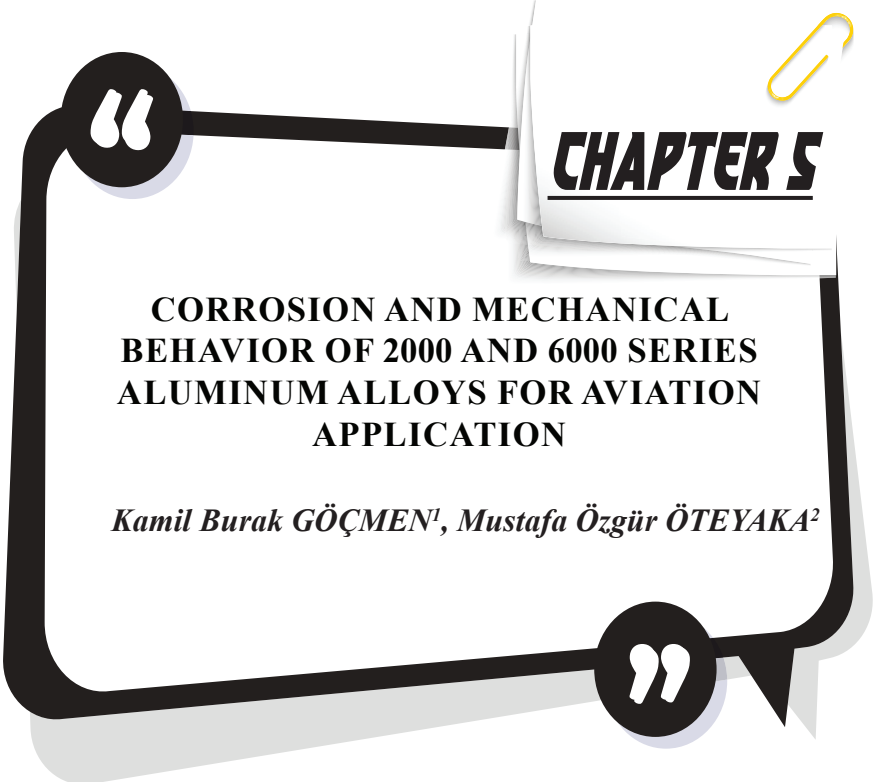
CORROSION AND MECHANICAL BEHAVIOR OF 2000 AND 6000 SERIES ALUMINUM ALLOYS FOR AVIATION APPLICATION

Kamil Burak GÖÇMEN[1], Mustafa Özgür ÖTEYAKA[2]

1   M.Sc.Kamil Burak GÖÇMEN, Eskişehir Osmangazi University, Institut of Science, Department of   Aviation and Automation, moteyaka@ogu.edu.tr, ORCID: 0000-0002-1488-6098.

2   Doç.Dr.Mustafa Özgür ÖTEYAKA, Eskişehir Osmangazi University, Eskişehir Vocational School, Department of Electronic and Automation, moteyaka@ogu.edu.tr, ORCID: 0000-0002-1488-6098.

1. INTRODUCTION

Aluminum (2.7 g/cm³) is used in the automotive and aerospace industries because it is 1/3 lighter than steels and because it reaches the strength values of common steels with heat treatments (Committee, 1990; Jovičević-Klug & Podgornik, 2020; Ma et al., 2004; Macário et al., 2019). The tensile strength of pure Al metal is 90 MPa. The addition of the alloying elements and the applied heat treatment to the pure metal, this value goes up to 455 MPa (2000 series). When the corrosion properties are examined, it provides protection by forming a metal oxide film in the air environment (Fahimpour et al., 2012; Mascagni et al., 2014). Although the oxide film is resistant in humid, industrial, and acidic environments, it is not resistant to alkaline environments (Kaseem et al., 2015; Macário et al., 2019; Reboul & Baroux, 2011). Aluminum alloys are easy to cast and produce as sheet metal. Forged alloys with a 4-digit coding system are classified; the most commonly used alloy series in aviation are the 2xxx, 5xxx, 6xxx, and 7xxx series. Aluminum alloys have an important place in the aviation industry. The reason is that they are light and with applied heat treatments, their strength is close to medium carbon steel. The most preferred aluminum alloy series are the 2xxx, 6xxx, and 7xxx series. On the other hand, aluminum parts used in aviation should be replaced after a certain period.

Cryogenic heat treatment is a heat treatment applied to materials in a liquid nitrogen environment at -196 ℃. This change in physical properties is a result of changes in microstructure at the end of the process. While this process gives good results in steel, however, the effect on light metals is under investigation. Overwork on aluminum alloys, it is observed that the microstructure becomes more homogenous and the secondary phases are resolved in the matrix. Specified after cryogenic heat treatment. In addition, it has been determined that there is an increase in strength and hardness for some alloys.

The effect of cryogenic heat treatment on light metals in recent times is being investigated. At the end of this process, it has been observed an increase in the mechanical properties and corrosion resistance. In this context, this study investigates the cryogenic heat treatment effect on the mechanical and corrosion behavior of 2024-T0, 2024-T3, 6061-T0, and 6061-T6 aluminum alloys.

2. Aluminum alloys and aviation application

Aluminum alloys are widely used in different industries such as automotive, aviation (*Figure 1*), etc.(Cole & Sherman, 1995; Committee, 1990; Dursun & Soutis, 2014; Jovičević-Klug & Podgornik, 2020; Salguero et al., 2020; Zheng et al., 2018); because of lightweight (2.74 g/cm³), good

mechanical properties (*Figure 2*) and corrosion resistance compared to other materials. In the automotive industry aluminum alloys were used in powertrain (casting), chassis (casting and wrought), and body (wrought) structure. For example, the Audi A8 has used 348 kg of aluminum alloys which reduced the car weight from 1348 kg to 1121 kg (Cole & Sherman, 1995).
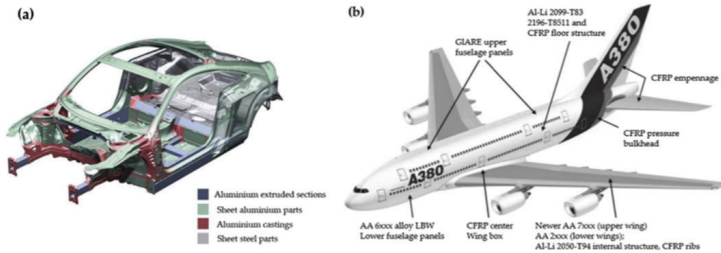

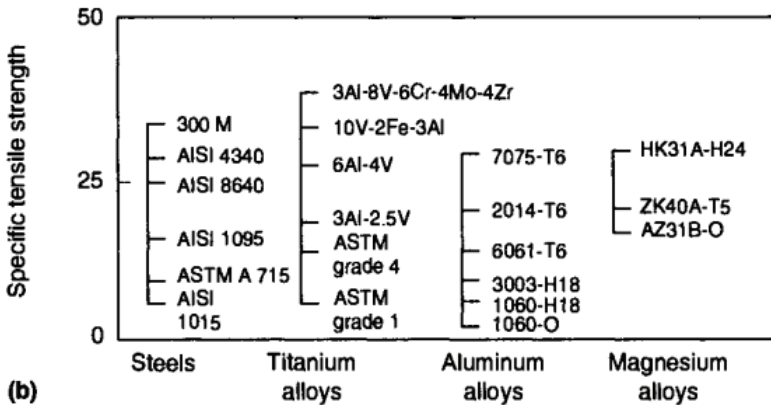*Figure 1. Aluminum use in automotive and aviation a) Audi TT coupé and b) A380 (Zheng et al., 2018).*

Figure 2. Comparisons of specific tensile strength of aluminum alloys versus different alloys (Committee, 1990).

On the other hand, the aviation also followed in parallel the performance of automotive to reduce the weight of the airplane (*Figure 3*). The weight reduction involves fuel reduction, increasing the range and the payload. Moreover, optimization of materials can also reduce the maintenance time and repair cost (Dursun & Soutis, 2014). It is especially used in 2xxx, 6xxx and 7xxx (*Table 1*) series aircraft fuselage and wings (Salguero et al., 2020). Various methods are used to increase the mechanical properties and corrosion resistance of these alloys. These are mainly heat treatment, addition of new alloying elements or their ratios modification and production methods.
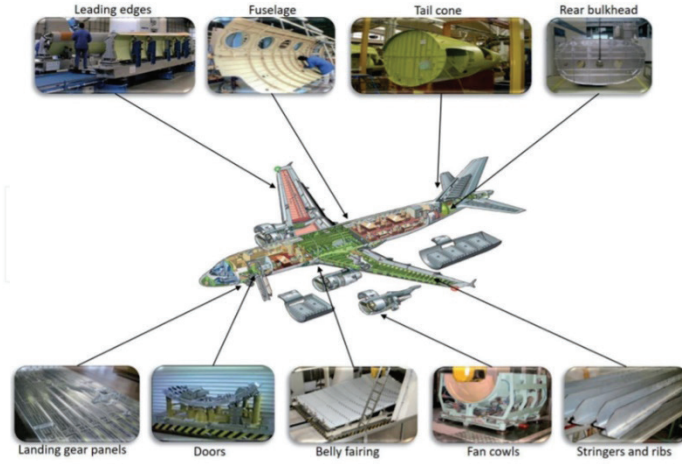
Figure 3. A319 aircraft structural parts (Salguero et al., 2020).

Table 1. Some aluminum alloys used in aeronautical; properties, composition and alloy designation (Salguero et al., 2020).

Identification	Aluminum Association	AA2024	AA7475	AA7050	AA7075
	UNS	A92024	A97475	A97050	A97075
	ISO	AlCu4Mg1	AlZn5.5MgCu(A)	AlZn6CuMgZr	AlZn5.5MgCu
Composition	Si	≤0.5	≤0.1	≤0.12	≤0.4
	Fe	≤0.5	≤0.12	≤0.15	≤0.5
	Cu	3.8–4.9	1.2–1.9	1.9–2.5	1.2–2.0
	Mn	0.3–0.9	≤0.06	≤0.1	≤0.3
	Mg	1.2–1.8	1.9–2.6	2.0–2.7	2.1–2.9
	Cr	≤0.1	0.18–0.25	≤0.04	0.18–0.28
	Zn	≤0.25	5.2–6.2	5.9–6.9	5.1–6.1
	Ti	≤0.15	≤0.05	≤0.06	≤0.2
	Al	Rem.	Rem.	Rem.	Rem.
Properties	Density (kg/m^3)	2.78	2.81	2.83	2.81
	Melting point (°C)	500–638	477–635	490–630	475–635
	Thermal conductivity (W/m°C)	121–151	163	157	130
	Thermal expansion (um/m°C)	23.2	23.2	24.1	23.6
	Young's Modulus (GPa)	73	72	72	72
	Percent elongation (%)	6–20	12	10	11
	Ultimate tensile strength-UTS (MPa)	440–495	531	495–550	525–570
	Heat treatment	T3, T4, T361, T6, T81,T861	T7651	T74	T6, T651, T73

Among them, the 2xxx series is the most preferred. The strength value after applied cold forming and heat treatment is equivalent to medium carbon steel. Airframe and wing It is used in parts of [9]. The 6xxx series, on the other hand, is preferred like the 2xxx series in aircraft fuselage and wing parts due to its easy welding ability and heat treatment (Fahimpour et al., 2012; Kaseem et al., 2015; Reboul & Baroux, 2011).

Different alloy ratios, production methods and heat treatments are applied to aluminum alloys to improve strength and corrosion properties [12]. Recently, researches to improve these properties with cryogenic heat treatment have gained momentum. This process was first applied to cutting steel tools in 1940 and an increase in mechanical properties was observed.

In the literature, cryogenic heat treatment has been applied to aluminum alloys at different times (Padmini, Sampathkumaran, Seetharamu, Jaiprakash, et al., 2019; Park et al., 2015). For example, 2024-T351 alloy was cryogenic heat treated for 2, 6, 8, 12 and 24 hours. At the end of this process, the defects in the microstructure and the precipitated secondary phases affect the distribution. They have observed. In addition, an increase in strength values and 24-hour cryogenic heat treatment. The highest value after 480.6 MPa was obtained (*Figure 4*). In this study, the hardness and corrosion properties have not been investigated (Zhou et al., 2016).
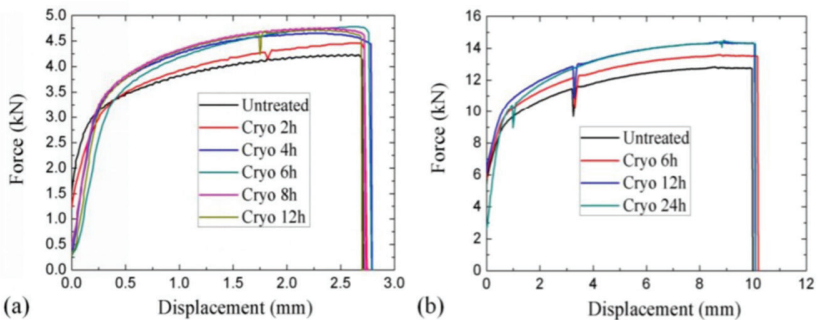

Figure 4. 2024-T351 aluminum alloy tensile curves; a) N1-0-N1-5 b) N2-0-N2-3(Zhou et al., 2016) .

The microstructure of the cryogenic treated sample 2024-T351 were presented at *Figure 5*. It was observed lower defects for the sample cryogenic treated for 6h (*Figure 5c)*. Moreover, the precipitates were more uniform dispersed in the microstructure compared to untreated sample (Zhou et al., 2016).
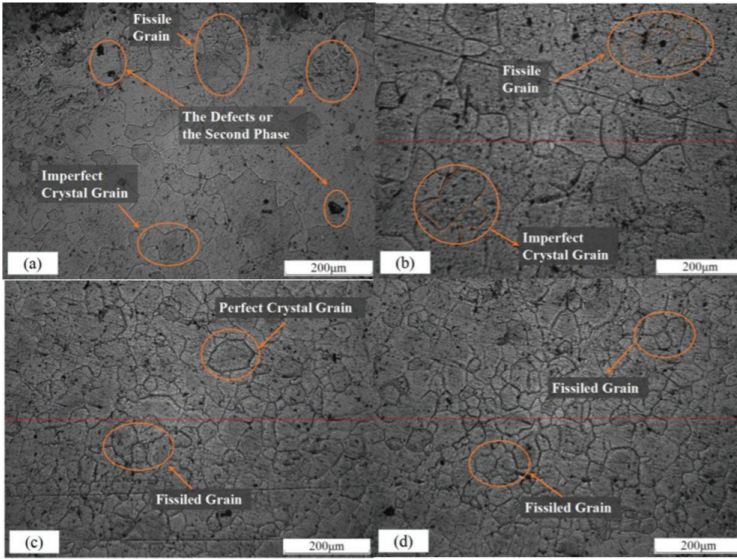
Figure 5. 2024-T351 aluminum alloy; microstructure images a) untreated, b) CT-2h, c) CT-6h and d) CT- 12h (Zhou et al., 2016).

A similar study was performed by Padmini et al. (Padmini, Sampathkumaran, Seetharamu, Jaiprakash, et al., 2019); 2, 9 and 64 hours of cryogenic treatment was applied to 2024, 7075 and 602 aluminum alloys and a 24% improvement was found for the wear amount of the 2024 alloy. Lulay et al. (Lulay et al., 2002) used 7075 alloy and applied cryogenic heat treatment at -196 °C at two different retention times; 2h and 48h. Because of the analysis, the shrinkage compared to the original sample increased the strength of 1.5% and the impact of 11.5% after 48 h of cryogenic heat treatment.

In another study, cryogenic heat treatment was applied to the welded aerospace Al alloys for 48 h. In the analyzes of the parts, the stress corrosion cracking was improved (*Figure 6*). Residual stress in the welded area from 23.9 ksi has fallen to to 12.2 ksi (*Table 2*) . On the other hand, a slight increase in strength and hardness was observed (Chen et al., 2001).
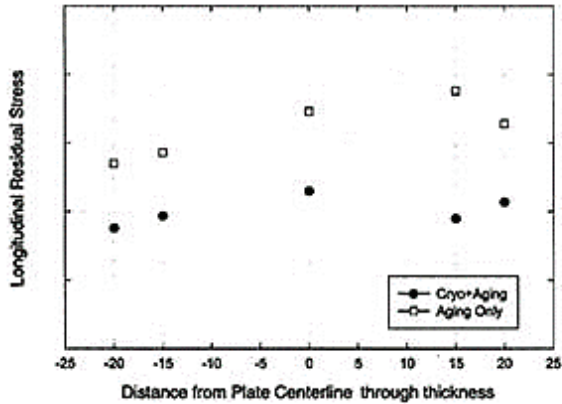
Figure 6.Longitudinal residual stress profiles of aluminum alloy (Chen et al., 2001).

Table 2. Aluminum alloys welds stress corrosion (Chen et al., 2001).

Specimen Condition	Stress Level (%YS)	Failure Ratio	Highest Residual Stress in HAZ	Days to Failure
As-welded	50	1/3	23.9 ksi	65
	75	2/3		3, 6
Cryogenically treated	50	0/3	12.2 ksi	--
	75	2/3		22, 84

On the other hand, the effect of short-term instead of long-term cryogenic treatment on LC4 (Al-Zn-Mg-Cu) aluminum alloy was investigated by Zhang et al. (Zhang et al., 2013). Cryogenic heat treatment was applied at -196 °C for 40 minutes. After this process, mechanical properties and corrosion resistance in 3.5 wt% NaCl solution were measured. It was observed that the precipitates in the microstructure after the cryogenic treatment dissolved in the matrix and the secondary phases were located in the form of chains at the grain boundary. In addition, the samples treated with cryogenic heat treatment and cryogenic heat treatment followed by 24 h aging at 120 °C were subjected to compression test; the cryogenic treatment improved 25.69 % and 59.72 % compared to the original sample. In the same study, the corrosion potential of the original sample which was -834 mV increased up to -805 mV after cryogenic treatment and aging. They found that this improvement resulted in the reduction of secondary phases in the microstructure and, as a result, a decrease in galvanic interaction (*Figure 7and Figure 8*).
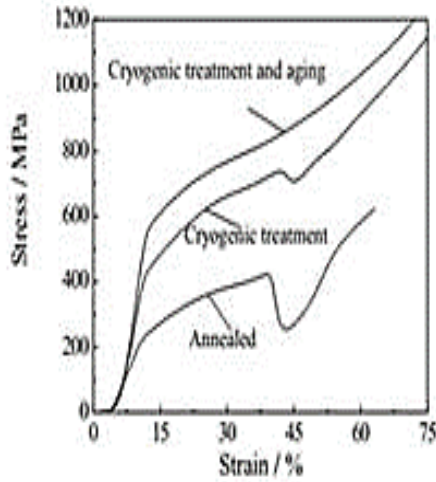
Figure 7. Untreated and treated LC4 (Al-Zn-Mg-Cu) alloy compression test results.
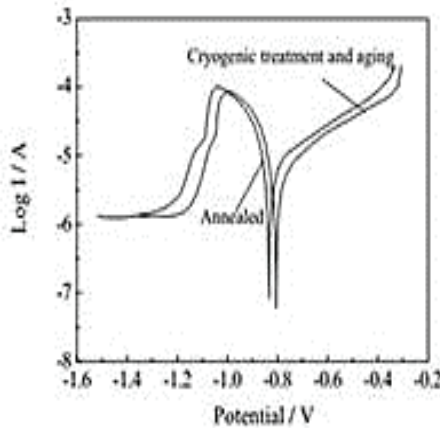

Figure 8. Potentiodynamic test of untreated and treated LC4 (Al-Zn-Mg-Cu).

A decrease in wear rate was observed after 12 hours of cryogenic heat treatment applied to 6101 aluminum alloy. The reason for this is related to that the GP regions (Guinier-Preston) dissolved in the matrix at the end of this heat treatment and therefore the wear performance is improved (Franco Steier et al., 2016).

Cryogenic heat treatment was applied to 6061 metal matrix composite materials. Varun Chandra et al. (Varun Chandra et al., 2018) applied cryogenic heat treatment by adding B4C+Gr to 6061 alloy at different level. At the end of this study, it was stated that there was an increase in strength and hardness in heat treated composites, and B4C+Gr (12

%) aluminum composite. In another study, an increase in mechanical properties was observed after cryogenic heat treatment applied to LC25 aluminum composite with SiC additives (Elango et al., 2014).

3   Corrosion behavior of 2000 and 6000 series of aluminum alloys

The corrosion of 2024 aluminum alloys was due mainly of intermetallic phase formation due to addition of Cu and Mg (Siskou et al., 2018). Different studies were performed on the corrosion of 2024 aluminum alloys. Localised corrosion was observed on the surface of aluminum alloy such as pitting, intergranular and stress corrosion cracking (Pantelakis et al., 2016; Pantelakis et al., 2012; Valerie & Georges, 1999) and galvanic corrosion (*Figure 9*) (Snihirova et al., 2019).
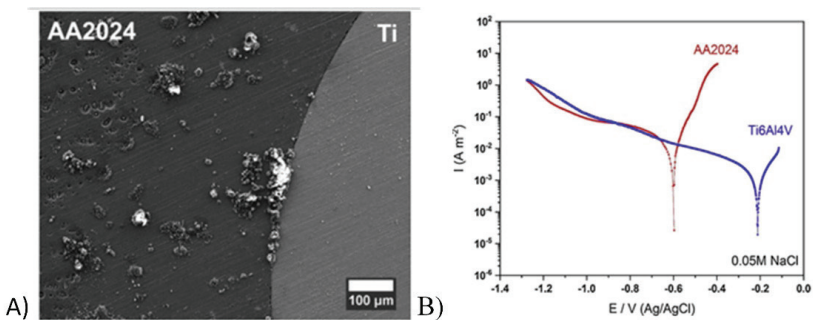

Figure 9. AA2024-Ti galvanic couple A) after 25 h of immersion and B) potentiodyanmic curves in 0.05 M NaCl (Snihirova et al., 2019).

For this reason, some coating was applied to reduce the corrosion rate. For example, Macario et al. applied diamond -like carbon (DLC) films on Al2024 -T3, Al5052 -H32, and Al6061 -T6 aluminum alloys (Macário et al., 2019). Different application was also applied on the surface of aluminum alloy such as anodization of the surface to protect the aluminum alloys against corrosion (Dasquet et al., 2000; Shi et al., 2013; Xiangfeng et al., 2013), plasma coating (Mascagni et al., 2014).

The corrosion performance of the 6063 alloy was studied by Prabhu and Rao (Deepa & Padmalatha, 2017) in sodium hydroxide medium and phosphoric acid medium. The tafel polarisation of the alloy in H_3PO_4 was presented at *Figure 10*. It can be seen that decreasing the amount of H_3PO_4 make more anodic the corrosion potential. Moreover, the corrosion behavior of 6063 alloy was evaluated using EIS (*Figure 11*). The results show that the corrosion was principally charge transfer controlled in H_3PO_4.
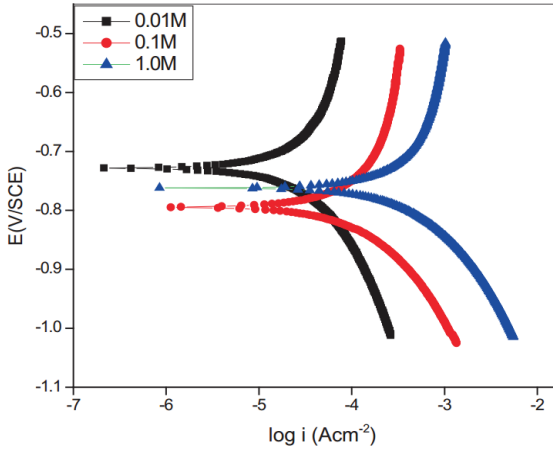
Figure 10. Anodic curve of 6063 alloy in different concentration of H_3PO_4 at 30 °C (Deepa & Padmalatha, 2017) .
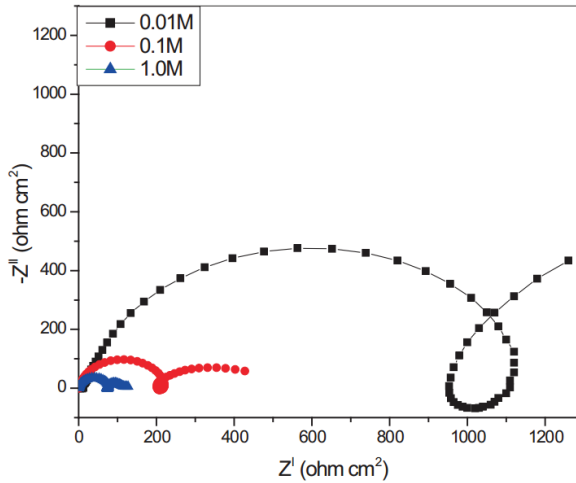

Figure 11. The Nyquist curves of 6063 alloy in different concentration of H_3PO_4 at 30 °C (Deepa & Padmalatha, 2017).

Fahimpour et al. examined the corrosion performance of 6061 alloy joined by friction stir welding (Fahimpour et al., 2012). The corrosion resistance was found lower in the weld region. Moreover, the T6 treatment increased the corrosion potential of 6061 alloy. In another work, Huang et al. (Huang et al., 2008) investigated by EIS the corrosion performance of anodized 6061 alloy. The results showed that the porous film formed using hard anodizing on the surface of 6061 alloy exhibited better corrosion resistance.

4. Mechanical performance of 2000 and 6000 series of aluminum alloys

The mechanical properties such as tensile strength, hardness, wear performance, etc. should be determined before to use in the industry. Bekheet et al. examined the wear and hardness of the composite 2024-SiC material (Bekheet et al., 2002). The hardness behaviour of 2024-SiC was presented at the *Figure 12*. It can be seen that after 150 h of ageing, the base material reached to 112 HV. However, the composite reached 120 Hv which was 8 Hv higher than untreated sample. The benefic on the hardness of cryogenic heat treated 2024 was also confirmed by the study of Padmini et al.(Padmini, Sampathkumaran, Seetharamu, Naveen, et al., 2019). The hardness of 2024 reached to from 135 to 140 Hv.
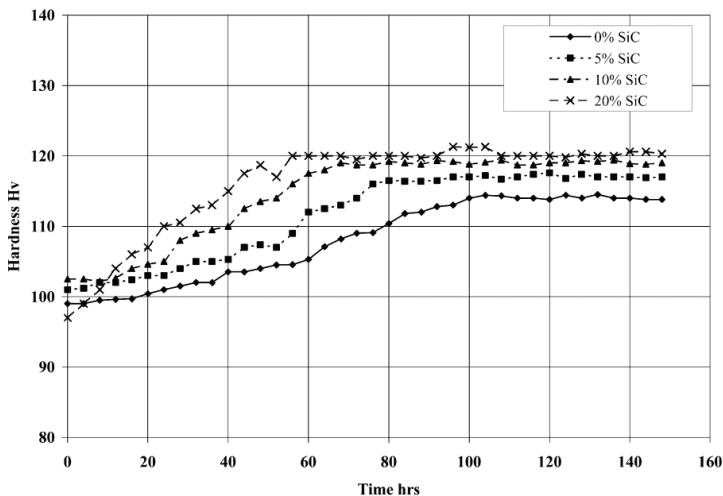

Figure 12. The hardness behaviour of composites (Bekheet et al., 2002).

On the other hand, 2026 aluminum alloy was subjected to tensile deformation and strain value was determined. An increase in the width of the sample, increased the strain concentration (Lam et al., 2010). Wang et al. examined the aged and deep cryogenic treated FSW joints of 2024-T351 aluminum alloy (Wang et al., 2014). They found that the yield stress, ultimate strength and elongation decreased after ageing and deep cryogenic heat treatment (*Figure 13*). Similar method was applied without cryogenic treatment to join 2024-T351 and 6056-T4 alloy (Amancio-Filho et al., 2008).
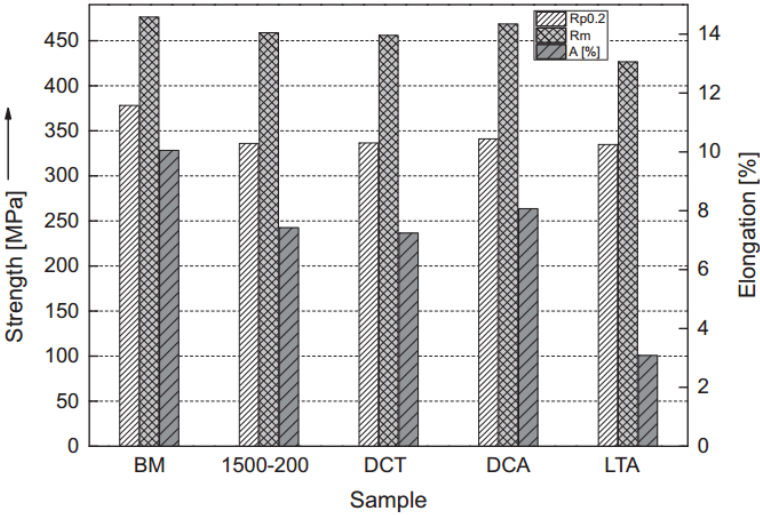
Figure 13. Tensile properties of 2024 with different heat treatment (Wang et al., 2014).

Moreover, the sample 2024 and 7075 subjected to the cryogenic heat treatment at -196 °C for 4h increased the yield strength 32 and 20 MPa and the tensile strength to 26 and 21 MPa (Faraji et al., 2018).

It is well documented that 6061 aluminum alloy had mild strength, heat treatable and good corrosion characteristic. The 6061 aluminum alloy is used in automotive and aviation industry to gain weight. The effect of ageing on the hardness was studied and they found that ageing at 180 °C for 24 h decreased the hardness from 105 Hv (180 °C for 11 h) to 95 Hv (Demir & Gündüz, 2009).

Ozturk et al. also worked on the mechanical properties of 6061 alloys. They found that after 120 min of ageing at the temperature of 200 °C, a decrease of hardness value was observed as seen at *Figure 14* (Ozturk et al., 2010).
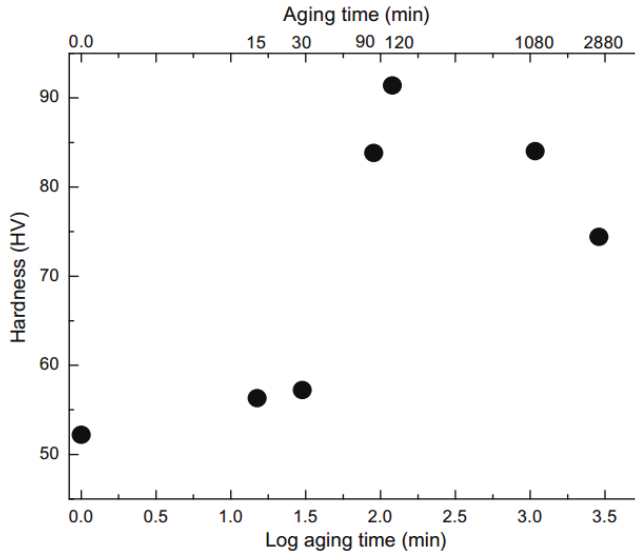
Figure 14.The hardness behavior with ageing time of the 6061 aluminum alloy (Ozturk et al., 2010).

According to the works realized, the T6 treatment lead β″ needle-shaped precipitates and the sequence of precipitation of Al-Mg-Si were given in the Table 3 (Maisonnette et al., 2011). Mariora et al. studied the effect of β″ phase on the hardness of 6xxx series of aluminum alloys (Marioara et al., 2006). In another study, the residual stress formed after cryogenic heat treatment to 6061 aluminum alloy was examined by Ko et al. (Ko et al., 2013).

Table 3. Al-Mg-Si composition of precipitate (Maisonnette et al., 2011).

Phase	Composition
GP zone	Mg_1Si_1
β″	Mg_5Si_6
β′	Mg_9Si_5
β	Mg_2Si

REFERENCES

Amancio-Filho, S. T., Sheikhi, S., dos Santos, J. F., & Bolfarini, C. (2008). Preliminary study on the microstructure and mechanical properties of dissimilar friction stir welds in aircraft aluminium alloys 2024-T351 and 6056-T4. *Journal of Materials Processing Technology*, *206*(1), 132-142. https://doi.org/https://doi.org/10.1016/j.jmatprotec.2007.12.008
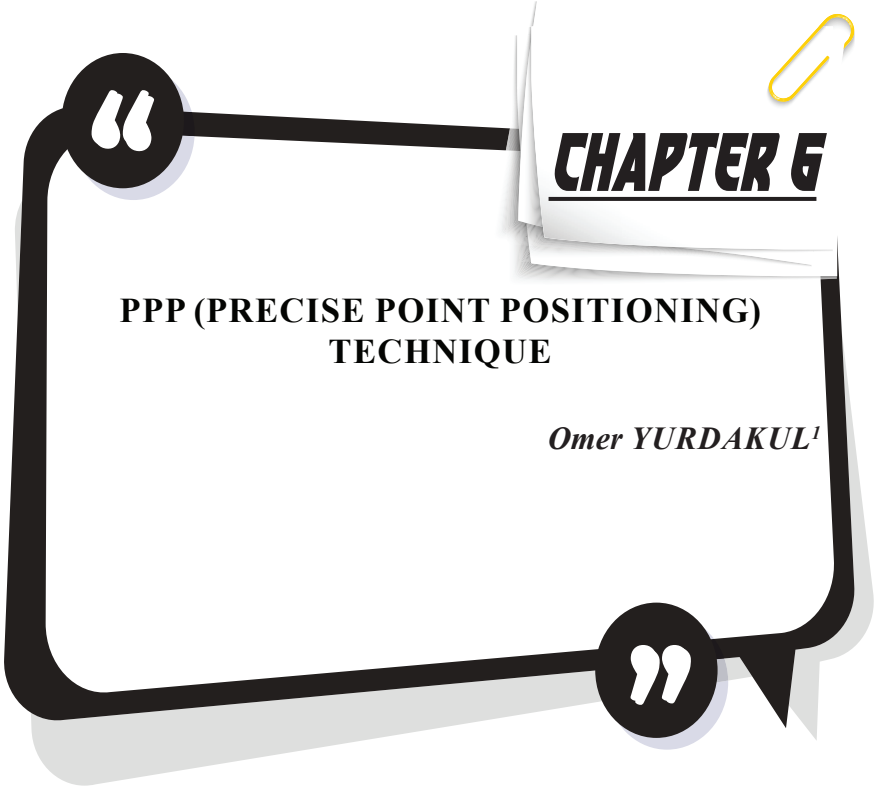
Bekheet, N. E., Gadelrab, R. M., Salah, M. F., & Abd El-Azim, A. N. (2002). The effects of aging on the hardness and fatigue behavior of 2024 Al alloy/SiC composites. *Materials & Design*, *23*(2), 153-159. https://doi.org/https://doi.org/10.1016/S0261-3069(01)00072-3

Chen, P., Malone, T., Bond, R., & Torres, P. (2001). Effects of Cryogenic Treatment on the Residual Stress and Mechanical Properties of an Aerospace Aluminum Alloy.

Cole, G. S., & Sherman, A. M. (1995). Light weight materials for automotive applications. *Materials Characterization*, *35*(1), 3-9. https://doi.org/https://doi.org/10.1016/1044-5803(95)00063-1

Committee, A. I. H. (1990). *ASM Handbook: Properties and selection*. ASM International. https://books.google.com.tr/books?id=1gcbGi1JF4UC

Dasquet, J. P., Caillard, D., Conforto, E., Bonino, J. P., & Bes, R. (2000). Investigation of the anodic oxide layer on 1050 and 2024T3 aluminum alloys by electron microscopy and electrochemical impedance spectroscopy. *Thin Solid Films*, *371*, 183-190. https://doi.org/10.1016/S0040-6090(00)01016-6

Deepa, P., & Padmalatha, R. (2017). Corrosion behaviour of 6063 aluminium alloy in acidic and in alkaline media. *Arabian Journal of Chemistry*, *10*, S2234-S2244. https://doi.org/https://doi.org/10.1016/j.arabjc.2013.07.059

Demir, H., & Gündüz, S. (2009). The effects of aging on machinability of 6061 aluminium alloy. *Materials & Design*, *30*(5), 1480-1483. https://doi.org/https://doi.org/10.1016/j.matdes.2008.08.007

Dursun, T., & Soutis, C. (2014). Recent developments in advanced aircraft aluminium alloys. *Materials & Design (1980-2015)*, *56*, 862-871. https://doi.org/https://doi.org/10.1016/j.matdes.2013.12.002

Elango, G., Raghunath, B., & Thamizhmaran, K. (2014). Effect of Cryogenic Treatment on Microstructure and Micro Hardness of Aluminium (LM25) - SiC Metal Matrix Composite. *Journal of Engineering Research*, *11*, 64-68. https://doi.org/10.24200/tjer.vol11iss1pp64-68

Fahimpour, V., Sadrnezhaad, S. K., & Karimzadeh, F. (2012). Corrosion behavior of aluminum 6061 alloy joined by friction stir welding and gas tungsten arc welding methods. *Materials & Design*, *39*, 329-333. https://doi.org/https://doi.org/10.1016/j.matdes.2012.02.043

Faraji, F., VAHDAT, S. E., & Nazarian, H. (2018). Effect of Deep Cryogenic Treatment on Precipitation Hardening of Aluminum 2024 and 7075. *METALLURGICAL ENGINEERING*, *21*(3 (71) #T001080), -. https://www.sid.ir/en/Journal/ViewPaper.aspx?ID=818936

Franco Steier, V., Ashiuchi, E., Reißig, L., & Araújo, J. (2016). Effect of a Deep Cryogenic Treatment on Wear and Microstructure of a 6101 Aluminum Alloy. *Advances in Materials Science and Engineering*, *2016*, 1-12. https://doi.org/10.1155/2016/1582490

Huang, Y., Shih, H., Huang, H., Daugherty, J., Wu, S., Ramanathan, S., Chang, C., & Mansfeld, F. (2008). Evaluation of the corrosion resistance of anodized aluminum 6061 using electrochemical impedance spectroscopy (EIS). *Corrosion Science*, *50*(12), 3569-3575. https://doi.org/https://doi.org/10.1016/j.corsci.2008.09.008

Jovičević-Klug, P., & Podgornik, B. (2020). Review on the Effect of Deep Cryogenic Treatment of Metallic Materials in Automotive Applications. *Metals*, *10*(4), 434. https://www.mdpi.com/2075-4701/10/4/434

Kaseem, M., Kamil, M. P., Kwon, J. H., & Ko, Y. G. (2015). Effect of sodium benzoate on corrosion behavior of 6061 Al alloy processed by plasma electrolytic oxidation. *Surface and Coatings Technology*, *283*, 268-273. https://doi.org/https://doi.org/10.1016/j.surfcoat.2015.11.006

Ko, D.-H., Ko, D.-C., Lim, H.-J., Lee, J.-M., & Kim, B.-M. (2013). Prediction and measurement of relieved residual stress by the cryogenic heat treatment for Al6061 alloy: Mechanical properties and microstructure. *Journal of Mechanical Science and Technology*, *27*. https://doi.org/10.1007/s12206-013-0601-1

Lam, D., Menzemer, C., & Srivatsan, T. (2010). A study to evaluate and understand the response of aluminum alloy 2026 subjected to tensile deformation. *Materials & Design*, *31*, 166-175. https://doi.org/10.1016/j.matdes.2009.06.040

Lulay, K. E., Khan, K., & Chaaya, D. (2002). The effect of cryogenic treatments on 7075 aluminum alloy. *Journal of Materials Engineering and Performance*, *11*(5), 479-480. https://doi.org/10.1361/105994902770343683

Ma, A., Saito, N., Shigematsu, I., Suzuki, K., Takagi, M., Nishida, Y., Iwata, H., & Imura, T. (2004). Effect of Heat Treatment on Impact Toughness of Aluminum Silicon Eutectic Alloy Processed by Rotary-Die Equal-Channel Angular Pressing. *Materials Transactions - MATER TRANS*, *45*, 399-402. https://doi.org/10.2320/matertrans.45.399

Macário, P. F., Vieira, A., Manfroi, L., da Silva, M. G. P., Leite, P., & Vieira, L. (2019). Corrosion behavior of Al2024-T3, Al5052-H32, and Al6061-T6 aluminum alloys coated with DLC films in aviation fuel medium, Jet A-1 and AVGAS 100LL. *Materials and Corrosion*, *70*(12), 2278-2291. https://doi.org/10.1002/maco.201911035

Maisonnette, D., Suery, M., Nelias, D., Chaudet, P., & Epicier, T. (2011). Effects of heat treatments on the microstructure and mechanical properties of a 6061 aluminium alloy. *Materials Science and Engineering: A*, *528*(6), 2718-2724. https://doi.org/https://doi.org/10.1016/j.msea.2010.12.011

Marioara, C. D., Nordmark, H., Andersen, S. J., & Holmestad, R. (2006). Post-β″ phases and their influence on microstructure and hardness in 6xxx Al-Mg-Si alloys. *Journal of Materials Science*, *41*(2), 471-478. https://doi.org/10.1007/s10853-005-2470-1

Mascagni, D. B. T., Souza, M. E. P. d., Freire, C. M. d. A., Silva, S. L., Rangel, R. d. C. C., Cruz, N. C. d., & Rangel, E. C. (2014). Corrosion resistance of 2024 aluminum alloy coated with plasma deposited a-C:H:Si:O films. *Materials Research*, *17*, 1449-1465. http://www.scielo.br/scielo.php?script=sci_arttext&pid=S1516-14392014000600013&nrm=iso

Ozturk, F., Sisman, A., Toros, S., Kilic, S., & Picu, R. C. (2010). Influence of aging treatment on mechanical properties of 6061 aluminum alloy. *Materials & Design*, *31*(2), 972-975. https://doi.org/https://doi.org/10.1016/j.matdes.2009.08.017

Padmini, B. V., Sampathkumaran, P., Seetharamu, S., Jaiprakash, N., & Niranjan, H. (2019). Investigation on the wear behaviour of Aluminium alloys at cryogenic temperature and subjected to cryo -treatment. *IOP Conference Series: Materials Science and Engineering*, *502*, 012191. https://doi.org/10.1088/1757-899X/502/1/012191

Padmini, B. V., Sampathkumaran, P., Seetharamu, S., Naveen, G. J., & Niranjan, H. B. (2019). Investigation on the wear behaviour of Aluminium alloys at cryogenic temperature and subjected to cryo -treatment. *IOP Conference Series: Materials Science and Engineering*, *502*, 012191. https://doi.org/10.1088/1757-899x/502/1/012191

Pantelakis, S., Setsika, D., Chamos, A., & Zervaki, A. (2016). Corrosion damage evolution of the aircraft aluminum alloy 2024 T3. *International Journal of Structural Integrity*, *7*(1), 25-46. https://doi.org/10.1108/IJSI-03-2014-0010

Pantelakis, S. G., Chamos, A. N., & Kermanidis, A. T. (2012). A critical consideration for the use of Al-cladding for protecting aircraft aluminum alloy 2024 against corrosion. *Theoretical and Applied Fracture Mechanics*, *57*(1), 36-42. https://doi.org/https://doi.org/10.1016/j.tafmec.2011.12.006

Park, D.-H., Choi, S.-W., Kim, J.-H., & Lee, J.-M. (2015). Cryogenic mechanical behavior of 5000- and 6000-series aluminum alloys: Issues on application to offshore plants. *Cryogenics*, *68*, 44-58. https://doi.org/https://doi.org/10.1016/j.cryogenics.2015.02.001

Reboul, M. C., & Baroux, B. (2011). Metallurgical aspects of corrosion resistance of aluminium alloys [https://doi.org/10.1002/maco.201005650]. *Materials and Corrosion*, *62*(3), 215-233. https://doi.org/https://doi.org/10.1002/maco.201005650

Salguero, J., Del Sol, I., Gómez-Parra, Á., & Batista Ponce, M. (2020). Machining of Al-Cu and Al-Zn Alloys for Aeronautical Components. In. https://doi.org/10.5772/intechopen.93719

Shi, H., Han, E.-H., Liu, F., & Kallip, S. (2013). Protection of 2024-T3 aluminium alloy by corrosion resistant phytic acid conversion coating. *Applied Surface Science*, *280*, 325-331. https://doi.org/https://doi.org/10.1016/j.apsusc.2013.04.156

Siskou, N., Charalampidou, C., Alexopoulos, N. D., & Kourkoulis, S. K. (2018). Effect of corrosion exposure on aluminum alloy 2024 for different artificial ageing conditions. *Procedia Structural Integrity*, *10*, 79-84. https://doi.org/https://doi.org/10.1016/j.prostr.2018.09.012

Snihirova, D., Höche, D., Lamaka, S., Mir, Z., Hack, T., & Zheludkevich, M. L. (2019). Galvanic corrosion of Ti6Al4V -AA2024 joints in aircraft environment: Modelling and experimental validation. *Corrosion Science*, *157*, 70-78. https://doi.org/https://doi.org/10.1016/j.corsci.2019.04.036

Valerie, G., & Georges, M. (1999). Localized corrosion of 2024 T352 aluminium alloy in chloride media. *Corrosion Science 41*, 421–438.

Varun Chandra, M., Sudarshan, M., Sumantha, H., & Harshith Gowda, K. I. (2018). Effect of with and without cryogenic treatment on Tensile, hardness and impact on hybrid Aluminium-6061 metal matrix composites. *International Journal of Engineering Research and General Science*, *6*(3).

Wang, J., Fu, R., Li, Y., & Zhang, J. (2014). Effects of deep cryogenic treatment and low-temperature aging on the mechanical properties of friction-stir-welded joints of 2024-T351 aluminum alloy. *Materials Science and Engineering: A*, *609*, 147–153. https://doi.org/10.1016/j.msea.2014.04.077

Xiangfeng, M., Wei, G., Hongliang, G., Yundan, Y., Ying, C., & Dettinger, H. (2013). Anodization for 2024 Al Alloy from Sulfuric-Citric Acid and Anticorrosion Performance of Anodization Films. *International Journal of Electrochemical Science*, *8*, 10660-10671.

Zhang, W. D., Yang, J., Dang, J. Z., Liu, Y., & Xu, H. (2013). Effects of Cryogenic Treatment on Mechanical Properties and Corrosion Resistance of LC4 Aluminum Alloy. *Advanced Materials Research*, *627*, 694-697. https://doi.org/10.4028/www.scientific.net/AMR.627.694

Zheng, K., Politis, D. J., Wang, L., & Lin, J. (2018). A review on forming techniques for manufacturing lightweight complex—shaped aluminium panel components. *International Journal of Lightweight Materials and Manufacture*, *1*. https://doi.org/10.1016/j.ijlmm.2018.03.006

Zhou, J., Xu, S., Huang, S., Meng, X. K., Sheng, J., Zhang, H., Li, J., Sun, Y., & Agyenim-Boateng, E. (2016). Tensile Properties and Microstructures of a 2024-T351 Aluminum Alloy Subjected to Cryogenic Treatment. *Metals*, *6*, 279. https://doi.org/10.3390/met6110279

CHAPTER 6

PPP (PRECISE POINT POSITIONING) TECHNIQUE

Omer YURDAKUL[1]

1 Dr., Necmettin Erbakan University, Department of Internal Auditing Unit, oyurdakul@erbakan.edu.tr, ORCID ID: 0000 – 0003 – 2591 – 9040

1. Introduction

PPP (Precise Point Positioning) technique, which is one of the positioning techniques in GNSS (Global Navigation Satellite Systems) systems, was first introduced by Anderle (1976). However, the use of GNSS systems in today's sense, Zumberge et al. (1997) to offer the accuracy obtained from IGS (International GNSS Service) to all users with global solutions (Anderle, 1976; Zumberge et al., 1997).

In general, the PPP technique is a positioning method that provides high accuracy location accuracy by processing both code and carrier phase observations with a single GNSS receiver using satellite clock and orbit products broadcast from a global network. The most important advantage over differential positioning techniques is that there is no need for one or more reference stations whose coordinates are known. On the other hand, the most important disadvantage of the technique is the long convergence time required for integer ambiguity resolution in applications that require position accuracy on the order of cm (centimeter). Generally, the convergence time is about one hour to achieve 5 cm accuracy from a standard static PPP solution. This is a limiting factor in the real-time applications of the PPP technique. In the PPP technique, accuracy of a few cm in static mode and a few dm (decimeters) in kinematic mode can be achieved. In the PPP technique, both code and carrier phase observations are required. With the spread of the technique; it is observed that it is used in areas such as geodetic studies, deformation measurements, detection of zenith tropospheric delays, monitoring and modeling of the atmosphere, precision agriculture applications, determination of earth crust movements, monitoring of landslides. In general, the PPP technique is a viable method in areas where precise positioning and navigation are required and there is no reference station infrastructure (Karauğuz, 2021; Ogutcu, 2019; Turgut, 2019; Öcalan, 2015; Martin, 2013; Rizos et al., 2012; Zumberge et al., 1997).

2. Mathematical Model of PPP Technique

In the PPP technique, there are two widely known basic mathematical models. The first of these is the traditional model developed by Kouba and Heroux (2001). The second model is the P1-P2-CP model developed by Gao and Shen (2001) (Bahadur, 2017; Öcalan, 2015; Shen, 2002; Gao and Shen, 2001; Kouba and Heroux, 2001).

2.1. Traditional Model

Kouba and Heroux (2001) developed a mathematical model for the office calculations of the PPP with the precision orbital and clock products of the IGS, using dual-frequency carrier phase (undifferenced) and code observations in their study. This model created the traditional mathematical model of PPP for cm-accuracy static and kinematic precision positioning

applications using a single dual-frequency GNSS receiver (Bahadur, 2017; Öcalan, 2015; Kouba and Heroux, 2001).

Dual-frequency GNSS observation models are adopted to reduce the effect of ionospheric errors in the traditional PPP technique. Accordingly, the ionosphere-free carrier phase and code observations were translated into a combined ionosphere-free structure known as L3. Thus, the refraction bias of the GNSS signal in the ionosphere layer is largely (99%) eliminated (Öcalan, 2015; Soycan, 2012; Kouba and Heroux, 2001).

The simplified mathematical equations of ionosphere-free PPP functional model combinations of dual-frequency carrier phase and code observations are shown below, using the position, time, troposphere, and integer ambiguity parameters as revealed by Kouba and Heroux (2001) (Bahadur and Nohutcu, 2020; Turgut, 2019; Kouba et al., 2017; Öcalan, 2015; Martin, 2013; Shen, 2002; Kouba and Heroux, 2001).

$$\ell p = \rho + c(dt - dT) + Tr + \varepsilon p \qquad (1)$$

$$\ell \Phi = \rho + c(dt - dT) + Tr + N\lambda + \varepsilon \Phi \qquad (2)$$

In the above equations;

ℓp: Ionosphere-free combination of P1 and P2 code measures *(P3 = 2.546P1 - 1.546P2),*

$\ell \Phi$: Ionosphere-free combination of L1 and L2 carrier phase measures *(L3 = 2.546$\lambda_1 \Phi_1$-1.546$\lambda_2 \Phi_2$),*

ρ: calculated geometric distance (between satellite and GNSS receiver),

c: speed of light in vacuum,

dt: difference between GNSS receiver clock time and GNSS time (receiver clock offset),

dT: difference between satellite clock time and GNSS time (satellite clock offset),

Tr: signal path delay in the atmosphere due to the tropospheric effect,

N: the integer ambiguity of the carrier phase ionosphere-free combination,

$\lambda_1, \lambda_2, \lambda$: the wavelength of the L1, L2 carrier phases and the combined L3 carrier phase (10.7 cm), respectively,

$\varepsilon p, \varepsilon \Phi$: it refers to the noise components, including the signal multipath effect.

Calculated geometric distance ρ between satellite and GNSS receiver; It can be calculated as a function of the satellite position *(Xs, Ys, Zs)* and the GNSS receiver *(x, y, z)* position broadcast at a t-epoch with the following equation.

$$\rho = \sqrt{(Xs - x)^2 + (Ys - y)^2 + (Zs - z)^2} \qquad (3)$$

In equations (1) and (2), the zenith path delay *(zpd)* and the tropospheric path delay, which is a function of the mapping function coefficient (Mapping Function: *M*), are associated with the satellite elevation angle, then the known satellite clocks are eliminated, and the following mathematical a model is obtained (Öcalan, 2015; Shen, 2002; Kouba and Heroux, 2001).

$$fp = \rho + c.dt + M_{zpd} + \varepsilon p - \ell p = 0 \qquad (4)$$

$$f\Phi = \rho + c.dt + M_{zpd} + N\lambda + \varepsilon\Phi - \ell\Phi = 0 \qquad (5)$$

The traditional ionosphere-free combination model has some disadvantages. This model does not include completely ionosphere-free combinations, as it cannot completely eliminate the high-level effects caused by the ionosphere. Although high-order ionospheric effects are less than 0.1% of all effects, the time-dependent path error of high total electron density can sometimes be many centimeters. The second disadvantage is that the combined ambiguity solution for a carrier phase observation (due to the integer ambiguity coefficient obtained for the L1 and L2 combinations) can only be estimated as a partial solution. This situation requires a long convergence time for the parameters to be estimated (Öcalan, 2015; Gao and Shen, 2002; Shen, 2002).

When the equations (4) and (5) are linearized with respect to approximate values and observations (X^0, ℓ), the matrix representation can be written as follows (Öcalan, 2015; Kouba and Heroux, 2001).

$$A\delta + W - V = 0 \qquad (6)$$

where;

A: coefficients matrix (the design matrix),

δ: the vector of corrections to the unknown parameters *X*,

W: reduced dimensions vector (the misclosure vector) [$W = f(X^0, \ell)$],

V: represents the correction vector (the vector of residuals).

Coefficients matrix (the design matrix) A obtained by taking the partial derivative of the observation equations according to *X*; GNSS receiver position (*x,y,z*), GNSS receiver clock (*dt*), carrier phase integer ambiguity (*N*) and tropospheric zenith path delay (*zpd*) includes four different parameters and can be written as follows according to these parameters (Öcalan, 2015; Kouba and Heroux, 2001).

$$A = \begin{bmatrix} \dfrac{\partial f(X,\ell p)}{\partial x} & \dfrac{\partial f(X,\ell p)}{\partial y} & \dfrac{\partial f(X,\ell p)}{\partial z} & \dfrac{\partial f(X,\ell p)}{\partial dt} & \dfrac{\partial f(X,\ell p)}{\partial zpd} & \dfrac{\partial f(X,\ell p)}{\partial N^j_{(j=1,nsat)}} \\ \dfrac{\partial f(X,\ell\Phi)}{\partial x} & \dfrac{\partial f(X,\ell\Phi)}{\partial y} & \dfrac{\partial f(X,\ell\Phi)}{\partial z} & \dfrac{\partial f(X,\ell\Phi)}{\partial dt} & \dfrac{\partial f(X,\ell\Phi)}{\partial zpd} & \dfrac{\partial f(X,\ell\Phi)}{\partial N^j_{(j=1,nsat)}} \end{bmatrix} \quad (7)$$

with

$$X^T = \begin{bmatrix} x\ y\ z\ dt\ zpd\ N^j_{(j=1,nsat)} \end{bmatrix} \tag{8}$$

With a priori weighted constraints (Px) according to the parameters, the least squares solution is obtained as follows;

$$\delta = -(Px^0 + A^T P\ell A)^{-1} A^T P\ell W \tag{9}$$

Thus, the estimated parameters are;

$$\hat{X} = X^0 + \delta \tag{10}$$

and the covariance matrix;

$$C_{\hat{X}} = P_{\hat{X}}^{-1} = (P_{X^0} + A^T P\ell A)^{-1} \tag{11}$$

can be calculated as.

2.2. P1-P2-CP Model

For the PPP solution made with the traditional method, the convergence time required for position determination is over 30 minutes in the analyzes involving office calculations of the data obtained by the static method. In order to reduce this time, either the number of unknowns or the measured noise level should be reduced. Therefore, Gao and Shen (2001) proposed a new observation model named P1-P2-CP, which can reduce noise levels and residual errors. This model also reduces the number of unknowns, allowing the solution of integer ambiguity to be fixed (Öcalan, 2015; Shen, 2002; Gao and Shen, 2001).

The P1-P2-CP model uses ionosphere-free combinations, similar to the traditional model. While in the traditional model of Kouba and Heroux (2001) separately combinations of phase and code measures are made between L1 and L2 signals, in the P1-P2-CP model of Gao and Shen (2001) the combination of phase and code observations is used as a new observation. The code and phase observations used in both models are at the same frequency and are exposed to the same rate of ionospheric effect. However, since this effect is reversed in both models, the total ionospheric effect is independent of the ionosphere (Öcalan, 2015; Gao and Shen, 2001).

The P1-P2-CP observation model includes the phase-code combination at both L1 and L2 frequencies and can be expressed with the following equation (Öcalan, 2015; Shen, 2002; Gao and Shen, 2001);

$$P_{IF,i} = 0.5(P(L_i) + \Phi(L_i)) \tag{12}$$

$$= \rho + c(dt - dT) + d_{orb} + d_{trop} + 0.5\lambda_i N_i + 0.5d_{mult/P(L_i)} + 0.5\varepsilon(P(L_i) + \Phi(L_i))$$

In this equation, $P_{IF,i}$ is the L_i ionosphere-free code-phase combination. The subscript (i) used here is the standard for L1 or L2. By recalculating the satellite-receiver distance in a combination of 0.5 scale coefficients and then applying the precise orbit and clock corrections to equation (12), the equation given below is obtained.

$$P'_{IF,i} = \rho + c.dT + d_{trop} + 0.5\lambda_i N_i + \varepsilon(P'_{IF,i}) \tag{13}$$

In this equation; $P'_{IF,i}$ is L_i corrected ionosphere-free code-phase combination, ε is random noise components, including residual errors of precise orbit and clock data, high level unmodelable ionospheric effects, signal multipath effect, and noise components.

According to this model, the given code-phase combinations are both ionosphere-free and at a greatly reduced level of noise when compared to the original code observations. The biggest advantage of this model is that it can calculate the integer ambiguity in both L1 and L2 separately, as well as successfully obtain the fixed solution value of the integer ambiguity. For this reason, in this model, the integer ambiguity solution was developed, shortening the convergence time required for positioning with a fixed ambiguity solution, and reducing the unknown parameters was used for this (Öcalan, 2015; Shen, 2002; Gao and Shen, 2001).

2.3. Comparison of the Traditional Model and the P1-P2-CP Model

First, the observations include two observations for each satellite, one code and one phase in the traditional model, while in the P1-P2-CP model, one phase and two codes for each satellite have one more observation than the traditional model, with a total of three observations. Second, the noise

level is 3 times the standard code noise level (containing more residual errors) in the traditional model, while it is about half the standard code noise level in the P1-P2-CP model. Thirdly, integer ambiguity solution can only perform partial ambiguity solution in the traditional model. In the P1-P2-CP model, on the other hand, by separating the integer ambiguity estimation in L1 and L2, both fixed and partial (float) ambiguity solutions can be performed and applied. Comparisons of both PPP data evaluation models are given in Table 1 (Öcalan, 2015; Shen, 2002; Gao and Shen, 2001).

Table 1. *Comparison of data evaluation models of the traditional model and the P1-P2-CP model (Öcalan, 2015; Shen, 2002)*

Comparison Criteria	The Traditional model	The P1-P2-CP model
Observations	There are 2 for each satellite, one for code, and one for phase.	There are 3 for each satellite, one for phase and two for code.
Noise	It is 3 times the standard code noise level.	It is about half the standard code noise level.
Integer ambiguity	Combined L1/L2 integer ambiguity, partial (float) resolution value can be obtained.	L1 and L2 integer ambiguity, (pseudointeger), can be applied to both fixed and partial (float) integer ambiguity resolution.
Unknown parameters	3D coordinates, receiver clock offsets, tropospheric wet zenith delay, N ambiguity.	3D coordinates, receiver clock offsets, tropospheric wet zenith delay, 2xN ambiguity.

The traditional ionosphere-free combination between L1 and L2 developed by Kouba and Heroux (2001) and the residual errors obtained by Gao and Shen (2001) for code-phase combinations are given in Table 2, comparatively. When these residual errors are examined, the calculated combinations for satellite orbit, satellite clock, and troposphere are similar. It is seen that the traditional ionosphere-free combination noise component is considerably larger than the noise component of code-phase combinations. At the same time, when the P1-P2-CP model is compared with the L1-L2 combination for code measures, it is seen that the total residual error amount is slightly less (Öcalan, 2015; Shen, 2002; Gao and Shen, 2001; Kouba and Heroux, 2001).

Table 2. *Comparison of residual errors between the traditional model and the P1-P2-CP model (Öcalan, 2015; Shen, 2002)*

Residual Errors	The Traditional model	The P1-P2-CP model
Satellite orbit	< 5 cm	< 5 cm
Satellite clock	< 3 cm	< 3 cm
Troposphere	< 5 cm	< 5 cm
Ionosphere	< 5 cm	< 5 cm
Noise	3σ *	$1/2\sigma$ *
Others	< 1 ~ 2 cm	< 1 ~ 2 cm
Total	< 32 cm (code observations) < 9 cm (phase observations)	< 10 cm

(*) σ is the noise measurement of code or phase observations. The noise level for code and phase observations in quality GNSS receivers is approximately 10 cm and 0.3 cm, respectively. Therefore, the noise level for code and phase observations in ionosphere-free combinations is approximately 30 cm and 1 cm, respectively.

3. Carrier Phase Integer Ambiguity Resolution in PPP

In order to achieve a good performance in PPP, an important parameter besides the basic quantities such as precision, integration and continuity is the convergence time. The concept of time defined here is the convergence time for position information to be obtained with high accuracy. At this point, the most critical situation is the solution of integer ambiguity (Öcalan, 2015; Martin, 2013; Kouba and Heroux, 2001).

The solution of integer ambiguity is mostly applied in the solution of binary difference observation algorithms, and data evaluation in relative positioning. At this stage, significant integer ambiguity and signal offsets are eliminated. In the PPP technique, on the other hand, some difficulties are experienced especially in the solution of integer ambiguity and, accordingly, in the convergence time, since differentiating techniques are not used in the data evaluation stage. For this reason, many methods have been developed to safely solve integer ambiguity in PPP (Ogutcu, 2020; Öcalan, 2015).

The process of estimating and solving carrier phase integer ambiguity in PPP technique can be divided into 3 parts. The first is a part of the integer (N) and the other two are the fractional part of the signal offset (FCBs: Fractional Cycle Biases). One of these fractional parts is related to the broadcasting satellite (b^j) and the other is related to the receiver (b_i) (Figure 1). Equation (14) shows all three components. If both of the fractional signal

offsets can be determined according to this equation, then it may be possible to use the techniques used in carrier phase integer ambiguity resolution in relative positioning for PPP as well (Öcalan, 2015; Martin, 2013).
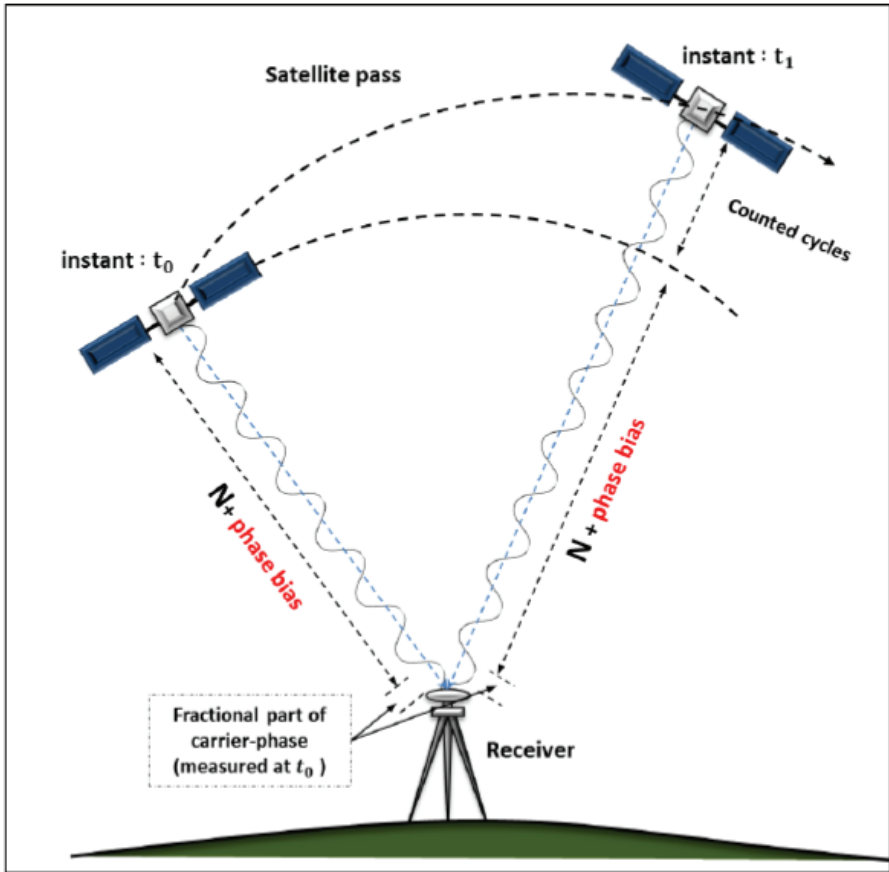

Figure 1. *Geometric representation of ambiguities and carrier phase biases in carrier phase measurements over a satellite pass (Oliveira, 2017).*

$$b = b^j + b_i + N \qquad (14)$$

For the calculation of the ionosphere-free carrier phase integer ambiguity, the ionosphere-free code and carrier phase observation equations given in equations (1) and (2) can also be written as follows (Ogutcu, 2019; Ogutcu, 2020);

$$P_{IF,r}^s = (f1^2 * P1^s - f2^2 * P2^s)/(f1^2 - f2^2) \qquad (15)$$

$$\Phi_{IF,r}^s = (f1^2 * \Phi1^s - f2^2 * \Phi2^s)/(f1^2 - f2^2) \qquad (16)$$

where; superscript s denotes satellite, subscript r denotes GNSS receiver, $f1$ and $f2$ are the two carrier phase frequencies in Hertz. P1, P2, Φ1 and Φ2 are the code and carrier phase measured in meters at the two frequencies. From here, the ionosphere-free wavelength and ionosphere-free carrier phase integer ambiguity can be written as;

$$\lambda_{IF} = \frac{f1^2}{f1^2 - f2^2} * \lambda_1 - \frac{f2^2}{f1^2 - f2^2} * \lambda_2 \qquad (17)$$

$$N_{IF} = \frac{f1^2 * N_1}{f1^2 - f2^2} - \frac{f2^2 * N_2}{f1^2 - f2^2} \qquad (18)$$

where; N_1 and N_2 are phase initial integer ambiguities at two frequencies relative to each observed satellite. Ionosphere-free ambiguity can only be estimated as a partial (float) ambiguity solution unless bias information from the network is used (Ogutcu, 2019; Ogutcu, 2020).

Collins (2008) proposes a model characterized by different clock parameters for code and phase measurements in solving carrier phase integer ambiguity. This model is known as the Decoupled Satellite Clocks model. By applying the estimated satellite decoupled integer clock and phase bias corrections through a GNSS reference network, receiver decoupled clock parameters and undifferenced ambiguities can be estimated. Laurichesse et al. (2009) corrected for wide-lane and narrow-lane ambiguities. In the results of both methods, narrow-lane FCB values are absorbed in satellite clock calculations, and therefore the clock products created are called integer corrected clocks. Geng et al. (2010) showed that the three-dimensional RMS (root mean square) value of static positioning accuracy for more than one hour decreased from 5 cm to 1.6 cm in the PPP technique in which ambiguity was corrected. However, the long duration here is an important problem (Öcalan, 2015; Martin, 2013; Geng et al., 2010; Laurichesse et al., 2009; Collins, 2008).

4. Real Time PPP (RT-PPP/PPP-RTK)

With the emergence of the need for real-time location data, new techniques have begun to be developed. The first of these is the DGPS/DGNSS (Differential GPS/Differential GNSS) technique, and since code observations are used in this technique, an accuracy of about meters can be achieved and cannot be used in precise studies. Later, for real-time and high-accuracy studies, real-time kinematics (RTK) positioning technique, in which carrier phase observations are used with dual or more frequency receivers, has been developed. In this technique, in order to obtain precise position information, the calculated correction data is sent to mobile receivers by various transmission means, and real-time position information is obtained.

The most important factor affecting accuracy and performance in the classical RTK method, where a single reference station is used, is the distance between the reference station and GNSS receiver. Rover receivers can be a maximum distance of 10-15 km from the reference station. The main reason for this limitation is satellite orbital errors and atmospheric errors. In order to better model the distance-related errors in the classical RTK technique and to obtain more accurate coordinates, the idea of developing a Network-Based RTK technique, which can make constant and continuous observations, has emerged. Thus, the Continuously Operating Reference Stations (CORS) model was developed, in which observations are made in many fixed and continuously broadcasting stations, faulty measurements are eliminated with statistical analyzes, systematic effects are better modeled and high-accuracy coordinates are obtained by using the principle of geodetic network structure. In this technique, the data of the observations received from all stations in the network are calculated in the network control center and sent as correction data to the mobile receivers by various communication tools. Today, in systems serving according to the Network-Based RTK principle, techniques called VRS, FKP and MAC are used, each of which calculates correction data according to different mathematical models and algorithms (Yurdakul, 2021; Kahveci, 2017).

In recent years, with the development of the PPP technique, different from classical and Network-Based RTK methods, PPP-RTK technique has been developed for real-time applications. The PPP-RTK technique has been developed in order to use the PPP technique anywhere in the world and in real-time with a single GNSS receiver device by making the precise orbit and clock correction data available in real-time, taking the post-measurement processing load of the users (Turgut, 2019; Teunissen and Khodabandeh, 2015; Öcalan, 2015).

The accuracy of the PPP-RTK technique depends on the resolution of the integer ambiguity, the number of satellites, and their geometry. The most important disadvantage of PPP is that it requires a long observation time to solve the integer ambiguity (in the ionosphere-free linear combination model). In order to overcome this problem, it is predicted that state space model (SSM) and state space representation model (SSR) can be used by using CORS networks. In CORS networks, correction data can be generated continuously and in real-time for each rover receiver. With this approach, integer ambiguity can be resolved in PPP using SSM or SSR and the level of accuracy obtained from CORS networks can be captured. The combination of these two models, namely the method that uses the SSM/SSR model and performs the RTK technique with a single receiver, is called PPP-RTK (Teunissen and Khodabandeh, 2015; Öcalan, 2015; Mervart et al., 2008; Wübbena et al., 2005).

The most important factor affecting position accuracy in Network-Based RTK applications is the solution of carrier phase integer ambiguity. There are geometry-free (GFAR: Geometry Free Ambugity Resolution) and geometry-based (GBAR: Geometry Based Ambugity Resolution) methods developed in this regard. In the GFAR method, linear combinations of different codes and carrier phase signals are used to resolve integer ambiguity. The most well-known of this method is the Melbourne-Wübbena model, in which the carrier phase is combined with the wide-line and narrow-lane of the code. In the GBAR method, more than necessary satellites are used for integer ambiguity resolution. The most well-known model of this method is LAMBDA (Öcalan, 2015; Wübbena, 2012; Teunissen, 1993).

In CORS networks, all errors affecting GNSS measurements are calculated within the network and sent to the rover receivers as correction data or as correction data with raw observations. This structure is called the Observation Space Representation (OSR) model. This model has been used for a long time in Network-Based RTK and classical RTK applications. In OSR, all error components are collectively represented in the observation space. Table 3 shows the parameter comparison of the OSR model used in Network-Based RTK and classical RTK and the SSR model used in PPP and PPP-RTK (Yurdakul, 2021; Geo++, 2015; Öcalan, 2015).

Table 3. *Parameter comparison of the OSR model used in Network-Based RTK and classical RTK and the SSR model used in PPP and PPP-RTK (EGA, 2019; Geo++, 2015; Öcalan, 2015)*

| | OSR (Observation Space Representation) | | | | SSR (State Space Representation) | | |
| | RTK | Network-Based RTK | | | Phase based PPP | Code based PPP | PPP-RTK |
	RS	FKP	MAC	VRS/PRS			
Broadcast possible	✓	✓	✓	X	✓	✓	✓
Accuracy	~ cm	~ cm	~ cm	~ cm	< dm	~ 3 dm	< cm
Required time*	< 5 sec	< 5 sec	< 5 sec	< 5 sec	~ 20 min	< 1 sec	< 5 sec - 1 min**
Service area	local	regional	regional	regional	global	global/ regional	global/ regional
Single frequency	X	X	X	X	X	✓	X
Required bandwidth	medium	medium	high	medium	low	low	low - medium
CORS network density requirement (km)	20 - 50	70 - 100	70 - 100	70 - 100	1000+	1000+	100+
* No signal multipath error is assumed. ** It depends on the update speed.							

In PPP-RTK applications, orbit/clock information provided from an external source and other correction parameters need to be transmitted to rover receivers in real-time. The performance of the PPP-RTK depends on the coverage, continuity, and reliability criteria for this transmission. As with all real-time techniques, international standards have been developed in the transmission of correction data to mobile receivers in PPP-RTK applications. Today, there are formats such as RTCM, NMEA, and CMR/CMR+ that are accepted as international standards and are widely used. Today, there are private and public institutions/institutes that support PPP-RTK. The most important of these is IGS's real-time service (RTS). By subscription, users can access RTS as a public service and use GNSS orbit and clock corrections in real-time Worldwide, PPP-related applications. RTS broadcasts GNSS orbit and clock corrections using IGS' global network of stations, and analysis centers. The main actors providing these services at RTS are NRCan (Natural Resources Canada), ESA/ESOC (European Space Agency/European Space Operations Centre), and BKG (Bundesamt für Kartographie und Geodäsie - German Federal Agency for Cartography and Geodesy) (Oliveira, 2017; Öcalan, 2015).

5. Error Sources in PPP Technique

The most important factors affecting position accuracy in the PPP technique are the existing error sources and the elimination of these errors. These error sources can be listed as follows (Karauğuz, 2021; Kouba et al., 2017; Bahadur, 2017; Öcalan, 2015; Martin, 2013; Shen, 2002);

- ➢ Satellite Orbit and Clock Error,
- ➢ Receiver Clock Error,
- ➢ Tropospheric Delay Error,
- ➢ Ionospheric Delay Error,
- ➢ Relativistic Effect,
- ➢ Satellite Orientation Effect,
- ➢ Antenna Phase Center,
- ➢ Phase Wind-up Effect,
- ➢ Noon and Midnight Turns Effect of the Satellite,
- ➢ Solid Earth Tide Effect,
- ➢ Ocean Tide Loading Effect,
- ➢ Polar Tide Effect,
- ➢ Atmospheric Pressure Loading Effect,
- ➢ Differential Code Biases (DCB),
- ➢ Cycle Slips,
- ➢ Signal Multipath Effect.

5.1. Satellite Orbit and Clock Error

The basic positioning principle of GNSS is based on calculating the distance between satellites and GNSS receivers. All GNSS satellites transmit ephemeris data in real-time, based on changing times. It includes ephemeris data, satellite orbit data, and time data. For this reason, ephemeris data should be known by GNSS receivers. The ephemeris data and other navigation data are calculated by the ground control center with the message parameters, uploaded to the satellites periodically, and broadcast to the users. The accuracy and precision of data sent from satellites are limited by satellite storage, link bandwidth, and the ground control center's processing strategy. Better quality satellite data is required for accurate positioning (Öcalan, 2015; Martin, 2013; Shen, 2002).

Cesium and rubidium atomic clocks are used in GNSS satellites to determine the moment when their signals are generated. Although these watches are highly accurate and stable, small deviations can occur. Considering that the speed of light is 3×10^8 m/sec on average, a time error of 1 nanosecond (1 ns = 1×10^{-9} sec) made by a satellite causes an error of 0,3 m in the calculation of the topocentric distance between the satellite and GNSS receiver. For this reason, the GNSS main control center calculates these

clock errors and broadcasts the clock correction parameters again with the satellite navigation message (Öcalan, 2015; Shen, 2002).

Using a global network, accurate satellite orbit and clock deviations can be calculated and distributed to GNSS users via the internet or communications satellites. This information can also be obtained from analysis centers such as IGS, which produces orbital and clock products (Martin, 2013).

5.2. Receiver Clock Error

It uses quartz crystal oscillators to keep the cost low in GNSS receivers. They are not as strong as the atomic clocks used in GNSS satellites and are affected by changes in ambient temperature. Some receivers experiment to synchronize their internal clocks with the reference timescale to avoid a rather large clock error. These types of receivers periodically add split clock jumps to keep the receiver clock below a threshold. Clock jumps typically happen as an integer millisecond (1 ms = 0,001 sec). The receiver clock error can be corrected by taking the difference between satellites or estimating it as a stochastic parameter with the receiver position, as in the standard approach in PPP. Receiver clock error affects all received signals equally (Bahadur, 2017; Martin, 2013).

5.3. Tropospheric Delay Error

The troposphere, which is the lowest layer of the atmosphere, is the layer in which the gases are most dense. It has an altitude of about 20 km from the earth's surface. Although its thickness changes according to the latitude values, it is about 18 km at the equator and decreases to 8 km towards the poles and is the layer where all meteorological events take place. The tropospheric delay effect occurs in satellite signals due to the dry and wet components of the troposphere. The magnitude of the tropospheric delay depends on many factors, including atmospheric pressure, temperature, water vapor, satellite elevation angle, and station altitude. The dry component of the troposphere is the higher part of the troposphere and the delay is around 2 m. It accounts for 90% of the tropospheric delay. Water vapor in the atmosphere is the wet component of the troposphere and is the lower part of the troposphere. The effect of the wet component is around 10 cm and accounts for 10% of the tropospheric delay. The effect of dry and wet components is eliminated by modeling the total tropospheric delay (Karauğuz, 2021; Öcalan, 2015).

5.4. Ionospheric Delay Error

Extending from about 50 to 1000 kilometers from the Earth's surface, the ionosphere forms the upper part of the atmosphere. Free electrons in the ionosphere affect the propagation of GNSS signals, where the ionospheric effect typically depends on electron density along the signal path. Solar and geomagnetic activities play important roles in electron creation and distribution. Total Electron Content (TEC) is equal to the number of free electrons in the unit area column through which the signal moves between the satellite and the receiver. Modeling the ionospheric effect on GNSS signals is often difficult due to the irregularities of electron density. On the phase and code measurements, the effects of ionospheric refraction have the same greatness but opposite signs. This means that the ionosphere advances the carrier phase measurements while delaying the code measurements. Also, the ionospheric effect is dependent on the system frequency as it is a dispersive medium. For this reason, the first-order ionospheric effect can be eliminated by combining GNSS observations. The traditional PPP approach uses the ionosphere-free combination to eliminate the first-order ionospheric effect, which is equal to 99% of the total ionospheric delay (Bahadur, 2017; Martin, 2013).

5.5. Relativistic Effect

The relativistic effect is an effect that results from the gravitational potential and velocity of movement of a satellite clock and receiver clock. Therefore, measurements based on time disparities are subject to relative effects. The secondary relativistic effect caused by the curvature of space-time caused by the gravitational field also causes a delay in GNSS signals. This effect, also called Shapiro signal propagation delay, should be considered only for applications that require high accuracy since it is less than 2 cm (Karauğuz, 2021; Bahadur, 2017).

5.6. Satellite Orientation Effect

It is significant to know the orientation of GNSS satellites to obtain accurate positioning. The satellite orientation effect affects phase center offsets, phase wind-up, and noon and midnight rotations of the satellite. The orientation of the GPS and GLONASS satellites are maintained with the antenna facing the center of the Earth. The unit vector in this direction is denoted by k. The solar panels of the satellites are oriented towards the Sun, so when the Sun unit vector e is given to the satellite, it is given the value j. The j value defined along the solar panel axis is calculated by the equation $j = k \times e$. The unit vector i exist in the Sun-satellite-Earth plane and completes the right-hand coordinate system. This situation is also expressed as "nominal deviation attitude" (Martin, 2013).

5.7.   Antenna Phase Center

Satellite coordinates represent the satellite's center of mass. Signal transmission and phase measurements are related to the antenna phase center of the satellite. In GNSS satellites, there are two centers: the satellite antenna phase center and the center of gravity. The offset between these two centers is expressed as the satellite antenna phase center offset. For this reason, the phase center offset values of the satellite mass and the satellite direction should be known. This factor, which is one of the most important components of satellite-based errors, is modeled by taking into account especially precise position determination studies (Öcalan, 2015; Karabatic, 2011).

5.8.   Phase Wind-up Effect

Because GNSS satellites emit right-hand circularly polarized radio waves, carrier wave phase observations depend on the mutual orientation of the satellite and GNSS receiver antennas. Rotating the satellite or receiver antenna one turn around its vertical axis causes the carrier wave phase to shift by 1 wavelength, and this effect is called phase wind-up effect. This effect is different in satellite antennas compared to receiver antennas. So much so that while the solar panels of satellite antennas are directed towards the sun, they are exposed to small rotations and the satellite-receiver geometry changes. For this reason, it is necessary to make corrections to the phase measurements. While this effect can be negligible in networks with a base length of several hundred kilometers in offset, for example, it causes an error of about 1 cm at a base length of 1000 km. In order to achieve dm level positioning accuracy in the PPP, phase wind-up correction should be introduced (Öcalan, 2015; Martin, 2013; Karabatic, 2011).

5.9. Noon and Midnight Turns Effect of the Satellite

When a satellite passes between the Sun and the Earth, the mass of the satellite requires it to spin very quickly; this is called the "noon turn of the satellite". Satellites have a restricted rotation speed, so during this rotation period, the actual orientation of the satellite delays behind the modeled orientation. In this case, the Earth comes between the Sun and the satellite, and a similar effect is seen, known as the "midnight turn of the satellite". Another situation is when the satellite enters the shadow of the Earth. Satellites use a Sun/light sensor to orient themselves towards the Sun. Once the satellite is in Earth's shadow, the Sun/light sensor can no longer track the Sun. For example, GPS Block II/IIA satellites begin to deviate with a deflection rate of about $0.10°$ s^{-1} to $0.13°$ s^{-1} during the time they are in shadow. The movement of the satellite during the post-shadow recovery period takes about 30 minutes and may not be identified. For this reason, it cannot be modeled properly. For advanced satellites, nominal deviation is maintained during shadow transit (Martin, 2013).

5.10. Solid Earth Tide Effect

The Earth is affected by the gravitational forces exerted by the Moon, Sun, and other planets, which causes deformations. This periodic effect that stations on the earth are exposed to is called the solid Earth tide effect. This effect can reach up to 30 cm vertically and 5 cm horizontally. The displacement effect caused by solid Earth tides is often expressed in spherical harmonics (numbers of Love and Shida). The values of these numbers are defined based on the geographic location of the station and the tidal frequency. The displacement caused by the solid Earth tide effect is divided into two parts as permanent and periodic parts. While the effect of the periodic part can be averaged mainly in the static positioning of the whole day, the effect of the permanent part remains in the average position for a while. The effect of the permanent part can reach up to 12 cm near mid-latitudes (Karauğuz, 2021; Bahadur, 2017).

5.11. Ocean Tide Loading Effect

The ocean tide loading effect has a deformation effect similar to the solid Earth tide effect and can be defined as ocean tides pressing on the underlying crust. Its effect is smaller than the solid Earth tide. These effects are much more local, largely confined to coastal areas, and have no permanent part. For coastal areas, it can reach values of a few cm and decrease with distance from the coast. This effect can be neglected in calculating the location of stations located inland at a distance of 1000 km or more from the ocean coast and in 24-hour long-term static observations. However, if the station is close to the ocean or if the receiver clock error is to be calculated with the tropospheric wet component, this effect must be taken into account even in 24-hour observations. Otherwise, this effect is reflected in the location calculation as receiver clock error and tropospheric effect (Kouba et al., 2017; Öcalan, 2015; Martin, 2013).

5.12. Polar Tide Effect

Changes in the Earth's instantaneous axis of rotation cause periodic deformations in the earth's crust. Unlike the solid Earth tide and the ocean tide loading effect, the polar tide is not the average of a 24-hour period. That is, the average does not approach zero over a 24-hour period. Displacements due to the polar tide effect can reach up to 25 mm vertically and 7 mm horizontally. Polar tide correction should be applied in positioning that requires sub-cm position accuracy (Karauğuz, 2021; Bahadur, 2017).

5.13. Atmospheric Pressure Loading Effect

The mass of the atmosphere causes a charge on the Earth's surface. This load, along with changes in atmospheric pressure, causes displacements on the Earth's surface both vertically and horizontally. On average, these

displacements have an RMS of 2.6 mm for the vertical component and 0.6 mm for the horizontal component (Martin, 2013).

5.14. Differential Code Biases (DCB)

Differential code biases (DCB) are referred to as the difference in signal transmitted times caused by hardware assembly delay differences in satellite and GNSS receiver equipment. For single frequency users, these errors need to be considered in positioning and timing applications. It also requires consideration of the effect of DCB if the signals used in the ionosphere-free linear combination for dual-frequency users are different from those used in the production of GNSS precise products. DCB is characteristically divided into satellite-specific and receiver-specific sections. The receiver-specific error is disregarded in most positioning applications, as its effect is added to the receiver clock error in the estimation process. But, the satellite-specific error needs to be corrected. In PPP applications, differential code biases cannot be corrected when evaluating the carrier phase and code measurements in case of using single-frequency receivers, whereas when using dual-frequency receivers, it is eliminated with the dual-frequency ionosphere-free model (Karauğuz, 2021; Bahadur, 2017; Öcalan, 2015).

5.15. Cycle Slips

During the carrier phase observations, instantaneous jumps, called phase cycle slip, occur. Phase cycle slip is a sudden jump in carrier phase observations reasoned by the failure of the GNSS receiver to trace the signal. A phase cycle slip characteristically occurs in measurements of a GNSS satellite over a period of time. The occurrence of cycle slip causes interruption in the measurements. If cycle slip remains unrepaired, they can degrade the accuracy and convergence time in the PPP. For this reason, cycle slips must be correctly detected and repaired in PPP applications. A number of methods based on dual-frequency combinations can be used successfully for phase cycle slips detection. Due to its low noise level and resistance to ionospheric changes, the Melbourne-Wübbena (MW) combination with wide-lane ambiguity is used for this purpose (Bahadur, 2017).

5.16. Signal Multipath Effect

GNSS signals may be subject to signal breakage or scattering by following multiple paths due to environmental effects during their travel from the satellite to the receiver's antenna. These signals, which can reflect from surfaces such as buildings, trees, lakes, and soil, are faced with the signal multipath effect, especially in urban areas. Although the magnitude of this effect is unlimited for code observations depending on the satellite elevation angle, it can be estimated by considering the signals reaching the receiver directly and indirectly in carrier phase observations. Signal

multipath effect; Although it is about 15 meters theoretically in P-code measurements, it is stated to be around a few meters, and in carrier phase observations, it reaches a maximum of about 5 cm. It is not possible to completely eliminate the signal multipath effect. However, it can be reduced by a number of methods such as the selection of the measurement location and the design of the GNSS receiver's antenna (Öcalan, 2015; Karabatic, 2011).

Error sources, which are among the most important factors affecting position accuracy, are explained above. Summary information on these is given in Table 4 below.

Table 4. Error sources and mitigation methods (Karauğuz, 2021; Erdogan et al., 2018; Abou-Galala et al., 2018; Öcalan, 2015)

Error source	Effect	Mitigation method
Orbital error	~1 m	With precise orbit correction
Satellite clock error	~ 2 ns (0.6 m)	With precise clock correction
Troposphere	~ 2.3 m	The dry component is estimated using empirical models (Saastamoinen et al.) and the wet component as unknown.
Ionosphere	-	With ionosphere-free (IF) combination
Relativistic effect in satellite clock	~1 m	Modeled with mathematical equations
Relativistic effect on signal propagation	~1-2 cm	
Satellite antenna phase center variation	~2 m	IGS ANTEX file
Satellite antenna phase center offset	~1-2 cm	IGS ANTEX file
Receiver antenna reference point	~10 cm	Observation file (RINEX)
Receive antenna phase center offset	~1 cm	IGS ANTEX file
Phase wind-up	~1 cycle	Modeled with mathematical equations
Solid Earth tide	~30 cm	
Ocean tide loading	~5 cm	
Polar tide	~2.5 cm	
Signal multipath	~0.1-3 m C/A code ~5 cm carrier phase	With filtering and modeling

6. Software Developed for PPP Processing

In addition to scientific software with different features for the PPP technique, which is still in development, free internet-based applications, which are widely used today, have also been developed. In addition to these scientific software and applications that allow post-measurement evaluation including office calculations, there are also open-source software that will support real-time PPP applications. There are also some commercial PPP software developed for static and kinematic PPP applications serving all GNSS users.

Various scientific and academic software have been developed that perform data processing and analysis for the office calculations of PPP. Among them, Bernese developed by the University of Bern, Switzerland, GIPSY-OASIS developed by NASA-JPL, WaPPP developed by Lambert Wanninger, gLAB developed by ESA, BNC developed by BKG and RTK-LIB developed by Tomoji Takasu. Among these software, especially BNC and RTK-LIB stand out for PPP users as they are open source and can be used free of charge in both office calculations and real-time PPP applications. Apart from these software packages, there are also software developed for real-time calculation of orbit and clock information used as antecedent corrections in PPP and ultra-rapid broadcasting with SSR messages. Especially CSRS-PPP developed by Natural Resources Canada, PANDA developed by Wuhan University, EPOS-RT developed by GFZ, BNC and RTNet developed by BKG (with GPS Solutions company), RETICLE developed by GSOC/DLR, developed by GMV company MagicGNSS, RETINA developed by ESA/ESOC, PPP-WIZARD developed by CNES and GNSMART software developed by Geo++ are the most well-known ones. Apart from these, there are software working with PPP algorithms such as Fugro's STARFIX, Veripos' Ultra, NavCom's StarFire, which provide services for real-time precise positioning on a global scale. The process of developing both scientific and commercial software packages for PPP by various universities, research centers, and commercial companies continues today (Atiz and Kalaycı, 2021; Öcalan, 2015; Soycan, 2012).

With the development of the PPP technique, internet-based service applications of the technique have also started to come into service. Information on some of these services, the number of which is increasing, is given in Table 5. Many of these internet-based PPP services, which are free for users, require a subscription. There are different options for GNSS RINEX data to be uploaded to the system, such as quota limitation and version type (such as RINEX v2 or RINEX v3), evaluation of data in static/kinematic mode, evaluation of receiver data, and serving according to GNSS antenna brand/model. The data published in real-time includes data such as GNSS satellite orbit and clock correction information (Atiz et al., 2021; Öcalan et al., 2015; Öcalan, 2015; Öcalan and Alkan, 2012).

Table 5. *Internet-based services providing PPP technique (Turgut, 2019; Öcalan et al., 2015; Öcalan, 2015; URL: 1-10)*

S.No	Service Name	Organization & Country of Origin	Data Type	Process Mode	Software	Datum
1	CSRS-PPP	NRCan/Canada	GNSS	Static/Kinematic	NRCanPPP	ITRF2014
2	GAPS	University of New Brunswick/Canada	GNSS	Static/Kinematic	GAPS	ITRF2014
3	APPS	NASA-JPL/USA	GPS	Static/Kinematic	Gipsy	ITRF2014
4	MagicPPP	GMV/Spain	GNSS	Static/Kinematic	MagicPPP	ITRF2014
5	Trimble Center Point RTX	Trimble/USA	GNSS	Static/Kinematic	Trimble RTX	ITRF2014
6	BKG Ntrip Client (BNC)	BKG/Germany	GNSS	Static/Kinematic	BNC	ITRF2014
7	RTNet	GPS Solutions/USA	GNSS	Static/Kinematic	RTNet	-
8	PPP-Wizard	CNES/France	GNSS	Static/Kinematic	PPP-Wizard	-
9	RTKLIB	T. Takasu and A. Yasuda/Japan	GNSS	Static/Kinematic	RTKLIB	ITRF2008
10	PANDA	Wuhan University/China	GNSS	Static/Kinematic	PANDA	-

7. Conclusions and Recommendations

Global technological developments have significantly affected the expectations for GNSS positioning techniques, and the need for real-time position data has gained importance. Therefore, efforts are made by GNSS communities to improve existing positioning methods with low-cost GNSS receivers in line with the demands of GNSS users. In particular, absolute positioning techniques are preferred among relative positioning techniques due to their simplicity of use and low cost. In this context, both the development process of the PPP technique continues and its usage area is becoming widespread. It is thought that this study prepared for this purpose will be beneficial to all GNSS users.

However, in order to increase the performance of the PPP technique, the interoperability of multiple GNSS systems should be made more effective, and integrated solutions of different observation types should be investigated. Correction models for the elimination of error sources, which are among the factors affecting position accuracy, should continue to be investigated. At the same time, the development of new models that will reduce the minimum time required for the solution of the carrier phase ambiguity will make the use of the PPP technique more common.

References

Abou-Galala, M., Rabah, M., Kaloop, M. and Zidan, Z.M. (2018), Assessment of the accuracy and convergence period of Precise Point Positioning, Alexandria Engineering Journal Vol: 57, 1721–1726, http://dx.doi.org/10.1016/j.aej.2017.04.019.

Anderle, R.J. (1976), Point Positioning concept using precise ephemeris, Proceedings of the International Geodetic Symposium, On Satellite Doppler Positioning, 12-14 October 1976, Las Cruces, New Mexico, 47-75.

Atiz, O.F. and Kalaycı, I. (2021), Performance Assessment Of PPP-AR Positioning And Zenith Total Delay Estimation With Modernized CSRS-PPP, Artificial Satellites, Vol: 56, No: 2, DOI: 10.2478/arsa-2021-0003.

Atiz, O.F., Ogutcu, S., Alcay, S. and Kalaycı, I. (2021), Analysis of the Static Positioning Performance of CSRS-PPP Service, FIG e-Working Week 2021, Virtual, 21–25 June 2021.

Bahadur, B. (2017), Improving The Performance Of Precise Point Positioning With Multi-GNSS, Master's Thesis, Institute of Science and Technology, Hacettepe University, Ankara, Turkey.

Bahadur, B. and Nohutcu, M. (2020), Hassas Nokta Konumlama İçin Robust Kalman Filtresi Yöntemlerinin Analizi, Journal of Harita, 164, 29-42.

Collins, P. (2008), Isolating and estimating undifferenced GPS integer ambiguities, In Proceedings of ION National Technical Meeting, San Diego, CA, USA, 28–30.

EGA. (2019), PPP-RTK market and technology report, European Global Navigation Satellite Systems Agency (European GNSS Agency), France.

Erdogan, B., Karlitepe, F., Ocalan, T. and Tunalioglu, N. (2018), Performance analysis of Real Time PPP for transit of Mercury, Measurement, Vol: 129, 358–367, https://doi.org/10.1016/j.measurement.2018.07.050.

Gao, Y. and Shen, X. (2001), Improving Convergence Speed of Carrier Pahase based Precise Point Positioning, Proceedings of ION GPS-2001, The Institute of Navigation, 11-14 September 2001, Salt Lack City, UT, USA.

Gao, Y. and Shen, X. (2002), A New Method For Carrier-Phase–Based Precise Point Positioning, Navigation: Journal of Institute of Navigation, 49(2), 109-116.

Geng, J., Meng, X., Teferle, F.N. and Dodson, A. (2010), Performance of precise point positioning with ambiguity resolution for 1-to 4-hour observation periods, Survey Review, 42(316), 155–165.

Geo++ (2015), Geo++ SSR, For Network-RTK, PPP and PPP-RTK, GmbH, SSR Flyer Version 3, September 2015.

Kahveci, M. (2017), Kinematik GNSS ve RTK CORS Ağları, Nobel Akademik Yayıncılık Eğitim Danışmanlık Tic. Ltd. Şti., 2nd Edition, Ankara, Turkey.

Karabatic, A. (2011), Precise Point Positioning (PPP) - an alternative technique for ground based GNSS troposphere monitoring, Ph.D. Thesis, Technology Faculty of Mathematics and Geoinformation, Vienna University, Austria.

Karauğuz, S.N. (2021), Küresel Navigasyon Uydu Sistemleri (GNSS) Ölçümlerinde Uydu Yükseklik Açısına Bağlı Ağırlıklandırma Stratejilerinin Hassas Nokta Konum Belirleme (PPP) Performansına Etkisi, Master's Thesis, Institute of Science and Technology, Necmettin Erbakan University, Konya, Turkey.

Kouba, J., Lahaye, F. and Tétreault, P. (2017), Precise Point Positioning, Teunissen, P.J.G. and Montenbruck, O. (Ed), in Springer Handbook of Global Navigation Satellite Systems, 723-751, Springer International Publishing, Switzerland.

Kouba, J. and Héroux, P. (2001), Precise Point Positioning Using IGS Orbit and Clock Products, GPS Solutions, Vol: 5, No: 2, 12-28.

Laurichesse, D., Mercier, F., Berthias, J.P., Broca, P. and Cerri, L. (2009), Integer ambiguity resolution on undifferenced GPS phase measurements and its application to PPP and satellite precise orbit determination, Navigation: Journal of The Institute of Navigation, Vol: 56, No: 2, 135–149.

Martin, I. (2013), GNSS Precise Point Positioning: The Enhancement with GLONASS, Ph.D. Thesis, School of Civil Engineering and Geosciences, Newcastle University, Newcastle, UK.

Mervart, L., Lukes, Z., Rocken, C. and Iwabuchi, T. (2008), Precise Point Positioning with Ambiguity Resolution in Real-time, Proceedings of the 21th International Technical Meeting of the Satellite Division of The Institute of Navigation (ION GNSS 2008), 397–405.

Oliveira, P.S. (2017), Definition and implementation of a new service for precise GNSS positioning, Ph.D. Thesis, Faculty of Science and Technology, São Paulo State University, Brazil.

Ogutcu, S. (2019), The contribution of Multi-GNSS Experiment (MGEX) to precise point positioning over Turkey: Consideration of observation time and satellite geometry, El-Cezerî Journal of Science and Engineering, Vol: 6, Issue: 3, 642-658, DOI: 10.31202/ecjse.563802.

Ogutcu, S. (2020), Performance Analysis Of Ambiguity Resolution On PPP And Relative Positioning Techniques: Consideration Of Satellite Geometry,

International Journal of Engineering and Geosciences (IJEG), Vol: 5, Issue: 2, 073-093, DOI: 10.26833/ijeg.580027.

Öcalan, T. (2015), GNSS Ağlarında GPS Hassas Nokta Konumlama (GPS-PPP) Tekniği Yaklaşımlı Çözümler, Ph.D. Thesis, Institute of Science and Technology, Yıldız Technical University, Istanbul, Turkey.

Öcalan, T., Cingöz, A., Duman, H., Hastaoğlu, K., Kara, T., Gezer, M.V., Özer, E. and Salgın, Ö. (2015), Büyük Ölçekli Harita Üretimi Standartlarının Geliştirilmesine Yönelik GPS PPP Tekniğinin Doğruluğunun Araştırılması, TMMOB Chamber of Surveying and Cadastre Engineers, 15th Turkey Scientific and Technical Survey, 25-28 March 2015, Ankara, Turkey.

Öcalan, T., and Alkan, R.M. (2012), Performance Analysis of Web-Based Online Precise Point Positioning (PPP) Services for Marine Applications, The 14th IAIN Congress 2012, Cairo, Egypt, 1-3 October,2012.

Rizos, C., Janssen, V., Roberts, C. and Grinter, T. (2012), Precise Point Positioning: Is the Era of Differential GNSS Positioning Drawing to an End?, FIG Working Week 2012, 6-10 May 2012, Rome, Italy.

Shen, X. (2002), Improving Ambiguity Convergence in Carrier Phase-Based Precise Point Positioning, Master's Thesis, Department of Geomatics Engineering, University of Calgary, Canada.

Soycan, M. (2012), A Quality Evaluation of Precise Point Positioning within the Bernese GPS Software Version 5.0, Arab J Sci Eng (2012), 37:147–162.

Teunissen, P.J.G. (1993), Least-Squares Estimation of the Integer GPS Ambiguities, General Meeting of the International Association of Geodesy, August 1993, Beijing, China.

Teunissen, P.J.G. and Khodabandeh, A. (2015), Review and principles of PPP-RTK methods, Journal of Geodesy (2015) 89:217–240, DOI: 10.1007/s00190-014-0771-3.

Turgut, M. (2019), Gerçek Zamanlı Hassas Nokta Konumlama (RT-PPP) Yönteminin Performansının İncelenmesi, Master's Thesis, Institute of Science and Technology, Necmettin Erbakan University, Konya, Turkey.

URL-1: CSRS-PPP Service, https://webapp.geod.nrcan.gc.ca/geod/tools-outils/ppp.php, (Accessed on: 15 February 2022).

URL-2: GAPS Service, http://gaps.gge.unb.ca/index.html, (Accessed on: 15 February 2022).

URL-3: APPS (Gipsy) Service, https://pppx.gdgps.net/, (Accessed on: 15 February 2022).

URL-4: MagicPPP Service, https://gmv.com/en-es/products/space/magicpppr, (Accessed on: 15 February 2022).

URL-5: Trimble RTX Service, https://www.trimblertx.com/, (Accessed on: 15 February 2022).

URL-6: BNC Service, https://igs.bkg.bund.de/ntrip/bnc, (Accessed on: 15 February 2022).

URL-7: RTNet Service, https://gps-solutions.com/, (Accessed on: 15 February 2022).

URL-8: PPP-Wizard Service, http://www.ppp-wizard.net/index.html, (Accessed on: 15 February 2022).

URL-9: RTKLIB Service, http://www.rtklib.com/, (Accessed on: 15 February 2022).

URL-10: PANDA Service, http://gpscenter.whu.edu.cn/index.shtml, (Accessed on: 15 February 2022).

Wübbena, G. (2012), RTCM State Space Representation (SSR) Overall Concepts Towards PPP-RTK, PPP-RTK & Open Standards Symposium, 12 March 2012, Frankfurt, Germany.

Wübbena, G., Schmitz, M. and Bagge, A. (2005), PPP-RTK: Precise Point Positioning Using State-Space Representation in RTK Networks, Proceedings of the 18th International Technical Meeting of the Satellite Division of The Institute of Navigation (ION GPS 2005), 2584–2594.

Yurdakul, Ö. (2021), CORS-TR Ölçmelerinde GLONASS'ın Konum Doğruluğuna Etkisi: Konya Örneği, Ph.D. Thesis, Institute of Science and Technology, Necmettin Erbakan University, Konya, Turkey.

Zumberge, J.F., Heflin, M.B., Jefferson, D.C., Watkins, M.M. and Webb, F.H. (1997), Precise point positioning for the efficient and robust analysis of GPS data from large networks, Journal of Geophysical Research, Vol:102, No:B3, 5005-5017.

CHAPTER 7

INVESTIGATION OF THE EVALUABILITY OF DIFFERENT PLANTS AND ANIMAL WASTES IN FOOD INDUSTRY

Bilge ÇELİK[1], Nil ACARALI[2]

1 Yildiz Technical University, Department of Chemical Engineering, Davutpasa Campus, 34210, Esenler-Istanbul, Turkey
2 Doç.Dr., Yildiz Technical University, Department of Chemical Engineering, Davutpasa Campus, 34210, Esenler-Istanbul, Turkey nilbaran@gmail.com

1. INTRODUCTION

1.1 Food Wastes

Food wastes are organic residues in liquid or solid form that are generally released during the harvesting, processing, or transportation of food raw materials. These substances are removed from the production process as unwanted materials.

Food wastes occur at all stages of the food life cycle, namely, during agricultural production, industrial production, processing and distribution. On the other hand, it is well known that many food wastes are the source of important compounds known to have benefits on human health. Especially plant-based foods attract attention as products rich in fiber, antioxidants and other phytochemicals (phenolic acids, flavonoids, etc.) [1].

In the current century, food waste has become an important problem to be examined by different disciplines. Different methods should be determined and applied by researchers and interested parties on how to reduce food waste. Examples of these methods are strong communication, information campaigns and programs between retailers and agricultural producers [2]. In the food industry, large amounts of solid and liquid waste occur because of production. Waste consisting of organic residues of raw materials is biodegradable. High moisture content, high organic loading, and high biological instability have importance in the identification of this type of waste. Therefore, it is very difficult to process such wastes. The use of inappropriate methods in the disposal of these wastes causes significant environmental problems. Thanks to the legislative requirements created in this context, more stringent measures have been taken recently [3].

2. EGGSHELL

Eggs, which play an important role in different products such as cakes, fast food and salad dressings, which cause significant production costs worldwide, cause several tons of egg waste per day as a result of production and are expressed as a by-product of the production facility [4]. Eggshell constitutes approximately 10% of chicken eggs, which are widely consumed in homes and industrial areas and are the basic nutrients [5].

With the increase in demand in the current century, it has brought a great increase in egg production. When we examine it worldwide, 76.7 million tons of eggs were produced in 2018 and this rate provided an increase of 14.95% in production [6].

High egg consumption is observed in developing countries as eggs are a quality protein source. A higher amount of eggshell production leads to the emergence of a larger amount of eggshell. In 2019, China took the

first place in global eggshell productions. The order of eggshell waste production by country is shown in Figure 1 [7].
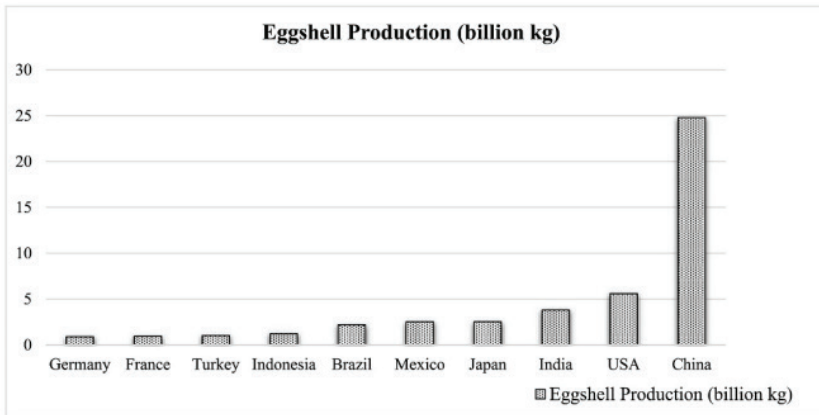

Figure 1. Eggshell waste production by country [7]

2.1. Structure of Eggshell

Basically, two main structures make up the eggshells. These are: calcified eggshell and eggshell membrane. The calcified eggshell membrane consists of calcite and calcium carbonate crystals. The eggshell membrane consists of organic materials [8]. Chemical composition of eggshell by weight is given in Table 1 [9].

Table 1. Chemical structure of eggshell [9]

Substance	Amount (%)
Calcium carbonate	94
Organic matter	4
Magnesium carbonate	1
Calcium phosphate	1

Eggshell is very thin and contains pores that allow gas and moisture exchange between the egg and the external environment. On the shell is an invisible, natural, protein-like film called the "cuticle" or "bloom". This film is considered the first line of defense against microbial entry into the egg. The second physical barrier is the eggshell. Inside the shell, there are two shell membranes, inner and outer. The structure of the eggshell is shown in Figure 2 [10].
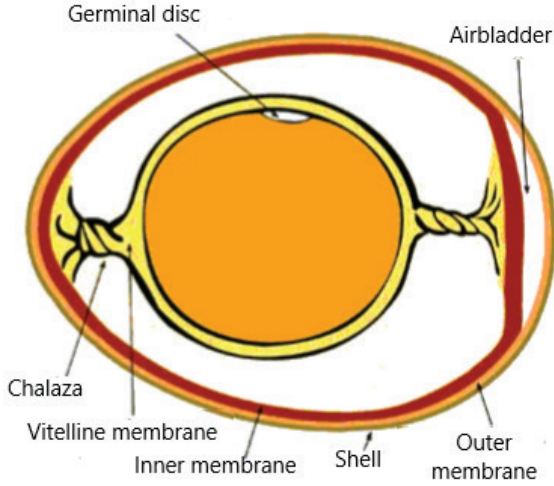
Figure 2. Structure of eggshell [10]

Eggshells, which contain many valuable minerals, are widely used as a low-cost catalyst for biodiesel production, building materials, agriculture, paper recycling and medical applications [11]. In Figure 3, there is an image of eggshell and eggshell powder.

Figure 3. Eggshell and eggshell powder sample [11]

2.1.1 Calcium oxide (CaO)

Calcium oxide is a member of the calcium oxide class with a 1:1 ratio of calcium and oxygen, odorless and white in solid form. It has strong irritant properties in contact with skin, eyes, and mucous membranes [11].

2.1.2 Calcium carbonate ($CaCO_3$)

$CaCO_3$ has importance in formation of sediments and rock types (limestone, chalk, etc.). At the same time, Calcium carbonate is widely found in seas where microorganisms that allow the growth of carbonate deposits are found. Calcium carbonate is a valuable component found

in abundance in systems such as shells, pearls, and eggshells of marine organisms [12].

$CaCO_3$ has three polymorphic structures: vaterite, aragonite and calcite. Vaterite and aragonite are more unstable structures than calcite and easily transform into calcite. These three polymorphs have different characteristics from each other. $CaCO_3$ dissolves very little in pure waters and partially dissolves in waters containing carbon dioxide to obtain calcium bicarbonate $Ca(HCO_3)_2$.

When calcium carbonate is heated, it decomposes to form quicklime and CO_2 gas is released into the environment.

$$CaCO_3 \longrightarrow CaO + CO_2$$

When calcium carbonate molecules react with acids, CO_2 gas is released.

$$CaCO_3 + 2HCl \longrightarrow CaCl_2 + H_2O + CO_2 \quad [13]$$

2.2 Bioavailability of Egg Shell Calcium and Its Importance for Health

About 90% of the calcium in the human body is found in bones and teeth, the remaining 1% in the blood and other tissues. Calcium plays a role in providing structure and strength to the skeleton. It is one of the important macro minerals required for the basic processes of the human body. In addition to being the main component of bones and teeth, it especially has functions through the channels, regulation of inflammatory processes, and protection of cell membrane permeability.

Insufficient dietary calcium is a common nutritional problem. Calcium intake from milk and dairy products is an appropriate way to meet the requirement. showed that only 10% of adults get enough calcium through their diet. A lack of calcium in the diet causes bone loss or osteoporosis. As a person ages, they experience gradual bone loss. Calcium is also important in the regulation of the cardiovascular system and adequate intake is required to prevent hypertension and preeclampsia [14].

3. SHRIMP SHELL

A large amount of waste is generated after the hunting of shellfish or the activities of processing factories. When the waste rates according to the species are analyzed on % body weight, it is around 88-86% in scallops, 86% in oysters and mussels, 77% in sea snails, 68% in crab, 60-65% in shrimp, 61% in crustaceans and 56% in lobsters. In species such as crab, lobster and shrimp, the structural components of these wastes (on dry weight) are chitin, recoverable protein, and calcium carbonate [15].

3.1 Chitin and Chitosan

Chitin is another most common biopolymer after cellulose in the world. It is that a long and linear polysaccharide found in the structure of living things such as algae, insects, ringworms, molluscs, arthropods, roundworms, algae, and fungi. Chitin is only commercially obtained from shell exoskeletons. In particular, the shells of creatures such as crabs and shrimps are used as an easily accessible source of chitin, as they are found as waste in the marine food industry [16].

Shrimp and crab shells, waste from the seafood industry, are converted to chitosan. Chitosan and chitosan derivatives produced by recycling waste shells, whose raw material has almost zero cost, have a high economic value. Today, chitosan is produced commercially in many countries.

Chitins can be found in different structures as α, β- and γ-chitin because of their hydrogen bonds. α-Chitin contains two chains especially antiparallel polysaccharide. α-Kit is the most stable of the three when compared, therefore it has the greatest content. The other two types of chitins tend to be converted to α-chitin when conditions are favorable. β-Chitin contains two parallel polysaccharide chains. γ-Chitin and β-chitin are usually found in soft parts [17].

Chitosan is obtained by treating chitin with an alkaline solution. It is natural and does not show toxic properties. Chitosan is insoluble in water but becomes soluble in solutions particularly aqueous organic acid. Many natural sources of chitin, containing crab and shrimp shells etc. do not include chitosan [18].

The structures for chitosan and chitin are shown in Figure 4. [19].

In order to obtain chitin from bark residues, the bark residues are treated with base and acid to remove protein and mineral substances from these residues. As a result, high quality chitin can be obtained by applying appropriate processing methods. The specific characters of these products; The molecular weight varies with the degree of acidification and processing conditions. The extraction of chitin from shrimp scraps can be done chemically. In addition, the process of obtaining chitin, which is also carried out using lactic acid fermentation, can be considered as an alternative method to expensive and environmentally unsuitable chemical processing. Figure 5 shows the production of chitin and chitosan from shellfish [20].

Chitosan is widely used in various industrial (pharmaceutical, cosmetic, medicine, agriculture, paper, textile and food) and academic fields due to its biodegradable, nontoxic and biocompatible properties. Chitosan has unlimited usage areas with its various functions such as

precipitation, moisture retention, film formation, antimicrobial effect, enzyme immobilization. In addition, chitosan is very valuable because it is natural, non-toxic, has beneficial effects such as preventing tumor formation and lowering serum cholesterol levels. Chitosan is among the dietetic excipients that have been mentioned frequently in recent years.
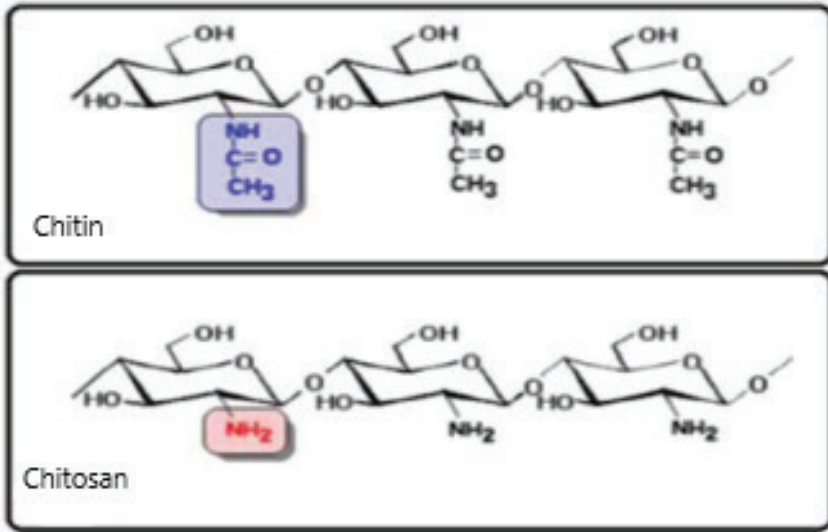

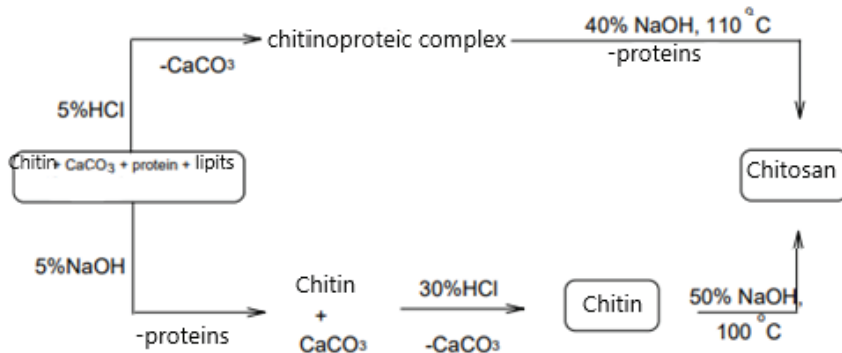*Figure 4. Chemical structures of chitin and chitosan [19]*

Figure 5. Obtaining chitin and chitosan from shellfish [20]

It can not be hydrolyzed by digestive enzymes, its high viscosity, gel forming and high water binding ability etc. For reasons, it is similar to plant dietetic fibers and creates similar effects in living organisms. In addition to its functional effects such as regulating bowel movements and digestive activities, supporting intestinal microflora (bifidobacteria), regulating

blood cholesterol level, lowering blood pressure, regulating liver functions, as well as reducing fat absorption (a positive charged substance) when taken through digestion. It is important in terms of supporting weight loss (by binding to negatively charged fatty acids due to its compound) [19].

3.1.1 Use of chitin, chitosan and derivatives in the food industry

As an antimicrobial agent:

- Preventing the growth of bacteria, mold,

-It is used in the measurement of mold contamination in agricultural raw materials.

In food industry:

-Control of moisture transfer between food and environment,

-Control of release of antimicrobial compounds,

-Control of release of antioxidants,

-Controlling enzymatic darkening in fruits,

- Reducing the partial pressure of oxygen,

The emergence of nutrients, sweeteners and drugs

control of the output,

-Reversing osmotic membranes,

-Controlling the respiratory rate,

-Temperature control.

As an additive:

-Acidification of beverages and fruits,

-Increasing natural sweeteners,

-Muscle structure control substance,

-Emulsifying agent,

-Thickening and stabilizing agent,

-Color stabilizer.

Nutritional quality:

-High cholesterol reducing effect,

-Reducing oil absorption,

-Additive in crustacean and fish nutrition,

-An anti-gastritis agent,

-Baby nutritional content,

-Single cell protein production [21].

4. CITRUS PEELS

Citrus fruits are a group of fruits belonging to the subfamily Aurantoideae of the Rutaceae family. Although there are many species, the most cultivated citrus fruits in our country are lemon, orange, tangerine and grapefruit. In the studies, it has been determined that the total phenolic substance, mineral substance and vitamin content of the peels is higher than the fruit and fruit juice. Except for the edible part of citrus fruits, it has been determined that the peels, which have 30-60% of fruit weight, contain important levels of essential oil, polysaccharide, sugar and antioxidant properties with antioxidant properties in terms of human health. Apart from the edible part of citrus fruits, the waste part, mostly consisting of peels and seeds, is used in the treatment of various diseases (diabetes, high blood pressure, etc.) among the people [22].

Citrus fruits grown in a temperate climate are mostly grown in the Mediterranean and Aegean Regions of our country, and they are also produced in the Marmara and Eastern Black Sea Regions, albeit a little. Turkey is an important producer country with a production amount of approximately 51 million tons of fresh fruit and vegetables in 2016. In general, a citrus consists of an outer shell called the exocarp, a multi-layered middle shell called the mesocarp, the fruit part and the juice vesicles located here, the core parts that can also be seeds. All these parts are given in Figure 6. [23].
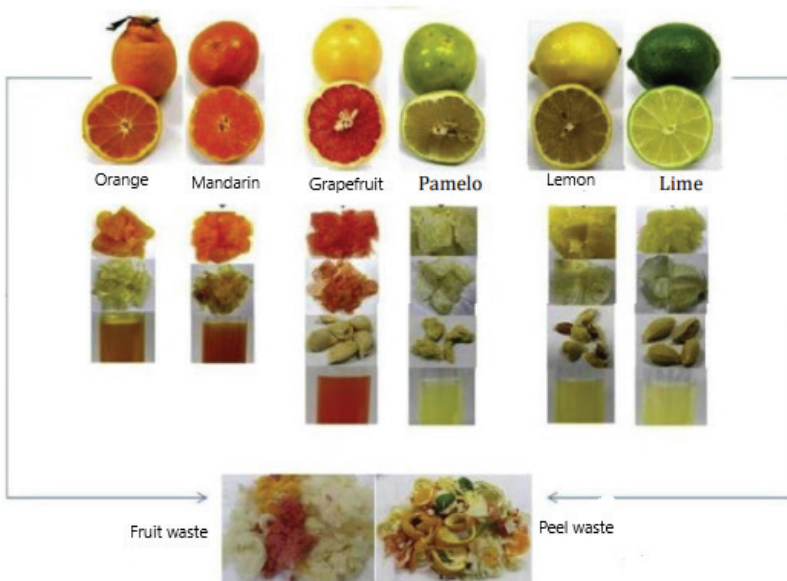
Figure 6. Parts of some citrus species [23]

## 4.1 Properties and Uses of Waste Citrus Peels

Although the peels of citrus fruits, approximately 40-50% of the citrus mass consists of peel which are widely used in the fruit product and fruit juice industries, are considered as waste, in fact, the high amount of flavonoids and carotenoid derivatives they contain makes them valuable. The most important advantages of citrus peels, which are industrial and domestic waste, are that they are economical and natural. In the food sector, these wastes can be used instead of chemical preservatives, as well as in the preparation of functional foods with positive effects on health. Citrus peels, like the edible parts of the fruit, are very rich in polyphenolic compounds, which have the ability to protect the cell against the effects of free radicals. Flavonoids and phenolic compounds are the most important and effective members of this group. When the whole fruit was examined, it was seen that the amount of phenolic acid in the peels was higher than the edible parts. Ferulic acid is the most important member of the phenolic acids found in the peels of common citrus fruits such as lemon, orange, tangerine and grapefruit [23].

Except for the edible part of the citrus fruits, the peels, which are 30-60% of the fruit weight, are not consumed raw because they have a bitter taste; It is also used in the production of marmalade, in the production of various alcoholic beverages (limocello), in various dishes in the Far East (chenpi: traditional Chinese dish), in food, beverages and confectionery as a spice, in dried cakes and milk desserts, in the production of essential oil and in medicine. It is also used in the treatment of various diseases (such as diabetes, high blood pressure) among the people. However, since it is very rich in pectin, which is a colloidal carbohydrate and makes use of its gel-forming feature, the most rational use is considered to be pectin production [24].

REFERENCES

[1] Özdemir, E.E., Görgüç, A., Gençdağ, E., Yılmaz, F.M. (2021), Principles of Spray Drying and Freeze Drying Techniques and Their Use in Powder Production from Food Wastes. The Journal of Food, 46(3), 583-607.

[2] Reynolds, C., Goucher, L., Quested, T., Bromley, S., Gillick, S., Wells, V.K., Evans, D., Koh, L., Kanyama, A.C., Katzeff, C., Svenfelt, A., Jackson, P. (2019), Review: Consumption-Stage Food Waste Reduction Interventions–What Works and How to Design Better Interventions. Food Policy, 83, 7-27.

[3] Nayak, A., Brushan, B. (2019), An Overview of the Recent Trends on The Waste Valorization Techniques for Food Wastes. Journal of Environmental Management, 233, 352-370.

[4] Arabhosseini, A., Faridi, H. (2018), Application of Eggshell Wastes as Valuable and Utilizable Products: A Review. Research in Agricultural Engineering, 64, 104-114.

[5] Laca, A., Laca, A., Diaz, M. (2017), Eggshell Waste as Catalyst: A Review. Journal of Environmental Management, 197, 351-359.

[6] Aditya, S., Stephen, J., Radhakrishnan, M. (2021), Utilization of Eggshell Waste in Calcium-Fortified Foods and Other Industrial Applications: A Review. Trends in Food Science & Technology, 115, 422-432.

[7] Waheed, M., Yousaf, M., Shehzad, A., Inam-Ur-Raheem, M., Khan, M.K.I., Khan, M.R., Ahmad, N., Abdullah, Aadil, R.M. (2020), Channelling Eggshell Waste to Valuable and Utilizable Products: A Comprehensive Review. Trends in Food Science & Technology, 106, 78-90.

[8] Yoo, S., Hsieh, J.S., Zou, P., Kokoszka, J. (2009), Utilization of Calcium Carbonate Particles from Eggshell Waste as Coating Pigments for İnk-Jet Printing Paper. Bioresource Technology, 100, 6416-6421.

[9] Gao, Y., Xu, C. (2012), Synthesis of Dimethyl Carbonate Over Waste Eggshell Catalyst. Catalysis Today, 190, 107-111.

[10] Güngör, E. (2013), Preparation of Natural Antibacterial from Egg Shell. Istanbul University, Institute of Science and Technology, Postgraduate Thesis, Istanbul.

[11] Razali, N., Musa, F.A., Jumadi, N., Jalani, A.Y. (2021), Production of Calcium Oxide From Eggshell: Study on Calcination Temperature, Raw Weight and Contact Time. RSU International Research Conference, 624-637.

[12] Omari, M.M.A., Rashid, I.S., Qinna, N.A., Jaber, A.M., Badwan, A.A. (2016), Chapter Two-Calcium Carbonate, Profiles of Drug Substances, Excipients and Related Methodology, 41, 31-132.

[13] Gürbüz, D. (2014), Controlled Synthesis of Calcium Carbonate Crystals. Yıldız Technical University, Institute of Science and Technology, Postgraduate Thesis, Istanbul.

[14] Zerek, E. (2021), Determination of Some Nutritional and Quality Properties of Egg Shell Powder Added Cookies. Istanbul Medipol University, Graduate School of Health Sciences, Istanbul.

[15] Özbay, T., Baştürk, Ö., Sungur, M.A. (2011), Physicochemical Characterization of Chitin and Chitosan Extracted from Shell Waste of Mantis Shrimp (Squilla sp.) and Blue Crab (Callinectes sapidus, Rathbun, 1896). Egirdir Faculty of Fisheries Journal, 7, 1-10.

[16] Bulut, M.O., Elibüyük, U. (2017), Production of Chitosan the Crab Chitin. Erzincan University Journal of Science and Technology, 10, 213-219.

[17] Tav, A. (2019), Production and Characterization of Chitosan with Different Methods From Shells Shrimp. Yalova University, Institute of Science and Technology, Postgraduate Thesis, Yalova.

[18] Liaqat, F. (2018), Enzymatic Synthesis of Chitooligosaccharides by Using Chitinolytic Bacillus Strains. Ege University, Institute of Science and Technology, Postgraduate Thesis, İzmir.

[19] Yıldız, P.O., Yangılar, F. (2014), The Use of Chitosan in Food Industry. Erciyes University Journal of the Institute of Science and Technology, 30, 198-206.

[20] Şahin, M., (2007), Synthesis of Chitosan Schiff Base Ligands and Investigation of Their Metal Complexes. Selcuk University, Institute of Science and Technology, Doctor of Philosophy Thesis, Konya.

[21] Çaklı, Ş., Kılınç, B. (2004), Utilization of Crustacea Processing Wastes. Ege University Journal of Fisheries & Aquatic Sciences, 21, 145-152.

[22] Güzel, M., Akpınar, Ö. (2017), Determination of Bioactive Compounds and Antioxidant Activities of Citrus Peels. Gümüşhane University Journal, 7, 153-167.

[23] Erkoç, N.T. (2021), Optimization of Extraction Method for Antioxidant Activities of Citrus Fruits by Applying Box-Behnken Experimental Design Method. Yıldız Technical University, Institute of Science and Technology, Doctor of Philosophy Thesis, Istanbul.

[24] Güzel, M., Akpınar, Ö. (2017), Comparison and Characterization of Pectins Obtained From Citrus Peels. Academic Food Journal, 15, 17-28.
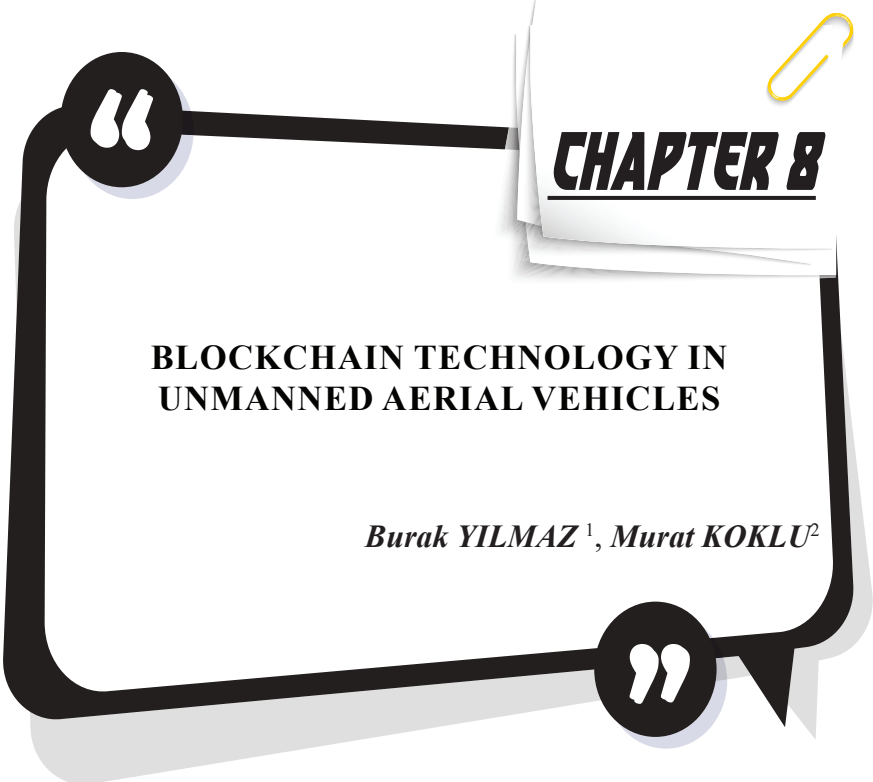
CHAPTER 8

BLOCKCHAIN TECHNOLOGY IN UNMANNED AERIAL VEHICLES

Burak YILMAZ [1], *Murat KOKLU*[2]

1   Burak YILMAZ, Selcuk University, The Graduate School of Natural and Applied Science, Computer Engineering, burak.yilmaz.064@gmail.com
ORCID ID: 0000-0002-7919-3815
2   Murat KOKLU, Selcuk University, Faculty of Technology, Computer Engineering, mkoklu@selcuk.edu.tr
ORCID ID: 0000-0002-2737-2360

1. INTRODUCTION

Unmanned Aerial Vehicle (UAV), which is at the forefront of today's technologies, is a kind of remotely controlled drone systems with advanced technological features. When the types of UAVs are examined in general terms, they are aircraft systems that are remotely controlled or carry out certain tasks without human supervision and display a flight plan with certain technologies.

Although the usage areas of UAVs vary, they are mostly used for military attack purposes today. UAVs have usage areas such as surveillance, reconnaissance, military destruction, transportation, spraying, camera shooting and fire extinguishing. These areas are continuously expanding. Because of the rapid developments of various technologies, Unmanned Aerial Vehicle Systems are also developing with technology.

Like in every military project, UAVs are systems that require intensive software and gain capabilities according to software subjects. Encryption, communication and ground station software of these systems have been studied and developed for years.

The aim of this study is to examine the sensors used in the UAVs and therefore flight management, camera surveillance, location-based monitoring and attack systems, telemetry communications and its encryption methods. As a solution to this centralized communication method and the reliability problem associated with it, blockchain technology is examined.

Unmanned Aerial Vehicles (UAVs) are accepted as key future technologies as they allow to perform repetitive and dangerous missions with virtually no human intervention or supervision. In recent years, UAVs have been actively used in areas such as remote sensing (eg mining), real-time monitoring, disaster management, border and crowd surveillance, military applications, goods delivery, precision agriculture, infrastructure inspection, media and entertainment (Tiago M. Fernández-Caramés, Blanco-Novoa, Froiz-Míguez, & Fraga-Lamas, 2019).

Studies are carried out continuously for the safety and reliability of UAVs used in many important areas. It is aimed to prevent security, transparency and reliability problems by making the encryption method and centralized communication method of UAVs using blockchain.

Thanks to the blockchain, it is aimed to make safe decisions during UAV control. Data stored on a single person reveals the possibility of error and security problems. When data storage is done on many people, safer decisions will be made. This study will reveal full transparency and other advantages to be created with blockchain in the ever-increasing usage areas of UAVs, which are used in many areas such as the defense industry, delivery, observation and discovery.

2. BLOCKCHAIN

A blockchain is a chain formed by blocks with numeric information in them. It is a distributed database system that provides encrypted transaction tracking. The infrastructure of Bitcoin and other crypto money transactions is created with blockchain technology. In money transfers, each step represents a block. These blocks are encrypted during the transfer process. Each information in the transfer steps points to a block. All of these blocks are encrypted. Blockchains are distributed to all individuals on the network, and this information is available to all individuals. The reason why the blockchain is centralized is based on this technology. The information on the blockchain can be processed by the buyer and seller (Nofer, Gomber, Hinz, & Schiereck, 2017).

Any content on the chain is known as a record. This information can be values such as money transfer customer information records. For virtual money transfers, this information indicates the money transfer. The money transfer made by a user to another user is kept as a record. New transfer requests are put in a queue. It is kept as a chain thanks to the records opened during the transaction (Nofer et al., 2017).

At certain times, records are combined and written into blocks. Issues such as how many records will be found in the block and after which transactions the records will be formed take shape as a result of the design of the blockchain. Cryptographic hash algorithms and digital signature are used to create a block (Leible, Schlager, Schubotz, & Gipp, 2019).

Blockchain, which has a wide working area, is used in many central and decentralized areas. There are formal and informal uses such as banks, governments, smart contracts, notary transactions. It is thought that the changes and transformations brought by technology can also lead to a revolutionary character (Leible et al., 2019).

Today's blockchain structure, security and reliability are also seen in important areas. Some countries have integrated the blockchain system into their voting systems. The control structure of supply chains becomes a transparent and consistent process with blockchain technology. Blockchain technology can be used in every system that needs to be trusted. Many systems under the control of people can become reliable, transparent and sensitive thanks to blockchain technology. Figure 1 shows the blockchain-based secure data collection system of the drone swarm. (Leible et al., 2019).
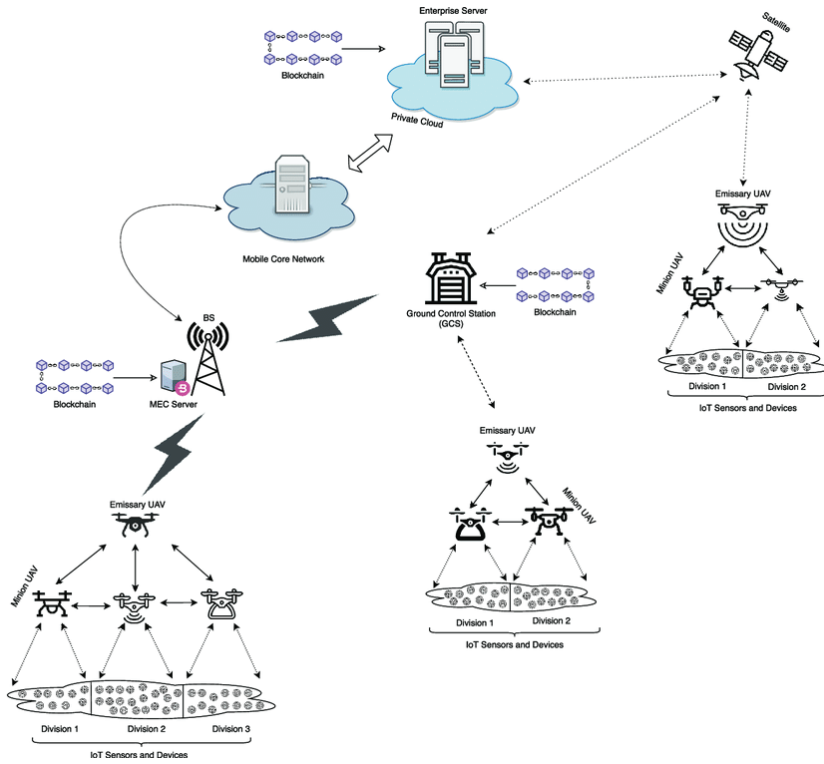
Fig 1. Blockchain-based secure data collection system of drone swarm

2.1. Blockchain Working Principles

In the blockchain, data is stored in blocks. Computers connected to the network, called miners, gather data in accordance with encryption standards during the process. These data are archived and kept in blocks. The data in each step of the operations is converted into a hash function (Pilkington, 2016).

SHA-256 encryption system is used to create hash function. Regardless of the input data length in SHA-256 encryption, it always provides 64-character output in hexadecimal number system (Günen, 2020).

Blocks and encryption information are controlled by voluntary participants (nodes) on the network. If a sufficient number of confirmations are received, the block is added to the chain. A chain occurs when blocks connected to each other with special ciphers are listed sequentially (Pilkington, 2016).

2.2. Node

Computer systems that are voluntarily connected to open blockchain networks and used to disseminate information about the transactions and the blocks created are called nodes (Günen, 2020).

Transactions such as the amount of coins produced according to the rules, the suitability of transfer signatures, and the accuracy of the data format of the blocks are carried out by nodes. Nodes working by using a peer-to-peer (P2P) protocol structure ensure the continuity of the blockchain network. Even if the data is located in a node, every computer in the network can access the data. The number of nodes on the network expresses the strength of the network (Günen, 2020).

2.3. Blockchain block structure

There are basic elements inside the blocks such as the block number, the block header, the summary of the data in the previous block function (hash) , the summary of the data in the block ciphers and information about the time (Günen, 2020).

Each block contains the hash of the previous block and takes security to the next level. Because when trying to make changes in any block, the digest password will also change and it will be incompatible with the password in the next block. Table 1 shows the block content of the block chain (Günen, 2020).

Table 1. Blockchain block content

BLOCK CHAIN BLOCK CONTENT			
Magic number		4 byte	Fixed value in the form of "0xD9C4AEF9" in 4 bytes
Height		4 byte	Block number
TITLE (HEADER)	Version	4 byte	Version used
	Previous title	32 byte	Title (hash) of previous block
	Merkle root	32 byte	Hash value of transactions (hash)
	Timestamp	4 byte	Time since January 1, 1970
	Difficulty	4 byte	Difficulty information of the network
	Nonce	4 byte	Random number adjusted for network difficulty
Number of operations		1-9 byte	Integer value of certain length (integer)
Transactions		-	List of transfers in the block

The block content in Table 1 contains a certain number of transactions. Each block is linked to the block chain by connecting to the previous block. The block at the beginning of the chain is called the genesis block. This block has no connection with another block before it (Taş & Kiani, 2018).

Block links are similar to the linked list structure. It is the reverse linked form of a linked list. A block holds the address of the previous block. The blockchain structure is a combination of blocks that are interconnected and hold each other's data. It is confirmed as a result of cryptographic and

mathematical operations performed by block miners. Confirmed blocks are added to the chain (Hamida, Brousmiche, Levard, & Thea, 2017).

The blockchain is kept in sync with end-to-end connected computers. Changes to be made are forwarded to all computers that concern the data. In this way, blockchains are not kept in a single center. It is maintained as a distributed center. Even if some computers on the network become inaccessible, operations can continue thanks to other computers on the network. Figure 2 shows the binding structure of blockchains. (Hamida et al., 2017).
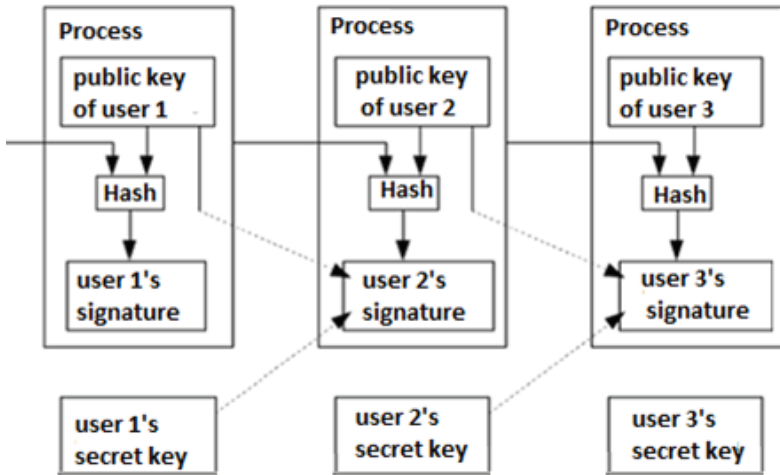
Fig 2. *Link structure of blockchains*

A block references the previous block. Thanks to this system, intervening blocks are prevented. An outlier block that will come between a block will affect other blocks that will come after it. With this effect, the chain structure will be disrupted. It is ensured that the interventions to the blockchain technology are prevented. Except for the starting block, each block also keeps the hash value of the preceding block and its own hash information. In this way, changing the blocks and the connections between the blocks is prevented (Günen, 2020).

2.4. Hash structure

Hash function is a mathematical operation that transforms the incoming data into a fixed-length output. The most important purpose of this process is to hide the data. The blockchain uses a 256-bit Cryptographic Hash known as SHA-256. The SHA-256 algorithm encrypts a data in an undecipherable way (Eastlake & Jones, 2001).

When a data is passed through the hash function, an encrypted result emerges. It is not possible to obtain the data again with this result value.

Small changes completely change the hash result (Eastlake & Jones, 2001).

When a data is passed through the hash algorithm, it always produces the same result. The block is produced as a result of mathematical operation and hash. The block generation process is called "Proof of Work". The block generation process requires high processing power and time (Oğuzhan & Kiani, 2018).

SHA (Secure Hash Algorithm); It is the name of hash algorithms developed by the US National Security Agency (Oğuzhan & Kiani, 2018).

This standard was first used with SHA-0 in 1993, and the performance of the standard was increased with SHA-1, which was developed in 1995. SHA-2 was developed in 2004 to close various security vulnerabilities detected. SHA-2 standard; It has subsets such as SHA-224, SHA-256, SHA-384 and SHA-512 (Günen, 2020).

The Bitcoin network structure uses the hash algorithm called SHA-256. The data encrypted with this algorithm provides an output of 64 characters on the hexadecimal number system without changing the data length. Hash algorithm is shown in Figure 3 (Günen, 2020).
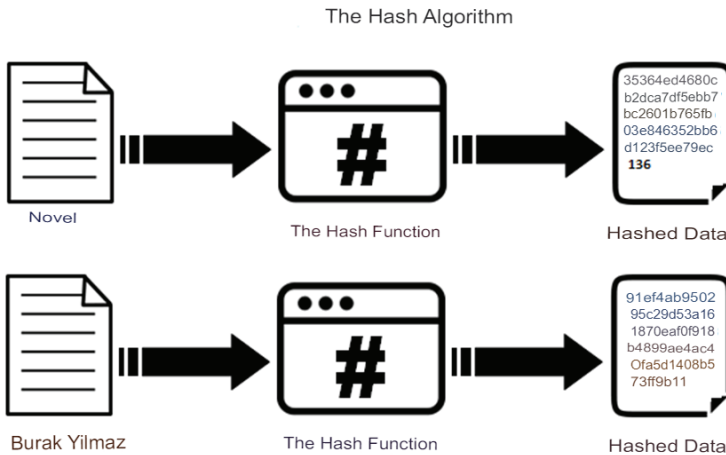
The Hash Algorithm

Fig 3. Hash algorithm

When Figure 3 is analyzed, it is expected that the "novel" and the words "Burak Yilmaz" will always output 64 characters when encrypted with the hash algorithm.

The block information, which includes the transactions between users in the Bitcoin network, is encrypted with the SHA-256 algorithm by combining the block number, nonce value and the hash code of the previous block (Günen, 2020).

2.5. Blockchain Reliability

When trying to perform two transactions at the same time, these attacks are called double-spend attacks on the blockchain side. When the same transaction is attempted at the same time, both transaction records are recorded in the Bitcoin unconfirmed transaction pool. The first transaction record is confirmed. The next block of transactions is added when verified by miners. (Zhang, Xue, & Liu, 2019).

During each transaction, transaction records are scanned. If the transaction has been done before, the miners consider this transaction as invalid. Thus the second transaction is not confirmed. It is dropped from the Bitcoin network (Lin & Liao, 2017).

If the transaction is processed simultaneously by the miners, their transactions are withdrawn from the pool at the same time. Even with the possibility of simultaneous broadcasting within the block, the blocks will be forked with the previous block. The longest chain between the two remains on the fork, and the other branch is deleted (Lin & Liao, 2017).

The most important reason why blockchain attacks were not successful before is the inability to fight against very high processing power. Once a block containing fraudulent transactions is added to the chain, this fraudulent block must be supported by other blocks in progress. For this process, half the processing power of the miners in the world is needed. In addition, new blocks must be added to the chain via the fake transaction block before other miners. It does not seem possible to reach this situation (Zhang et al., 2019).

2.6. Merkle Tree

In the concept of the Merkle Tree, which is used in cryptography and computer science, there are blocks sorted down like a pedigree. Upper blocks have the Cryptographic hash value of the blocks below them. The Merkle tree provides fast and secure verification of big data structures (Han & Richard, 2019).

Merkle Trees can be used to verify all data found between computers. The Merkle Tree contains a lot of data. It is the compression of the data contained in it into a simple character string that proves its accuracy without providing information about this data (Han & Richard, 2019) .

The tree concept is an idea often used in science. The tree concept is used for a structure containing parents(parent) and children(children). Merkle Trees are generally used as a binary tree structure. According to this structure, each node can have two subnodes before it (Karaarslan & Akbaş, 2017).

In the Merkle Tree structure, every transaction is passed through the hash function. This summary data is converted into leaf nodes. Each hash value created after this process combines with another hash value to create a new node value. This process continues until the root reaches a hash value. This root hash value constitutes the main hash value of the block. The Merkle Tree is shown in Figure 4 (Karaarslan & Akbaş, 2017).
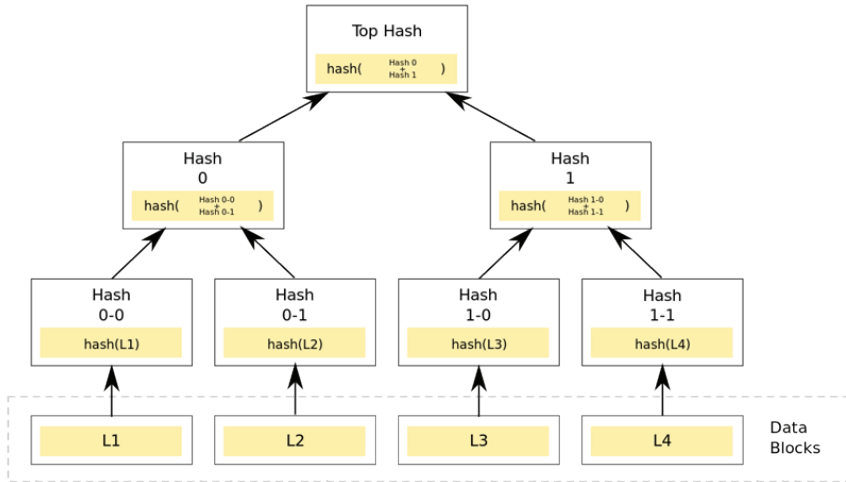

Fig 4. Merkle Tree

These processes have many advantages such as speed, security and efficiency. Verification of the data can be provided by matching each data with the Merkle Tree, and it can be verified quickly without revealing any real data. After any node value changes, the Merkle Tree will have to be recreated. Thanks to the decentralized blockchain structure, this data will be difficult to change (Han & Richard, 2019).

The speed of a network structure can be accelerated with this technology. Files to be sent after verification will be able to be verified and sent by a computer thanks to this structure. In case of inconsistency, subtrees can be requested to find and replace the defective block. This will be faster than searching the entire file for an error. At the same time, resources will be used efficiently (Han & Richard, 2019).

2.7. Using Blockchain in Unmanned Aerial Vehicles

Thanks to the digital transformations experienced, defense systems are developing technologically. Today, UAV and SİHA systems are also used for controlling areas, coordinating air attacks, supply and logistics chains (Lei, Zhang, Lou, Bai, & Xu, 2019).

Thanks to developing new technologies such as artificial intelligence, drone systems and robots, military defense systems become dependent on technology. With this developing technology, the defense systems of countries become dependent on safe, fast and accurate data (Lei et al., 2019).

Blockchain, which is a distributed system, is a prominent technology for increasing reliability in unmanned aerial vehicles. For information to be exchanged between any two nodes in a blockchain system, all nodes (or most nodes depending on the structure) must agree that the information exchange is legitimate. In this way, all transactions are approved within the open network. In order to change the data of the blockchain, most nodes in the block must be captured at the same time. This process requires a great deal of processing power. Smart contracts or decision boards, core functions are also coded into the blockchain (Adams, 2019; Tiago M Fernández-Caramés, Blanco-Novoa, Suárez-Albela, & Fraga-Lamas, 2018).

3. UAANET

Recent advances and rapid adoption in unmanned aerial vehicles (UAVs) are creating UAA ad hoc networks (UAANET), an emerging type of communication network that faces several challenges such as high mobility, heterogeneous communication protocols, security vulnerabilities, and stringent latency restrictions. The TCP/IP-based internet is an end-to-end, location-oriented communication architecture with a channel-based security model that cannot overcome these unique challenges. To support rapid content deployment and strong data security, researchers have explored the named data network (NDN), an example of the information-centric network (ICN) to build efficient, durable, and content-based secure UAANETs. In this architecture, a consumer broadcasts a packet of interest specifying the name of the requested content, and any NDN entity with matching data can return a signed data packet in the opposite direction of the path of the packet of interest. Content may be cached by intermediate routers to serve future Interests. Such a consumer-oriented access paradigm and an in-network caching technique enable fast and energy-efficient content delivery on high-mobility UAANETs (Lei et al., 2019; Saxena, 2020).

When dialing phone numbers, physical addresses are actually names. If it is desired to send a package to someone, shipping is provided to a physical address with a name attached. These names can be descriptive and hierarchical. According to the NDN process, shipping can be done to many people in the neighborhood thanks to the zip code. Names can be classified according to the hierarchical structure of the postal code without knowing the full address of these people. Examples of hierarchy can be given as an example of the concept of Named Data Networks (NDN) (Besse, Pirovano, Garcia, & Radzik, 2010).

However, the properties of NDN can cause content poisoning, which has become a significant security threat in the ICN network. In this attack, one or more malicious attackers inject fake or corrupted content into the cache of network devices to prevent or delay the retrieval of real data. Although NDN provides content-based security by verifying the signature of each data packet, it is impractical for routers to operate due to the high cost of signature verification per packet. It is complex and time consuming for routers to learn different trust model and obtain public keys (PK) for each content generating application. Therefore, toxic content can easily contaminate routers' local caches and harm the reliability and usability of NDN-based UAANETs. UAANET is shown in Figure 5 (Lei et al., 2019).
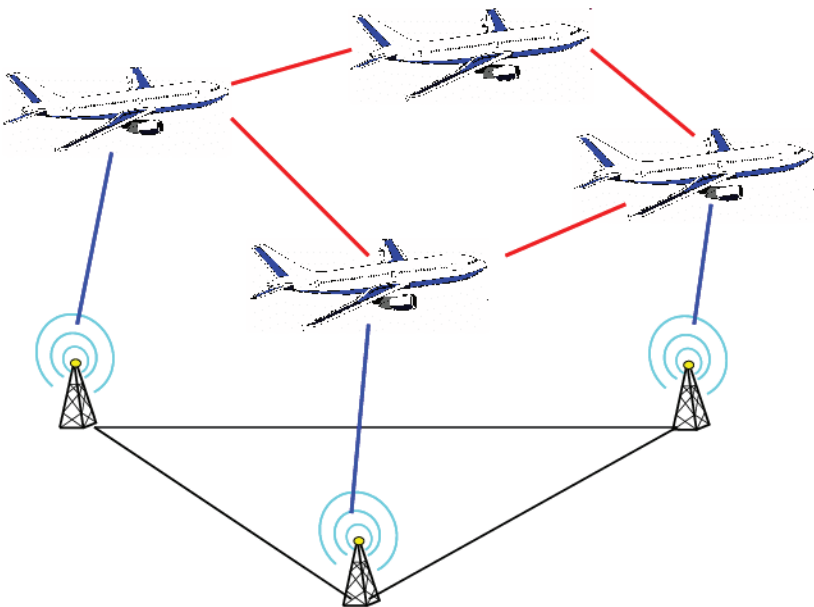
Fig 5. *UAANET*

3.1. UAANET Security Issues

Due to its structure, UAANET can be exposed to different types of threats and attacks. The purpose of the attack targeting the network consists of absorbing the network traffic, controlling it, disrupting the routing function and injecting the malicious nodes (Jean aime, Ben Mahmoud, & Larrieu, 2017).

There are several security threats to a UAV system. Substances that may cause damage to UAV systems are examined in Figure 6 (Javaid, Sun, Devabhaktuni, & Alam, 2012).
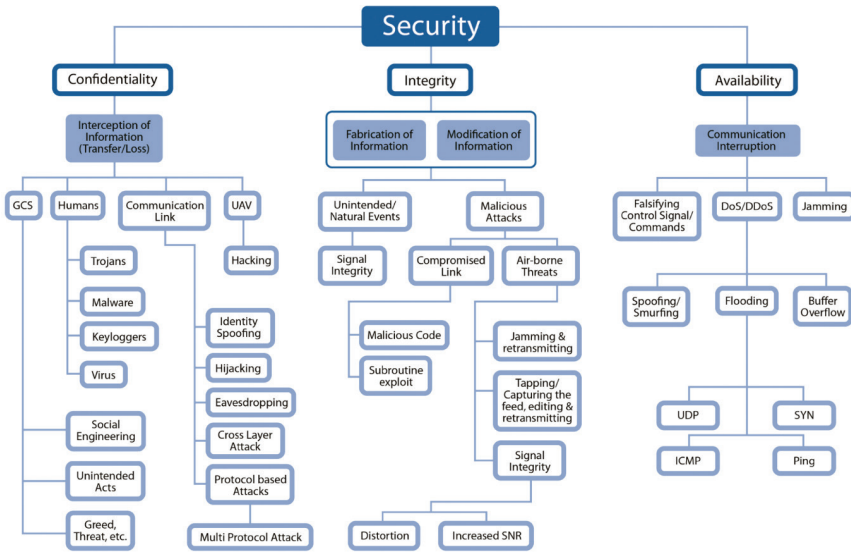
Fig 6. *UAV Security*

3.2. Black Hole Attack

The attacker is trying to announce that he has a new route to the network on the UAV. By creating fake control packets, the node is able to become part of the network path. Then, when selected as the intermediate node, the attacker invalidates the packets instead of processing them. It asks the ground control station to select the node containing the new route as the better one. The attacker can selectively forward some packets and discard others to avoid detection from their neighbors (Jean aime et al., 2017).

3.3. DOS attack

DOS attack on UAANETs allows the enemy to act as legitimate nodes in the network. The purpose of this attack is that exclude a UAV from the network by disrupting or suspending its communication with other nodes. The attacker consumes energy by constantly generating data packets and sends them to the target UAVs. For small UAVs with limited storage, DOS attack may cause other UAVs to fail to respond to the route request or to process fraudulent packets added by the attacker (Jain, Khoshelham, Zhu, & Tiwari, 2020).

There are many types of attacks on unmanned aerial vehicles. Figure 7 shows the types of attacks on unmanned aerial vehicles (Altawy & Youssef, 2016).
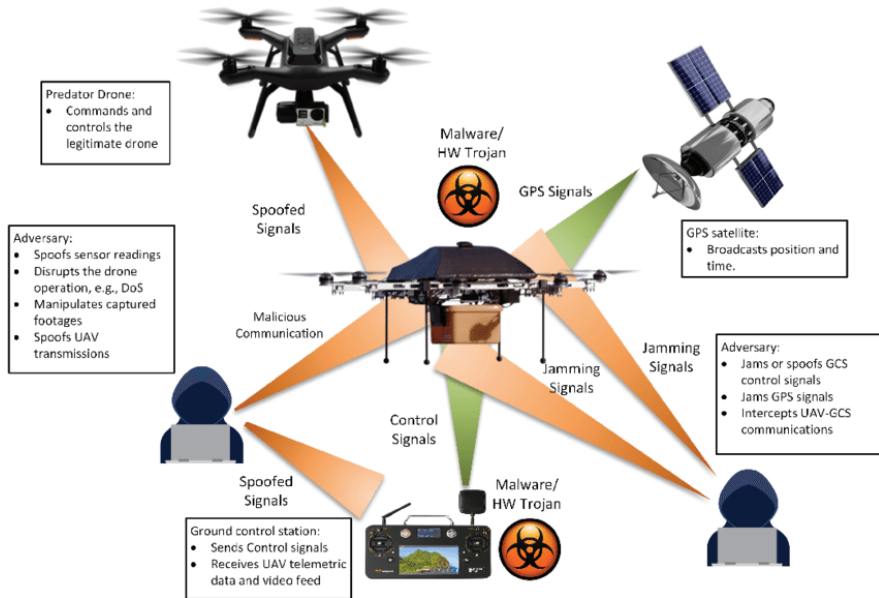
Fig 7. *UAV Security Attack*

3.4. Wormhole attack

Wormhole attack has attack structure similar to black hole attack. A wormhole attack requires at least two attackers. Two or more attackers form a private network. On this network, they do not deliver the packages that come to them to the place where they need to be sent but send them between each other over the network they have established. Packets that need to be transmitted cannot be forwarded, they will circulate on the network formed between the attackers and will be dropped (Mintemur, 2016) .

Wormhole Attack can be given as an example of attacks on the UAV. Wormhole Attack is shown in Figure 8 (Maxa, Ben Mahmoud, & Larrieu, 2015).
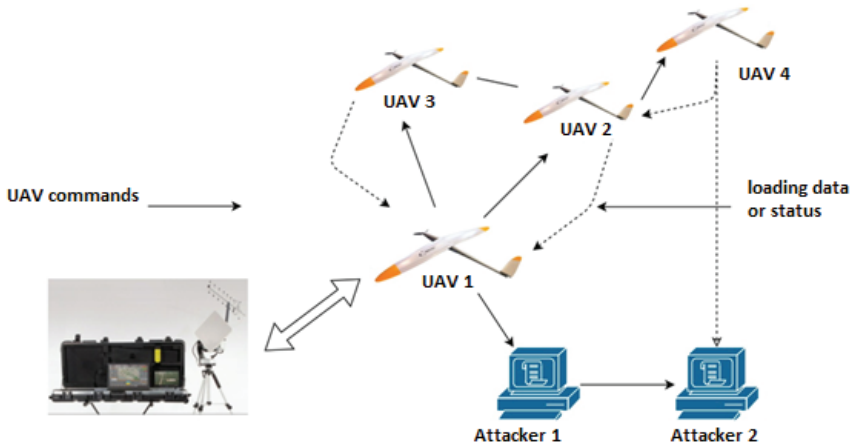
Fig 8. *Wormhole Attack*

3.5. Sybil attack

It can be used to disable all connections to a UAV or a series of UAVs. The attacker can try to send more than one control packet using different identities. In this attack, the attacker can pretend to be more than one node (Jain et al., 2020).

An identity is generated for each UAV that enters the system, and UAVs connected to the network have only one identity. In a spoofing attack, the attacking tool also accesses the identities of other vehicles. It can send messages to the network by collecting the identities of other vehicles. It can use random IDs or the ID of another node to create confusion in the routing process (Mintemur, 2016) .

3.6. Byzantine attack

In a Byzantine attack, a compromised intermediate node or a set of compromised intermediate nodes perform attacks such as creating routing loops, forwarding packets via non-optimal paths, or selectively dropping packets. The attacking node can send the information it receives to a different location or destroy it. These actions cause interruption or disruption of routing services (Rai, 2010).

4. CONCLUSION and DISCUSSION

4.1. UAANET Security Issues Solution

Integrating blockchain technology into the UAANET structure aims to prevent hacker attacks by distributing content to a large number of nodes. Blockchain significantly reduces the possibility of data being modified by unauthorized persons. The attacks will be invalidated unless

more than half of the nodes on the network are changed at the same time with the blockchain, which will be preferred to protect the data. To destroy or disrupt a blockchain, a hacker would have to destroy the data stored in each UAV on the network, having a copy of some or all of each data. It will be difficult for the hacker to shut down the entire network at once (Jain et al., 2020; Mehta, Gupta, & Tanwar, 2020).

4.2. Weapon Defense Systems

Figure 9 provides an example of how the command and control system works. On the system, the UAV receives a data from the sensor. Threats are reported to system authorities over this data. Commands are sent by the system authorities to respond to the threat attack on the UAV. The centralized nature of the system used makes it easier to suffer an external attack, which is the disadvantage of its centralized nature. Thanks to the centralized system, it is easier for authorities or UAV to receive deceptive information. This command may cause unauthorized use of the UAV system (Adams, 2019).
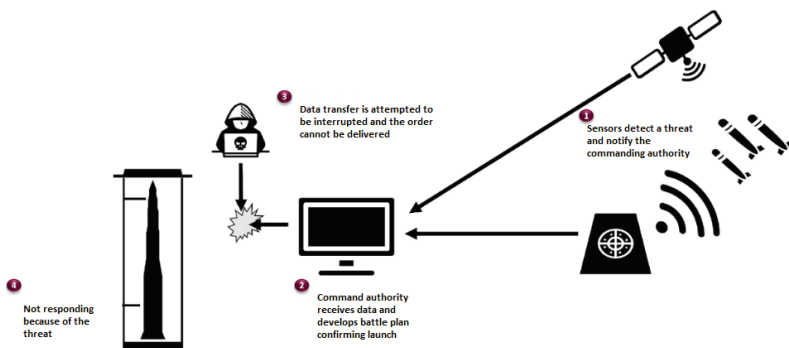

Fig. 9. Interference with weapon defense systems

This system can be made more secure by using the blockchain. When Figure 10 is examined, data communication as a result of incoming data describes the use of a distributed system to verify the source of the data. All or most nodes on the network must be approved for the transaction to be valid. Since the nodes are independent of each other and the nodes have their own encryption method, significant processing power will be needed to attack the system. As the number of nodes increases, the reliability of the system increases. Increasing the number of nodes will increase the processing power required to verify communications during the system's decision needs (Adams, 2019).
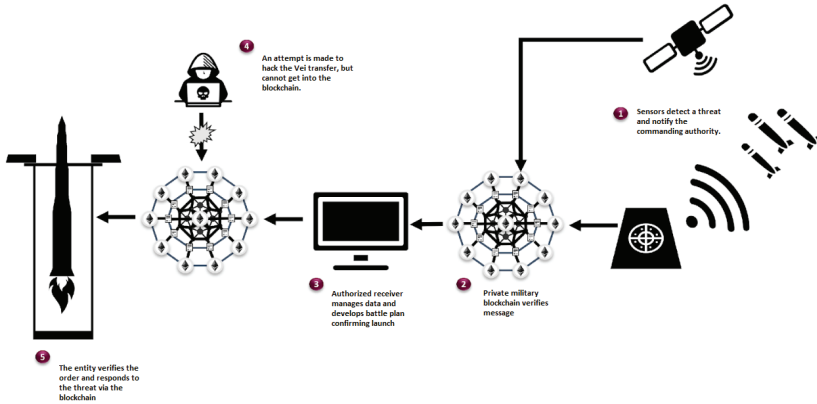
Fig. 10. *Blockchain-based decentralized control of the critical weapon system*

4.3. Swarm UAV and Blockchain

Swarm robotics is the combination of mostly physically simple robots, which is formed by the coordination of many robots, to form a system. As a result of the interaction of robots with each other or with environmental factors, a collective behavior emerges. This behavior is modeled after artificial herd intelligence and herd behaviors. The concept of swarm robotics has emerged as a result of examining the behavior of insects, ants and other factors in nature. In the military field, multiple Drones or robots function in parallel to destroy an opponent's defenses and destroy the target (Adams, 2019).

The dependencies of the members of the herd on communication and interaction make the system less secure against attacks on the network. The need for coordinated communication between each element in the swarm reveals the security vulnerabilities of the swarm UAV system. Blockchain herd defense is shown in Figure 11 (Adams, 2019).
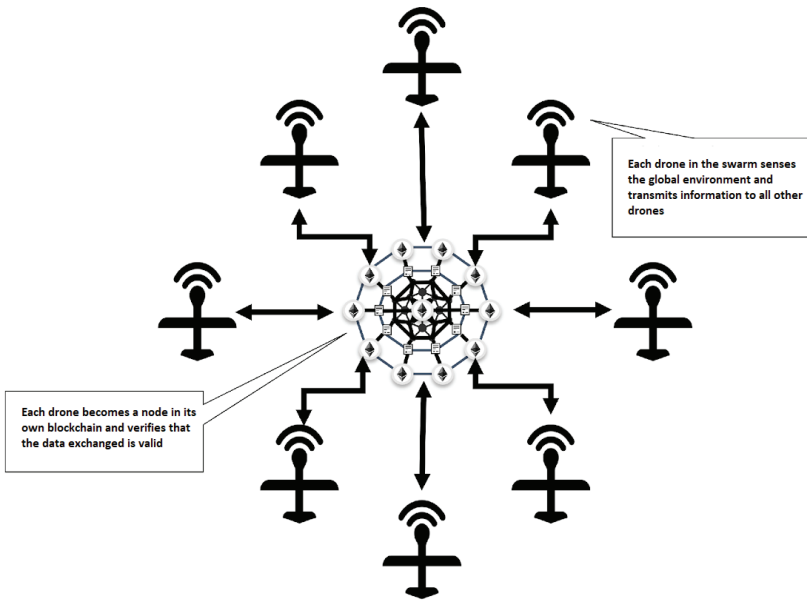
**Fig. 11.** *Blockchain Swarm Defense*

Thanks to the blockchain, communication and coordination within the herd will be maintained. Blockchain provides a mechanism that can maintain communication and coordination within the herd. In a system, each element of the swarm becomes a node within their own blockchain. The swarm will be able to verify the communication within itself. It will use a collective, decentralized decision-making approach to manage its operation and disseminate information. Thus, the herd will be able to share necessary information while protecting itself from cyber-attacks (Adams, 2019).

5. REFERENCES

Adams, V. (2019). Why Military Blockchain is Critical in the Age of Cyber Warfare. https://media.consensys.net/why-military-blockchain-is-critical-in-the-age-of-cyber-warfare-93bea90be7619.

Altawy, R., & Youssef, A. M. (2016). Security, Privacy, and Safety Aspects of Civilian Drones: A Survey. *ACM Trans. Cyber-Phys. Syst., 1*(2), Article 7. doi:10.1145/3001836

Besse, F., Pirovano, A., Garcia, F., & Radzik, J. (2010). Aeronautical ad hoc networks: A new Datalink for ATM. *Proceedings of the 9th Innovative Research Workshop and Exhibition, INO 2010*.

Eastlake, D., & Jones, P. (2001). US secure hash algorithm 1 (SHA1): RFC 3174, September.

Fernández-Caramés, T. M., Blanco-Novoa, O., Froiz-Míguez, I., & Fraga-Lamas, P. (2019). Towards an Autonomous Industry 4.0 Warehouse: A UAV and Blockchain-Based System for Inventory and Traceability Applications in Big Data-Driven Supply Chain Management. *Sensors, 19*(10), 2394.

Fernández-Caramés, T. M., Blanco-Novoa, O., Suárez-Albela, M., & Fraga-Lamas, P. (2018). *A UAV and blockchain-based system for industry 4.0 inventory and traceability applications.* Paper presented at the Multidisciplinary Digital Publishing Institute Proceedings.

Günen, E. (2020). En Sade Anlatımla Blockchain Nedir, Nasıl Çalışır?

Hamida, E. B., Brousmiche, K. L., Levard, H., & Thea, E. (2017). *Blockchain for enterprise: overview, opportunities and challenges.* Paper presented at the The Thirteenth International Conference on Wireless and Mobile Communications (ICWMC 2017).

Han, E. S., & Richard, M., Annie. (2019). Merkle Tree. *Journal of Chemical Information and Modeling, 53*, 1689-1699.

Jain, K., Khoshelham, K., Zhu, X., & Tiwari, A. (2020). *Proceedings of UASG 2019 Unmanned Aerial System in Geomatics: Unmanned Aerial System in Geomatics*.

Javaid, A. Y., Sun, W., Devabhaktuni, V. K., & Alam, M. (2012). Cyber security threat analysis and modeling of an unmanned aerial vehicle system. *2012 IEEE Conference on Technologies for Homeland Security (HST)*, 585-590.

Jean aime, M., Ben Mahmoud, M. S., & Larrieu, N. (2017). Survey on UAANET Routing Protocols and Network Security Challenges. *Ad-Hoc and Sensor Wireless Networks, 37*.

Karaarslan, E., & Akbaş, M. F. (2017). blokzinciri tabanli siber güvenlik sistemleri. *Uluslararası Bilgi Güvenliği Mühendisliği Dergisi, 3*(2), 16-21.

Lei, K., Zhang, Q., Lou, J., Bai, B., & Xu, K. (2019). Securing ICN-based UAV ad hoc networks with blockchain. *IEEE Communications Magazine, 57*(6), 26-32.

Leible, S., Schlager, S., Schubotz, M., & Gipp, B. (2019). A Review on Blockchain Technology and Blockchain Projects Fostering Open Science. *Frontiers in Blockchain, 2*. doi:10.3389/fbloc.2019.00016

Lin, I.-C., & Liao, T.-C. (2017). A survey of blockchain security issues and challenges. *IJ Network Security, 19*(5), 653-659.

Maxa, J. A., Ben Mahmoud, M. S., & Larrieu, N. (2015). Secure routing protocol design for UAV ad hoc networks. *AIAA/IEEE Digital Avionics Systems Conference - Proceedings*: Institute of Electrical and Electronics Engineers Inc.

Mehta, P., Gupta, R., & Tanwar, S. (2020). Blockchain envisioned UAV networks: Challenges, solutions, and comparisons. *Computer Communications, 151*, 518-538.

Mintemur, Ö. (2016). *ARAÇSAL TASARSIZ AĞLARDA SALDIRILARIN ANALİZİ*.

Nofer, M., Gomber, P., Hinz, O., & Schiereck, D. (2017). Blockchain. *Business & Information Systems Engineering, 59*(3), 183-187.

Oğuzhan, T., & Kiani, F. (2018). Blok zinciri teknolojisine yapılan saldırılar üzerine bir inceleme. *Bilişim Teknolojileri Dergisi, 11*(4), 369-382.

Pilkington, M. (2016). Blockchain technology: principles and applications *Research handbook on digital transformations*: Edward Elgar Publishing.

Rai, R. (2010). Different Types of Attacks on Integrated MANET-Internet Communication. *International Journal of Computer Science and Security, 4*.

Saxena, S. (2020). BLOCKCHAIN & UAV: SECURITY, CHALLENGES AND RESEARCH ISSUES.

Taş, O., & Kiani, F. (2018). Blok Zinciri Teknolojisine Yapılan Saldırılar Üzerine bir İnceleme. *Bilişim Teknolojileri Dergisi*. doi:10.17671/gazibtd.451695

Zhang, R., Xue, R., & Liu, L. (2019). Security and privacy on blockchain. *ACM Computing Surveys (CSUR), 52*(3), 1-34.
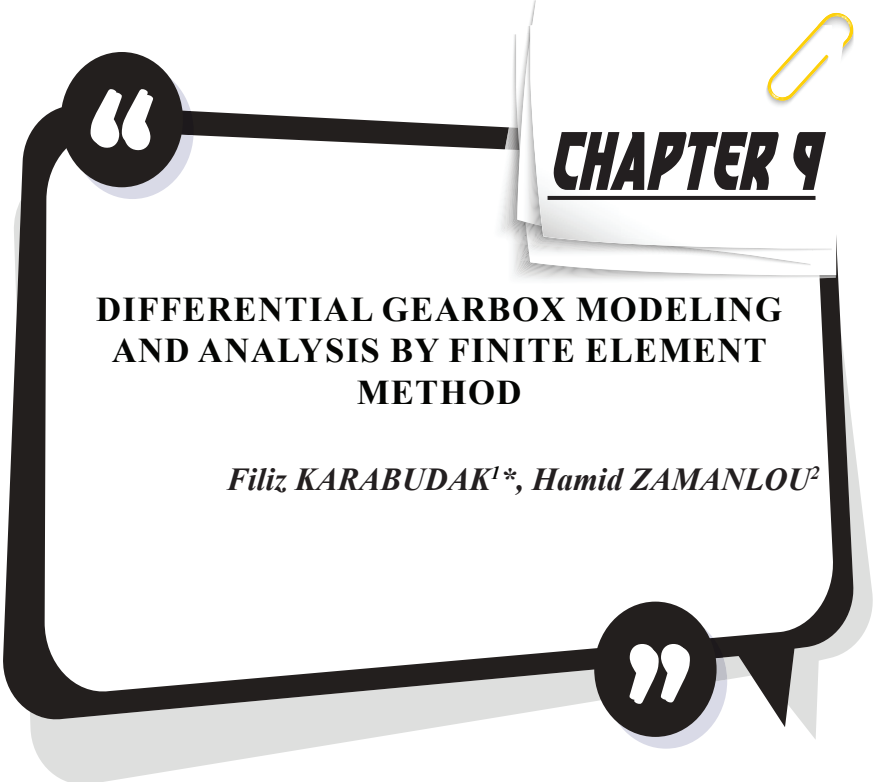
DIFFERENTIAL GEARBOX MODELING AND ANALYSIS BY FINITE ELEMENT METHOD

Filiz KARABUDAK[1]*, Hamid ZAMANLOU[2]

1 Gümüşhane University, Faculty of Engineering and Natural Sciences, Department of Machine Engineering, Gümüşhane, filizkarabudak@gumushane.edu.tr, ORCID ID:0000-0002-7365-0333
2 Atatürk University, Faculty of Engineering, Department of Machine Engineering, Erzurum, zamanloohamid@gmail.com, ORCID ID:0000-0002-7365-0333

1.INTRODUCTION

The differential is one of the basic transmission systems in the rapidly developing automotive industry in today's world. The differential system, which was invented in its most basic form by the French inventor Onésiphore Pecqueur in 1827, is one of the basic needs of the industry. The classic automotive differential, which was first used in steam powered cars, has become one of the most basic needs of the automotive industry with the development of the internal combustion engine since the end of the 19th century (Patil & Pise, 2013).

The wheels of the vehicle moving on the straight road rotate at the same speed since the distance covered in unit time is equal. However, while the vehicle is cornering, the outer wheels rotate faster than the inner wheels. For this reason, the outer wheels must travel longer than the inner wheels in order for the vehicle to make the expected turn. However, if the wheels are cornering at the same speed, there is no difference in distance and the wheels can spin at certain rates. If this happens, the vehicle may not turn the corner as expected. Failure of the vehicle to turn the corner successfully has the potential to shorten the tire life, to cause negative consequences such as the vehicle overturning and an accident. The need for a mechanism that will eliminate the movement differences experienced in cornering and turns has led to the design of the mechanism called differential gearbox (Veeranjaneyulu & Hari Babu, 2012).

One of the important issues about the differential is where it is in the vehicle. Because many drivers do not know the location of this very important part of the vehicle. Although the position of the differential differs according to the vehicle types, it is located in the transmission box on the front axle in front wheel drive vehicles. In rear wheel drive vehicles, it is located in the middle of the rear axle. Four-wheel drive vehicles, which have been preferred by many vehicle users in recent years, have three different differentials: front, rear and transmission shaft, unlike the others (Sill & Ayalew, 2013).

2. STRUCTURE AND OPERATING PRINCIPLE OF DIFFERENTIAL GEARBOX

The engine propels the vehicle by producing a certain amount of power. But for this to happen, it must be transmitted from the front to the rear or from the four-wheel drive wheels. The purpose of the differential, which is a drivetrain used for this purpose, is to deliver the propeller shaft torque to the axles and drive wheels. In the image below, the gear parts of the differential are shown (Figure1)
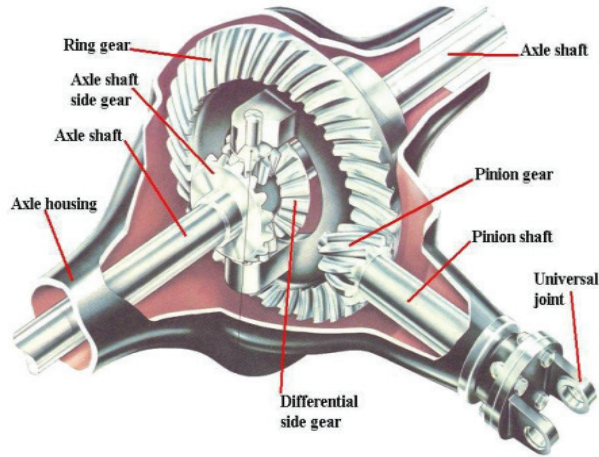
Figure 1. Parts of the Differential Gearbox *(Singh, Kumar, kumar dewangan, kumar sen, & kumar bohidar, 2014)*

The movement transmitted by the drive shaft to the rear axle goes to the differential on the rear axle via the pinion. The conical bevel gear changes the angle of rotation along the vehicle axis by 90 degrees and transmits it to the rear axle. The bevel gear, which is another bevel gear, is always intertwined with the pinion. The ring gear is larger in diameter and number of teeth than the pinion. Therefore, the torque from the transmission is increased and transmitted to the rear axle. The pinion is mounted in the bracket housing of the differential gearbox. The bevel gear is attached to the differential gearbox with bolts or rivets. The case is in this form and when the pinion turns the sun gear, the case rotates with it (Kazar, Asal, Soyhan, & Demirtaş, 2016).

The differential gearbox and rear axles are in the rear bridge. The two sleeves of the rear bridge extending from the middle to the sides and serving as a cover for the axles are called axle sleeves. The ends of the axles connecting to the wheels are flanged. There are bevel axle gears at the ends inside the differential gearbox, which are located on the inside. These bevel axle gears are milled to the axles. Therefore, when the gears rotate, the axles rotate as well. However, while the box is rotating, the axle gears do not rotate with the box. Other conditions are necessary for this rotation to occur. Another gear in the differential gearbox is the cross gears. These two or four gears are resting on a fork called a cross. The cross, on the other hand, is inserted into the box and is bedded in such a way that it can rotate with the box (Mori & Shibata, 2003).

As the vehicle turns a corner, the wheels form different angles from each other. As the front and rear axles cover the radius of the bend, there

are revolutions between the wheels. At this point, the task of the differential is to equalize the speed differences and bring them to the same ratio. Bevel gears are generally used to balance the wheels. The differential box creates power flow during forward and reverse motion, and turns the bevel, bevel and cross gears together, and from there, the power transmission is carried to the axle shafts via the axle shaft gears. The revolution difference created by the moving wheels, on the other hand, is balanced with the rotational movement of the cross gears around their own axis. A locking mechanism is placed in the differential to increase the axle handling ratio (Saravanakumar, Sampathkumar, & Rajendrakumar, 2018).

The differential has three main functions:

1. To transmit the movement from the shaft to the wheels. Here the circular motion is rotated 90 degrees. The axes of rotation of the shaft and the wheel are perpendicular to each other in vehicles with rear-wheel drive with the engine positioned in the front. Therefore, the movement of the shaft must reach the wheels with a 90 degree change of direction. The first task of the differential is to ensure that the mentioned direction change is completed (Yavuz & Özek , 2020).

2. One of the important points for the vehicle is to turn the corner safely. The differential is a part that performs this task, and it ensures that the inner wheels turn less and the outer wheels turn more during the bend, thus ensuring a safe turn. During cornering, the wheels rotate on certain circles. However, the outer wheel rotates on a larger circle than the inner wheel. Two wheels spinning at the same speed can have some consequences. For example, the wheels may drag for more than one meter, wear may occur on the wheels, or there may be a decrease in the safety of the vehicle and person as a result of the difficulty of vehicle control (Yavuz & Özek, 2020) (Alirezaei, Kanarachos, Scheepers, & Maurice, 2013).

3. It reduces the speed and creates a torque increase, making the gearbox smaller and reducing the amount of torque transmitted by the shaft (Bono & Kryger, 2007).

As can be seen in the items explained above, the differential is a mechanism that enables many tasks to be done in the vehicle and helps the vehicle to run smoothly. From this point of view, if the vehicles did not have a differential, many problems could occur in the vehicle and serious safety problems could arise.

In this study, a 3D solid model of the differential gearbox, whose design calculations were made, was created in Solidworks 2020 software and analyzed with the Finite Element method in ANSYS Workbench 2020 R1 software.

3. DIFFERENTIAL BOX DESIGN, MODELING AND ANALYSIS

3.1. Calculations

The calculations required for the design are given below (Nıemann, 1960).

Dg : 170 mm,   Dp :90mm, Zg :18,   Zp :15,   Ng :3500 rpm ɳ=0,98
P:82 kW ve N:110 It is determined as Hp (Horsepower).

Module account m:

- D = Dg + Dp = 170 + 90 = 260mm
- T = Zg + Zp = 18 + 15 = 33
- Module: m = D/T

m = 260/33 = 7,88 ≈ 8 (according to the standards)

Torque calculation on the axle gear, Md:

$$Md = \frac{9554 * P * ɳ}{Ng} = \frac{9554 * 82 * 10^3 * 0,98}{3500} = 223,8 \text{ N.m}$$

Calculation of the rotational speed of the pinion gear:

- VxR = Zg/Zp = Dg/Dp = Np/Ng

Dg/Dp = 1,88 çıkar.

1,88 = Np/3500 = Np =6580 rpm

$$Mp = \frac{9554 * P * ɳ}{Np} = \frac{9554 * 82 * 10^3 * 0,98}{6580} = 116,8 \text{ N.m}$$

- $\theta_{p_1} = \tan^{-1}\left(\frac{1}{VxR}\right)$

  $\tan^{-1}\left(\frac{1}{1,88}\right) = 28,0129°$

- $\theta_{p_2} = 90° - 28,0129° = 61,987°$
- Gear calculation for pinion, Zep:

$$Zep \times \sec\theta_{p_1} = 15 \times \sec 28,0129 = 16,991$$

- Gear calculation for main gear, Zeg:

$$Zeg \times \sec\theta_{p_2} = 18 \times \sec 61,987 = 38,325$$

Interval cone distance (AO):

$$AO = (((D_1/2)x2) + ((D_2/2)x2)) \times \frac{1}{2})$$

AO = 92,7

Face Width (b):

- $b = \frac{AO}{3} = \frac{92,7}{3} = 30,9$

Shaft diameter calculation d:

$$d = \sqrt[3]{\frac{32Me}{\pi\sigma em}} = \sqrt[3]{\frac{32*223.8}{3.14*228}} = 2.15 \text{ cm} = 21,5\text{mm} \approx 24$$

3.2. Design

The differential box was designed in line with the calculations and the assembly model was obtained by drawing solid models of all parts with appropriate design dimensions using the Solidworks 2020 program (Figure 1,2,3,4,5,6)
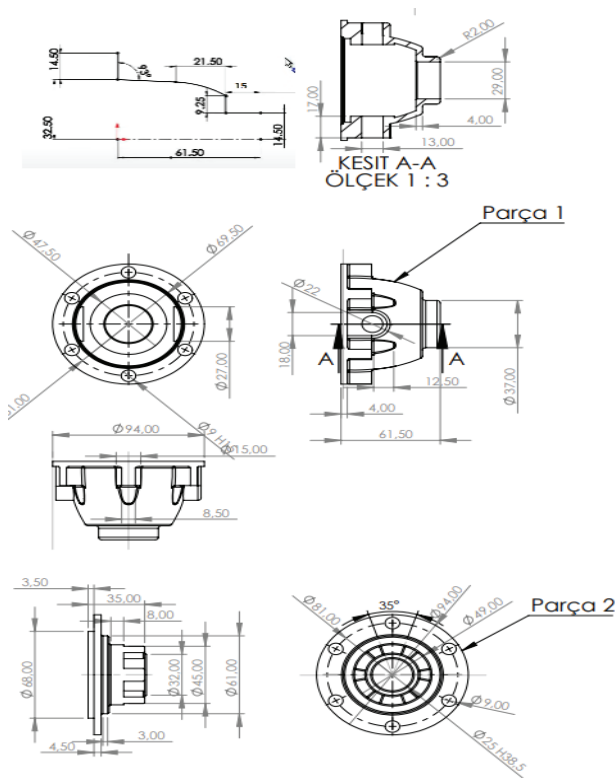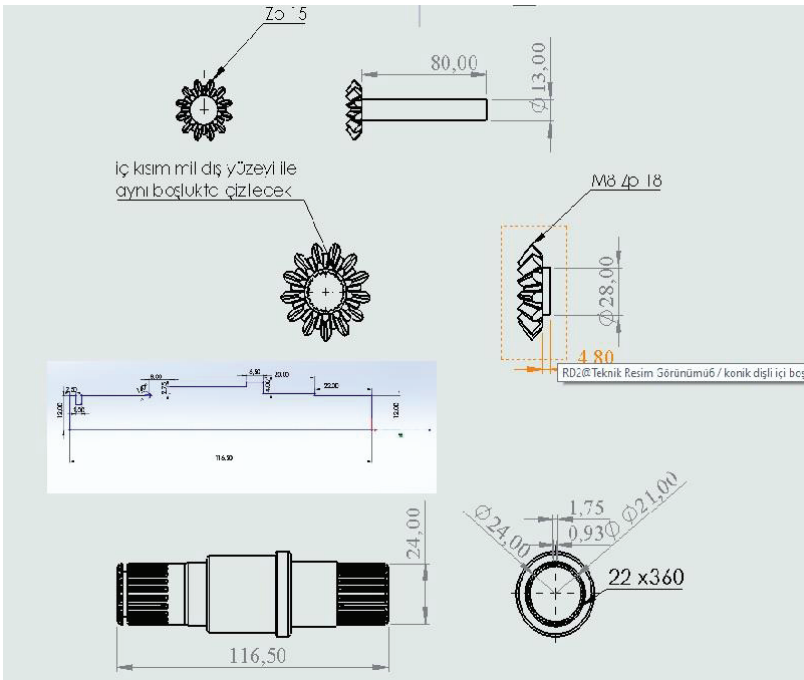

Figure 2 *Dimensioning of the Drawing*

Figure 3 Dimensioning the Drawing (continued)

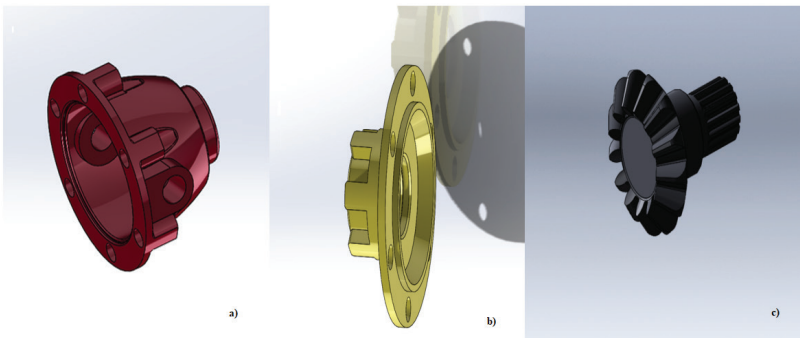## 3.3. Modelling

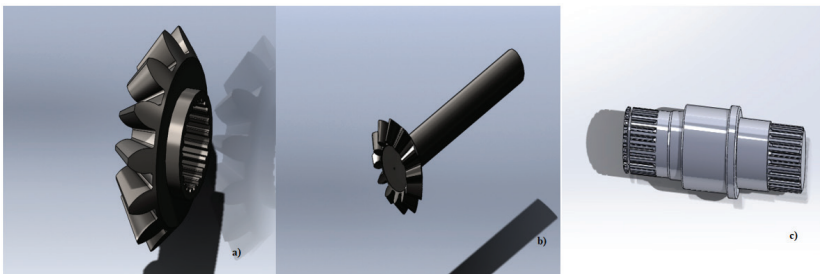*Figure 4* a,b)Differential Box Main Body Parts c)Bevel gear

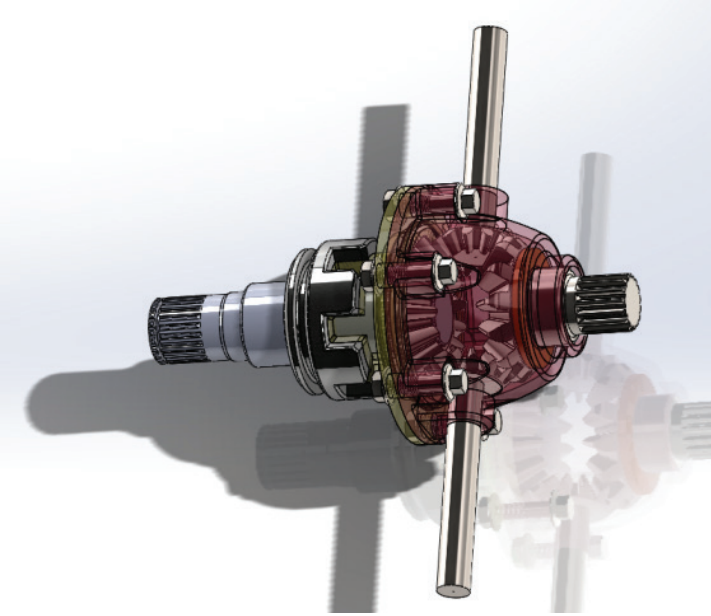*Figure 5* a) Hollow bevel gear b) Pinion gear c) Shaft

Figure 6 Assembly Picture

3.4. Analysis

The friction parts will affect the system as losses. The purpose of the design is to minimize this effect. Gray cast iron, Aluminum (Pio, 2011) and Magnesium alloys are preferred for transmission and differential box parts in automobiles. Aluminum alloy or Magnesium alloy is preferred due to its lightness, since transmission in automobiles has a significant weight for light commercial vehicles.

This study consists of two stages: modeling and finite element analysis. Modelling; While it consists of design and solid modeling steps, a comparison is made between 2 different materials in the finite element analysis.

The mechanical properties of Aluminum Alloy (356.0-T6) and Magnesium alloy (AZ91) materials used in our study are given in Table

Tablo 1 Aluminum Alloy 356.0-T6 (Kammer, 2018) (George, Totten, MacKenzie, & Dekker, 2003) and Magnesium alloys' AZ91 (Mert, Özdemir, & Karataş, 2010) Mechanical Properties

Property (356.0-T6)	Value	Units	Property (AZ91)	Value	Units
Elasticity Module	72400	N/mm^2	Elasticity Module	45000	N/mm^2
Poisson Ratio	0.33	-	Poisson Ratio	0.35	-
Tensile Strength	227.5	N/mm^2	Tensile Strength	250	N/mm^2
Yield Strength	165	N/mm^2	Yield Strength	160	N/mm^2
Hardness (HB)	70	-	Hardness (HB)	70	-
% Elongation	8.9	-	% Elongation	7	-

In Figure 7, the Finite Element mesh model of the differential box prepared using 174917 element number and 315608 node points is seen. While establishing the finite element analysis geometric model, the connection contact points in the solid model were determined as 'No Separation' and 'bonded'.

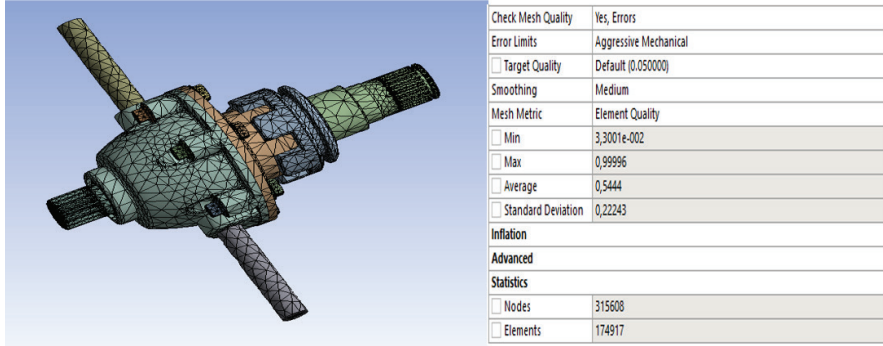| Check Mesh Quality	Yes, Errors
Error Limits	Aggressive Mechanical
Target Quality	Default (0.050000)
Smoothing	Medium
Mesh Metric	Element Quality
Min	3,3001e-002
Max	0,99996
Average	0,5444
Standard Deviation	0,22243
Inflation	
Advanced	
Statistics	
Nodes	315608
Elements	174917

Figure 7 Finite Element Model of Differential Box

A differential gearbox in an automobile is a collection of gears. It is designed to divide the speed of the wheel under turning conditions and is based on the Torque variation. The speed of the input shaft is the highest, and the speed of the output shaft is the lowest, resulting in a higher torque value. The resulting torque is largely transferred to the drive shaft.

The boundary conditions (Fixed Support, Moment) of the differential box that transmits the motor torque from the bevel gear to the planetary gears via the cross shaft are given in Figure 8. The moment of 223.8 N.m applied to point B and the moment of 116.6 N.m applied to points C,D, were calculated above.
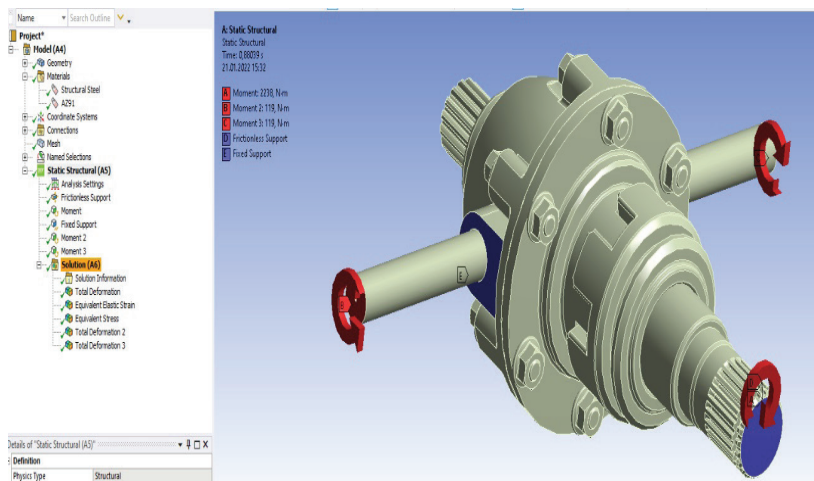

Figure 8 *Torques in the differential box*

4. CONCLUSIONS

After entering the necessary data for the static structural analysis, 356.0 T6 and AZ91 materials were assigned and the Total Deformation, Equivalent Elastic Strain and Equivalent Stress analyzes were solved separately for both materials, and maximum analysis results were given in the parts forming the differential box (Figure 9,10,11,12, Fig. 13,14,15,16).

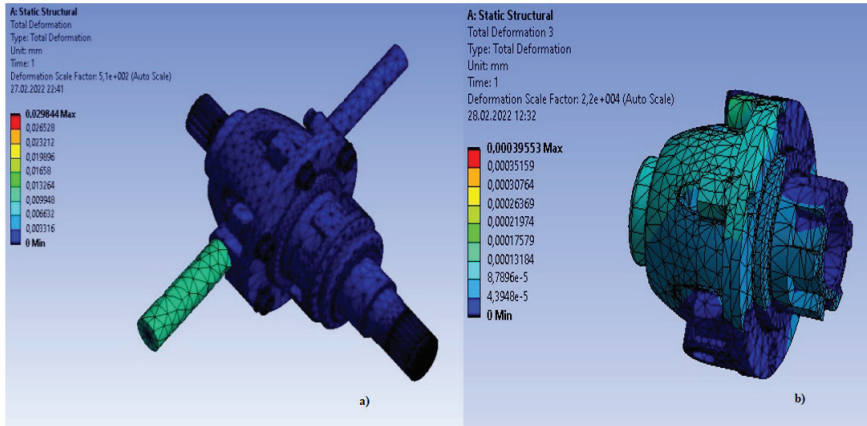** Deformation Analysis Results for AZ91 Magnesium Alloy:*

Figure 9 *Total deformation a) Assembly and b) Main body*

Figure 10 a) *Equivalent Stress Analysis b) Equivalent Elastic Strain*

Figure 11 *Deformation a) axle shaft b) axle shaft section*

Figure 12 *Deformation axle gear*

A356-T6 Aluminum Casting Alloy Deformation Analysis Results:
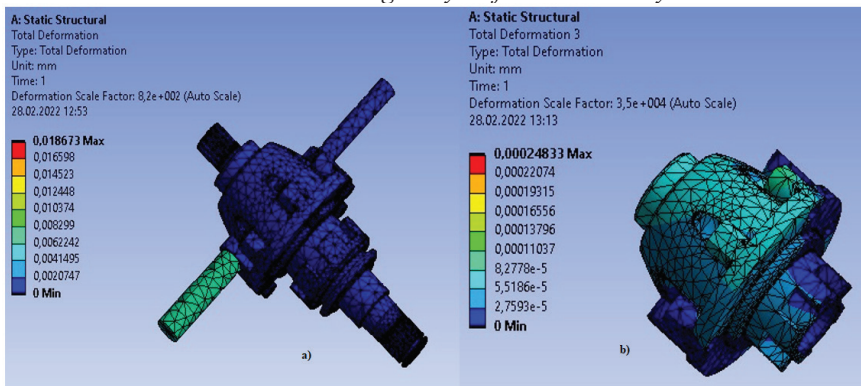
Figure 13 *Total deformation a) Assembly and b) Main body*
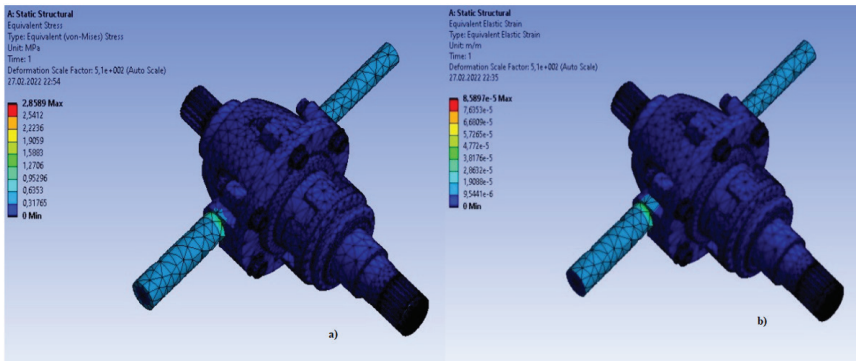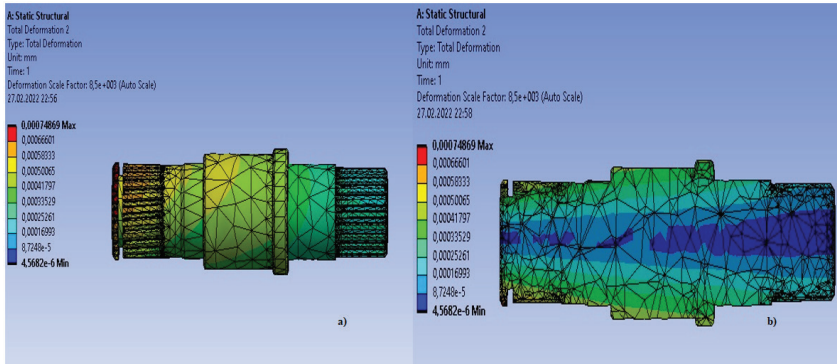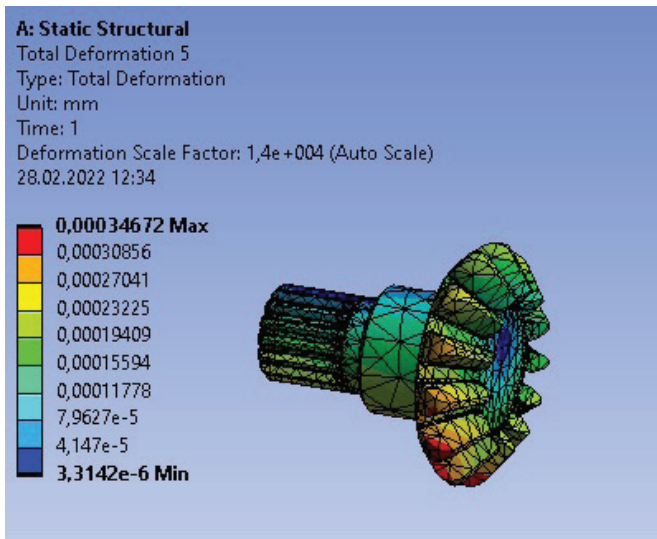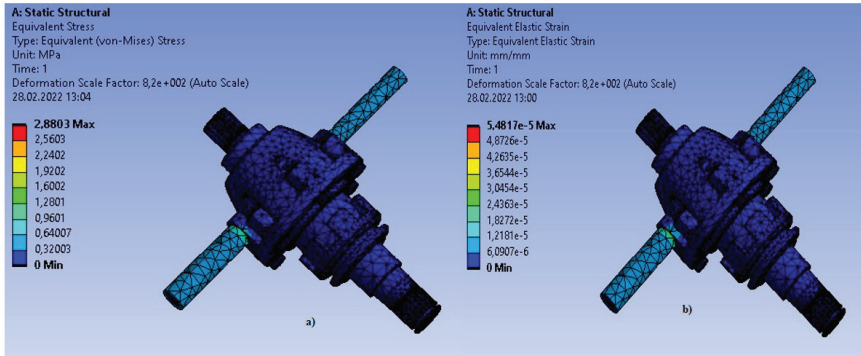
Figure 14 *a) Equivalent Stress Analysis b) Equivalent Elastic Strain*
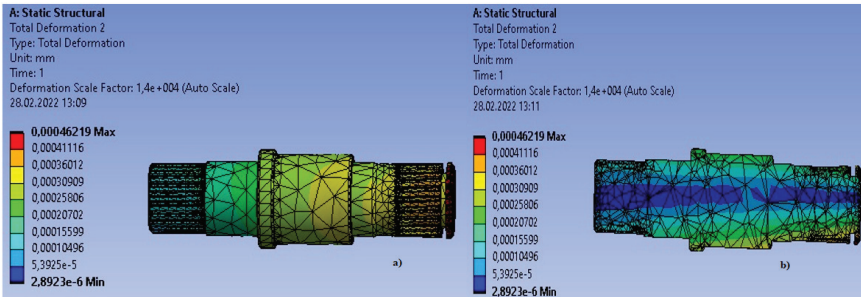
Figure 15 *Deformation a) axle shaft b) axle shaft section*
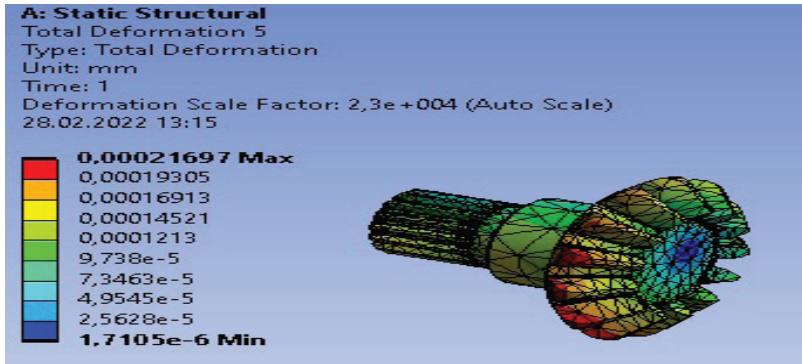
Figure 16 *Deformation axle gear*

In this study, a comparative static structural analysis was carried out using Aluminum (A356 T6) and Magnesium (AZ91) alloys in the differential box, which was designed and modeled. Max. Equivalent Stress value 2.8589 MPa, Total Deformation 0.029844 mm and max. Equivalent Elastic Strain is determined to be $8,598*e^{-5}$ mm/mm. A356-T6 Al alloy max. Equivalent Stress value 2.8803 MPa, Total Deformation 0.018673 mm and max. Equivalent Elastic Strain is calculated as $5.4817*e^{-5}$ mm/mm.

5. RESULTS

Considering the analysis results, the results of Al alloy and Mg alloy were close to each other. Magnesium alloy (1.74 g/cm3 density) is approximately 30% lighter by volume than aluminum (it is the lightest structurally used metal in the world) and has a greater strength-to-weight ratio. In today's conditions, since lightness and cost reduction are aimed in passenger cars, production with magnesium alloy has started to increase with the development of technology. Magnesium alloy is a very suitable production type for economic vehicles, that is, for vehicles that do not operate in extreme conditions. Many vehicle differentials and engine blocks are produced from magnesium alloy. It is a suitable alloy type both to be cheap and to minimize fuel consumption.

References

Alirezaei, M., Kanarachos, S., Scheepers, B., & Maurice, J. (2013). Experimental Evaluation of Optimal Vehicle Dynamic Control based on the State Dependent Riccati Equation Technique. Proceeding of the American Control Conference (s. 408-412). Washington: (ACC).

Bono, G., & Kryger, J. (2007). Auto Technology Teory and Service. Delmar Publishers Inc.

George, E., Totten, D., MacKenzie, S., & Dekker, M. (2003). Handbook of Aluminum (Cilt 1). içinde Physical Metallurgy and Processes.

Kammer, C. (2018). Handbook of Materials Data-Aluminum and Aluminum Alloys. içinde Springer.

Kazar, T., Asal, C., Soyhan, H., & Demirtaş, V. (2016). Design of a Differential Gear Box For The Backhoe Loaders. Journal of FCE – Scientific Paper, 4, 72-73.

Mert, F., Özdemir, A., & Karataş, Ç. (2010). A Moldability Evaluation of Magnesium Alloys in The High Pressure Die Casting Method. Journal of Polytechnic, 13(3), 165-176.

Mori, K., & Shibata, Y. (2003). Optimum Design of Hypoid Gear Dimension and Tooth Surface. JOURNAL OF PASSENGER CAR: MECHANICAL SYSTEMS, 112(6), 802-809.

Nıemann, G. (1960). Makine Elemanları (Cilt 3). Güven kitapevi.

Patil, S., & Pise, S. (2013). Modal and Stress Analysis of Differential Gearbox Casing with Optimization. Int. Journal of Engineering Research and Application, 3(6), 188-193.

Pio, L. (2011). Effect of T6 Heat Treatment on the Mechanical Properties of Gravity Die Cast A356 Aluminium Alloy. Journal of Applied Sciences, 2048-2052.

Saravanakumar, R., Sampathkumar, S., & Rajendrakumar, S. (2018). Automatic Differential Locking System. International Journal of Scientific Research and Review, 7(10), 240-247.

Sill, J., & Ayalew, B. (2013). A Saturation Balancing Control Method for Enhancing Dynamic Vehicle. İnternational Journal of Vehicle Design, 61, 1-27. doi:10.1504/IJVD.2013.050839

Singh, C., Kumar, L., kumar dewangan, B., kumar sen, P., & kumar bohidar, S. (2014). A Study on Vehicle Differential System. International Journal of scientific research and management (IJSRM), 2(11), 1680-1683.

Veeranjaneyulu, C., & Hari Babu, U. (2012). Design And Structural Analysis Of Differential Gear Box At Different Loads. International Journal of Advanced Engineering Research and Studies, 1(2), 65-69.

Yavuz , İ., & Özek , A. (2020). Effect Of Friction Coefficient Of Different Curve Diameters On Wheel Speeds For Electronic Differential. Afyon Kocatepe University Journal of Science and Engineering, 20, (1138-1146.

Yavuz, İ., & Özek, A. (2020). Effect Of Friction Coefficient Of Different Curve Diameters On Wheel Speeds For Electronic Differential. Afyon Kocatepe University Journal of Science and Engineering, 20, (1138-1146.

CHAPTER 10

MICROWAVE ACTED MICRO SLURRY GRINDING - VERTICAL BALL MILL GRINDING OF ŞIRNAK FLY ASH AND SLAG WASTE /WOOD CHAR/ ASPHALTITE CHAR FOR CEMENT PRODUCTION

Yıldırım İsmail TOSUN[1], Fethullah CHICHEK[2]

1   Şırnak University, Engineering Faculty, Mining Engineering Department, Şırnak, 73000, Turkey   yildirimismailtosun@gmail.com
2 Azerbaijan National Academy of Science, Radiation Institute, Baku, Azerbaijan fcicek66@gmail.com

1. Introduction

Fly ash, clinker and puzzolonic additives as coal ash are consumed in cement production among various wastes under natural concerns [1]. The quality of cement using fly ash needs sufficient grinding and less energy consumption in grinding techniques. By the high yield ash and slag production, the coal power plants with the stockpiles field exceeding 600 million tons per annum in the world are dissociated or disposed to land in forest areas dumping wastes during construction debris output. In Southeast Anatolian Region, Şırnak coal power electricity production located need the evaluation of high amount of fly ash at 200 thousand tons (2). The microwave acted grinding of coal ash reduces the cost of coal and clinker and additives grinding, produces high quality cement production. The use of microwave action in long time period grinding plant managed much coal shale breakage and higher desulfurization in coal preparation plant [2-3]. The coal shale and marl were treated by microwave oven with moisture as sand size in the compact texture resulted out developing of internal stresses in porous coal provided the much selective thermal crack formation, and followed by desulfurization under 10mm size(2).

Cement technology includes the crushing-grinding, autogenous or semi autogenous tube grinding units following a very fine 90 micron and 40 micron grinding is performed [4]. The vertical mill design of the fine grinding and ultrafine grinding plant, grinder selection is important for the energy reduction and grinding costs[5-6].
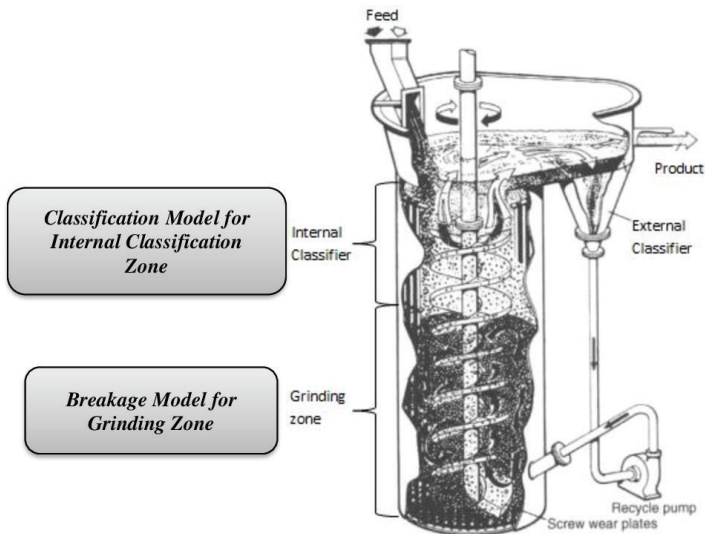

Figure 1. *The vertical ball mill model [5-6]*

Fly ash and wood char, coal char have the soft rock hardness. However, coal slag, marl, steel slag, and limestone are needed to excessive grinding prior to addition to cement. If the microwave did not act over fly ash of Şırnak asphaltite, slag and shale silicate grains would be difficult to grind. the varied ultrafine grinding methods are given in below Table 1. [5-17]

Table 1. Common vertical slurry and air fluidized flow mills and their main features [5-6]

Type	Name	Speed ,m/s	Media Type	Media Size, mm	Feed, mm	Product,μm	Material
Gravity Mill Low Speed	Vertimill	3	Steel Balls Cylpebs	5-38	6	15-75	Metalic Ore, Gold ore
	Tower mill						Industrial minerals ,coals, cement
Fluidized Mill High Speed	Isa mill	21-23	Ceramic Beads Sands	2-3.5	0,15	7	Gold ore
	Stirred Media Detritors	11	Ceramic Balls Sands Silica Pebbles	1-3	0,25	10	Ultrafine metaliferrous ore
	VXP Milll	10-12	Zirconium	1,5-3	0,3-0,4	10	Base metal ore, ındustrial minerals
	HIG Mill		Ceramic Beads Steel Balls	1-6	0,3-0,07	100-20	Base metal ore

Unit energy consumption for their production is calculated and compared. The grindability differences of raw materials, the amount of energy consumed in cement production is revealed by experimental and industrial tests.(7-14) has been put. It was observed that the easiest to grind was clay stone and the hardest to be clinker. HGI and Industrial-

scale cement production with materials that are easy to grind as a result of bond tests when desired, using truss, limestone and marble residue as a substitute for clinker, which is difficult to grind. The grinding energy needs of the blended cements produced are less than that of lightweight concrete cement. It has been confirmed that they can be milled more easily.

Microwave energy radiate waves under 300 MHz to 3 GHz even super high frequency (SHF: 3 GHz and 30 GHz and extremely high frequency EHF 30 GHz to 300 GHz. The microwaves penetrated the inner of the sample is encapsulated through halogenic wave. The electromagnetic energy increases the temperature of whole volume, as not happen in conventional heating (12-13).

In the vertical slurry mill the breakage energy need is decreasing with decrease of grinding size as seen in Figure 2 in comparison to ball mill.[7]
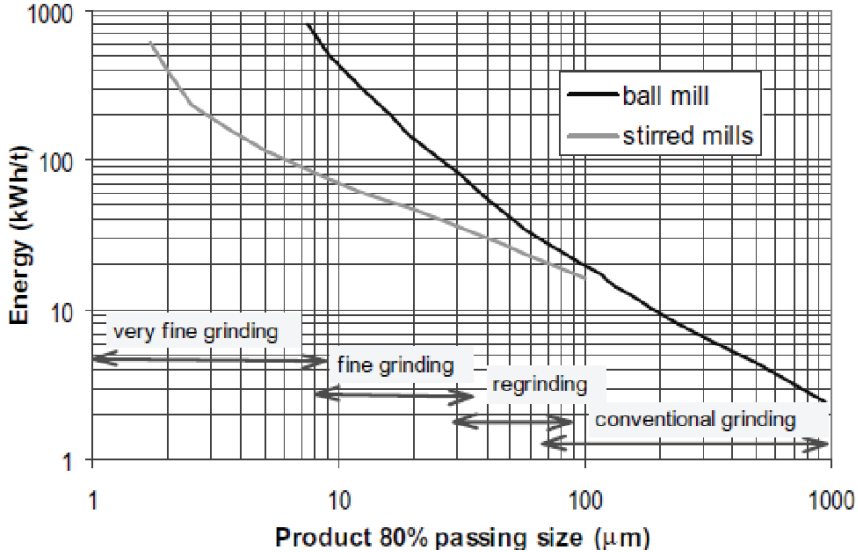
Figure 2. The micronized grinding size change vs energy limits in ball milling models [5-6]

Breakage Theory

Breakage energy and type for every mineral is greatly affected by hardness of material and texture . The hard materials in char and slag are generally low weight percent stay on a certain sieve as a result of metamorphism or alteration they are ground to the delicacy described as residue. Fly ash and slag grindability also varies. Before starting the grinding process at a specific to the type of cement to be produced and the amounts of the raw materials homogenization must be well managed

with tests for cement quality. All clinker production processes is carried over calcination furnace requiring higher a surface area that depends on the fineness on standards. (13-19).

Gates-Gaudin- Schuman particle size distribution reformed the Charles size reduction energy equation(8)

$$dE(x) = -C\frac{dx}{x^n} \tag{1}$$

$$E = \int_0^y \int_{x_0}^x (-C\frac{dx}{x^n})dP \tag{2}$$

$$dP = \alpha w \frac{x^{n-1}}{y^n}dx \tag{3}$$

$$\frac{d^2P(x,t)}{dtdx} = \int_{y=x}^{x_{max}} S(y)_f \frac{dB(x,y)}{dx}\frac{dP(x,y)}{dy}dy - S(x)\frac{dP(x,t)^f}{dx} \tag{4}$$

$$\text{Grinding Index} = W\frac{dP(x,y)}{dt} = W\int_{y=x_f}^{x_{max}} S(y)_f\ B(x_f,y)_f\ \frac{dP(y,t)^f}{dy}\ dy \tag{5}$$

with constant size range $$\frac{dW_{if}}{dt} = -Sw(t)_f + \sum_{i=1}^j S_i\,b_{ji}W_i(t) \tag{6}$$

$$\frac{dW_{if}}{dt} = -Sw(t)_f \tag{7}$$

for coarse size feed the grinding energy for i size fraction

$$W(t) = w(0)_i e^{-S_i t} \tag{8}$$

sample particle size reduction with breakage rate parameters of and ϕ, β, γ

$$B(x,y) = \phi(\frac{x}{y})^\gamma + (1-\phi)\left(\frac{x}{y}\right)^\beta \tag{9}$$

Mill sizes to be selected in the cement industry Clinker is also a result of a cement production process. above the guaranteed performance of the rotary kiln It is a manufactured product. Some factories clinker potential production the amount of will realize limestone to produce, some marble waste, some in the way ration are being. Many cement factories use marl or even low-siliceous marl for clinker. The grinding capacity is changed by many different parameters of mill and types of grinding medium and limestone hardness, including high siliceous marl. In addition to the clinker produced within the quality standards use hard raw materials such as bauxite, corundum or iron scrape (2-4), gypsum and other slag or pozzolan. Many plants need hard silica taking into account as the additives. Autogenous mill work and grindability at lower size limits developes some certain grinding facilities.

The grindability properties of the raw material to be ground affect the grinder machine preferences as a result of their variable product size

and shape and the type of milling system. easily ground rocks is wished in cement industry. However, it comes out certain difficulty to grind, while reducing energy costs (24), increases by silica matter. Silicate module grinding represents a clinker silicate ground. Silicate grinding in cement technology is more difficult than soft limestone rocks with low modulus.

Cement industry may use the largest fly ash output in the world about 38% of coal fly ash, even blast furnace slag. The breakage energy just consumed at 3,5% rate of grinding in ball milling as consumed energy. Simulation and model for ball optimization is greatly needed. The grinding aid by surfactants or dispersants makes easy grinding on raw materials in cement production. The optimization studies of grinding method and grinding elements (balls) and changing process conditions for each material do need adaptation.

2. MATERIALS AND METHODS

In addition to these, many new assessment in the cement industry of purchased marble waste (including travertine) and two clinker samples from different facilities. Hardgrove and Bond work indexes were calculated. Then, all the main raw materials and auxiliary industrial scale is using light weight raw materials, additives light weight cement from milled raw material mixtures and 35, 45 and 90 µm of blended cement samples. Their ultra fine rate and ultra fine grinding ability has been compared. The limestone and fly ash samples of two different plants 35 and 45 minutes 90 µm sieve by grinding during the analysis tests were carried out.

2.1. The Standard Bond Grindability Test

The studied materials such as coal asphaltite coal shale and regional limestones are ground under 45 mikron and fineness matter of under 20 micron considered as grindabilty as bond grinding and the results compared with the values of standard test of grinding under 100 micro size. The modified 10 mm diameter ball mill used for micronized grinding specific work input (kWh/t) in order to reduce the fineness under 20 micron material from feed size of 106 micron size and 80% passing 106 micron. The comparison made between the values of standard Bond mill results for 106 micron grinding in 30 cm diameter Bond mill, in that is used with 20 kg grinding steel ball media but over 70 weight % finer ball content (5-10)

2.2. Hardgrove Index Method

By using the standard Hardgrove Index method the materials under 0,6 mm ground two times longer than the standard revolution. For a comparative study,modified HGI values determined for 106 micron sized

feed ground under 75 μm 20 micron size fractions was determined and weight balance determination drawn on the chart Hardgrove Grindability lines and modified chart line by comparison standard index values determined and calibrated before(29-30).

2.3. Microwave Treatment

The representative ground samples under 106 micron size pressed by 20kg weight rolled under loading machine to 10 mm thick paste in order to increase microwave radiation effect over the paste feeds. 10 minutes radiated sample pastes are subjected to following grinding tests for fine grinding and ultra fine grinding. Microwave improved the inner atomic plane vibration resulting high heat and interfacial cracks were seen [20-30]. In this grinding experiments, microwave radiated samples such as below 90 micron feed of limestone, Şırnak asphaltite coal and shale samples are ground under 45μm to 20μm and the effect of microwave radiation on ultra grinding ability are determined by passing weight amount rate. The material composition is given in Table 2. The proximate analysis of Turkish coals and Şırnak asphaltite is given in Table 3.

Table 2. The chemical composition of Şırnak fly ash, limestone and shale in Şırnak Province

Oxide %	Şırnak Fly Ash	Şırnak Marl	Şırnak Shale
SiO_2	21	24,14	48,53
Al_2O_3	7,88	12,61	24,61
Fe_2O_3	11,23	7,34	7,59
CaO	21,34	29,18	9,48
MgO	3,41	4,68	3,28
K_2O	1,25	3,32	2,51
Na_2O	2,25	1,11	0,35
Ign.Loss	11,6	21,43	3,09
SO_3	3,55	0,20	0,32

Table 3, Chemical composition of Wood char, Şırnak Asphaltite Char and Lignite samples used in experiments.

Carbons	Fixed Carb,%	Volatile Mat.%	Ash,%	Total S,%	Calor.Value ,kcal/kg
Oak Wood Char	54.5	45.6	0.5	.2	3207
Şırnak Asphaltite Char	40.2	45.5	7.4	6.7	7820
Soma Lignite	62.8	5.5	14.1	2.0	4820

The effect of the 10 min. microwave radiation keeping on samples prior to ultra grinding is tested after the thermal radiation breakage and compared with the original as illustrated in Figure 3.

2.4. Particle size analysis

Using sieve standard √2 series Tyler sequenced size fraction contents for grinding materials is determined regarding Gaudin approach. Gaudin size plot with log distribution of soft materials at ultra fine size distribution regressed much suitable for evaluation grinding energy of whole materials.[31-38] Regarding Figure 3, it is determined that distribution factor over 0,7 provided a fineness content of this study was over 10-15 % in the shale and fly ash soft materials.
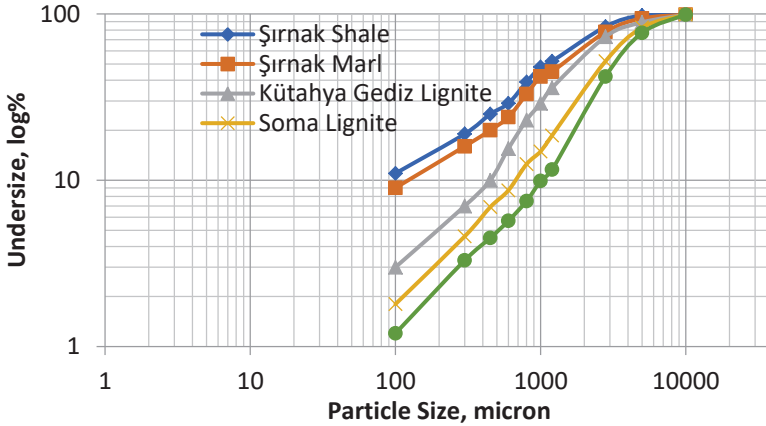

Figure 3. Şırnak Asphaltite, marl and shale samples of Gaudin Schumann Particle Size Distribution.

2.5. Breakage Rate, Standard and HG Bond Work Index Test

106 μm ground soft studied materials were tested following finer grinding tests using the longer milling time and the amount 45 and 20 micron ultra grinding rate is determined as weight of 20 micron below weight rate percent of each specimen following the microwave interaction in the grinding equipment.(Figure 4)

The ultra grinding ability characteristics to 20 micron and 45 micron of the microwave treated samples were compared and defined in Table 4.

HGI standard test device was used in order to determine the weight of under 20 μm after 1min. grinding, so HGI and modified HGI values are determined in the amount and scale (Table 4).

2.6.Experimental Grinding Tests as Standard

In this study, vertical slurry milling on Şırnak asphaltite char, fly ash and wood char ball mill grindability tests is made. The vertical milling tests are made for 120, 480 minutes on fly ash, wood char and asphaltite char samples, The fineness values below 20 micron of the clinkers were investigated for breakage below 45 micron at the end of the grinding

period. Different coals with 106 micron sized at 50 gr weight are grinded to 74 μm in the identical mills belonging to the facilities. 45 μm and 20 μm ground yields are determined, Different types of coals ground in micronized industrial mills such as laboratory vertical micro slurry mill used in the experiments is illustrated below.

Figure 4. *Vertical slurry mill for experimentation*

Table 4, *The Bond Work Index, HGI Grindability values of Samples.*

Material	Wi (Kwh/t)	HGI	Modified HGI	Density (g/cm³)	Porosity %	Water Absorption, %
Şırnak Asphaltite	7.1	87	56	1.63	0,4	0,2
Soma Coal	7,7	63	45	1,65	15,1	8,6
Şırnak Fly Ash	8.7	47	22	2.64	2,7	1,9
Şırnak Shale	6.6	65	45	2.41	4,6	3,5
Oak wood Char	5,1	76	56	1,2	56,5	22,4

3. RESULTS AND DISCUSSION

3.1. Interaction of Microwave Radiation on Breakage

Coal samples were soft as compared to medium soft limestone in Şırnak asphaltite quarries the grinding under to fraction of 45 and 20 micron size from a feed size of 106 with 10 minutes microwave radiation periods were resulted highest effect on coal shale samples (Figure 5). Due to semimetalic pyrite content of 9%, microwave radiated grinding rate values increased at about 12% to 32% for Turkish lignites and 34% for Şırnak asphaltite(Figure 6) below 45 micron.
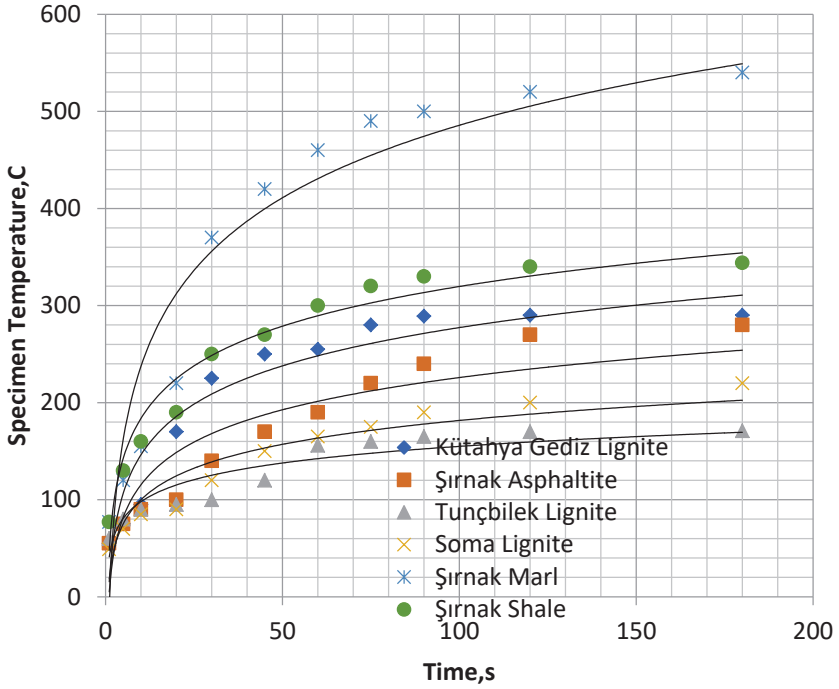
Figure 5. *The microwave radiated pellet temperature changes of grinding materials prior to finer grinding to under 20 micron*
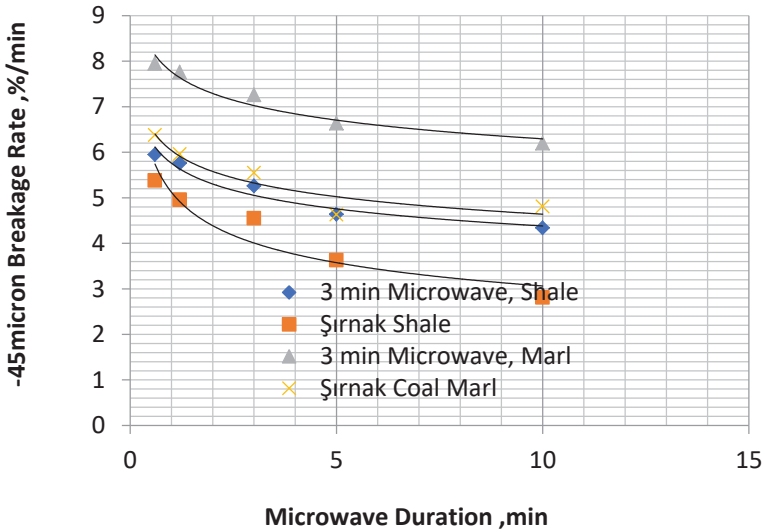
Figure 6. *The breakage rate of Şırnak quarry shale 45□m under Microwave Interaction*

HGI index of studied materials is given in Table 4 over microwave radiation treatment. Under 45μm and 5 micron grinding change over HGI (Figure7) and Bond mill values is illustrated in Figure 8-9.
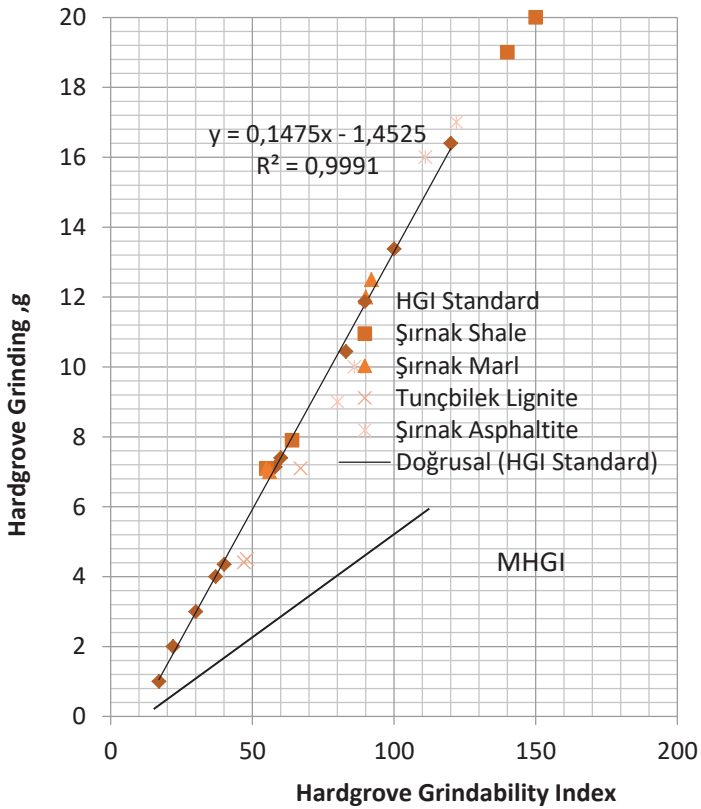
Figure 7. *HGI Chart and Modified HGI at 10 min Microwave radiated materials studied.*

Figure 8. The Bij Breakage rate change for -20micron finer grinding at 30 min.
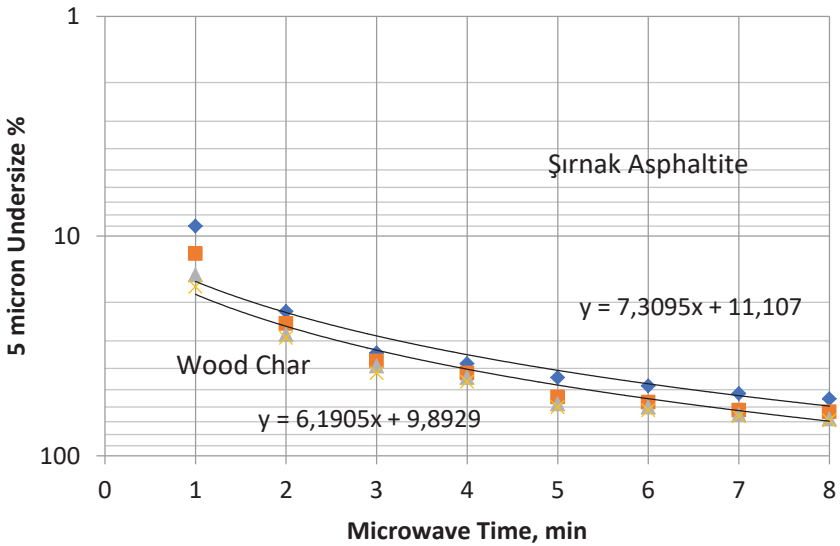
Figure 9. The Bij Breakage rate change for -5μm finer grinding at 30 min.

Over fudamental less grinding periods in a vertical ball mill, there was not any process deteriorations by finer grşnding. The advantageous way was as an fine feed size and fluctuations in max feed size entering the ball mill did not disturbed the grinding media. The mill outlet cause not any change on the material bed in a comparatively shock blocking time. Finer grinding under 5 micron was efficient by slurry medium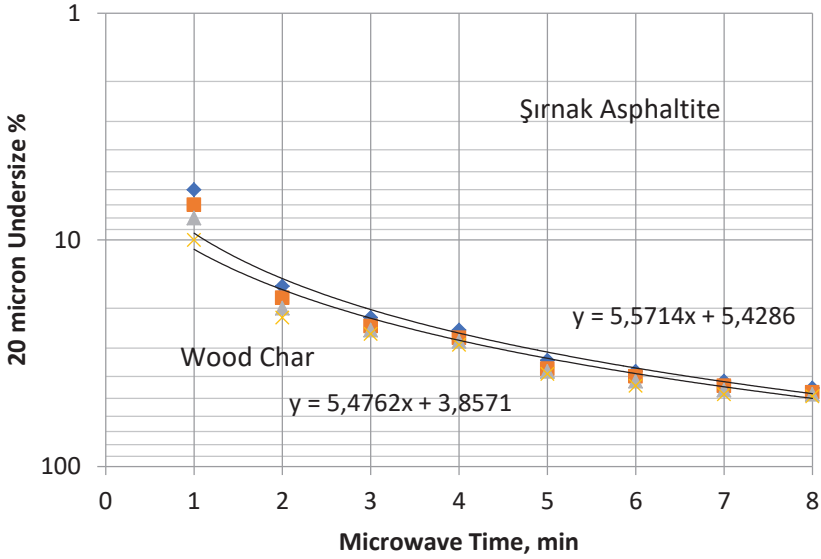 in a vertical ball mill. The ground finer slurry output was so critical for finer size output exceeding the countered time by long term injection of slurry water on the grinding bed.

Bond grndibality and Hardgroove indice value were resulted as 6.6 and 72 for Şırnak shale as given in Table 4. Coal samples were determined much softer than shale samples. Şırnak limestone was medium soft character in comparison to shale and fly ash samples, as illustrated infigure the Bond work of 7.7 value and the values for other lignites reduced from 6.1 to 6.4 identified as soft coals. Bond value of Wood char was 5,1 .HGI values raised from 67 to 89 and MHGI values raised from 46 to 76.

$y = 97,071x^{-0,087}$

$y = 129,61x^{-0,199}$

$y = 80,352x^{-0,169}$

◆ Şırnak Asphaltite Char

■ Fly Ash

▲ Wood Char
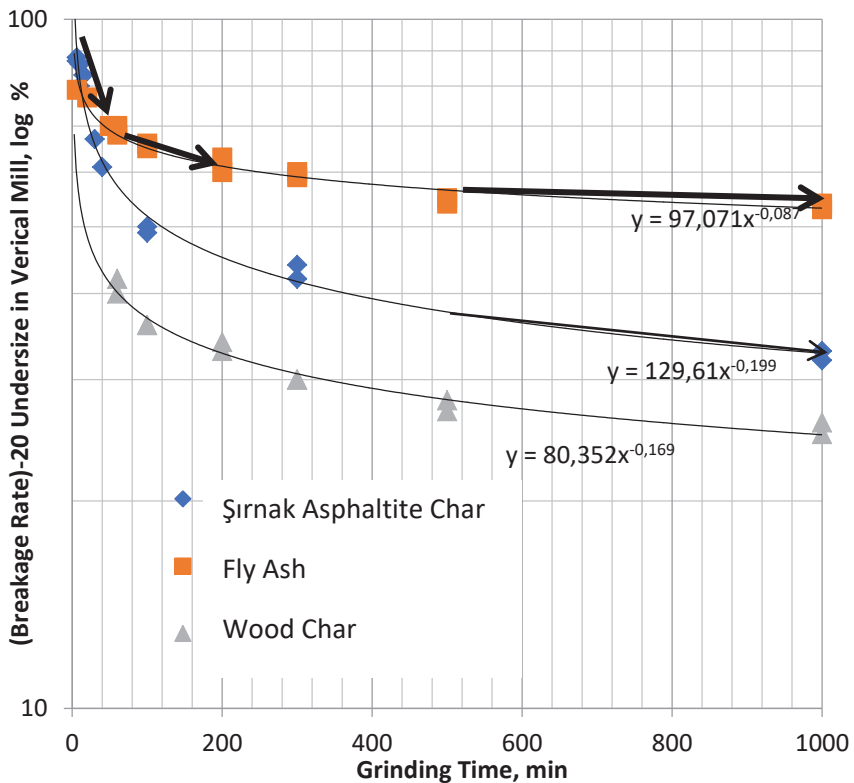
Figure 10. Ultrafine Grinding rate Change over the microwave radiated samples of charbelow20 micron .

At higher size grinding acted by microwave radiation caused to high thermal stress cracks and even propagate length of cracks. As seen from Figure 2 microwave act at 10 minutes time increased cracking and grindability on asphaltite coal samples from 54% and 61%HGI grindability, respectively and 20 micron size grinding rate increased to 22 and 27%, respectively (Figure 7).

The lignite texture showed high amount of inert hard maceral groups was more heterogeneous and even high pore contents in the coarse fractions were a barrier for radiation of microwaves through pores. Coal shale containing over radiated heating and thermal cracked in the coal showed higher grindability.
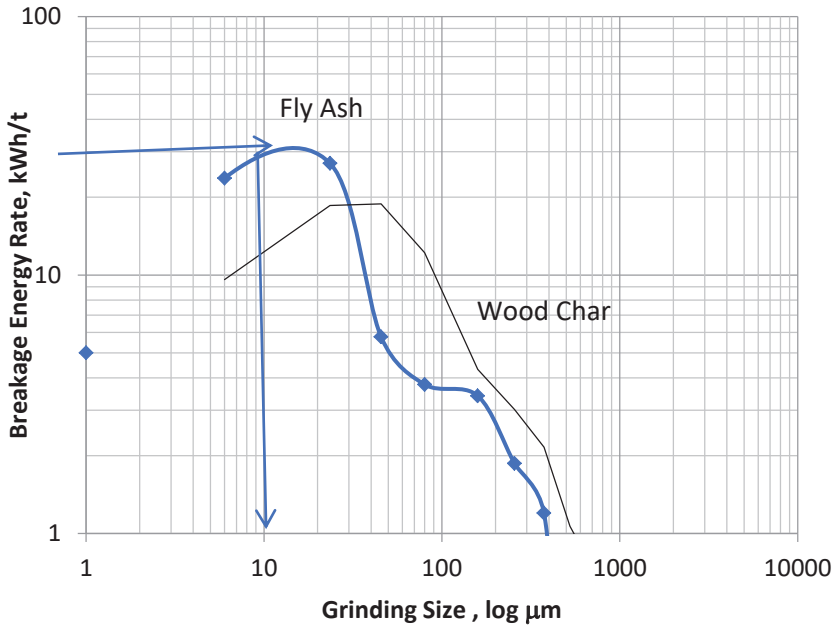
Figure 11. *Breakage Energy Change by the microwave interacted fly ash and wood char samples.*

***Table 5**, Breakage Quality and Energy Change by the product size in vertical slurry mill for calcite samples regarding capacity change.*

Material		Ground Calcite				
Capacity	Tonnes/h	10-12	7,5-9,5	7-8	5-6	3-4
Specific surface area	cm^2/g	11000	14000	15500	17000	19000
$\leq$ 325 M	%	0.015	0.015	0.01	0.002	0
$\leq$2micron	%	32	38	42	50	60
Size: d_{50}	micron	4,5	3,2	2,4	2,0	1,4
Size: $d97$	micron	23	20	16	12	9
Cut point of grain size d_{67}	micron	49	42	35	28	18
Energy	kW/ton	38-40	40-50	54-56	65-72	110-125

The proposed flow sheet for ultrafine grinding of char and carbon materials for pigment and cement additives is illustrated as shown in Figure

Figure 10. *Vertical slurry grinding for char*

4. CONCLUSIONS

The relationships between grinding ability of ultrafine material and flow behavior in the grinder are main operating variables even using radiation act for improve thermal inner cracks. it can be understood that the feed flow rate and media agitation speed are main functions related the ultra fine grinding. The parameters can be developed regarding mill sizes.

The retention time in grinding media and size distribution Gaudin model in the regressed numerical expression changed by the slurry rate function.

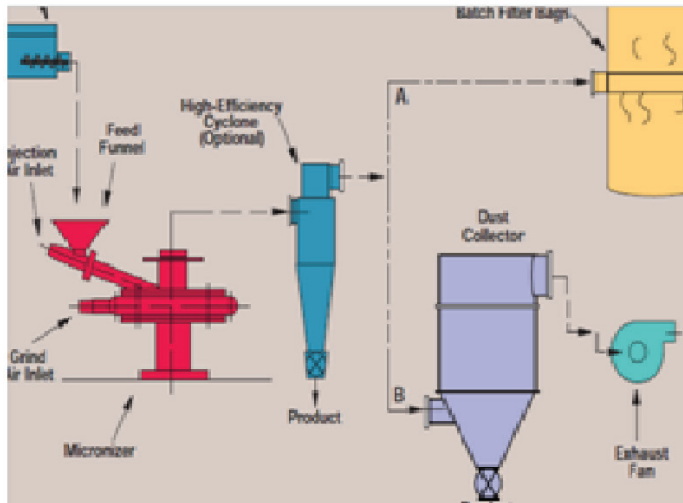Pore size and distribution of the coal, shale and stone massive texture contained micron sized pyrite in 3-1 microns and determined the resistance to wave transfer clogged action with microwave. Bond grinding and HGI Standard index values are tested in this study for Şırnak asphaltite coal and coal shale. The results are determined as advantageous for fine grinding at 200 micron size.

The microwave radiated fly ash and asphaltite samples at each 1-3mm and 0,6-1mm fractions of Şırnak asphaltite, shale and Şırnak marl tested in bond mill showed that radiation time of 10 minutes decreased the index values to 21%, 18% and 11%, respectively and HGI test weight raised to 36%, 21% and 12%. The coal and wood chars and slag as refractive and hard materials showed high ultrafine grinding energy; while it is considered that the optimized model is varied with higher duration time on microwave radiation for ultra fine grinding process.

Mineralogical structure of each char and fly ash, chemistry must be investigated. This is physical properties individually porosity and density and, breaking and grinding qualities of every raw material.

Specific surface area and ultrafine grinding products of clinker and cement affect ultra fine grinding ability, size functions and breakage prompting behaviors. Therefore many optimization and modeling studies should be carried out for the laboratory and pilot scale. In this study, the microwave prompted cracks for both the main raw materials such as limestone and clay aided hard slag and fly ash grinding.

The grinding energy rate kWh/t in conventional ball mill and vertical mill has increased by 22%, 19% for Şırnak asphaltite, 17%, 14% for fly ash, 19%,13% for wood char 17%,11% for asphaltite char, respectively.

Microwave interaction time of 2 min the sample was sufficient heat conduction and thermal expansion explosion may be at 1min exposure while at the same time and shale, high shale coal samples.

Even the porous of wood char was showed an advantage of the resulted crack formation over thermal expansion. Considering the ideal time to increase the interaction of microwave energy costs are defined as the interaction time 2min. The volumetric heating effect with a microwave interaction so that temperature rise over 300°C was observed which would lead to micro cracking and even pressure fractures. Due to magnetite and pyrite in the Şırnak fly ash and Şırnak asphaltite shale at lamella crystals the effect of microwave radiation decreased. However, Şırnak marl and asphaltite shale have showed sufficient fracturing

providing coming off oxidized pyrite surfaces prior to microwave radiations and HGI value increased from 52 to 83. The ultra fine grinding rate of 3.42%/min increased to 5.1. 900 W microwave radiation level of 300 seconds has raised more than 7-8 % /min with higher inter thermal fractures occurred in Şırnak shale particles. Fly ash is differed even after the effect of the radiation pose of 10 min duration.

Abbrevations

W Bond Energy Term

S Specific Surface Brekage Energy

i,j Size Fractions

B Breakage rate by time

**d** Size diameter

n Distribution factor

t time

References

[1]. Armstrong, D.G., 1986. An alternative grindability test: an improvement of the Bond procedure. Int. J. Min. Process. 16, 197–208.

[2]. Austin, L.G., Brame, K., 1983. A comparison of the Bond method for sizing wet tumbling ball mills with a size-mass balance simulation model. Powder Technol. 34, 261–274.

[3]. Berry, T.F., Bruce, R.W., 1966. A simple method of determining the grindability of ores. Can. Min. J. 87, 63–65.

[4]. Bond, F.C., , 1952, The third theory of comminution. Trans. Soc. Min. Eng. AIME 193, 484–494.

[5]. A. Jankovic, 2001, Effect of grinding parameters on the rheology of pyrite–heptane slurry in a laboratory stirred media mill, Engineering, 31

[6]. M. Hasan, 2016, Process modelling of gravity induced stirred mills, Engineering, DOI:10.14264/UQL.2016.507

[7]. Austin L.G., Bhatia V.K., 1973. Note on conversion of discrete size interval values of breakage parameters S and B to point values and vice versa. Powder Technol., 7, 107–110. DOI: 10.1016/0032-5910(73)80013-0.

[8]. Austin L.G., 1999. A discussion of Equations for the analysis of batch grinding data. Powder Technol., 106, 71-77. DOI: 10.1016/S0032-5910(99)00047-9.

[9]. P. J. Hill and K. M. Ng, "New discretization procedure for the breakage equation", AIChE J., 41, 1995, 1204–1216.

[10]. Chen TT, Dutrizac JA, Haque K, Wyslouzil W, Kashyap S. The relative transparency of minerals to microwave radiation. Canadian Metallurgical Quarterly, 1984; 123 (3): 349-51.

[11]. Çayırlı S., Gökçen H.S.,Uçbaş Y., Kayacı K., 2012, Wet Grinding of Sodium Feldspar in a Stirred Ball Mill, Proceedings of XIII International Mineral Processing Symposium, Bodrum, Turkey, pp83-90

[12]. Eyüpoğlu KA., Kaya E, Yavuzkan O., 2012, Breakage Properties of Pumice and Perlite Materials at Different Powder Fillings and Ball, Proceedings of XIII International Mineral Processing Symposium, Bodrum, Turkey, pp57-66

[13]. Genç Ö., Benzer AH., M., 2012, Size Reduction Performance Evaluation of Open Circuit Three Compartment Industrial Scale Cement Grinding Tube Mill, Proceedings of XIII International Mineral Processing Symposium, Bodrum, Turkey, pp67-74

[14]. Gabriel C, Gabriel S, Grant EH, Halstead BSJ, DMP Mingos. Dielectric Parameters Relevant to microwave dielectric heating. Chemical Society Reviews and 1998; 27: 213-23.

[15]. Gökçen HS., Çayırlı S, Ucbas Y.,Kayacı K, 2012, Dry Grinding of

Sodium Feldspar in a Stirred Ball Mill, Proceedings of XIII International Mineral Processing Symposium, Bodrum, Turkey pp21-28

[16]. Haque K. Microwave energy for mineral treatment Processes-a brief review. International Journal of Mineral Processing 1999; 57 (1): 1-24.

[17]. Hosseinzadeh H., Ergün, L., 2012, Determination of Breakage Distribution Function of Fine Chromite Ores with Bed Breakage Method, Proceedings of XIII International Mineral Processing Symposium, Bodrum, Turkey, pp39-48

[18]. Jacob J, Chia LHL, FYC Boey. Review-thermal and non-thermal interaction of microwave radiation with materials. Journal of Materials Science 1995; 30 (21): 5321-7.

[19]. Karra, V.K., 1981. Simulation of Bond grindability tests. CIM Bull. 74, 195–199.

[20]. Kelly RM, NA Rowson. Microwave the reduction of oxidised ilmenite concentrates. Minerals Engineering1995; 8 (11): 1427-38.

[21]. Kingman SW, W Vorster, NA Rowson. The influence of mineralogy on microwave assisted grinding. Minerals Engineering 1999; 13 (3): 313-27.

[22]. Marland S, Han B, Merchant, Rowson N. The effect of microwave radiation on coal grindability. Fuel2000; 79 (11): 1283-8.

[23]. Reimers, G.W., Franke D.W., 1991, Effect of Additives on Pyrite Oxidation, RI:9353, Bureau of Mines

[24]. Şahan H., İpek H., 2012, Dry Grinding Kinetics of Ulexite, Proceedings of XIII International Mineral Processing Symposium, Bodrum, Turkey, pp75-82

[25]. Şener M., Erdemoğlu, M., 2012, Milling of Gypsum for Mechanical Activation, Proceedings of XIII International Mineral Processing Symposium, Bodrum, Turkey pp29-38

[26]. Sword, Ö., 2009, the limestone calcination Microwave Effect of Heat Treatment Applications, Mining, 48, 3, pp 45-53.

[27]. TKI, 2009, The Turkish Ministry of Energy, Energy, Dept., Lignite Coal Report

[28]. Toroman Ö.Y., Uçurum, M., 2012, The effect of various operating parameters on fine grinding in a pilot scale Ball Mill, Proceedings of XIII International Mineral Processing Symposium, Bodrum, Turkey pp13-10

[29]. Tosun YI, a 2014 Chemical Activated Coal Grinding of Turkish Coals by Acidic Mine Water, Geo 14th Conference of SGEM 2014, Bulgaria, p 853-857, doi 10.5593 / sgem2014b13, www.sgem.org

[30]. Tosun YI, b 2014 Chemical Activated Grinding of Cement Raw Materials and Shale by Acidic Waters, 14th imps, Kusadasi, s1-7

[31]. Tosun YI, Rowson NA, Veasey TJ, 1994, Bio-column flotation of Coal

for Desulfurization and Comparison with Conventional and Column Flotation, 5th Int. Conf. of Mineral Processing, Nevşehir

[32]. Vanwyk EJ, Bradshaw SM, JB de Swardt. The dependence of microwave regeneration of activated carbon on the time and temperature. Journal of Microwave Power and Electromagnetic Energy 1998; 33 (3): 151-7.

[33]. Veasey TJ, Fitzgibbon Ka. Thermally assisted liberation-a review. Minerals Engineering 1990; 3 (1/2): 181-5.

[34]. Walkiewicz JW, Kazonich G, McGill SL. Microwave heating andcompounds Characteristics of selected minerals. Minerals and Metallurgical Processing, 1988; 5 (1): 39-42.

[35]. Walkiewicz JW Clarke, McGill, SL. Microwave assisted grinding. IEEE Transactions on ındustryapplications 1991; 27 (2): 239-43.

[36]. Wheelock T.D., 1979. Chemical Cleaning. Pp 20-29-49. J. W. Leonard K.K. Humphrey (Eds) Coal Preparation (4th Edt.), AIME, NewYork.

[37]. Xie DK, Pickles CA. Microwave caustic leaching of electric arc furnace dust. Minerals Engineering2000; 13 (1): 79-94.

[38]. Yoon, R.H.,1991. Advanced Coal Cleaning, Part2. J. W. Leonard and B. C. Hardinge (Eds) Coal Preparation (5th Edt.), SME-AIME, Colorado.
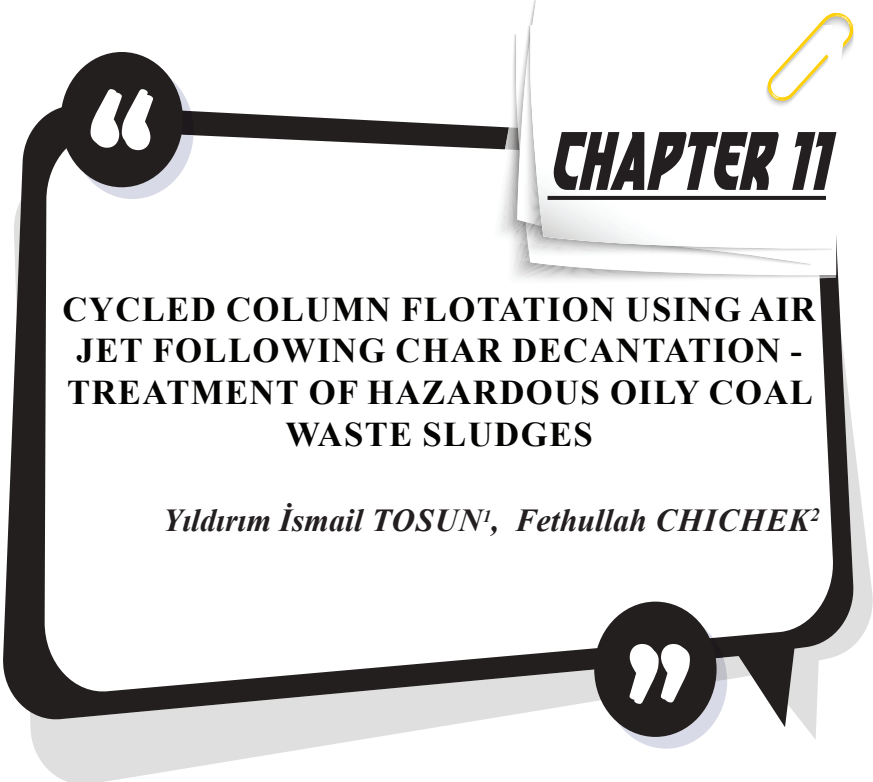
CHAPTER 11

CYCLED COLUMN FLOTATION USING AIR JET FOLLOWING CHAR DECANTATION - TREATMENT OF HAZARDOUS OILY COAL WASTE SLUDGES

Yıldırım İsmail TOSUN[1], Fethullah CHICHEK[2]

1   Şırnak University, Engineering Faculty, Mining Engineering Department, Şırnak, 73000, Turkey   yildirimismailtosun@gmail.com
2 Azerbaijan National Academy of Science, Radiation Institute, Baku, Azerbaijan fcicek66@gmail.com

1. Introduction

Oily slime column flotation process, char slime and ashes physical, chemical qualities, type of char, microwave act improves sludge treatment. Flotation of oil sludges is a valuable method by taking advantage of its physicochemical properties of oil foam separation flotation with carrier materials such as char is one of common treatment methods for toxic slurries [1-3]. Flotation separation is basically efficient in washing treatmentr of oily slurries, leachate or toxic metal effluents realized by taking advantage of their is a type of distinction [4-7]. Oily seepages have low oil solutions as slurry (10^{-2} M). The susceptor char heat the oily slurries in microwave radiation [8]. Column flotation is even practised in counter current air sluryy feed flows in Jameson cell. The following clarification operation use thickeners or plate settler type separators and drum type filters. Microwave aided column flotation, the surface of chars carry oily hydrocarbon droplets on the char particles affiliated with char [8]. Flotation used in different industrial applications [9-20], in the waste water treatments commonly using the frothing parameter, depending on the bubble – oil contact, sludge load of tank by an agitation. The interacting the magnitude of microwave radiation of the loads in terms of separation performance is gaining importance. The different flotation methods and equipment and major industries are summarized as given below.

- In the food industry, separating the shell from grain grains,

- Environmental engineering, cleaning of polluted water,

- Acquisition of bacteria and micellar crystals in biology and pharmacy,

- In the recovery of silver from photography, bath water and films,

- Removal of oils from industrial and refinery plant residues,

- Textile industry, removal of sulfur from rayon baths,

- Removal of blood from slaughterhouse waste water,

- Lalex, carbon black, activated carbon and soot recovery,

- Removing dyestuffs from residual water,

- In the processing of nuclear reactor wastes,

- Biochemical oxygen demand of wastewater in sewage treatment plants in reducing,

- In the processing of white waste water in the paper industry,

Among these methods, cycling column frothing, cycling washing effect of the waste waters containing toxic chemicals and oily metal effluents, the principle of frothing change. Aeration of waste waters is also managed for various sparging regarding capacity, preference of O2 mass transfer to water is based as given in Table 1. [6-20]

Table 1. Aeration method used for waste water treatment [6-20]

Aeration	Method	Advatageous	Disadvantageous	O2 Mass Transfer Rate(%)	O2 Mass Rate (kg O2/kW.h)
Fine bubble	Ceramic diffusor	Well mixing, Well transfer, Low energy, Low cost of operation	High capital and low life time.	10–30	1,2–2,0
Coarse Bubble	Flexible disk	Low cost of operation, fix no clugged	Low transfer High energy	4–8	0,6–1,2
Mecanic	Blade distribution	Low energy Low cost	Low mixing Low rate		1,2–2,6
Jet sparging	Pneumatic Air	Low cost High capacity Well transfer	clugged nozzle and pump need	10–25	1,2–2,4
Radial Flow	Rotor 20–60 rev/min	Rotor fixed, Revelotion is change,	Capital high, thaw , Cost of fix	-	1,2-2,4
Axial Flow	300–1200 rev/min	Well mixing, mass transfer Capital low	Thaw in cold, High cost of fix		1,2-2,4
Retort	High flow	Well oxidation	High capital not flexible		1,2-2,4
Turbine	High turbulent flow	Well mixing High capacity	Nozzle, Reductor, High energy High capital		1,0–1,5

Char particles contact to hydrophobic oil water bubble interface by each micelles bond at the long apolar molecular level.

The cavitation system is a team of bubbles generated by the cavitation system preaction or Feed Air Jet developed by Eriez Flotation Division for increase the recovery of fine and super-fine particles [22-23]. This type of sprinkler uses the principle of the cavitation system is made up of the hydrodynamic cavitation for the generation of Cavitation Tubes (Figure 1). A pump yields extremely small bubbles recirculated. The air is passing through the pulp manifolds in parallel pipes. In the column pico-bubbles yield, as little the operation a fraction of the non-floated pulp bubbles [24-37] by the greater the surface area of the bubbles volume. In the leach tanks slimes favor the probability of bubble contact recirculation and through a

pipe leach tank system – oxidation of particle by gas injection (Figure 2), and therefore it will improve the carried air/slurry gas uptake quality fed to the pulp manifold.

Figure 2. Pumping cavity circulated Aeration of slurry in Column Flotation tank (Eriez Company)[23]

The micro-bubbles generated by cavitation adhere naturally to the surface from the particle, increasing the probability of flotation, since the micro-bubbles act as a secondary collector, reducing thus the collector consumption, in addition improvement the probability accession particles - bubble, and increase the probability of attachment.[38-44] This micro bubbles caused by cavity circulation slurry leads to a substantial improvement in recovery, especially of particles fine / super-fine which are usually difficult to recover, and has also observed that it improves the recovery of coarse particles.
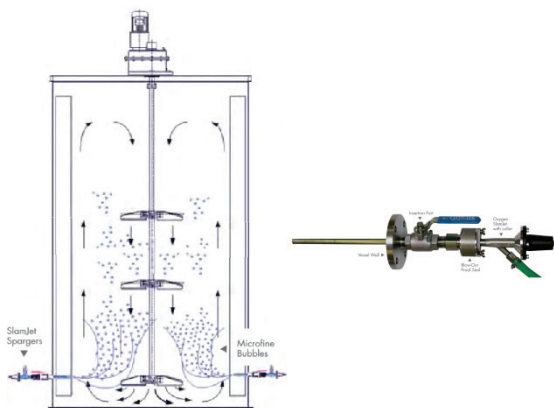

Figure 2. Jet Gas Aeration of slurry in Column Flotation tank (Eriez Company)[23]
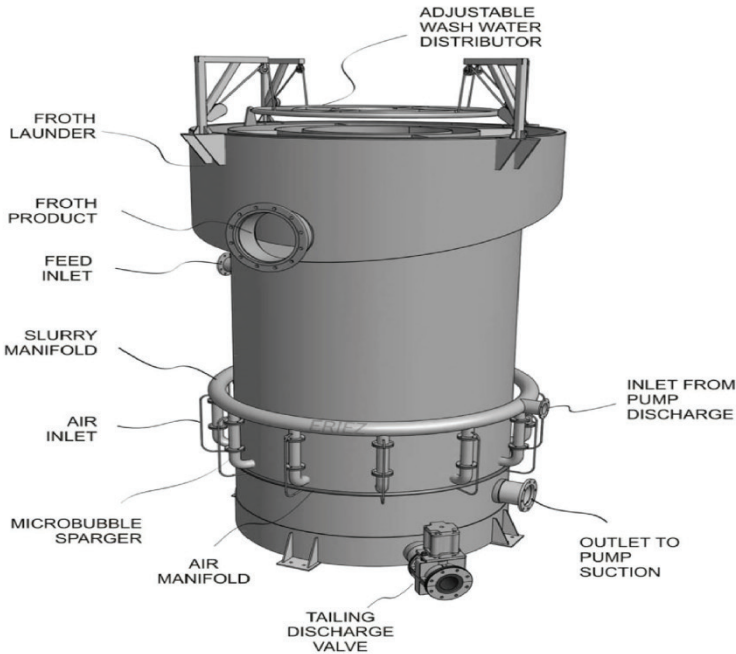
Figure 3. Column Flotation Tank with SlamJet sparging *(Eriez Company)[23]*

SlamJet sparging systems promt the high carrier attachment and recovery of oily hydrophobic particles through the generation of a fine bubble dispersion distributed across the flotation column. Eriez Flotation sparging systems are designed to generate a large amount of bubbles at the optimum size for the carrier column floation application of oily waste waters.

The horizontal flow settlingand aeration and skimming oily froth in waste water treatment plants as using gravity tanks makes very difficult in slimes at finer sizes below 75 micron. Main problems in gravity settling and oily slime effluents mix to clean water at some yield, without decantation [38-41]. The toxic effluents split is caused by the reuse of spoiled chemical ingredients.

The occurrence of situations that may cause pollution such as can be listed as. In this context, active carbon is alternative to water treatment approachs using microwave radiation needed. Flotation separation with cycling column flotation included in the literature recently use char carbon as carrier to froth for separating from pulp as sorbent for heavy metals and oil [32-44].

The rotary drum filtration and decantation treatment with following cycling column flotation in this tests used the slurry of oily seepages in

tailing ponds and industrial mechanics area of Şırnak determined that 2.58% oily particles of the coal slime sludge can be washed char carrier flotation as mentioned [51-53]. Nevertheless, high quality final clean water is concluded that the clean water product could not be obtained. In the studies, high shale content of coal char manages that high metal loaded washing performances are obtained. Fine grain sizes of our country's coals chars and wood char with cycling flotation separation for the reasons stated was examined for waste water treatment. The main critical parameters causin oil floation in waste water treatment are given below: [6-20]

- The pulp must be kept in suspension. To achieve this, the pulp must be stirred. Pulp mixing should be done at a speed that can keep the grains suspended. Precipitate inside the cellmust be prevented. Sandblasting as a general problem. Settled collapse leads to a decrease in cell volume and mineral yield.

- Venting throughout the cell should allow fine air bubbles to be dispersed.

- The amount of ventilation is between 0.1-2 m3 per minute for each 1 m3 volume of the cell volume.

- the important factor in washing oily waste waters by flotation is the weight of the feed. It is to clarify what percentage should be floated.

- Small bubbles (db: 1-5 mm) in the flotation cell as an important factor should be created and distributed. This is a fundamental problem of flotation machines. this is a function. The propellers do not create a dead zone, without any must be able to distribute the air.

- It is necessary to provide calm pulp conditions under the foam phase. A lot of flotation machines are manufactured according to the turbulence conditions in order to ensure the suspension of the grains.

- Again, in these cells, movements are mostly controlled in order to reduce turbidity. the mixing mills used plates (barriers). The turbulence in the pulp should not pass into the foam phase. Otherwise, foam strength and mineral recovery efficiency will decrease.

- The coagulated particles are coming. Mechanical transport of gangue grains with turbulent foam result in recovery increases and decreases the selectivity.

- If the gangue coming into the foam area unintentionally drained back into the pulp (back return) must be allowed. Adding washing water to the foam is the solution for this.

- The desired mineral size must be fed into the foam phase and the slime- bubble coalescence should be increased. Surface property between precious and gangue grains the more the difference, the more successful the selective discrimination.

- Automatically with pulp and foam zone height, propeller speed and air flow rate must be controllable.

- Inner feeding to the surplus short circuit to do must be prevented-cell-to-celltransition It should be facilitated and appropriate equipment should be made to remove the residue in the circuit.

- Froth and residual slime should be taken from separate places.

- After a breakdown, the machine should be easily reactivated and easy to maintain should be.

- Sparging air or oxygen jet sparging system sistemi

2. Microwave Radiated Waste Sludge Oxidation

Coal Char /wood char particle size

Hazardous toxic waste sludges require practical oxidation cracking for hydrocatbon conent and even toxic chelate breakage in the sludge by oxidative chemical reagents or thermal processes [54-61]. Microwave radiation is a thermal cracking mehod feasible due to the fact that the shorter retention time in thin sludge bed with low energy consumption than in other solid-sludge thermal processes. This provides sufficient chemical bond breakage for cracking to ease discard by micelle persistent foaming. Furthermore, high chars allows an sufficient sorption to carbon surface pores and gas sorptions [56]

Microwave Radiated Bed porosity

The bubling gas matter in the froth production reduce the microwave radiation emissivity due to less radiated zone in the gas cavities in the slurries but not on sludge mixtures and sands [53-61]. The sludge was more radated by microwave act on high densed fluid sludges. This is comprised of a sellective radiation base on solid contents of sludge high-performance oxidation by help a suitable solid matter of inhibitor or stabilizer [55-61].

3. Experimental Method

3.1. Cycling column flotation Experiment

Micro Bubble Establishing the Mechanism

The inner column slurry feed and separating iner column circulation of feed with produced air sparging developed within the scope of this study is illustrted in Figure 8. The designed cycling column flotation is

basically consists of 2 parts. The first part of the feed column, froth can be produced regularly by micro bubble feed jet inlet counter current manner as occurred in Jameson cell consists of column feed mechanism[16]. In the second part a traditional main froth column cells through which froth generated in the section is transferred without shower primary oily froth available. In the main part, in order to produce cycling pump taking upper cell slurry to bottom cell part so as slime particles at cycling with micro bubbles produced. The most efficient testing load generatied in half an hour flotation time with sufficient froth load weight received and observed. The types of column flotation parameters are given in Table 2. Flowsheet view of cycling column flotation equipment is used in experimentation as illustated in Figure 4.

Table 2.*Cycling column flotation parameters, and froth generation reagents and dosages*

Bias Rate	0,1
Feed Rate	300ml/min
Air Flow Rate	400ml/min
Foam Height	33cm
Column Height	200cm
Feed Column Height	150cm
Column Width	8
Feed Column Width	5
Frother Dosage	150g/t
Collector Dosage	50gr/ton
Char Dosage	%10

In the oil froth recovery, It is evaluated as collector reagent in experimental studies kerosene; at 20-100 /ton feed weight rate reagent. As frothing agent MIBC [(CH3) 2CHCH2CHOHCH3] at 50-150 gr/ton feed weight rate.

As seen in circulation inner column changed micro bubble slime contact with higher yield oily sludge flotation as seen in Figure 4. The schematic drawing of inner bubbling column of the froth generation of column flotation unit does let the char addition. The char and slime mixing and frort product showed the froth color by black char loading in the unit design,

3.2. Preparation of Coal char and wood char Samples

In adjustable way, the jet slurry feeder is provides feeding at the desired speed. Although samples prior to ecolumn flotation the char solid matter is wetted and mixed at weight rate 10 % of wet oily slime and wet conditioned in microwave radiation by fine wood char mix, as happen in conventional thermal oxidations in certain times.
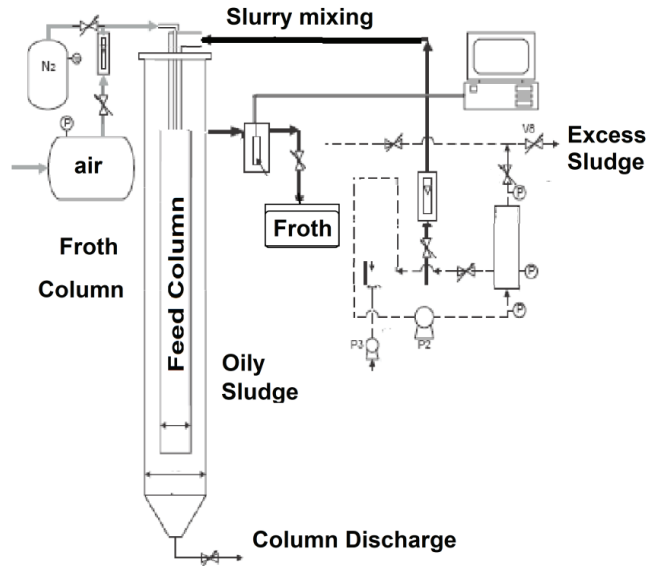
Figure 4 *Cycling column flotation equipment and Froth generation schematic views*

Decantation circuit is illustrated in Figure 5 using experimentation sludges of char and slime sorbed oily matter. The hydrocylone over flow size distributions are given in Figure 6. The oily matter floated in column flotation units are discarded as froth and following hydrocylone decantation overflow is sent to thickner decantation unit rinsing with water in order to receive clean water product even without dissolved oil matter. The particle size distribution was high for wood char and fly ash reaching to below 74 micron at d_{67} value.

Within the scope of this study, different asphaltite char samples obtained from the Şırnak asphaltite mines sized suitable for cycling flotation under 75 micron prepared and used in experiments.
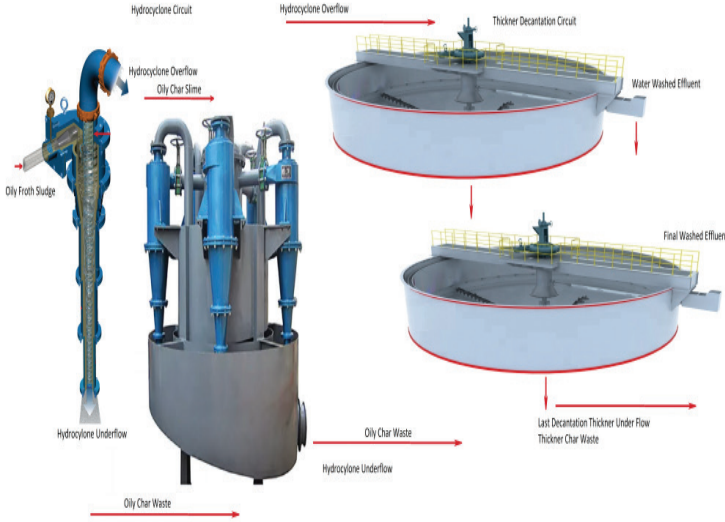
Figure 5. *Decantation circuit, equipment for Oily Froth washing.*

Figure 6. *Particle size distribution of Hydrocyclone Decantation circuit for Oily Froth Overflow.*

Coal samples of Avgamasya 2-1, Avgamasya 2-2 char, Uludere-1 and Uludere-2 char It was obtained from four different chars. Coal char in Avgamasya 2 can not be put into the pile taken from the plant feed Samples represented by the quartering method broken down to -425 μm
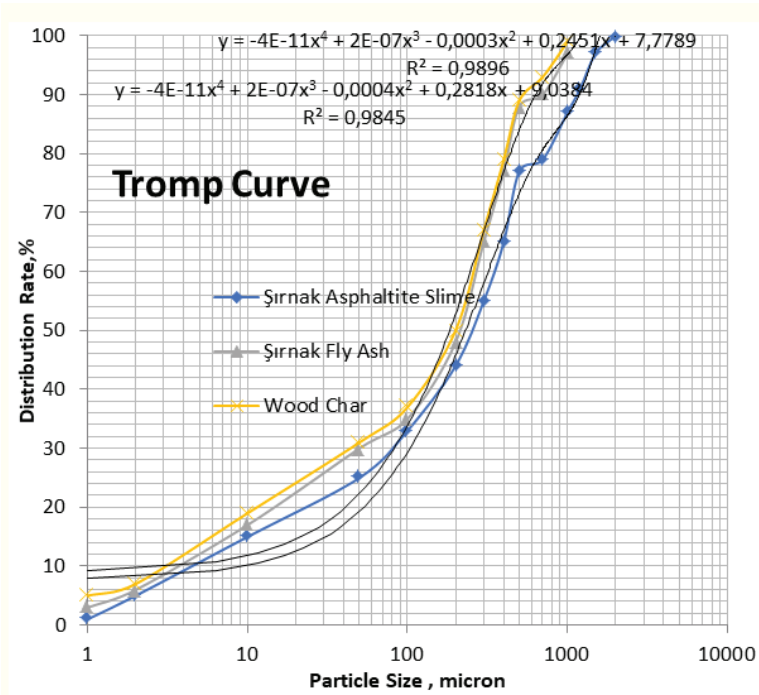
grain size and sieved -212 + 100 and 75 μm grain size fraction has been obtained. The ground 75 μm samples, Avgamasya and Uludere asphltite coals is carbonized at 900 °C in the muffle furnace at 20 mins period as shiny char and hard with low moisture content.

However, the cycling column flotation, the washing method used in studied tests is controlled by equipment parameters are given in Table 2. The chemical compositions of the oily sludge received from mechanic sites and copper leaching plant waste leachate used in the experiments are given in Table4 and 5.

Table 3.*Char types and chemical parameters for hazardous waste water treatment washing*

Oxide Element (%)	Fly Ash	Avgamasya 3 Char	Uludere 2 Char
SiO2	23,35	43,35	41,35
Al2O3	15,68	13,68	16,68
K2O	2,55	2,55	2,55
Fe2O3	12,44	7,24	6,24
Na2O	1,43	2,43	2,43
CaO	21,24	3,24	12,24
MgO	12,64	1,64	2,64
TiO2	0.23	0.21	0.25
MnO	0.27	0.22	0.21
P2O5	0,42	1,42	2,42
Cr2O3	0.1	-	-
Lost in Fire	13.7	-	-
Total	99.53	99.73	99.73

Table 4. *The chemical parameters of Oily sludge for hazardous waste water treatment washing*

Oil,%	Fe	SiO_2	Al_2O_3	CaO
5,93	5.11	54,57	31,33	6.25

Table 5. *The chemical parameters of copper waste leachate liquors for hazardous waste water treatment washing*

Fe (ppm)	Co	Ni	Cu	Zn	As	Cd	Mn	S	P2O5
1251,68	14.98	44.77	13.83	121.94	38.86	81 8	122,5	4264	768
16,8	0.,38		174.67	267,5	41.43	13,17	735,36	27,31 3.	282

Char carbon content is imroving the oily slurry flotation by apolar micelles carried by char to froth easily without dispersion in the treated water phase. The heavy metal sludges in cycling flotation with slurry circulation will improve separation in micro sized bbuble contacts time lengths. The treatment method in this study prompts high washing efficiency oily sludges. In addition, the flotation efficiency with char froth experiments, the weight samples with char sized of -75 μm is determined. This char and fly ash carrier column flotation with circulation in the column

use is tested for the reason of carrying the heavy metal contents in acidic media with neutralization prior to washing decantation. The all parameters and conditions are kept constant with low rate of feeding provided. In sweeping froth is constant with 30 cm height holding position of froth, while pulp level is slightly changed at positive bias rate of 0.1 cm/sn.

4. Results and Discussion

4.1. Avgamasya 2 CharTests

The char froth separation is obtained at first stage cycling separation oil needed to a washing step and a final froth and washing waste water is received as effluent and froth is received as oily char sludge for burning recycle. The results as illustrated in Figure 7, for the cyclic column flotation frothts withwood char 90% oil recavery at 20 mins flotation time, indeed 80% recovery received at 10 minutes column flotation time with microwave conditioned samples. The main advantage of microwave radiation is that of cracking of oily matters and oil carrying to char at low molecular micel weight. The long molecular chains of char micels or coagulates so that will not separate from micro bubbles.
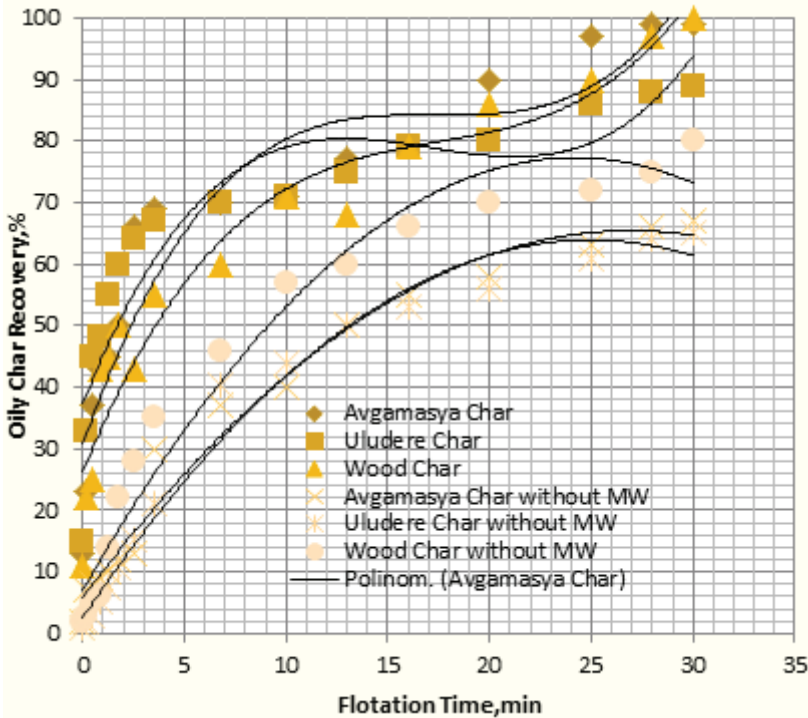

Figure 7. *Char carrier cycling column flotation washing results*

The distinctive method in this study as efficient way of waste water treatment was use of microwave radiated conditioned slurry prior to cycling column flotation with the char samples activatedunder radiation period more.

Various set of oil carrier cycling column flotation by fly ash of Şırnak Thermal power plant is shown in Figure 8.
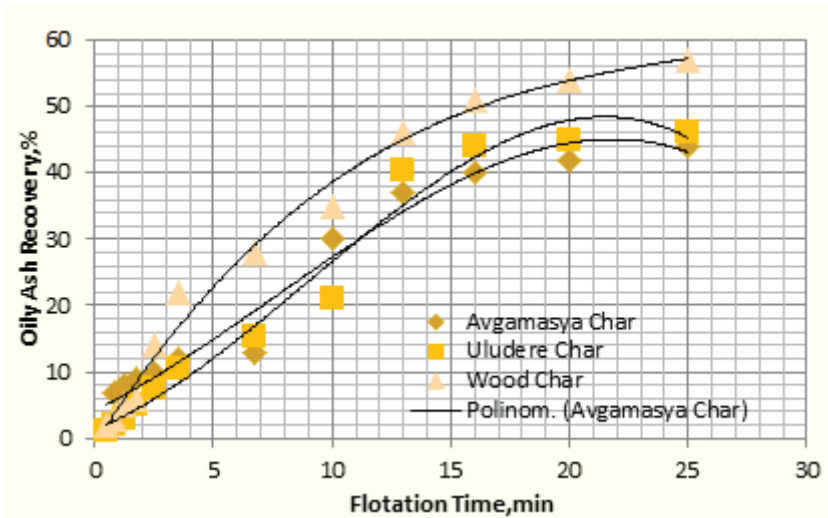
Figure 8 *Char carrier cycling column flotation washing results with 10 % weigh rate fly ash use*

The results of the lower oil capturing by fly ash use at weight rate of 10% , however the density is nearly similar to char about 1,4 -1,6. The fly ash is allowing a good sorption of oil in column flotation by coagulated micel contact to micro particles. They are pulling the oil and coagulated micro oil froth contact is observed. However, this test made, in the feeding char and fly ash total rate is reaching 22.4% reduced to oil yield 57.2%. In char and fly ash cycling column column flotation increased the flotation time in frot zone recovery for oil separation form waste waters, the oil rates are 55.0%. 47.5% and 44.5% of washing phase with wood char, Avgamasya char and Uludere char, respectively.

In char slurry with copper waste leachate content is tested by the micro sparging and flyash use separately as determined high froth load observed. Thus, feeding with the leachate treated with microwave radiation oxidation conditioning at 20 mins time peeriod. Wood char used in froth generated by jet of the slurry samples show that the metal contents yielded in char carrier froth phase reach 54,0%. 52.5% and 44.1% of Fe , Pb, Cd phase yields using washing decantation. (Figure 9)

Fly ash use decreased carrier micro froth load rather than coal char and wood char. Fe, Pb and Cd yields in froth products of copper spent liquor results are given in Figure 8. In addition,
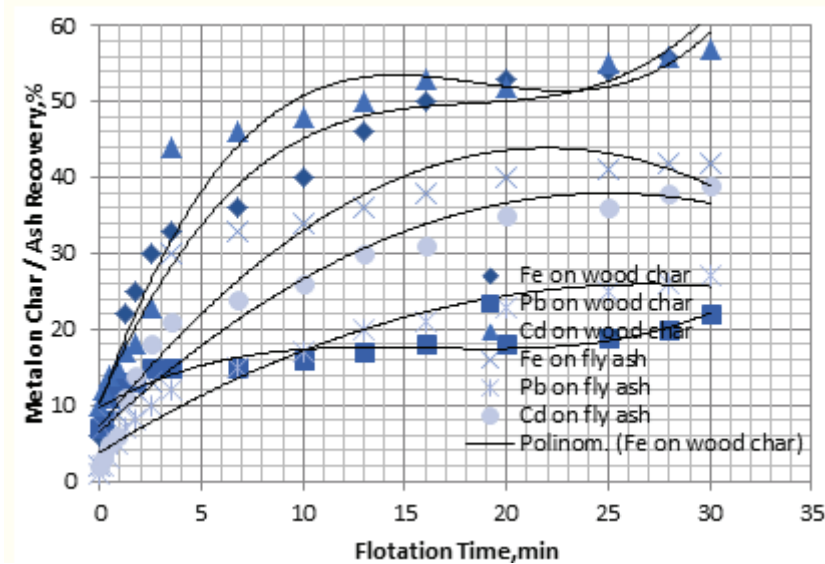

Figure 9. The wood char cycling column flotation washing results

The results shows that 54,4% Pb with char 37,2% Cd with fly ash froth in cycling flotation. However, Pb washing increased to 25,5% with fly ash and dropped to 19,6 % with char. While fly ash Fe carried in finer cycling column flotation at rate of 25% as char use increased to 50,6%. The wood char cycling flotation removed with a yield of 54,1% Cd and 50,6%Fe.

5. Conclusions

This study using cycling column flotation, air jet sparging, microwave conditioned pre treatment prior to column flotation and following washing decantation under consideration oil or spent leachate such as oil, metal cyanides, and heavy metals. As carrier additive to column flotation the use of char managed sorption of oil, sufficient separation at froths was obtained as a result of two stages of washing treatment. By increasing the stage timing or step levels, the froth and decanted clean water is potentially to increase clean washed water quality with oer 8.7 mg/l DO content. However, the carrier char as micro particles at low solid density in the cyclic column flotation in this washing method is economically practiced.

This study using hydrocylone/thickner decantation with following the column flotation offer better washing of oily sludges in microwave sorption separation equipment. In order to investigate effects of active carbon and char fine, its use in the washing treatment was capable for washing hazardous waters of the major industrial refinery and nuclear facilities in

our country. The oily sludge samples contained high level of Pb, Fe, Zn and oil reaching overlimits. The oily asphaltite coal slimes was obtained from two different areas in the Cizre and Şırnak to use in experimental studies. The column flotation separation mechanism developed in Mining Engineering Department was proved to clarification to 3-5 mg/l for the use in agricultural irrigation and tap water. Following the preliminary tests regarding the required microwave load by sorption columns sorption of effluent neutralization and reduction of heavy metals were carried out with hazardous oily sludge samples. As a result of the experimental studies carried out with two different slurries obtained from two different regions, it has been observed that with oil and toxic metal removal efficiencies exceeding 90% in fine grain sizes can be obtained depending on the slurry quality of the oil type and content.

In the sludge microwave radiated oxidation tests were made with asphaltite char at 10 % solid content in the 100 gr sludge containing 25% water decreased to dissolved metal 53mg Fe and total 112mg of Pb, Zn and Cu in the first column output. Likewise, the reduced dissolved effluent heavy metal content at the last column reduced to 6 mg Fe after 10 min microwave radiation oxidation at 47% of final oxidation performance.

References

[1]. Anonymous,2019, DSİ, Water Reports, 10th Regional Directorate, 2018

[2]. K. Kanagamani, P. Geethamani and M. Narmatha, 2020, Hazardous Waste Management, Environmental Issues and Sustainable Development, Suriyanarayanan Sarvajayakesavalu and Pisit Charoensudjai, IntechOpen, DOI: 10.5772/intechopen.94080.

[3]. M. D. LaGrega, P. L. Buckingham, J. C. Evans,2001, Hazardous Waste Management: Chap 13. Land Disposal, pp.812-864, Second Edition, Waveland Press, Illinois,

[4]. Dobby, G., 2002. Column Flotation. In: Mular, A.L., Halbe, D.N. and Barratt, D.J. (Eds.), Mineral Processing Plant Design, Practice and Control, SME Inc., Littleton.

[5]. Yoon, R.H., "Microbubble flotation", "Recovery of coal from waste fines by column, Minerals Engineering, 6, 4, pp. 619-630. (1993)

[6]. Anon. 1973. Outlook: waste water treatment with air flotation. Environ. Sci. Technol., 7: 996

[7]. Arnoldi, H. W., Corning, D. P. and Sykes, R. L. 1980. The application of flotation techniques to the treatment of tannery waste waters. J. Soc. Leather Technol. Chem., 64: 69

[8]. Azad, H. S., ed. 1976. Industrial Wastewater Management, New York: McGraw-Hill.

[9]. Barbery, G., 1984. Engineering Aspects of Flotation in the Minerals Industry: Flotation Machines, Circuits and Their Simulation, in The

[10]. Scientific Basis of Flotation, (K. J. Ives, Ed.), NATO Advanced Institute Services, Series E: Applied Sciences, No. 25, Martinus Nijhoff Publishers, Boston, M.A., pp. 289-348

[11]. Barker, J. E., Foltz, V. W. and Thompson, R. J. 1971. "Treatment of waste oil: wastewater mixture". In Water—1970, AIChE Symposium Series Edited by: Cecil, L. K. Vol. 67, 423New York: AIChE. No. 107

[12]. Churchill, R. J. and Tacchi, K. J. 1978. "A critical analysis of flotation performance". In Water—1977, AIChE Symposium Series Edited by: Bennett, G. F. 290New York: AIChE.

[13]. Clarke, A. N. and Wilson, D. J. 1978. Separation by flotation. Sep. Purif. Methods, 7: 55

[14]. Collins, G. L. and Jameson, G. J. 1977. Double-layer effects on the flotation of fine particles. Chem. Eng. Sci., 32: 239

[15]. Conway, R. A., Nelson, R. F. and Young, B. P. 1981. High-solubility gas flotation. J. Water Pollut. Control Fed., 53: 1198

[16]. Currin, B. L., Kennedy, R. M., Clarke, A. M. and Wilson, D. J. 1979. Electrical aspects of adsorbing colloid flotation. X. Pretreatments, multiple removals, interferences, and specific adsorption. Sep. Sci. Technol., 14: 669

[17]. David, H. T. and Perrett, F. Method of Separating Oil or Similar Impurities from Water. U.S. Patent No. 744171. March 17, 1903.

[18]. Degner, V. R. and Colbert, W. V. Dispersed Gas Flotation Process. U.S. Patent 4,110,210. August 29, 1978.

[19]. Degner, V. R. and Winter, M. K. 1979. "Recent advances in wastewater treatment using induced-air flotation". In Water—1978, AIChE Symposium Series Edited by: Bennett, G.F. Vol. 75, 119New York: AIChE. No. 190,

[20]. Degremont. 1979. Water Treatment Handbook, 191New York: John Wiley & Sons.

[21]. Ellis, M. M. and Fischer, P. W. 1973. Clarifying oil field and refinery waste waters by gas flotation. J. Pet. Technol., April: 426

[22]. Eimco Flotation, 2019, equipment brochure, Envirotech, Salt Lake City, UT

[23]. Eriez Flotation, 2019, Column Flotation, https://www.eriezflotation.com/flotation/column-flotation/

[24]. Yoon, R.H., "Advanced Coal Cleaning and Coal flotation", Journal of Solid Waste Technology and Management, Vol.29, No.3, pp.168-178. (2003)

[25]. Tao, D., Luttrell, G.H., Yoon, R.H., "A parametric study of froth stability and its effect on column Recovery", Meeting, April, 4-5, Virginia. (2006)

[26]. Yoon, R.H. ve Ruttrell, G.H., "MicrocelTM column flotation scale-up and plant practice" flotation of fine particles", International Journal of Mineral Processing, Vol.59, pp.25-43. (2000)

[27]. Tao, D., Li, B., Johnson, B.K., Parekh, B.K., "A flotation study of refuse pond coal slurry", Fuel Processing Tech, Vol.76, pp.201-210. (2000

[28]. Mineral Processing, CIM, paper 12.(1994)Proceeding of the 26 th Annual Meeting Canadian

[29]. Zipperian, D.E., Svensson, U., 2005, "Plant practice of flotaire column flotation machine for metallic and glycol/MIBC mixtures", Minerals Engineering, 18, pp.179-188.

[30]. Tan, S.N., Pugh, R.J., Farnasiero, D., Sedev, R.,Raltson, J., 1988, "Foaming of polypropylene glycols and coal flotation" Column Flotation '88, K.V.S. Sastry (ed), Chapter 7, 43-54. (1988)

[31]. Lai, R., "Cyclonic flotation column for minerals benefication", Mining engineering, 54, No.3,

[32]. Fan, MM. et al, "Nanobubble generation and its application in froth flotation (part I): nanobubble generation and its effects on properties of microbubble and millimeter scale bubble solutions", Mining Sci. & Tech, 20, pp 1-19, (2010).

[33]. T.M. Morris, "Measurement and Evaluation of the Rate of Flotation as a Function of Particle Size", Mining Engineering, Vol. 4, No. 8, 1952, 794-798.

[34]. Jameson, G.J., Manlapig, E.V., "Application of the Jameson cell", Agar, G.E., Huls, B.J., Hyma, D.B., (ed.), Column'91, 2, 675-687. (1991)

[35]. Mankosa, M.J., Luttrell, G.H., Adel, G.T., Yoon, R.H., "A study of axial mixing in column flotation".International Journal of Mineral Processing, 35, 51-64 (1992)

[36]. Peres, A.E.C., Araujo, A.C., Shall, H., Zhang, P., Abdel-Khalek, N.A., 2007. Plant practice: nonsulfide minerals. In: Fuerstenau, M.C., Jameson, G., Yoon, R-H (Eds.), Froth Flotation – A Century of Innovation, SME, Littleton.

[37]. I, Oboh, E. Aluyor,T. O. K. Audu, 2013, Second-order kinetic model for the adsorption of divalent metal ions on Sida acuta leaves, International Journal of Physical Sciences 8:1722-1728

[38]. P. Senthil Kumar*, C. Vincent, K. Kirthika, and K. Sathish Kumar, 2010, Kinetics and equilibrium studies of Pb2+ in removal from aqueous solutions by use of nano-silversol-coated activated carbon,Braz. J. Chem. Eng. vol.27, no.2, São Paulo, https://doi.org/10.1590/S0104-66322010000200012

[39]. H Medhi, P R Chowdhury, P D. Baruah, and K G. B, 2020, Kinetics of Aqueous Cu(II) Biosorption onto Thevetia peruviana Leaf Powder, ACS Omega 2020, 5, 23, 13489–13502, https://doi.org/10.1021/acsomega.9b04032

[40]. Barrera, H.; Ureña-Núñez, F.; Bilyeu, B.; Barrera-Díaz, C. Removal of chromium and toxic ions present in mine drainage by Ectodermis of Opuntia. J. Hazard. Mater. 2006, 136, 846– 853, DOI: 10.1016/j.jhazmat.2006.01.021

[41]. Ahamed, J. A.; Begum, A. S. Adsorption of copper from aqueous solution using low-cost adsorbent. Arch. Appl. Sci. Res. 2012, 4, 1532– 1539

[42]. Medhi, H.; Bhattacharyya, K. G. Kinetics of Cu(II) Adsorption on Organo-Montmorillonite. J. Surf. Sci. Technol. 2015, 31, 150– 155

[43]. Bhattacharyya, K. G.; Gupta, S. S. Adsorption of a few heavy metals on natural and modified kaolinite and montmorillonite: A review. Adv. Colloid Interface. Sci. 2008, 140, 114– 131, DOI: 10.1016/j.cis.2007.12.008

[44]. Gupta, S. S.; Bhattacharyya, K. G. Adsorption of Ni(II) on clays. J. Colloid. Interface. Sci. 2006, 295, 21– 32, DOI: 10.1016/j.jcis.2005.07.073

[45]. Bhattacharyya, K. G.; Gupta, S. S. Adsorption of Fe(III), Co(II) and Ni(II) on ZrO-kaolinite and ZrO-montmorillonite surfaces in aqueous medium. Colloids Surf. A Physicochem. Eng. Asp. 2008, 317, 71– 79, DOI: 10.1016/j.colsurfa.2007.09.037

[46]. M. Abatal, V. C. Quiroz, M. T. Olguín, A. R. Vázquez-Olmos, J. Vargas, F. Anguebes-Franseschi, G. Giácoman-Vallejos, 2019, Sorption of Pb(II) from Aqueous Solutions by Acid-Modified Clinoptilolite-Rich Tuf-

fs with Different Si/Al Ratios, Appl. Sci. 2019, 9(12), 2415; https://doi.org/10.3390/app9122415

[47]. X. Xu, L. Lin, C. Papelis and Pei Xu, 2019, Sorption of Arsenic from Desalination Concentrate onto Drinking Water Treatment Solids: Operating Conditions and Kinetics, Water 2018, 10(2), 96; https://doi.org/10.3390/w10020096

[48]. Ofomaja, A. E.; Naidoo, E. B.; Modise, S. J. Biosorption of copper (II) and lead (II) onto potassium hydroxide treated pine cone powder. J. Environ. Manage. 2010, 91, 1674– 1685, DOI: 10.1016/j.jenvman.2010.03.005

[49]. Bajpai, S. K.; Jain, A. Removal of copper (II) from aqueous solution using spent tea leaves (STL) as a potential sorbent. Water SA 2010, 36, 221– 228

[50]. Chen, H.; Dai, G.; Zhao, J.; Zhong, A.; Wu, J.; Yan, H. Removal of copper(II) ions by a biosorbent—Cinnamomum camphora leaves powder. J. Hazard. Mater. 2010, 177, 228– 236, DOI: 10.1016/j.jhazmat.2009.12.022

[51]. Anonim a, 2015, *Multotec* Şirket web sayfası, http://www.multotec.com/category/ industry/coal

[52]. Anonim b, 2015, *MBE* Şirket web sayfası, http://www.mbe-cmt.com/en/products/pneuflot% C2% AE/pneuflot%C2%AE

[53]. Anonim c, 2015, *CWP* Şirket web sayfası, http://cwp.com.tr/en/products.aspx?id=30

[54]. Salsman J.B., Williamson R.L., Tolley W.K., Rice D.A., 1996, Short-pulse microwave treatment of disseminated sulphide ores. Minerals Engineering, 9, 1, s.43–54.

[55]. Standish, N., Worner, H.K., Gupta, G., 1990. Temperature distribution in microwave heated iron ore–carbon composites. J. Microwave Power Electromagnet Energy 25 _2., 75–80.

[56]. Standish, N., Worner, H.K., Obuchowski, D.Y., 1991. Particle size effect in microwave heating of granular materials. Powder Technology 66, 225–230.

[57]. VanWyk EJ, Bradshaw SM, de Swardt JB., 1998 The dependence of microwave regeneration of activated carbonon time and temperature, Journal of Microwave Power and Electromagnetic Energy ,33, 3, s.151–7

[58]. Veasey TJ, Fitzgibbon KE., 1990, Thermally assisted liberation—a review. Minerals Engineering , 3, 1/2, s.181–5.

[59]. Walkiewicz J.W., Clark A.E., McGill S.L., 1991, Microwave assisted grinding. IEEE Transactions on Industry Applications, 27, 2, s.239–43.

[60]. Walkiewicz JW, Kazonich G, McGill SL., 1988, Microwave heating characteristics of selected minerals and compounds. Minerals and Metallurgical Processing , 5, 1, s.39–42.

[61]. Xia D.K., Pickles C.A., 2000, Microwave caustic leaching of electric arc furnace dust, Minerals Engineering, 13, 1, s.79–94.

INFLUENCE OF ZN COMPOSITION ON THERMAL, ELECTRICAL, MICROSTRUCTURE, AND CORROSION PROPERTIES OF SN-ZN ALLOYS

Fazıl Hüsem[*1], Fatma Meydaneri Tezel[2], Buket Saatçi[3]*

1* Assist. Prof. Dr. Fazıl HÜSEM, Modern Surface Engineering Laboratory (MSE-LAB), Karabuk University, Karabuk 78050, Turkey; TOBB Technical Sciences Vocational School, Karabuk University, Karabuk 78050, Turkey, fazilhusem@karabuk.edu.tr, ORCID ID:0000-0001-9248-365X

2 Karabük University, Faculty of Engineering, Department of Metallurgy and Materials Engineering, 78050, Karabük, Turkey, E-mail: fatmameydaneri@karabuk.edu.tr, ORCID ID: 0000-0003-1546-875X

3 Erciyes University, Faculty of Sciences, Department of Physics, 38039, Kayseri, Turkey. E-mail: bayender@erciyes.edu.tr, ORCID ID: 0000-0002-1351-5279

1. Introduction

Pb and Pb-containing compounds are prohibited from using in European Union because of damaging the environment and human health. Most countries emphasize the limit of lead used in the industry for more appropriate development policies to protect the environment. In this context, significant efforts are made to develop lead-free alternative alloys instead of Pb-Sn eutectic solder alloy [1-3]. Physical and chemical requirements of lead-free solder alloy should be met economically and in other aspects. Sn-Zn eutectic alloy of lead-free solder alloy prominently provides electronic merge without modification. It is expected to be one of the best candidates to maintain the existing production line [1-9]. In addition, both micromechanical and metallurgical properties in terms of controlling the microstructure, strength, a casting alloy is complex in terms of silence and ductility. Thermal variables and their impact on the microstructure morphology depend on the heat transfer solidification conditions, which are affected by the temperature and composition. They have affected all the features directly [11-16]. There are studies related to the effect of temperature, Zn composition, microhardness, and used method; however, the electrical and thermal properties are rarely available in the literature. In this study, our purpose is to examine some physical properties and microhardness according to Zn composition, and the results are discussed.

2. Experimental Procedure

In the current work, the thermal conductivity variation according to composition and temperature were measured first by a radial heat flow apparatus for pure Sn, pure Zn, and Sn-1 wt. % Zn, Sn-9 wt. % Zn, Sn-14 wt. % Zn, Sn-50 wt. % Zn, Sn-80 wt. % Zn alloys. In the second step, the variations of electrical conductivity and resistivity values depending on the temperature and composition were determined from the Wiedemann-Franz law using the thermal conductivity values and their Lorenz coefficients. As the third, the fusion enthalpies (ΔH) and the specific heat capacity changes (ΔC_P) were determined via the DSC device. Finally, the materials' structural properties, surface morphologies, grain sizes, microhardness, and corrosion properties were investigated.

2.1. Sample Preparation and Measurement of the Thermal Conductivity

For various classes of materials having different ranges of thermal conductivity and temperature, various measurement methods are applied for the experimental determination of the thermal conductivity of materials [17-32]. The radial heat flow method is a well-known technique to measure solids' thermal conductivity. In this method, a sample in the form of a circular cylinder with a coaxial central hole, which contains

either a heater or a heat sink, is used [17]. This method was initially applied for measuring the thermal conductivity of solids for pure materials by Callendar and Nicolson [20], Niven [21], Powell [20], McElroy and Moore [22].

At the steady-state conditions, the thermal conductivity of a solid can be obtained by using Fourier's law with appropriate boundary conditions for the radial heat flow, and the temperature gradients are given as

$$\left(\frac{dT}{dr}\right)_S = -\frac{Q}{2\pi r \ell \kappa_S} \tag{1}$$

where κ_S is the thermal conductivity of the solid phase, Q is the total input power from the center of the sample, ℓ the length of the heating element, and r is the distance from the center. Integration of the Eq. (1) for the radial heat flow gives

$$\kappa_S = a_0 \frac{Q}{T_1 - T_2} \tag{2}$$

where a_0 is an experimental constant ($a_0 = \ln(r_2/r_1)/2\pi\ell$), ℓ the length of the heating element, r_1 and r_2 fixed distances from the center of the sample ($r_2 > r_1$), and T_1, T_2 are the temperatures at the fixed positions r_1 and r_2, respectively. Provided that the vertical temperature variation is zero or minimum, the thermal conductivity of the solid phase can be obtained via Eq. (2) by measuring the temperature difference between the two fixed points for a given power level. In the current work, the radial heat flow apparatus was chosen to obtain the thermal conductivity of solids due to its symmetrical characteristics. The details of experimental measurements, graphite crucible, and the radial heat flow apparatus was given in Refs. [20-32]. The thermal conductivity variation according to temperature and composition for pure Sn, pure Zn, and Sn-1 wt. % Zn, Sn-9 wt. % Zn, Sn-14 wt. % Zn, Sn-50 wt. % Zn, Sn-80 wt. % Zn alloys are shown in Fig. 1.
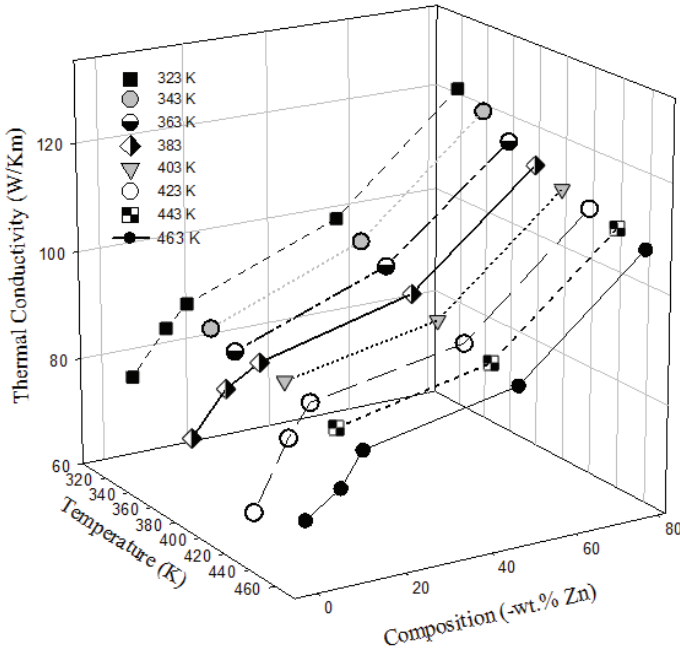
Fig. 1. *Thermal conductivity vs. temperature and composition of Sn-(x) wt. % Zn (x= 1, 9, 14, 50, 80) alloys.*

The temperature coefficients of the alloys were obtained from Eq.(3) for a given composition, the dependence of the thermal conductivity of solid-phase on temperature can be given as [33];

$$\alpha_{TTC} = \left(\frac{1}{\kappa_1}\right)\left(\frac{\Delta\kappa}{\Delta T}\right) \tag{3}$$

where κ_1 is the thermal conductivity at the initial temperature T_1, α_{TTC} is the temperature coefficient of thermal conductivity vs. temperature between $\Delta T = T_2 - T_1$. $\Delta\kappa = \kappa_2 - \kappa_1$, κ_1 and κ_2 are the thermal conductivity at T_1 and T_2, respectively. α_{TTC} can be obtained from thermal conductivity vs. temperature graph, given in Table 1.

2.2. Determination of the electrical conductivity and electrical resistivity

Electrical conductivity is influenced by substances' chemical composition and the stress state of crystalline structures. The electrical and thermal conductivity of metals and alloys in solid and liquid states is mainly carried by free electrons. Therefore, the Wiedemann-Franz-Lorenz law explains the relation between thermal conductivity and electrical resistivity [34, 35]:

$$\frac{\kappa \rho_e}{T} = \frac{\pi^2 k^2}{3e^2} = L_0 \qquad (4)$$

where k is the Boltzman constant, e is the electron charge, and T is the absolute temperature. The constant

$$L_0 = \frac{\pi^2 k^2}{3e^2} = 2.445 x 10^{-8} W\Omega K^{-2} \qquad (5)$$

is the Lorenz number. The Wiedemann-Franz law gives the relation between electrical conductivity and thermal conductivity as,

$$\sigma = \frac{\kappa_S}{LT} \qquad (6)$$

where σ is electrical conductivity, κ_S thermal conductivity of the solid phase at temperature T, and L is the Lorenz number. This relationship is based on the fact that free electrons transport both the heat and electricity in the metals. In the current work, the variation of electrical conductivity according to temperature and composition was determined from the Wiedemann-Franz law by using S and L values. According to Eq. (6), the value of L seems to be constant and independent of the properties of materials. On the other hand, the value of L depends on the properties of materials in the literature. The values of L are well-known for pure materials, but they are unknown for alloys. To determine the variation of electrical conductivity according to temperature and the composition from the Wiedemann-Franz law, the value of L and κ_S. are required. The Lorenz numbers for pure Sn and pure Zn are 2.49×10^{-8} and 2.31×10^{-8} WΩ/K^2 [36], respectively.

$$L_{alloy} = \sum_{n=1}^{2} x_n L_n \qquad (7)$$

Lorentz values for Sn-Zn binary alloys were calculated from Eq. (7). X_n is the percent by weight of the nth component; L_n is the percent of the Lorentz value's n[th] component. The electrical conductivities of Sn-Zn binary alloys according to temperature were determined using L_{alloy} and κ_S values.

Electrical resistivity indicates how strongly a material impedes the flow of electric current, and it is an intrinsic, bulk (not thin-film) property of a material. Electrical resistivity is inversely proportional to electrical conductivity. The variation graphs of electrical conductivity and electrical resistivity with temperature and composition for Sn-[x] wt. % Zn [x=1, 9, 14, 50, 80] alloys are shown in Fig. 2 (a-b) and Fig. 3 (a-b).
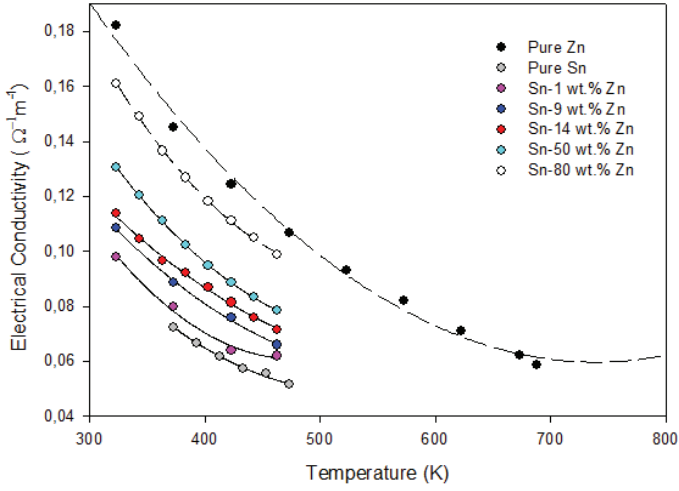
(a)
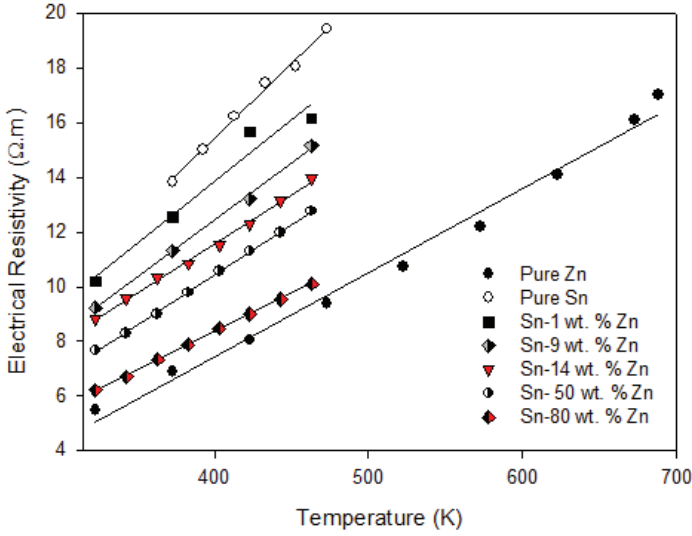
(b)

Fig. 2. a) *Electrical conductivity* **b)** *Electrical resistivity vs. temperature of Sn-x wt. % Zn (x= 1, 9, 14, 50, 80) alloys.*
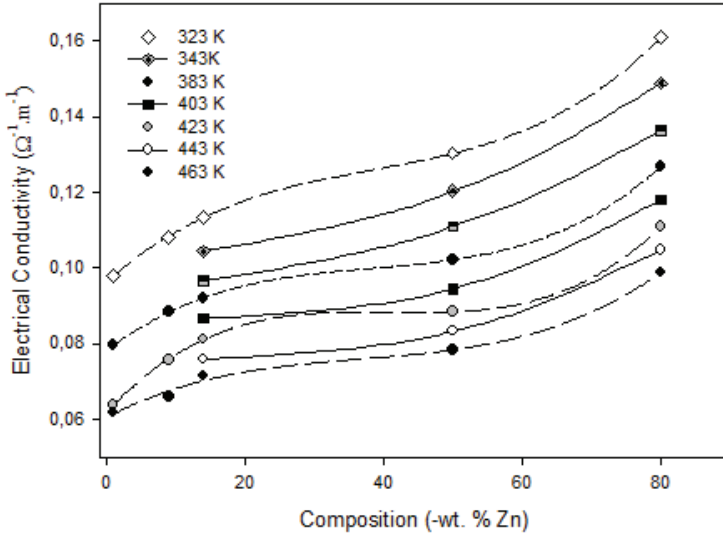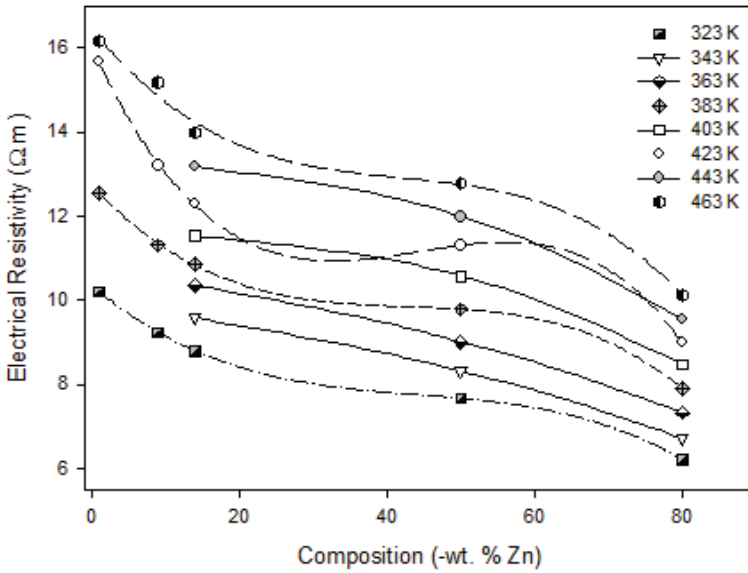
Fig. 3. a) *Electrical conductivity* **b)** *Electrical resistivity vs. composition of Sn-x wt. % Zn (x= 1, 9, 14, 50, 80) alloys.*

The dependence of electrical conductivity on temperature is often expressed as a slope in electrical conductivity vs. temperature graph and can be given as

$$\alpha_{ETC} = (\frac{1}{\sigma_0})(\frac{\Delta\sigma}{\Delta T}) = \frac{\sigma - \sigma_0}{\sigma_0(T - T_0)} \qquad (8)$$

where σ is the electrical conductivity of the solid phase at temperature T, σ_0 is the electrical conductivity at the initial temperature T_0, and α_{ETC} is the electrical temperature coefficient. The electrical temperature coefficients for Sn-[x] wt. % Zn [x=1, 9, 14, 50, 80] alloys were obtained from the electrical conductivity vs. temperature graph and given in Table 1.

Table 1. *Several thermal and electrical properties of Sn-x wt. % Zn (x= 1, 9, 14, 50, 80) alloys.*

Sample	T_0 (K)	T (K)	κ_0 (W/Km)	κ (W/Km)	α_{TTC} (K^{-1})	σ (W-F) (Ω^{-1}m^{-1})	ρ (W-F) (Ωm)	α_{ETC} (W-F) (K^{-1})
Sn-1 wt. % Zn	32	46	78.49	71.08	0.00067	0.0619	16.15	0.00262
Sn-9 wt. % Zn	32	46	86.39	75.42	0.00090	0.0659	15.16	0.00279
Sn-14 wt. %	32	46	90.22	81.39	0.00069	0.0715	13.99	0.00263
Sn-50 wt. %	32	46	101.123	87.06	0.00099	0.0783	12.76	0.00284
Sn-80 wt. %	32	46	121.72	107.10	0.00085	0.1033	9.683	0.00274

2.3. Determination of enthalpy change and specific heat capacity

The molecular structure and phase determine a material's specific heat capacity. Knowledge of the latent heat of phase transitions and the heat capacity of materials are required to understand phase transitions and the thermodynamics of materials. C_P= Specific heat capacity at constant pressure, and the heat supplied to the system will not increase its melting temperature. However, it will supply the enthalpy of fusion (the latent heat of melting) required to convert from solid to liquid. For a transformation from the solid phase to the liquid phase, enthalpy change can be expressed as

$$\Delta H = \Delta C_p Tm \qquad (9)$$

where T_m is the melting temperature and ΔC_P is the specific heat change.

The DSC (Perkin Elmer Diamond model) thermal analysis was performed in the temperature range of approximately 300-900 K with a heating rate of 1°C/min and under a constant stream of nitrogen at atmospheric pressure. The DSC curve of Sn-[x] wt. % Zn [x=1, 9, 14, 50, 80] alloys are shown in Fig. 4. The alloys' enthalpies of fusion (*ΔH*) were calculated as the area under the peak by integration. The values of

specific heat change (ΔC_P) were determined by dividing it by the T_m temperatures of the enthalpies of fusion.
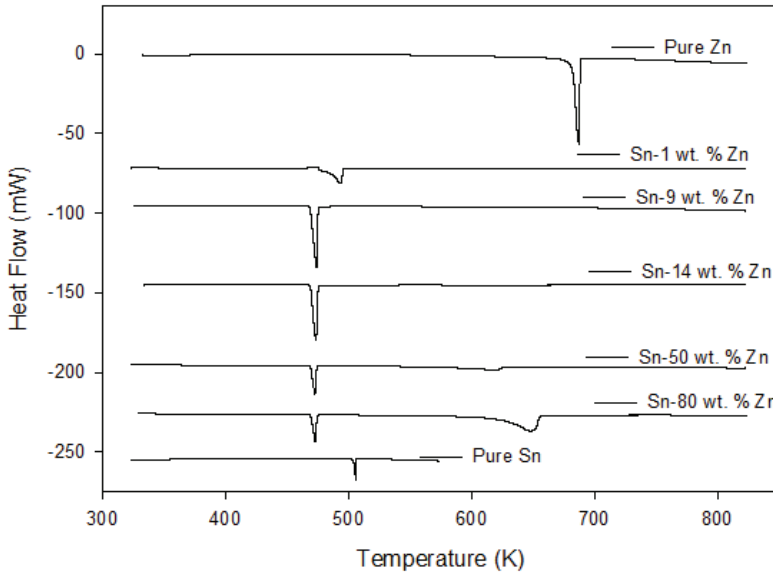
Fig. 4. *Heat flow curves vs. the temperature for Sn-x wt. % Zn (x= 1, 9, 14, 50, 80) alloys.*

2.5. Structural Properties

The samples' surface morphology was investigated using a computer-controlled LEO 440 scanning electron microscope (SEM) equipped with an energy dispersive x-ray (EDX) spectrometer. The sample was cut transversely with ~ 2-4 mm thickness to obtain the SEM images. Transverse sections were ground flat with SiC papers and mechanically polished using 6 μm, 3 μm, 1 μm, and 1/4 μm diamond paste. Then, the etching process was also made to observe the microstructures on samples with 10 ml nitric acid and 90 ml distilled H_2O. The ratio of chemical compositions was measured by an EDX spectrometer attached to the SEM. SEM images and EDX analyses are shown in Fig. 5. A Bruker AXS D8 Advance Model XRD diffraction device was used to determine the grain sizes and crystal structure parameters of the samples; the powder diffraction patterns were taken at room temperature with a 40 mA current and a 0.02 $^{\circ}$/s scanning speed (CuK$_\alpha$ radiation). Grain size (D) was obtained by using Scherrer's formula [37]:

$$D = \frac{0.9\lambda}{\beta\cos\theta} \tag{11}$$

where λ is the wavelength of X-ray used (1.5406 Å), β is the half-width of the peak with maximum intensities, θ is Bragg's angle. XRD diffraction patterns of samples are depicted in Fig. 6. The samples' crystal structural parameters vs. compositions and grain sizes (DSn and DZn) are given in Tables 2 and 3, respectively.
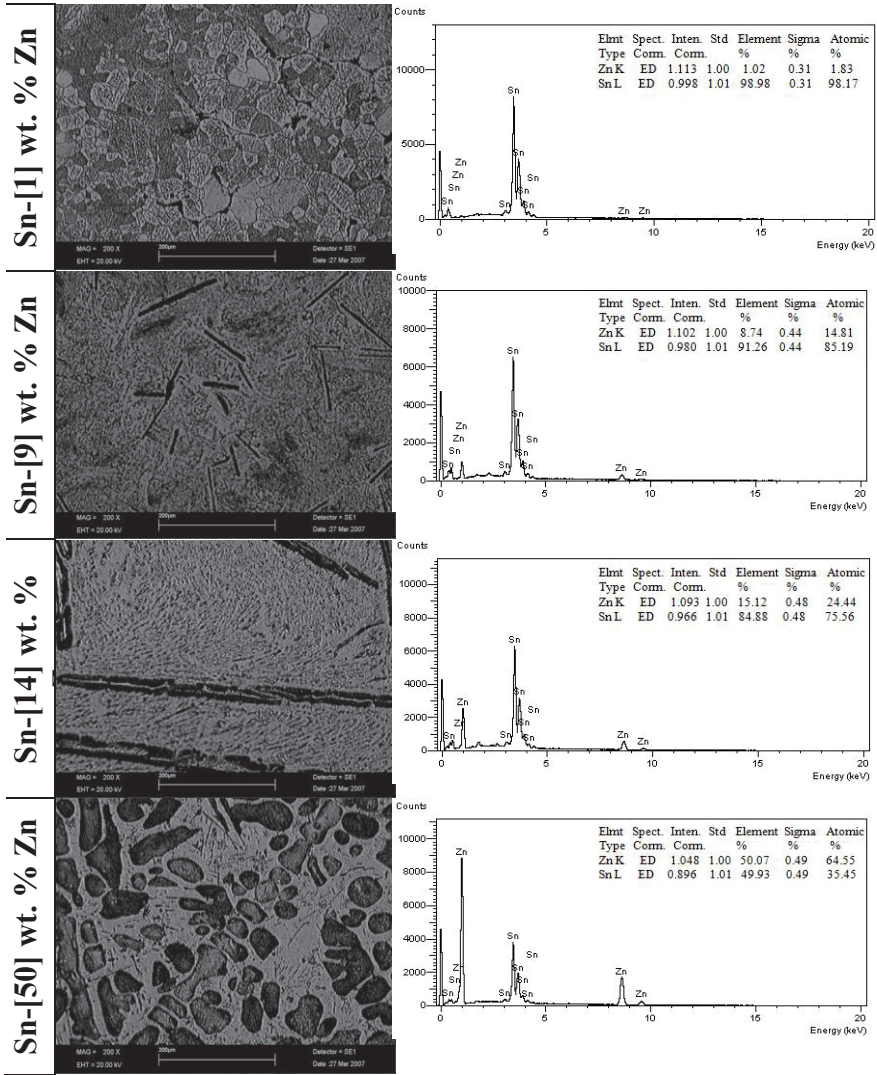
Fig. 5. *SEM images and EDX analyses of Sn-x wt. % Zn (x= 1, 9, 14, 50, 80) alloys.*
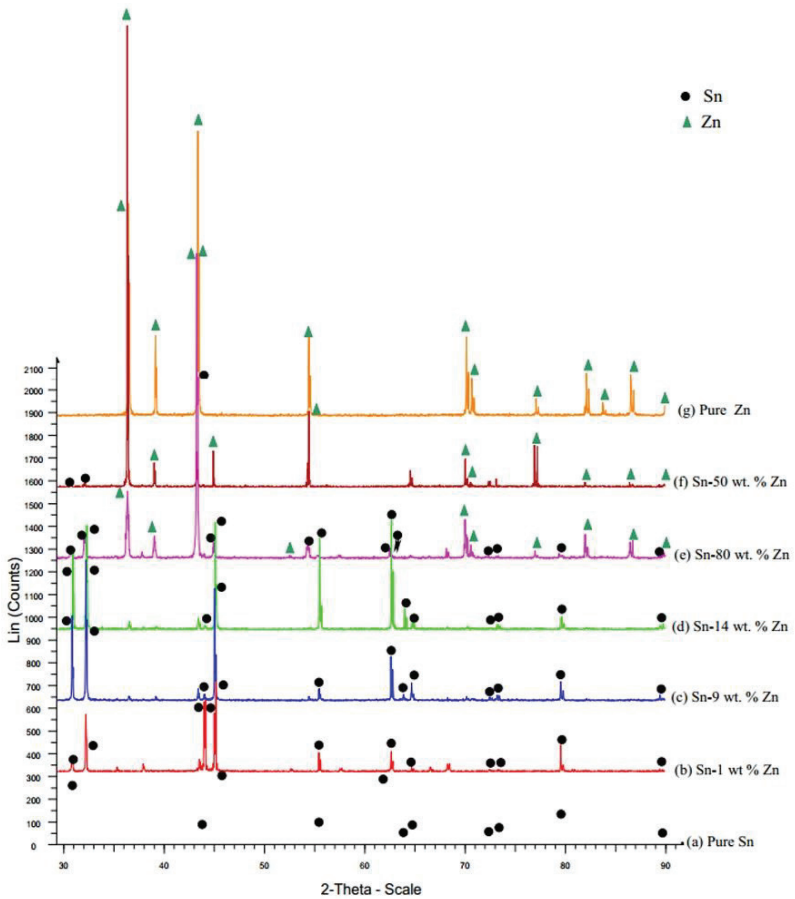
Fig. 6. *XRD Patterns of Sn-x wt. % Zn (x= 1, 9, 14, 50, 80) alloys.*
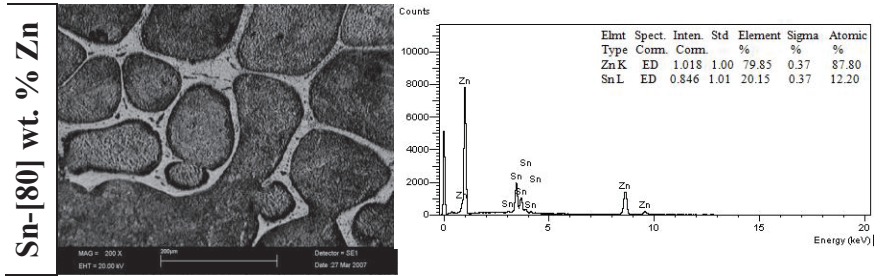
Table 2. *XRD structural analyses of Sn-x wt. % Zn (x= 1, 9, 14, 50, 80) alloys.*

Sample	a (Å)	b (Å)	c (Å)	V (Å)³	2θ (°)	d (Å)	Crystal System
Pure Sn	5.82823 **5.83160***		3.17959 **3.18130***	108.00 108.19	30.680 32.060 43.920 44.940 55.380 62.580 63.840 64.620 72.477 73.180 79.560 89.461	2.91179 2.78952 2.05986 2.01543 1.65768 1.48314 1.45687 1.44116 1.30306 1.29226 1.20389 1.09453	Tetragonal **Tetragonal***
Sn-1 wt. % Zn	5.8215	5.8153	3.1719	107.38	30.681 32.090 43.908 44.060 44.961 45.108 55.399 62.630 64.671 72.468 73.310 79.580 89.483	2.91166 2.78698 2.06038 2.05363 2.01453 2.00831 1.65715 1.48208 1.44015 1.30319 1.29030 1.20364 1.09432	Monoclinic Beta= 90.195
	2.66402		4.94651	30.40	36.297 39.040 43.249 54.349 70.097 70.697 77.063 82.073 83.781 86.569 89.936	2.47300 2.30532 2.09022 1.68665 1.34135 1.33143 1.23655 1.17327 1.15364 1.12351 1.08998	Hexagonal
Sn-9 wt. % Zn	5.82507		3.17762	107.82	30.710 32.091 43.969 44.990 55.431 62.600 63.860 64.670 72.500 73.222 79.580 89.511	2.90899 2.78692 2.05765 2.01333 1.65628 1.48272 1.45647 1.44016 1.30270 1.29162 1.20364 1.09405	Tetragonal
	2.65937	4.61228	4.94560	60.66	36.351 39.053 43.300 54.382 70.148 70.700 76.941 82.161 83.844 86.541 89.930	2.46944 2.30461 2.08791 1.68571 1.34051 1.33139 1.23820 1.17224 1.15294 1.12380 1.09003	Orthorhombic

Sn-14 wt. % Zn	5.8215	5.8090	3.1719	107.27	30.800	2.90070	Monoclinic Beta= 90.039
					32.180	2.77938	
					43.971	2.05759	
					45.050	2.01075	
					55.460	1.65548	
					62.660	1.48143	
					63.980	1.45402	
					64.758	1.43843	
					72.590	1.30130	
					73.280	1.29074	
					79.654	1.20271	
					89.556	1.09361	
	2.6610	4.6018	4.9389	60.48	36.380	2.46759	Monoclinic Beta= 90.375
					39.081	2.30305	
					43.338	2.08613	
					54.578	1.68012	
					70.249	1.33882	
					70.757	1.33045	
					77.148	1.23540	
					82.221	1.17153	
					86.695	1.12220	
					89.839	1.09090	
Sn-80 wt. % Zn	5.83387		3.18294	108.33	30.638	2.91563	Tetragonal
					32.021	2.79282	
					43.879	2.06168	
					44.898	2.01721	
					55.315	1.65947	
					62.513	1.48456	
					63.726	1.45920	
					64.575	1.44206	
					72.383	1.30451	
					73.153	1.29267	
					79.437	1.20545	
					89.379	1.09532	
	2.66530		4.94876	30.45	36.277	2.47437	Hexagonal
					38.978	2.30888	
					43.211	2.09199	
					54.297	1.68815	
					70.045	1.34223	
					70.634	1.33246	
					77.023	1.23709	
					82.050	1.17354	
					86.543	1.12378	
					89.894	1.09038	
Sn-50 wt. % Zn	5.83026	5.83360	3.18438	108.31	32.029	2.79218	Orthorhombic
					43.848	2.06307	
					44.840	2.01970	
					55.264	1.66088	
					64.524	1.44308	
					72.385	1.30449	
					73.134	1.29296	
					79.474	1.20498	
					89.383	1.09528	
	2.66992	4.61037	4.94934	60.92	36.255	2.47581	Orthorhombic
					38.951	2.31043	
					43.174	2.09371	
					54.386	1.68559	
					70.048	1.34218	
					70.683	1.33167	
					76.994	1.23748	
					82.071	1.17330	
					86.488	1.12435	
					89.901	1.09031	

Pure Zn	2.66314	4.94172		30.35	36.360	2.46888	Hexagonal
	2.66500*	**4.94700***		**30.43***	39.060	2.30424	**Hexagonal***
					43.280	2.08881	
					54.401	1.68518	
					70.158	1.34033	
					70.700	1.33138	
					77.120	1.23577	
					82.160	1.17225	
					83.800	1.15343	
					86.600	1.12318	

*Sn Literature: Proc. Phys. Soc., London, volume 67, page 737, (1954): Lee, J.A., Raynor, G.V. *Zn Literature: Natl. Bur. Stand. (U.S), Circ. 539, vol. 0, page 16, (1953) primary reference: Swanson, Tatge.*

2.4. Investigation of Microhardness and Corrosion Properties

The mechanical properties, such as microhardness, mainly depend on the composition, microstructure, and processing temperature [38]. The mechanical properties of any solidified material are usually obtained by tensile strength test, hardness test, ductility test. Therefore, the mechanical properties were monitored by hardness testing since it is one of the easiest methods to apply to determine the structure's mechanical properties. The microhardness measurement was performed at room temperature using a hardness tester device (HMV-2 Micro Hardness Tester Shimadzu). The microhardness measured by the Vickers method is defined as the ratio of the load applied (in kg) to the projected area of the indentation (in mm^2). Vickers hardness measurement was performed to clarify the relationship between microstructure and microhardness.

An optimum load value of 10 g was chosen, and it was applied for 10 s to the sample. Indentations were made at seven different places on the sample to include hardness variation. The accuracy of the microhardness measurement was about ±1%. Due to variation in crystallographic orientations of the sample, the average microhardness value was taken into account, and they are given in Table 3.

Table 3. *Grain sizes and Vickers microhardness values of Sn-x wt. % Zn (x= 1, 9, 14, 50, 80) alloys.*

Samples	Vickers Microhardness (Hv 0.01)	D, Grain Size (nm)	
		D_{Sn}	D_{Zn}
Sn-1 wt. % Zn	11.50±0.11	125.66	45.20
Sn-9 wt. % Zn	12.60±0.12	114.60	53.60
Sn-14wt. % Zn	15.06±0.15	100.50	57.00
Sn-50 wt. % Zn	18.27±0.18	96.00	82.00
Sn-80 wt. % Zn	37.70±0.37	51.63	90.20

The corrosion test was carried out by immersion method. The samples cut with the Secotom 50 precision cutting device were sanded in the range of 240-3000. Their polishing was completed using 9, 6, and 3 µ diamond suspensions. The initial weights of the polished samples were measured with a Kern brand precision balance. Then, their width, thickness, and height were measured using a caliper. A solution was prepared by adding 3.5% NaCl into pure water, and the samples were immersed in the solution and kept suspended for two days. Then they were removed at the end of the second day, dried, placed in a solution consisting of 18% chromic acid-pure water, and cleaned with ultrasonic polishing. They were kept here for 5 minutes, cleaned with alcohol, and dried, and their weight was measured again. The same procedures were applied for the other days. Weight loss vs. time and corrosion rate vs. time graphs are given in Fig. 7a and 7b.
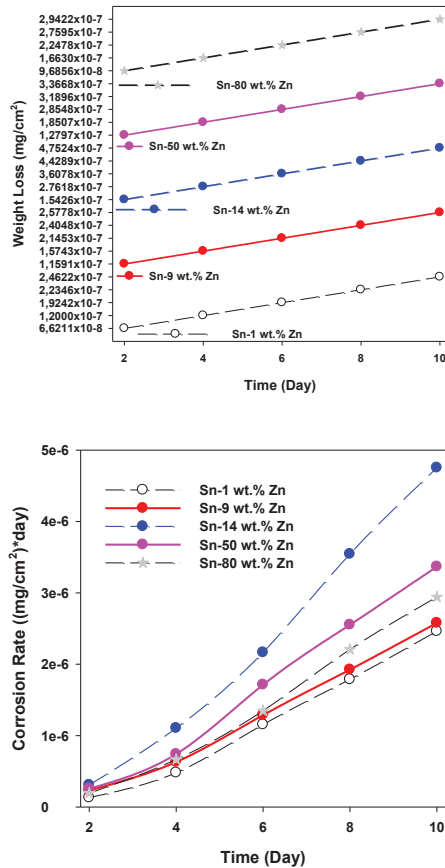

Fig. 7. a) *Weight loss vs. time graph,* **b)** *Corrosion vs. time graph of Sn-x wt. % Zn (x= 1, 9, 14, 50, 80) alloys.*

3. Results and Discussions

3.1. The thermal conductivity and thermal temperature coefficient

The eutectic melting temperature of the Sn-Zn binary system is about 471 K. The thermal conductivities of the solid phase κ_S vs. temperature and composition of Sn-[x] wt. % Zn [x=1, 9, 14, 50, 80] alloys are shown in Fig. 1 and Table 1. According to the current experimental results, the thermal conductivity of Sn-Zn alloys linearly decreases with increasing temperature but linearly increases with increasing Zn's composition for a given temperature. The thermal conductivities vs. temperature of solid phases for pure Sn, pure Zn, and Sn-[x] wt. % Zn [x=1, 9, 14, 50, 80] alloys at approximately their melting temperature are obtained to be 60.60 ± 4.84, 93.28 ± 7.46, 71.08 ± 8.52, 75.42 ± 9.80, 76.08 ± 6.08, 82.53 ± 6.60, 89.62 ± 7.16 W/Km, respectively, and thermal temperature coefficients of the same materials are also calculated to be 0.00098, 0.00086, 0.00067, 0.00090, 0.00069, 0.00099, 0.00085 K^{-1}, respectively. In the current work, the obtained κ_S values are consistent with κ_S values of Sn-based alloys found by Arı et al. and Kaygısız et al. [39-41]. The thermal conductivity values differ depending on alloys' bulk stoichiometry and structural defects. In addition, phonon-phonon and phonon-electron inelastic scattering at high temperatures are more intense. Also, Sn-Zn solubility is limited due to the atomic radius, valence values, and crystal structures of Sn and Zn; crystal lattice is distorted, and while thermal conductivity with temperature is decreased, it is raised by increasing Zn composition.

3.2. The electrical conductivity, resistivity, and electrical temperature coefficient

The electrical conductivity and electrical resistivity vs. temperature and composition of Sn-Zn alloys are shown in Figs. 2-3. The variation of electrical conductivity and electrical temperature coefficients according to the component and temperature for the same materials were determined to be 0.0619 ± 0.007, 0.0659 ± 0.007, 0.0715 ± 0.008, 0.0783 ± 0.009, 0.1033 ± 0.011 (1/Ωm) and 0.00289, 0.00185, 0.00262, 0.00279, 0.00263, 0.00284, 0.00274 K^{-1}, respectively, from the Wiedemann-Franz law by using the values of thermal conductivity, and are also given in Table 1. The dependency of electrical conductivity on the composition of Zn linearly increases with the increasing Zn composition for a given temperature. According to these results, the linear increase of the electrical conductivities for Sn-Zn alloys may be considered transmission provided by the maximum electrons on the composition of Zn. The number of mobile charge carriers in a metal depends on the carrier's concentration on Fermi energy. Free electron concentration in metals (finite temperatures like at room temperature) does not change with

increasing temperature since it is already too high to contribute new electrons. The obtained κ_S values are consistent with Sn-based Sn-Zn and Sn-Cd alloys found with the four-point probe technique by Arı et al. [39, 40].

3.3. Determination of enthalpy change and the specific heat

Regarding DSC analysis of Sn-[x] wt. % Zn [x=1, 9, 14, 50, 80] alloys, the peaks are increased with increasing Zn composition. However, there are two peaks of Sn-50 wt. % Zn and Sn-80 wt. % Zn alloys. According to Sn- Zn phase diagram, Sn solubility in the Zn phase is negligible (less than 0.06 wt.%). Since the matrix phase creates Zn, two peaks, which belong to both Sn and Zn phases, occurred. The sum of the area under the two peaks for these alloys gives the fusion enthalpy. The specific heat capacities of Zn and Sn peaks are calculated by dividing the enthalpy of fusion changing by the melting temperatures that these peaks are observed. For other pure and alloy systems, specific heat capacity change is calculated by dividing the fusion enthalpy values, the area under the curve, by the melting temperature that peaks occurred. At melting temperatures, the enthalpy values of fusion (ΔH) of pure Sn, pure Zn, and Sn-[x] wt. % Zn [x=1, 9, 14, 50, 80] alloys were calculated to be 62.96 J/g, 113.19 J/g, 68.95 J/g, 71.71 J/g, 77.88 J/g, 95.64 J/g, 109.38 J/g, respectively. Also, the change of specific heat (ΔC_P) for pure Sn, pure Zn, and Sn-[x] wt. % Zn [x=1, 9, 14, 50, 80] alloys were detected to be 0.124 J/gK, 0.145 J/gK, 0.151 J/gK, 0.165 J/gK, 0.202 J/gK, 0.221 J/gK and 0.239 J/gK, respectively. In literature, the values determined for enthalpy of fusion for Zn and Sn are 108 and 58.9 J/g [42, 43], respectively, and the values of specific heat change for pure Zn and Sn are 0.390 0.117 J/gK [42-44], respectively. ΔH values for Sn-based alloys found by Wu et al. [45] have changed from 43.1 to 50.1 J/g, and ΔC_P values at 303 K from 0.210 to 0.269. There is no study involving the enthalpy and heat capacity changes according to composition and temperature for Sn-Zn alloys. However, our results seem to be in line with Wu et al.'s results, obtained from Sn-based alloys.

3.4. Structural Properties

The crystal structure and crystallization orientation were determined with XRD measurement (Fig.6). The crystal orientation, the diffraction angles and Bragg's interplanar spacing, crystal structures, and their parameters are given in Table 2. The average grain size (D) for Sn and Zn phases of each alloy system was calculated by the X-Powder computer program according to the higher intensity peak of XRD patterns using Debye Scherrer's Formula and are given in Table 3. In this study, the solubility decreases with increasing Zn, and the Sn phase gets thinner while Zn grain size increases. Similarly, as the amount of Zn increases,

the tetragonal crystal structure will turn to a monoclinic crystal structure, then to orthorhombic, and finally to the hexagonal structure. Surface morphologies are explored by SEM with 20.000x magnification and given in Fig. 5. According to the SEM analyzes, the surfaces are made up of different-sized spheres. There is no crack on the surface. In the Sn-based Sn–Zn binary alloy, the acicular-shaped α-Zn phases are homogeneously distributed in the β-Sn matrix. While the matrix phase moves to Zn, in other words, Zn composition increases, grains tend to get a spherical shape, and a small amount of dissolved needle-like eutectic structure, which also contains the Zn phase, is located along the grain boundaries. The EDX profile and the elemental analysis confirmed that the phase consisted of Sn and Zn, as presented in Fig. 5.

3.5. Microhardness and Corrosion Properties

Microhardness measurements of Sn-[x] wt % Zn [x=1, 9, 14, 50, 80] alloys were calculated from average microhardness measurements of Sn and Zn phases and Sn-Zn grain boundaries in microstructures. Solidification conditions of Sn-[x] wt. % Zn [x=1, 9, 14, 50, 80] alloys are same. So, microhardness values only depend on the composition and the increase of Zn composition. Average microhardness values of Sn-[x] wt. % Zn [x=1, 9, 14, 50, 80] alloys are given Table 3. The variation of Zn amount highly impacts the grain size, and flake or needle shape distributions of Zn phase in Sn matrix result in different effects on hardness. Also, the microstructures shift from the tetragonal solid solution phase to the monoclinic and orthorhombic solution phase and then the hexagonal phase. Lattice distortion increases because of the difference in radii. Grain sizes increase by dissolving in each other with the increase of Zn composition. The grain boundaries between two different phases also form a barrier against the movement of dislocations, and dislocations in the grain boundaries with large-angle are accumulated in the grain boundaries and play an important role in increasing the microhardness of the alloy. In literature, the microhardness values of Sn-based Sn-1.2wt.% Cu [46] and Sn-9Zn-0.5Al [47] alloys are, on average, 11.36 and 18.3, respectively. The microhardness values of Sn-based Sn–Zn, Sn-Zn-Ag, Sn–8Zn–3Bi, Sn–8Zn–3Bi–0.25Ni, Sn–8Zn–3Bi–0.5Ni, Sn–8Zn–3Bi–1Ni alloys by Ahmed et al. [48] and Billah et al. [49] are in agreement with microhardness values measured in the current work.

As shown in Figure 7 in the 10-day immersion corrosion test results, the mass loss of Sn-[x] wt % Zn [x=1, 9, 14, 50, 80] alloys increases with the increase of Zn composition. The corrosion rate for all samples also increased with the increase of the Zn ratio in the structure. The sample with the highest corrosion rate is Sn-[14] wt. % Zn, the eutectic sample. The reason for the low corrosion rate in alloys with a high Sn ratio (Sn-[x] wt. % Zn [x=1, 9) is the formation of a passive $SnCl_2$ or SnO_2 thin

film. The formation of a ZnO thin film layer on the surface prevented the corrosion rate in alloys with a high Zn ratio (Sn-[80] wt. % Zn) [50].

4. Conclusions

The main conclusions of this review may be summarized as follows:

The thermal and electrical conductivity values for Sn-Zn alloys were investigated by using a radial heat flow apparatus. The thermal conductivity of the Sn-(x) wt.% Zn (1, 9, 14, 50, 80) alloys linearly decreases with increasing temperature but linearly increases with increasing Zn composition. The thermal temperature coefficients for Sn-Zn alloys were determined from the thermal conductivity vs. temperature graph. The electrical conductivity variation according to temperature for Sn-Zn binary alloys was also determined from the Wiedemann-Franz law by using the values of κ_S and L_{alloy}. According to these results, the linear increase of the electrical conductivity for Sn-(x) wt.% Zn (1, 9, 14, 50, 80) alloys may have resulted from the transmission provided by the maximum electrons the composition of Zn. The number of mobile charge carriers in a metal depends on the carrier's concentration on Fermi energy. The electrical temperature coefficients were determined from the electrical conductivity vs. temperature graph. The enthalpy of fusion (ΔH) and the specific heat change values (ΔCP) for Sn-x wt. % Zn (x=1, 9, 14, 50, 80) alloys were obtained by DSC, and good agreements are observed between our results and Wu et al.'s results, which are obtained for Sn-based alloys. The variation of Zn amount significantly impacts the grain size and flake or needle shape distributions of the Zn phase in the Sn matrix. The crystal structure of the alloys changed first from tetragonal to monoclinic, then hexagonal, and finally to the orthorhombic structure. In short, with the increase of Zn composition, some physical properties such as thermal conductivity of solid phases, electrical resistivity, change of fusion enthalpy, and change of heat capacity are increased. The increase of the Zn ratio in alloys increased the weight loss; the passive thin film layers formed on the surface of the alloys with high Zn and Sn ratios decreased the corrosion rates.

REFERENCES

[1] K. Suganuma, S.H. Huh, K. Kim, H. Nakase, Y. Nakamura, Effect of Ag Content on Properties of Sn-Ag Binary Alloy Solder, Materials Transactions, 42 (2001) 286-291.

[2] K. Suganuma, Y. Nakamura, Microstructure and strength of interface between Sn-Ag eutectic solder and Cu, Journal of Japan Institute Metals, 59 (1995) 1299-1305.

[3] W. Jillek, Training Course on Manufacturing Green Electronics, Effect of Micron Size Ni Particle Addition on Microstructure, Thermal and Mechanical Properties of Sn-9Zn Lead-Free Solder Alloy, City University of Hong Kong, Organized by the EPA Centre, City University of Hong Kong, December 30, 2003.

[4] M.O. Alam, Y.C. Chan, K.N. Tu, Effect of 0.5 wt % Cu in Sn-3.5%Ag Solder on the Interfacial Reaction with Au/Ni Metallization, Chemistry of Materials, 15 (2003) 4340-4342.

[5] M.O. Alam, Y.C. Chan, K.N. Tu, Effect of reaction time and P content on mechanical strength of the interface formed between eutectic Sn-Ag solder and Au/electroless Ni (P)/Cu bond pad [J], Journal of Applied Physics, 94 (2003) 7904-7909.

[6] Y. Chonan, T. Komiyama, J. Onuki, R. Urao, T. Kimura, T. Nagano, Influence of P Content in Electroless Plated Ni-P Alloy Film on Interfacial Structures and Strength between Sn-Zn Solder and Plated Au/Ni-P Alloy Film, Materials Transactions, 43 (2002) 1887-1890.

[7] S.P. Yu, H.J. Lin, M.H. Hon, M.C. Wang, Effects of process parameters on the soldering behavior of the eutectic Sn-Zn solder on Cu substrate, Journal of Materials Science-Materials in Electronics 11 (2000) 461-471.

[8] Y.S. Kim, K.S. Kim, C.H. Hwang, K. Suganuma, Effect of composition and cooling rate on microstructure and tensile properties of Sn-Zn-Bi alloys, Journal of Alloys and Compounds 352 (2003) 237-245.

[9] L. Qi, J. Zhao, X. Wang, L. Wang, Proceedings of the International IEEE Conference on Electronic Product Reliability and Liability, 27-30 April 2004, Shanghai, China, pp. 42-46.

[10] J. Wiese, A. Goedecke, S. Audiger, S. Grebner, W. Schmitt, M. Scheikowski, Development of a Lead Free Solder Paste during the IMECAT Project, EMPC 2005, June 2005, pp. 423-426.

[11] C.T. Lin, K.L. Lin, Contact angle of 63Sn-37Pb and Pb-free solder on Cu plating, Applied Surface Science 214 (2003) 243-258.

[12] I. Shohji, T. Nakamura, F. Mori, S. Fujiuchi, Interface Reaction and Mechanical Properties of Lead-free Sn-Zn Alloy/Cu Joints, Journal of Materials Transactions 43 (2002) 1797-1801.

[13] A Sharif, YC Chan, Effect of substrate metallization on interfacial reactions and reliability of Sn-Zn-Bi solder joints, Microelectron Eng 84 (2007) 328-335.

[14] WR Osório, PR Goulart, GA Santos, C Moura Neto, A Garcia, Effect of dendritic arm spacing on mechanical properties and corrosion resistance of Al 9 Wt Pct Si and Zn 27 Wt Pct Al alloys, Metall Mater Trans., 37 (A) (2006) 2525-2538.

[15] WR Osório, PR Goulart, A Garcia, Effect of silicon content on microstructure and electrochemical behavior of hypoeutectic Al-Si alloys, Mater Lett., 62 (2008) 365-369.

[16] X Wei, H Huang, L Zhou, M Zhang, X Liu, On the Advantages of Using a Hypoeutectic Sn-Zn as Lead-Free Solder Material, Mater Lett. 61 (2007) 655-658.

[17] YS Touloukian, RW Powell, CY Ho, P.G Klemens, Thermal conductivity metallic elements and alloys, vol. 1, Plenum, New York, , 1970, p. 17a.

[18] H.L. Callendar, J.T. Nicolson, Experiments on the condensation of steam. Part I. A new apparatus for studying the rate of condensation of steam on a metal surface at different temperatures and pressures, Br. Assoc. Adv. Sci., Rept. Ann. Meet. 22 (1897) 418-422.

[19] C. Niven, On a method of finding the conductivity for heat, Proc. Roy. Soc. A76 (1905) 34.

[20] R.W. Powell, Further measurements of the thermal and electrical conductivity of iron at high temperatures, Proc. Phys. Soc. 51 (1939) 407.

[21] D.L. McElroy, J.P. Moore, Thermal conductivity, vol. I, Academic Press, London, 1969 pp. 185-239.

[22] M. Gündüz, J.D. Hunt, The measurement of solid-liquid surface energies in the Al-Cu, Al-Si and Pb-Sn systems, Acta Mater., 33 (1985) 1651-1672.

[23] M. Gündüz and J.D. Hunt, Solid-liquid surface energies in the Al-Mg systems, Acta Metall., 37 (1989) 1839-1845.

[24] N. Maraşlı, J.D. Hunt, Solid-Liquid Surface Energies in the Al-CuAl$_2$, Al-NiAl$_3$ and Al-Ti Systems, Acta Mater., 44 (1996) 1085-1096.

[25] F. Meydaneri, B. Saatçi, M. Gündüz, M. Özdemir, Determination of Thermal Conductivities of Sn Zn Lead Free Solder Alloys with Radial Heat Flow Apparatus and Bridgman Type Apparatus, Continuum Mechanics and Thermodynamics, 25 (2013), 691-704.

[26] B. Saatçi, M. Arı, M. Gündüz, F. Meydaneri, M. Bozoklu and S. Durmuş, Thermal and electrical conductivities of Cd Zn alloys, J. Phys: Condens. Mater., 18 (2006) 10643-10653.

[27] B. Saatçi, N. Maraşlı and M. Gündüz, Thermal conductivities of solid and liquid phases in Pb-Cd and Sn-Zn binary eutectic alloys, Thermochim. Acta, 454 (2007) 128-134.

[28] F. Meydaneri and B. Saatçi, Thermal conductivity of solid and liquid phases for Pb-Cd alloys, Journal of Thermophysics and Heat Transfer, 27 (2013), 767-776.

[29] F. Meydaneri, B. Saatçi, M. Özdemir, Experimental determination of solid liquid interfacial energy for solid Sn in the Sn-Mg system, Appl. Surf. Sci., 257 (2011) 6518-6526.

[30] F. Meydaneri, B. Saatçi, M. Gündüz, M. Özdemir, Measurement of solid liquid interfacial energy for solid Zn in the Zn-Cd eutectic system, Surf. Sci., 601 (2007) 2171-77.

[31] B. Saatçi, F. Meydaneri, M. Özdemir, E. Yılmaz, A. Ülgen, Experimental determination of interfacial energy for solid Sn in the Sn-Ag alloy by using radial heat flow type solidification apparatus, Surf. Sci., 605 (2011) 623-631.

[32] F. Meydaneri, B. Saatçi, M. Özdemir, Thermal Conductivities of Solid and Liquid Phases for Pure Al Pure Sn and Their Binary Alloys, Fluid Phase Equilibr., 298 (2010) 97-105.

[33] Y. Terada, K. Ohkubo, T. Mohri, T. Suzuki, Thermal conductivity in Pt-based alloys, J. Alloy Compd., 285 (1999) 233-237.

[34] http://www.rrcap.unep.org

[35] E. Yamasue, M. Susa, H. Fukuyama, K. Nagata, Deviation from Wiedemann-Franz law for the thermal conductivity of liquid tin and lead at elevated temperature, Int. J. Thermophys., 24 (2003) 713-730.

[36] E. Jerry Sergent, A. Krum, Thermal management handbook: for electronic assemblies, Chapter 7, 1998, p. 26.

[37] Robert Mamazza Jr., Don L. Morel, Christos S. Ferekides, Transparent conducting oxide thin films of Cd_2SnO_4 prepared by RF magnetron co-sputtering of the constituent binary oxides, Thin Solid Films 484 (2005) 26.

[38] D. Frear, H. Morgan, S. Burchett, J. Lau, The mechanics of solder alloy interconnects, Van Nostrand Reinhold, New York, 1994.

[39] M. Arı, B. Saatçi, M. Gündüz, M. Payveren, S. Durmuş, Thermo-electrical characterization of Sn-Zn alloys, Materials Characterization, 59 (2008), 757-763.

[40] M. Arı, B. Saatçi, M. Gündüz, F. Meydaneri and M. Bozoklu, Microstructure and Thermo electrical Transport Properties of Cd-Sn Alloys, Materials Characterization, 59 (2008), 624-630.

[41] Y. Kaygısız, Y. Ocak, S. Aksöz, N. Maraşlı, K. Keşlioğlu, E. Çadırlı, H. Kaya, Thermal conductivity and interfacial energies of solid Sn in the Sn-Cu alloy, Chem. Phys. Lett. 484 (2010) 219-224.

[42] R. Hultgren, R.L. Orr, P.D. Anderson, K.K. Kelley, Selected values of thermodynamic properties of metals and alloys, University of California, Jhonson Wiley & Sons, Inc., Berkeley, 1963, pp. 260-264.

[43] http://www.comparisonofmetals.com/en/thermal-properties-of-zinc/model-21-7

[44] http://www.tainstruments.co.jp/application/pdf/Thermal_Library/Applications_Notes/TN011.PDF

[45] Y.K. Wu, K.L. Lin, and B. Salam, Specific heat capacities of Sn-Zn-based solders and Sn-Ag-Cu solders measured using differential scanning calorimetry, J. Elect. Mater., 38 (2009), 227-230.

[46] E. Çadırlı, U. Böyük, S. Engin, H. Kaya, N. Maraşlı, Variations of microhardness with the solidification processing parameters and thermo-electrical properties with the temperature in the Sn-Cu alloy, Kovove Met. Mater., 47 (2009) 381-387.

[47] S.K. Das, A. Sharif, Y.C. Chan, N.B. Wong, W.K.C. Yung, Influence of small amount of Al and Cu on the microstructure, microhardness and tensile properties of Sn-9Zn binary eutectic solder alloy, J. Alloy Compd., 481 (2009) 167-172.

[48] M. Ahmed, T. Fouzder, A. Sharif, A. K. Gain, Y.C. Chan, Influence of Ag micro-particle additions on the microstructure, hardness and tensile properties of Sn-9Zn binary eutectic solder alloy, Microelectronics Reliability, 50 (2010) 1134-1141.

[49] Md. M. Billah, K. M. Shorowordi, A. Sharif, Effect of micron size Ni particle addition in Sn-8Zn-3Bi lead-free solder alloy on the microstructure, thermal and mechanical properties, Journal of Alloys and Compd., 585 (2014) 32-39.

[50] Udit Surya Mohanty and Kwang-Lung Lin, Electrochemical corrosion study of Sn-XAg-0.5Cu alloys in 3.5% NaCl solution, J. Mater. Res., 22 (2007) 2573-2581.